

Copyright © 1997, by the author(s).
All rights reserved.

Permission to make digital or hard copies of all or part of this work for personal or classroom use is granted without fee provided that copies are not made or distributed for profit or commercial advantage and that copies bear this notice and the full citation on the first page. To copy otherwise, to republish, to post on servers or to redistribute to lists, requires prior specific permission.

**CHARACTERIZATION OF EXTREME
ULTRAVIOLET IMAGING SYSTEMS**

by

Edita Tejnil

Memorandum No. UCB/ERL M97/81

12 November 1997

**CHARACTERIZATION OF EXTREME
ULTRAVIOLET IMAGING SYSTEMS**

Copyright © 1997

by

Edita Tejnil

Memorandum No. UCB/ERL M97/81

12 November 1997

ELECTRONICS RESEARCH LABORATORY

College of Engineering
University of California, Berkeley
94720

Abstract

Characterization of Extreme Ultraviolet Imaging Systems

by

Edita Tejnil

Doctor of Philosophy in Engineering - Electrical Engineering and Computer Sciences

University of California at Berkeley

Professor Jeffrey Bokor, Chair

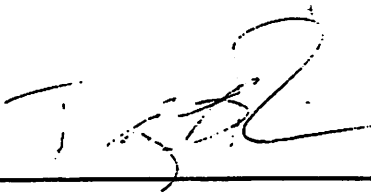
The optical performance of extreme ultraviolet (EUV) imaging systems is investigated. Wavefront-measuring point diffraction interferometry is implemented at extreme ultraviolet wavelengths near 13 nm to evaluate aberrations in near diffraction-limited, all-reflective, multilayer-coated optical systems intended for use in projection lithography at critical dimensions of 0.1 μm and below. Measurements at the operating wavelength yield the overall EUV wavefront quality, which is influenced both by mirror surface profiles and by multilayer coatings. The interferometer design, based on the properties of light diffracted from small pinhole apertures, is suited for highly accurate measurements of wavefront aberrations over a wide range of wavelengths.

A phase-shifting point diffraction interferometer is used to characterize the aberrations of a 10 \times Schwarzschild multilayer-coated reflective optical system at an operating wavelength of 13.4 nm. A sub-aperture of the optic with a numerical aperture of 0.07 is measured to have a wavefront error of 0.090 wave (1.21 nm) rms at 13.4-nm wavelength, due mainly to astigmatism. Chromatic vignetting effects due to the limited transmission passbands of the multilayer coatings are observed via measurements at different wavelengths. The multilayer coating properties that match the measured wavelength-dependent coating effects are found and compared to the coating characteristics from previously reported measurements on individual mirrors.

The EUV interferometry experiments indicate measurement repeatability of ± 0.008 wave (± 0.11 nm) rms at 13.4-nm wavelength in a numerical aperture of 0.07. The

wavefront measurement accuracy is assessed by defocusing the wavefront, by detecting known systematic effects, and by investigating the alignment sensitivity. The measurement quality is probably limited by reference wavefront errors caused by somewhat over-size reference pinhole apertures. The errors in the reference wave are estimated to be roughly ± 0.015 wave (± 0.20 nm) rms in a numerical aperture of 0.07. An independent qualitative verification of the interferometric measurements is also obtained from photore-sist exposure experiments performed on the extreme ultraviolet lithography system for which the Schwarzschild optic was designed. The image quality observed experimentally is consistent with calculations that include the effects of the measured aberrations.

The performance of lithographic optical systems is also investigated analytically by considering the image degradation caused by aberrations. The relationships between the spatial frequencies of the aberrations, the object feature dimensions, and the degree of partial coherence are explored using the theory of imaging with partially coherent light. The effects of aberrations are also evaluated by using aerial image calculations for aberrations having spatial frequencies up to ten cycles over the radius of the imaging system pupil. The aberrations considered correspond to the spatial-frequency regime represented by the first several hundred Zernike polynomials. Furthermore, two figures of merit for quantifying permissible aberrations in imaging systems are proposed.



Prof. Jeffrey Bokor

Committee Chair

Table of Contents

CHAPTER 1. Extreme Ultraviolet Optics and Interferometry - An Overview	1
1.1. Motivation - Extreme Ultraviolet Lithography	1
1.2. Optics and Lithography at Extreme Ultraviolet Wavelengths	2
1.2.1. Optical Properties of Materials at EUV Wavelengths	2
1.2.2. Multilayer-Coated Optics for EUV Lithography	4
1.2.3. Elements of Extreme Ultraviolet Lithographic Systems	7
1.3. Interferometric Characterization of Extreme Ultraviolet Optics.....	11
1.3.1. Testing of Individual Mirrors.....	12
1.3.2. At-Wavelength Characterization of Imaging Systems	13
1.4. Optical Aberrations and Image Quality in Lithography.....	14
1.5. Thesis Organization.....	15
CHAPTER 2. Point Diffraction Interferometry for Testing EUV Optics	17
2.1. Introduction	17
2.2. Conventional Point Diffraction Interferometer	18
2.3. Phase-Shifting Point Diffraction Interferometer	20
2.3.1. PS/PDI Configurations.....	22
2.4. Practical Issues in Point Diffraction Interferometry.....	24
2.4.1. Illumination and Reference Pinholes	24
2.4.2. Beam Overlap and Spatial Filtering of the Test Beam (PS/PDI).....	32
2.4.3. Grating Beamsplitter and Fringe Contrast	38
2.4.4. Source Bandwidth.....	44
2.4.5. Source Spatial Coherence	45
2.4.6. Systematic Coma Effect and Use of Pupil Reimaging Optics.....	57
2.5. Data Analysis Techniques	58
2.5.1. Phase-Shifting Techniques.....	60
2.5.2. Fourier Transform Methods for Single Interferogram Analysis.....	61
2.5.3. Phase Unwrapping and Zernike Polynomial Fitting.....	63
2.5.4. Zernike Polynomial Fitting	63
2.5.5. Removing Systematic Coma Effect	64
2.6. Comparison of Phase-Shifting PDI and Conventional PDI	64
2.7. Conclusion.....	65
CHAPTER 3. Evaluation of Zone Plate Lenses	67
3.1. Introduction	67
3.2. Zonal Placement Errors in Zone Plate Lenses.....	68
3.2.1. Experimental Observations of Far-Field Intensity Patterns.....	68
3.2.2. Calculations of Zonal Error Effects	72
3.2.3. Zone Positioning Errors and Far-Field Diffraction.....	75
3.2.4. Zonal Errors and Optical Performance	77
3.3. Point Diffraction Interferometry of Zone Plate Lenses.....	79
3.3.1. Interferometry Results	79

3.3.2.	Understanding of the Measured Astigmatism.....	80
3.4.	Conclusions	84
CHAPTER 4. Evaluation of the Phase-Shifting Point Diffraction Interferometer with Visible Light..... 85		
4.1.	Overview	85
4.2.	Description of the Visible-Light Interferometer	85
4.2.1.	Interferometer Components	86
4.2.2.	Alignment Considerations	86
4.3.	Verification of Interferometer Capabilities	87
4.4.	Conclusions	93
CHAPTER 5. At-Wavelength Interferometry of a Schwarzschild Optic for EUV Lithography 94		
5.1.	Overview	94
5.2.	Light Source and Beamline Optics.....	94
5.3.	The 10× Schwarzschild System	100
5.4.	Interferometer Configuration	103
5.4.1.	Beamsplitter	105
5.4.2.	Sub-resolution Pinholes	105
5.4.3.	Detector.....	107
5.4.4.	Alignment Strategy	108
5.5.	Results of Interferometric Measurements	112
5.5.1.	Contamination of Mirror Surfaces and Its Influence on Data Analysis	112
5.5.2.	First Measurements - Carbon Contamination Problem	115
5.5.3.	The Aberrations of the 10× Schwarzschild Objective	120
5.6.	Assessment of Measurement Quality	123
5.6.1.	Measurement Stability	123
5.6.2.	Reference Wavefront Quality	125
5.6.3.	Illumination Wavefront Quality.....	130
5.6.4.	Measurement Repeatability	134
5.6.5.	Effect of the Grating Illumination.....	137
5.6.6.	Accuracy Considerations	139
5.7.	Conclusions	145
CHAPTER 6. Characterization of Chromatic Effects Due to Multilayer Coatings 147		
6.1.	Introduction	147
6.2.	Wavelength-Dependent Transmission and Phase	147
6.3.	Understanding the Measured Coating Properties.....	151
6.3.1.	Transmission Properties of the Schwarzschild Optic	154
6.3.2.	Investigation of the Coating Characteristics	156
6.4.	Conclusions	165

CHAPTER 7. Verification of Interferometry with Imaging Experiments	166
7.1. Overview	166
7.2. Imaging Experiments on an EUV Exposure Tool.....	166
7.3. Image Calculations Based on Interferometry Measurements.....	168
7.4. Comparison of Calculated and Measured Image Quality	169
7.5. Conclusion.....	175
CHAPTER 8. Effects of Higher-Order Aberrations on Image Quality in Lithographic Optics	176
8.1. Introduction	176
8.2. Partially Coherent Image Formation in Aberrated Optical Systems.....	178
8.3. Aberration Frequency, Object Properties, and Coherence	182
8.3.1. Effect of a Single-Frequency Phase Aberration.....	183
8.3.2. Aberrations Described by Zernike Polynomials	184
8.3.3. Aberrations and Pattern Properties	186
8.3.4. Dependence of Aberration Effects on Spatial Coherence.....	188
8.4. Investigation of Aberration Effects with Image Calculations	189
8.4.1. Calculation Parameters	190
8.4.2. Calculation Results	193
8.5. Figures of Merit Including Object Properties.....	199
8.6. Conclusion.....	201
CHAPTER 9. Summary and Future Work	203
9.1. Summary of the Research.....	203
9.1.1. Point Diffraction Interferometry	204
9.1.2. Proof-of-Principle Experiments	206
9.1.3. Properties of a Multilayer-Coated Schwarzschild Optic	207
9.1.4. Evaluation and Verification of Interferometer Performance	208
9.1.5. Influence of Residual Aberrations on Lithographic Imaging	209
9.2. Suggestions for Future Work	211
Appendix	213
A. The Zernike Circle Polynomials.....	213
Bibliography	216

List of Figures

CHAPTER 1.	1
Figure 1-1.	Reflectivity and phase of multilayer coatings.....	6
Figure 1-2.	Extreme ultraviolet projection lithography system.	7
CHAPTER 2.	17
Figure 2-1.	Conventional point diffraction interferometer.	19
Figure 2-2.	Phase-shifting point diffraction interferometer.....	21
Figure 2-3.	Power transmission for two PS/PDI configurations.	23
Figure 2-4.	Spatial filtering of lowest-order aberrations by circular pinhole apertures.....	27
Figure 2-5.	Spatial filtering of higher-order aberrations by circular pinhole apertures.....	28
Figure 2-6.	Examples of reference wavefront error in PDI.....	30
Figure 2-7.	Transmission of test and reference beams through the test-beam window.....	33
Figure 2-8.	Spatial filtering of the test beam.	35
Figure 2-9.	Contrast of two-beam interference.	36
Figure 2-10.	Transmission of reference beam through the test-beam window. ...	37
Figure 2-11.	Aberrations of a grating illuminated by a converging/diverging beam.....	41
Figure 2-12.	Fringe contrast and power transmission vs. pinhole size.	43
Figure 2-13.	Probability density function of the phase at two points.....	50
Figure 2-14.	The calculated mutual coherence factor in the illumination wavefront.	56
CHAPTER 3.	67
Figure 3-1.	Measurement of a far-field diffraction pattern from a zone plate...	69
Figure 3-2.	Measured far-field intensity patterns from zone plates.	71
Figure 3-3.	Calculated far-field diffraction patterns from zone plates.	74
Figure 3-4.	Calculated rms variation in the far-field intensity.....	75
Figure 3-5.	Calculated Strehl ratio of zone plates with errors.....	78
Figure 3-6.	Wavefront aberrations of a zone plate lens.....	81
Figure 3-7.	Astigmatism in the reference wavefront.....	83
CHAPTER 4.	85
Figure 4-1.	Introduction of defocus into the tested wavefront.	89
Figure 4-2.	Consistency measurements with the rotation of interferometer components.....	91
Figure 4-3.	Aberrations in a microscope objective.	92

CHAPTER 5.	94
Figure 5-1. Schematic of ALS beamline 12.0.	95
Figure 5-2. Profile of the K-B illuminator focus.	97
Figure 5-3. Flux at beamline 12.0.	98
Figure 5-4. Tunable spatially coherent radiation diffracted from pinhole apertures.	99
Figure 5-5. The 10× Schwarzschild optical design.	100
Figure 5-6. Wavefront error variations over the field of view.	102
Figure 5-7. Configuration of the PS/PDI for testing the Schwarzschild objective.	104
Figure 5-8. Image-plane pinhole spatial filters.	106
Figure 5-9. Intensities obtained during alignment and their Fourier transforms.	111
Figure 5-10. Measured transmission through the Schwarzschild optic.	113
Figure 5-11. Test wave, reference wave, fringes, and analysis domain.	114
Figure 5-12. Change in measurements due to carbon contamination.	116
Figure 5-13. The effect of carbon contamination on phase measurements.	118
Figure 5-14. First measurements of aberrations of the Schwarzschild optic.	119
Figure 5-15. Aberrations in three sub-apertures of the Schwarzschild optic.	121
Figure 5-16. Changes in the measured aberrations with time.	124
Figure 5-17. Image-plane sub-resolution pinholes.	126
Figure 5-18. The average measured wavefront for different reference pinholes	128
Figure 5-19. The effect of reference pinhole misalignment.	129
Figure 5-20. The effect of nonuniform illumination wavefront.	131
Figure 5-21. The effect of input pinhole misalignment.	132
Figure 5-22. Wavefront aberrations on 0.07-NA sub-aperture.	135
Figure 5-23. Long-term reference pinhole changes.	137
Figure 5-24. The effect the grating line placement.	138
Figure 5-25. The change in the measured aberrations with defocus.	140
Figure 5-26. The systematic coma effect.	144
CHAPTER 6.	147
Figure 6-1. Measured transmission and phase vs. wavelength.	148
Figure 6-2. Chromatic aberrations and transmission vs. wavelength.	151
Figure 6-3. Transmission vs. wavelength in different portions of the aperture.	155
Figure 6-4. The center and the bandwidth of the multilayer transmission curves.	156
Figure 6-5. Field of view variations in the multilayer transmission curve.	157
Figure 6-6. Effect of graded multilayer interfaces on transmission.	158
Figure 6-7. Effect multilayer passband mismatch on transmission.	159

Figure 6-8.	Multilayer coating period of Schwarzschild mirrors.....	160
Figure 6-9.	Multilayer model to explain transmission data.....	161
Figure 6-10.	Measured and calculated transmission through the Schwarzschild optic.	163
Figure 6-11.	Measured and calculated chromatic aberrations in the Schwarzschild optic.	164
CHAPTER 7.	166
Figure 7-1.	Schematic of Sandia 10×I EUV exposure system.	167
Figure 7-2.	Exposure field of the 10× Schwarzschild optic.	168
Figure 7-3.	Calculated and printed star resolution patterns.....	170
Figure 7-4.	Calculated contrast of line/space patterns.	172
Figure 7-5.	Line/space patterns printed by the 10× Schwarzschild optic.	173
Figure 7-6.	Printed 0.1- μm line/space patterns.	174
CHAPTER 8.	176
Figure 8-1.	Aberrations with different spatial frequencies.....	177
Figure 8-2.	Description of an optical lithography system.	179
Figure 8-3.	High-order Zernike polynomials.	186
Figure 8-4.	Examples of test aberrations.....	192
Figure 8-5.	Exposure-defocus latitude definition.	193
Figure 8-6.	Dark-field exposure latitude vs. aberration frequency and line pitch.	195
Figure 8-7.	Bright-field exposure latitude vs. aberration frequency and line pitch.	196
Figure 8-8.	Exposure latitude vs. aberration frequency and coherence factor.	198
Figure 8-9.	Periodic bright and dark line ratios vs. aberration frequency and line pitch.	201
CHAPTER 9.	203

List of Tables

CHAPTER 1.	1
Table 1-1. Optical properties of selected materials at 13.4-nm wavelength.....	3
CHAPTER 2.	17
CHAPTER 3.	67
Table 3-1. Estimated zonal errors in several zone plates.....	76
CHAPTER 4.	85
CHAPTER 5.	94
Table 5-1. Optical design parameters of the 10× Schwarzschild system.....	101
Table 5-2. Measurement variations due to different pinholes and their alignment.	133
CHAPTER 6.	147
Table 6-1. Multilayer coating design and measurement for the Schwarzschild objective.....	152
CHAPTER 7.	166
CHAPTER 8.	176
Table 8-1. Image calculation parameters.	190
CHAPTER 9.	203
Table A-1. Zernike circle polynomials used in the data analysis.	214

Acknowledgments

I would especially like to express my appreciation to my advisor Prof. Jeff Bokor for his guidance, support, and encouragement. His useful suggestions and interesting ideas were instrumental to the progress of this work. I would also like to thank Prof. Andrew Neureuther and Prof. Roger Falcone for reviewing this thesis. Additionally, I thank Prof. David Attwood, Prof. Andrew Neureuther, and Prof. William Oldham for their insights and support.

I would like to thank the researchers at the Center for X-Ray Optics at Lawrence Berkeley Laboratory for making the extreme ultraviolet interferometer possible. I appreciate having the opportunity to learn from Hector Medeck. I also thank fellow graduate student Ken Goldberg for his contributions to this work. I acknowledge the technical support provided by Paul Denham, Phillip Batson, Drew Kemp, Senajith Rekawa, and others. I would also like to thank Werner Meyer-Ilse for his help and insightful discussions.

I gratefully acknowledge Charles Fields and Kim Chan of the University of California at Berkeley for their help with the pinhole fabrication. I wish to thank Richard Livengood of the Intel Corporation for providing access to the focused ion beam tool for pinhole fabrication. I also appreciate the pinholes supplied by Erik Anderson of Lawrence Berkeley Laboratory.

I am grateful to Avijit Ray-Chaudhuri and Kevin Krenz of Sandia National Laboratories for the opportunity to perform imaging experiments on their exposure tool and for their help with the experiments.

I would like to express my gratitude to fellow graduate students for helpful and interesting research discussions. I especially thank Bob Socha, Richard Schenker, Regina Soufli, and Charles Fields.

I very much thank my family and friends for their help and encouragement that have in the end allowed me to complete this work.

Lastly, I acknowledge the sponsors who funded this research. This work was funded by the National Science Foundation Graduate Fellowship, the Intel Foundation Graduate Fellowship, the Semiconductor Research Corporation, the Intel Corporation, the Department of Energy Office of Basic Energy Sciences, and by DARPA Defense Advanced Lithography Program.

1 Extreme Ultraviolet Optics and Interferometry - An Overview

1.1. Motivation - Extreme Ultraviolet Lithography

Extreme ultraviolet (EUV) projection lithography is a promising candidate for the mass production of future integrated circuits with 0.1- μm and smaller features [1-6]. This lithography technique is an extension of traditional optical projection lithography to extreme ultraviolet wavelengths. The image of a desired circuit pattern is formed on a semiconductor wafer with an optical imaging system that operates at a wavelength of about 13 nm and a numerical aperture around 0.1. Unlike conventional lithography based on refractive optical components, extreme ultraviolet projection lithography utilizes only reflective multilayer-coated optics because refractive optics are limited by strong absorption of extreme ultraviolet radiation by all materials.

One of the critical challenges for extreme ultraviolet lithography is the fabrication and testing of the optical imaging system that produces the image of the mask on the wafer. In principle, the all-reflective imaging system with a moderate numerical aperture can provide the desired resolution and a sizeable depth of focus at EUV wavelengths. In practice, the desire for nearly diffraction-limited imaging performance at extreme ultraviolet wavelengths places stringent requirements on the optics fabrication. Residual aberrations may be produced by imperfect optical surfaces as well as by multilayer coating defects [7, 8]. The nec-

essary surface and multilayer quality to obtain acceptable residual aberrations on the order of 0.02 waves rms [9] at EUV wavelengths is difficult to achieve. To develop EUV lithography technology, it is important both to experimentally characterize the optical aberrations and to understand the effects of residual wavefront errors on the image quality.

Wavefront-measuring interferometry plays a key role in the fabrication, alignment, and qualification of optical systems, including lithographic stepper lenses. Interferometric characterization of EUV projection lithography optics is necessary to achieve the near diffraction-limited optical performance required for lithography at critical dimensions of 0.1 μm and below. To characterize the aberrations, interferometry with sub-nanometer wavefront-measuring accuracy is required. In addition, measurements at the operational wavelength of 13 nm are needed to characterize the system EUV wavefront, produced both by the figure of mirror surfaces and by multilayer coating properties.

1.2. Optics and Lithography at Extreme Ultraviolet Wavelengths

1.2.1. Optical Properties of Materials at EUV Wavelengths

The primary interactions of radiation with matter, from the extreme ultraviolet to the low-energy x-ray spectral region, are photoabsorption and coherent scattering [10-12]. In the extreme ultraviolet regime, loosely defined as the wavelength range from 40 nm to 5 nm (or the photon energy from 30 to 250 eV), absorption through the photoelectric effect represents the dominant contribution to the overall attenuation. Except for photon energies near the electron binding energies, materials may be modeled as collections of noninteracting atoms and their optical properties described through the atomic scattering factors [10,

11, 13]. Since the specific chemical state of the material is only relevant near the absorption edges, the refractive index can be determined solely from the density of the constituent atoms and the tabulated atomic scattering factors over most of the spectral range.

Material	Density [kg/m ³]	δ	β	10× attenuation thickness [nm]	2 π phase shift thickness [nm]
Silicon	2.33	0.0000573	0.00182	1350	234000
Molybdenum	10.22	0.0765	0.00735	334	175
Silicon Nitride	3.44	0.0257	0.00913	269	522
Nickel	8.90	0.0515	0.0716	34.3	260
Indium Antimonide	7.31	0.0647	0.0700	35.1	207
Cobalt	8.90	0.0660	0.0653	37.6	203
Gold	19.32	0.100	0.0498	49.3	134
Germanium	5.32	0.00539	0.0319	77.0	2490
Carbon	2.20	0.0378	0.0674	364	354
PMMA ^a	1.19	0.0240	0.00551	446	559
SAL 601 ^b	1.15	0.0227	0.00430	570	589
Oxygen gas at 300K	0.00171 ×P [torr]	3.11×10 ⁻⁸ × P [torr]	1.43×10 ⁻⁸ × P [torr]	1.72×10 ⁸ / P [torr]	4.32×10 ⁸ / P [torr]
Nitrogen gas at 300K	0.00150 ×P [torr]	2.79×10 ⁻⁸ × P [torr]	8.20×10 ⁻⁹ × P [torr]	2.99×10 ⁸ / P [torr]	4.80×10 ⁸ / P [torr]

Table 1-1. Optical properties of selected materials at 13.4-nm wavelength.

The refractive index ($n = 1 - \delta - i\beta$), the density, the material thickness needed for optical attenuation by one order of magnitude, and the thickness needed for 2 π optical phase shift relative to free space at 13.4-nm wavelength are listed for several materials and gases. The optical properties of gases depend on the pressure P .

a. stoichiometry: C₅H₈O₂

b. 90% novolak resin (C₈O₁H₉) and 10% melamine (C₃H₆N₆) by volume

At the extreme ultraviolet wavelengths, the complex refractive index of any medium, typically denoted by $n = 1 - \delta - i\beta$, is very close to one [13]. The refractive indices of several materials, including multilayer coating materials, efficient absorbers, photoresists, and gases, are given in Table 1-1 for 13.4-nm wavelength. Since the refractive index components δ and β are often comparable in magnitude, the radiation is usually significantly attenuated before its phase shift changes by a full cycle relative to propagation in free space. In solid materials, the thickness that produces attenuation of about one order of magnitude is commonly in the sub-micron range. Even in gaseous media, the order of magnitude attenuation lengths are typically less than a few meters for pressures above 100 mtorr. As a result, the extreme ultraviolet radiation must be manipulated in a moderate vacuum.

1.2.2. Multilayer-Coated Optics for EUV Lithography

The near unit refractive index, in combination with the strong absorption, make refractive focusing optics at EUV wavelengths unfeasible. Grazing-incidence reflective optics are possible through the specular reflection at grazing angles of incidence [14]. High reflectivities can be achieved by utilizing the total external reflection from mirrors made of materials that have a refractive index whose real part is less than one. However, the imaging performance of grazing-incidence mirrors, which operate over a restricted range of incidence angles, is limited by aberrations [15, 16]. Diffractive zone plate lenses can achieve diffraction-limited resolution over a small field of view at EUV wavelengths [17] but require spectrally pure illumination to avoid chromatic aberrations. The only optical elements that can efficiently manipulate radiation at near-normal incidence angles over a sizeable field of view are multilayer-coated mirrors. The capability to deposit the multilayer

coatings [18-20], comprised of alternating layers of two different materials approximately one-quarter wavelength in thickness, has enabled the development of the extreme ultraviolet optical systems that achieve near diffraction-limited performance and a large field size.

The reflective multilayer coatings produce high reflectivities at EUV wavelengths via constructive interference of the weak reflections from multiple layer interfaces between two materials with dissimilar refractive indices. At an incidence angle θ measured from the surface normal, the reflectivity enhancement is possible at a wavelength λ when the multilayer period d satisfies the Bragg condition for m^{th} -order constructive interference, or $m\lambda = 2d\cos\theta$ [21]. Thus at near-normal incidence the required multilayer period is about $\lambda/2$ and the layer thickness about $\lambda/4$. Owing to the strong absorption at EUV wavelengths, the reflectivity is usually maximized when the more absorptive layer is somewhat thinner than the more transparent layer [21, 22]. Among the useful multilayer material systems [23-25], the highest reflectivities, in excess of 70% near normal incidence [13], can be achieved in principle with molybdenum/silicon (Mo/Si) multilayers near 13.0 nm and with molybdenum/beryllium (Mo/Be) multilayers near 11.5 nm. Because the throughput of the EUV optical system depends critically on the mirror reflectivity [1, 2], the development of multilayers for EUV lithography applications has focused on Mo/Si [26-34] and more recently on the Mo/Be [35].

An example of the reflective properties of a Mo/Si multilayer is given in Figure 1-1, showing the reflectivity and the reflection phase of a perfect 40-bilayer coating with a period d of 6.96 nm and molybdenum-to-silicon thickness ratio Γ of 0.36. For both transverse elec-

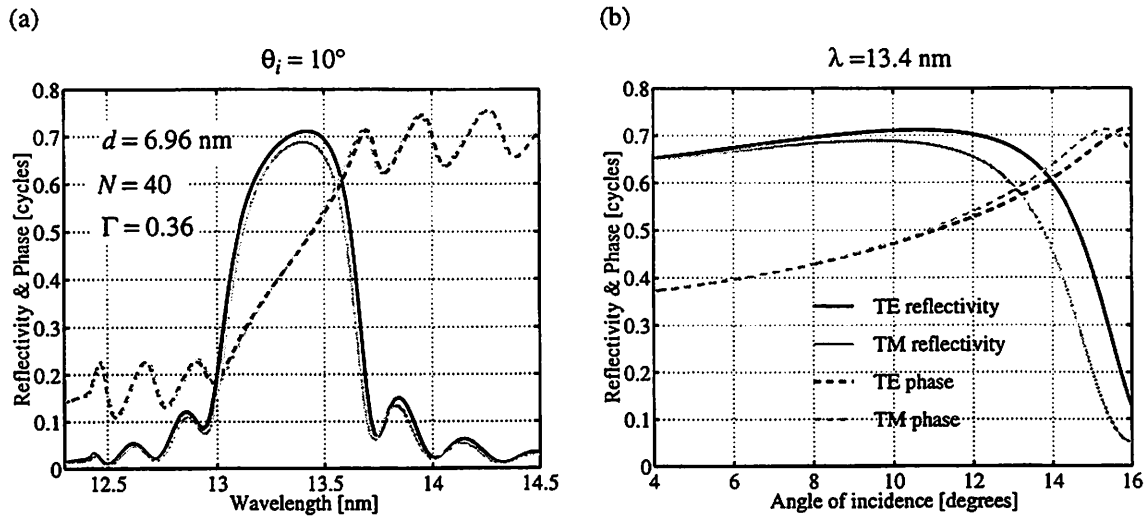


Figure 1-1. Reflectivity and phase of multilayer coatings.

The reflectivity and the reflection phase of an ideal molybdenum/silicon multilayer coating as functions of (a) the wavelength and (b) the incidence angle, for both TE and TM polarizations. The multilayer with $N = 40$ bilayers has multilayer period d of 6.96 nm and molybdenum-to-silicon thickness ratio Γ of 0.36.

tric (TE) and transverse magnetic (TM) polarizations, the reflectivity and phase are shown as functions of the wavelength in Figure 1-1(a) at a 10° incidence angle and as functions of the angle of incidence in Figure 1-1(b) at 13.4-nm wavelength. Since the multilayer is a resonant structure, the high reflectivity is possible within a relatively narrow spectral region and a limited angular range. As a result, the optical designs for EUV projection lithography systems must account for the limited passband of the multilayers in order to achieve uniform transmission through the optics over the entire field of view [8]. As in the reflectivity, the resonant nature of the multilayer coating is also demonstrated in the phase of the reflected wavefront. Within the central transmission lobe, the reflection phase changes by about half a cycle, as shown in Figure 1-1(a). Since phase nonuniformities over the mirror apertures in an imaging system correspond to phase aberrations, the multilayer coating properties can affect the imaging performance. Thus to qualify the performance of

EUV imaging systems, both the multilayer reflectivity and the overall wavefront phase must be characterized [36, 37].

1.2.3. Elements of Extreme Ultraviolet Lithographic Systems

The concept of an EUV projection lithography wafer exposure system is shown schematically in Figure 1-2. The radiation from an EUV light source, collected with a multi-mirror condenser, illuminates a reflective mask. Then a multilayer-coated imaging system produces a demagnified image of the mask pattern on the wafer. A photoresist material on the wafer records the image, which is subsequently transferred into integrated circuit device features. Since the beam is attenuated upon each reflection, the number of mirrors in the system must be small in order to achieve sufficient throughput and to minimize the mirror

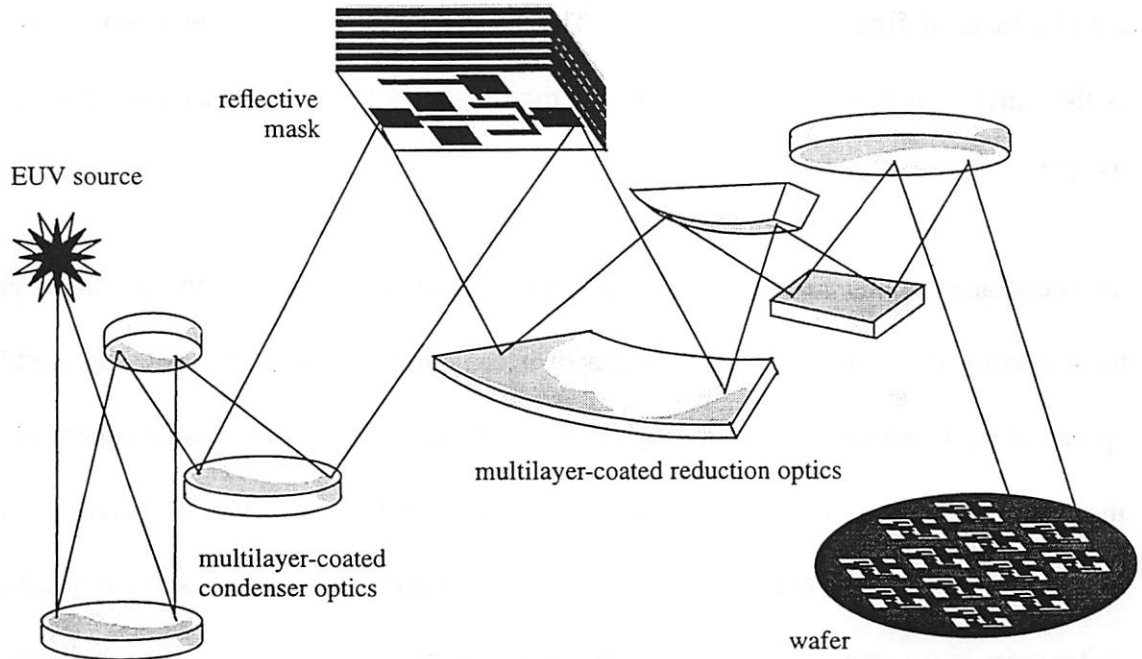


Figure 1-2. Extreme ultraviolet projection lithography system.

The all-reflective EUV projection lithography system consists of a radiation source, condenser optics, a patterned reflective mask, imaging optics, and a photoresist-coated wafer.

heating in the condenser. The small number of surfaces in the imaging optics allows aberration correction over a limited field of view. Thus in order to expose a significant area of the wafer, the mask and the wafer are scanned over the illuminated area of the corrected field, typically a ring segment several millimeters wide and several centimeters long.

The possible radiation sources for EUV lithography include laser plasma sources [38-41], synchrotron radiation [24, 42], and lithium discharge sources [43]. The lithium discharge sources, based on a radiative transition in hydrogen-like lithium at 13.5 nm, are in relatively early stages of development [43, 44]. The large footprint and significant cost of synchrotron radiation sources have restricted their application to EUV lithography. Currently, the most promising candidate for a compact EUV lithography source is a laser plasma source that emits comparatively broadband EUV radiation from a hot dense plasma generated by focused high-power laser pulses. The primary challenge for laser plasma sources is the mitigation of debris from the target that degrades the light collection optics [41, 45-47].

The condenser optics are required to efficiently collect the radiation from the source and to uniformly illuminate the mask pattern over the corrected field of view. The angular spread of the beam incident on the object plane, which determines the spatial coherence in the image formation, must also be uniform over the field. In addition, the beam angular divergence should be symmetric with respect to the desired object features to minimize the differences in the spatial coherence for different feature orientations. Another challenge is posed by the relatively large heat load on the first few condenser mirrors in EUV lithogra-

phy applications [48, 49]. Several condenser designs for ring-field imaging systems operated with a laser plasma source have been proposed [50, 51].

The mask in an EUV exposure system consists of a patterned multilayer mirror. The circuit pattern may be etched in the multilayer structure or defined in an absorber material on the mirror surface [52, 53, 24]. Since the formation of the desired pattern on the wafer relies on a defect-free mask, printable mask substrate and pattern defects must be avoided [54]. As a result, EUV mask fabrication depends critically on the defect inspection capabilities, including the detection of defects on the uncoated substrates, within the multilayer coating, and in the mask pattern [6, 55, 56].

The performance of the imaging system directly affects the transfer of the mask pattern onto the wafer. With all-reflective optics, the EUV imaging systems have moderate image-side numerical apertures of about 0.1. Aspheric optics are necessary to correct the wavefront aberrations over the sizeable field of view with a minimum number of mirror surfaces [57-60]. At the desired demagnification of 4 to 5, three-mirror designs are feasible [61] but four-mirror systems simplify the system integration [62-64]. The required near diffraction-limited optical quality of the aspheres at EUV wavelengths places stringent demands on optics fabrication and metrology, as discussed in Section 1.3.

The photoresist material is needed to record the mask image on the wafer. The absorption of EUV radiation in the photoresist, or any other material, confines the exposed region within the first few hundred nanometers of the surface. As a result, only relatively thin resist layers produce feature steep sidewall angles [65-67]. Since resist thicknesses on the order of 1 μm are required to obtain sufficiently low defect density, photoresists with sur-

face imaging capability must be employed at EUV wavelengths. Other key photoresist properties include exposure sensitivity, resolution, contrast, etch resistance, linewidth control, and line edge roughness [68, 69]. Both multilayer resists and single-layer silylation resists are potential candidates for EUV lithography [70-72].

The minimum size of the printable features and the latitude of the fabrication process, directly related to the resolution and the depth of focus of the imaging optics, determine the performance of the lithography system. For optics with a given numerical aperture (NA) operating at a wavelength λ , the resolution R and the depth of focus (DOF) are given respectively by

$$(1-1) \quad R = k_1 \frac{\lambda}{NA}, \text{ and}$$

$$(1-2) \quad \text{DOF} = \pm k_2 \frac{\lambda}{NA^2},$$

where k_1 and k_2 account for the imaging system performance as well as for other aspects of the pattern transfer process, such as partial coherence, phase-shift masks, and photoresist properties. At the 13-nm wavelength and 0.1-NA, resolution of about 0.1 μm with a focal tolerance of $\pm 0.7 \mu\text{m}$ can be achieved with near diffraction-limited optical systems having $k_1 \sim 0.7$ and $k_2 \sim 0.5$ [1]. At higher numerical apertures, the resolution can be further improved, in principle. Thus extreme ultraviolet imaging promises the fabrication of 0.1- μm device features with a possible extension to sub-0.1- μm feature sizes. However,

the ultimate usefulness of EUV lithography depends on the development of several key components of the exposure system.

1.3. Interferometric Characterization of Extreme Ultraviolet Optics

The size of the printable image features and the robustness of the imaging process are limited by the imperfections in the imaging optics. Only near diffraction-limited optics, with admissible low-order wavefront aberrations on the order of 0.02 wave rms [9] at EUV wavelengths (or 0.26 nm rms at 13 nm), can achieve the desired performance. The mirror surface roughness, which reduces the multilayer coating reflectivity as well as the image contrast, must be less than approximately 0.1 nm rms [73]. Such stringent aberration tolerances pose serious challenges not only for the fabrication of the complex aspheric optical systems but also for the metrology needed for the fabrication, the alignment, and the performance characterization. The focus of this discussion is phase-measuring interferometry used to evaluate the low-order aberrations that critically affect the resolution of optical systems. The metrology of high-frequency aberrations caused by surface roughness is considered elsewhere [74, 75]. Ideally, the resolution and the accuracy of the interferometers used for optical metrology should be significantly better than the wavefront under test, or about 0.01-0.002 wave rms at EUV wavelengths (0.13-0.026 nm rms at 13 nm). Furthermore, wavefront phase measurement at the operational wavelength is needed to characterize the possible multilayer coating phase effects.

Many phase measuring methods, including the traditional Twyman-Green or Fizeau interferometers, rely on reference surfaces, beamsplitters, and long-coherence-length light

sources [76-80]. Since neither reference surfaces nor beamsplitters with diffraction-limited optical performance at EUV wavelengths are available, interferometry schemes that bypass their use are suited for EUV optics testing. Furthermore, because even highly monochromatized EUV sources have coherence lengths less than a few tens of microns, common-path interferometry techniques are necessary for testing of EUV optics at their operational wavelengths.

1.3.1. Testing of Individual Mirrors

The complete evaluation of individual aspheric mirrors consists of the characterization of the mirror substrates, the deposited multilayer coatings, and the coated mirrors. On coated or uncoated surfaces, the figure errors are determined with phase-measuring interferometry using laser sources in the visible and ultraviolet spectral region. Interferometers based on reference wavefronts that are generated by diffraction from pinholes and optical fibers have been demonstrated to evaluate aspheres with 0.5-nm rms wavefront accuracy [81, 57]. To prevent excessive fringe densities when the spherical diffractive reference wavefront is interfered with the aspheric wavefront from the mirror, several subregions of the aspheric surface may be measured individually and “stitched” together. An alternative approach to testing aspheres with subnanometer figure tolerances, which utilizes holographic nulls, has also been reported [82].

The multilayer coating properties are currently characterized with reflectometry measurements that provide a map of the coating reflectivity over the surface of the mirror [32]. To probe the phase of the reflected wavefront, interferometric phase measurements at the operational wavelength of the coating may be necessary. Since, the test of a single mirror

almost always requires additional optical components, not readily available at EUV wavelengths, at-wavelength interferometry of a single multilayer-coated component has not yet been attempted.

1.3.2. At-Wavelength Characterization of Imaging Systems

Several interferometry techniques are available to assess the EUV wavefront, produced by the mirror surfaces and by the multilayer coatings, in an optical system that can form an image. Due to the lack of long-coherence-length EUV light sources, at-wavelength wavefront characterization of the assembled EUV systems utilizes common-path techniques, such as point diffraction interferometry [37, 83-88], lateral shearing interferometry [89-93], and moiré interferometry [94].

In moiré interferometry, the optical system under test images a grating in the object plane onto a second grating in the image plane. The properties of the optical system may be inferred from the distortions in the pattern transmitted through the second grating [94]. While moiré interferometry may be used with an incoherent source, such as a laser plasma source, it relies on well characterized gratings and a high-resolution detector in the image plane.

Lateral shearing and point diffraction interferometries detect the beam diverging from the image plane of the test optic, allowing relatively straightforward determination of the wavefront shape. The lateral shearing interferometry measures the derivative of the test wavefront from the laterally sheared version of the wavefront, produced with a transmission grating placed near the image plane. To obtain interference fringes, the test wavefront

must be spatially coherent over distances that correspond to the shear. The point diffraction interferometry measures the unknown wavefront directly by interfering it with a spherical reference wavefront generated by diffraction from a small pinhole in the image plane. In this case, a high degree of spatial coherence is required to obtain good fringe contrast. In both the lateral shearing and the point diffraction interferometries, the test optic must be illuminated with a spherical wavefront from a sub-resolution pinhole in the object plane to ensure that the measured aberrations are caused solely by the test optic. To transfer sufficient flux through the small entrance pinhole, relatively powerful EUV sources are needed in both techniques. Since point diffraction interferometry also requires spatially coherent radiation, it is most practical with high-brightness undulator synchrotron radiation sources [36, 86, 88]. Lateral shearing interferometry has been tested on both synchrotron [91] and laser plasma sources [93].

1.4. Optical Aberrations and Image Quality in Lithography

The performance of imaging systems in lithography is degraded by wavefront aberrations. Optical wavefront errors over the entire range of spatial frequencies, from low-order “figure” errors to high-frequency “finish” errors, influence the image quality. Low-frequency aberrations, with no more than a few cycles of variation over the aperture of the optical system, correspond to the classical aberrations that degrade the resolution. In optical systems with circular or annular pupils, the low-order wavefront errors are often described with Zernike polynomials [95-98], which allow an expansion of the wavefront in terms of mutually orthogonal aberrations. The high-frequency errors of hundreds of cycles across the aperture are known to reduce the contrast of the image by producing background flare in

the image plane. The high frequency aberrations are typically represented in terms of the statistical properties of the optical surfaces [73, 99-101].

The range of spatial frequencies between the two extremes, termed mid-spatial-frequency aberrations, has not been extensively studied. These aberrations, with about ten to a about a hundred of cycles over the diameter of the optic aperture affect both the resolution and the contrast of the image features with dimensions near the diffraction limit [99, 102]. The desire for diffraction-limited optical performance warrants further consideration of the impact of mid-spatial-frequency wavefront errors on the image quality. In lithography applications, the interplay of the object pattern size, the degree of partial coherence, and the aberration frequency requires evaluation.

1.5. Thesis Organization

This thesis concerns the characterization of the optical performance in extreme ultraviolet imaging systems with point diffraction interferometry. The motivation for this study is the development of near-diffraction-limited multilayer-coated optics required for extreme ultraviolet projection lithography at 0.1- μm critical dimension and beyond. The principles of evaluation of wavefront aberrations in optical systems using point diffraction interferometry are considered in Chapter 2. In Chapter 3, the properties of diffractive zone plate lenses are studied near 13-nm wavelength using transmission measurements and conventional point diffraction interferometry. Chapter 4 describes the first measurements at visible wavelengths to demonstrate the capabilities of a novel phase-shifting point diffraction interferometer design. In Chapter 5, the phase-shifting point diffraction interferometer is

used at EUV wavelengths to evaluate the aberrations in a multilayer-coated Schwarzschild objective designed for a proof-of-principle EUV lithography system. The repeatability and consistency of the interferometry measurements are also considered. Chapter 6 concerns the measured chromatic effects produced by the multilayer coatings in the two-mirror Schwarzschild system. In Chapter 7, the results of the interferometric wavefront measurements are confirmed qualitatively using the consistency between the interferometry-based calculations of image quality and the developed photoresist patterns printed with the Schwarzschild objective. In Chapter 8, the effect of high-order aberrations on image quality in lithography applications is considered in general, using the theory of image formation with partially coherent light and the verification with image calculations. In Chapter 9, the results of this work are summarized and some future research directions are suggested.

2 Point Diffraction Interferometry for Testing EUV Optics

2.1. Introduction

Interferometric characterization of optical aberrations is necessary to achieve near diffraction-limited imaging capability for extreme ultraviolet (EUV) projection lithography. Both at-wavelength optical system qualification and sub-nanometer wavefront measurement accuracy are needed to evaluate future multilayer-coated EUV lithographic optics with resolution near $0.1 \mu\text{m}$ at the operational wavelength of 13 nm [36].

Point diffraction interferometry enables direct wavefront aberration measurements by detecting the interference between the unknown aberrated wavefront and a reference wave that is generated by diffraction from a sub-resolution pinhole. The pinhole must be smaller than the diffraction-limited resolution of the optic under test. This type of interferometry, applicable over a wide spectral range including the extreme ultraviolet, can potentially achieve high absolute accuracy by utilization of a diffractive reference wavefront. Furthermore, point diffraction interferometers do not require long-coherence-length light sources because the test and reference beams follow nearly common paths.

The conventional point diffraction interferometer (PDI) [81, 103-106], developed and used for a variety of applications, has been proposed as one of the alternatives for testing

of extreme ultraviolet optics [36, 37]. At EUV wavelengths, it has been used to evaluate aberrations in diffractive zone plate lenses at the wavelength of 13 nm [84, 85, 87]. These initial experiments, described in part in Chapter 3, enabled the conception of the phase-shifting point diffraction interferometer (PS/PDI) [107, 87]. This interferometer design preserves the advantages of the conventional point diffraction interferometer, yet provides phase-shifting interferometry capability and significantly higher throughput. The PS/PDI is more versatile than another previously reported method for incorporating phase-shifting in the PDI design [108]. The PS/PDI has been used to characterize a prototype reflective optical system for EUV lithography [86, 88] and is described in further detail in Chapter 5.

In this chapter, the principles of operation of both the PDI and the PS/PDI are described and compared. Practical issues relating to the implementation and the accuracy of the two interferometer designs are also considered.

2.2. Conventional Point Diffraction Interferometer

The principle of characterizing aberrations in an optical system with the conventional point diffraction interferometer [103-105, 109] is depicted in Figure 2-1. The optical system under test is illuminated by a spatially coherent spherical wavefront from a pinhole source placed in the object plane of the optic. To ensure a spherical illumination wavefront, the entrance pinhole must be smaller than the diffraction-limited spot size resolvable by the test optic on the object side. The “perfect” illumination wavefront becomes aberrated due to errors in the optical system under test. The unknown aberrated test wave-

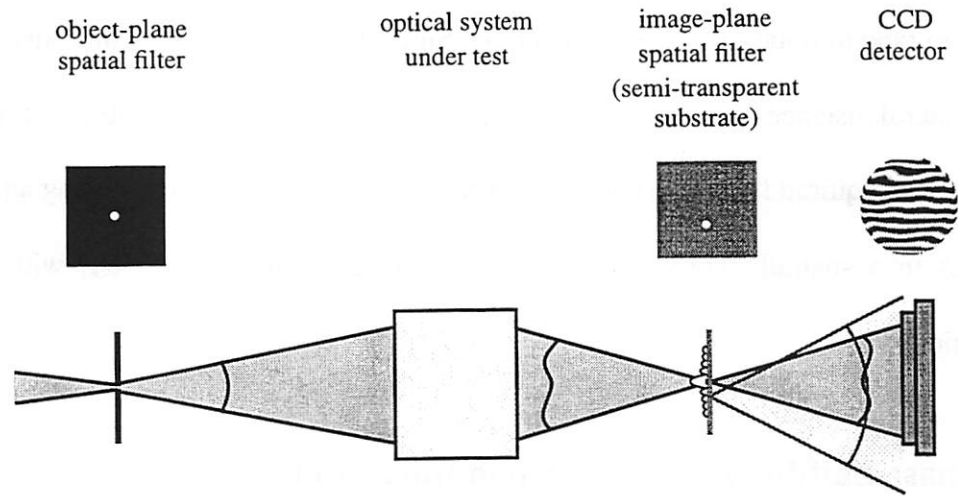


Figure 2-1. Conventional point diffraction interferometer.

Principle of testing of optical systems with the conventional point diffraction interferometer.

front is transmitted through a thin semi-transparent membrane, placed near the image plane. The reference wavefront needed for the measurement is generated by diffraction from a sub-resolution pinhole in the membrane. To produce a spherical reference wavefront, the pinhole must be smaller than the diffraction-limited focus of the test optic. The test and reference wavefronts interfere, and the resulting interference fringe pattern can be recorded and analyzed to reveal the aberrations in the optical system.

The pinhole samples the intensity distribution of the test wavefront to produce the reference wave, and as a result, it is not possible to introduce an adjustable phase shift between the test and reference waves. Without phase shifting capability, the pinhole must be placed a relatively large lateral distance from the test wave focus to produce a sufficient number of “tilt” fringes for accurate fringe analysis of individual interferograms. Consequently, the amount of light incident on and transmitted through the pinhole is small and

the test wave must be attenuated by three to four orders of magnitude in passing through the membrane to obtain good fringe contrast. Since the reference wave intensity depends on the lateral distance from the test wave focus, a range of different membrane transparencies may be required for fringe contrast control. This can be achieved by using an array of pinholes in a spatially graded partially transmitting membrane [37, 84] with varying absorption.

2.3. Phase-Shifting Point Diffraction Interferometer

Although the conventional point diffraction interferometer is attractive for its compactness and relaxed temporal coherence requirements, it has practical limitations due to its low efficiency and lack of phase-shifting. The phase-shifting point-diffraction interferometer maintains the appealing features of the PDI and provides both phase-shifting and high efficiency. In contrast to the PDI, the PS/PDI employs a low-angle beamsplitter to separate the test and reference wavefronts, as shown in Figure 2-2(a). A coarse diffraction grating that splits an incoming beam into multiple diffraction orders is suitable for this purpose. The wavefront division produces multiple foci in the image plane of the test optic, of which two are selected with an opaque spatial filter containing a sub-resolution pinhole and a relatively large window. One of the beams is spatially filtered with the sub-resolution pinhole to generate the diffracted reference wavefront, while the aberrated test beam passes through the window without appreciable spatial filtering or attenuation. In contrast to the conventional PDI, the test and reference wave intensities are not greatly mismatched and an attenuation of the test wavefront is not needed to obtain satisfactory fringe visibility. Since the test and reference beams must not significantly overlap in the

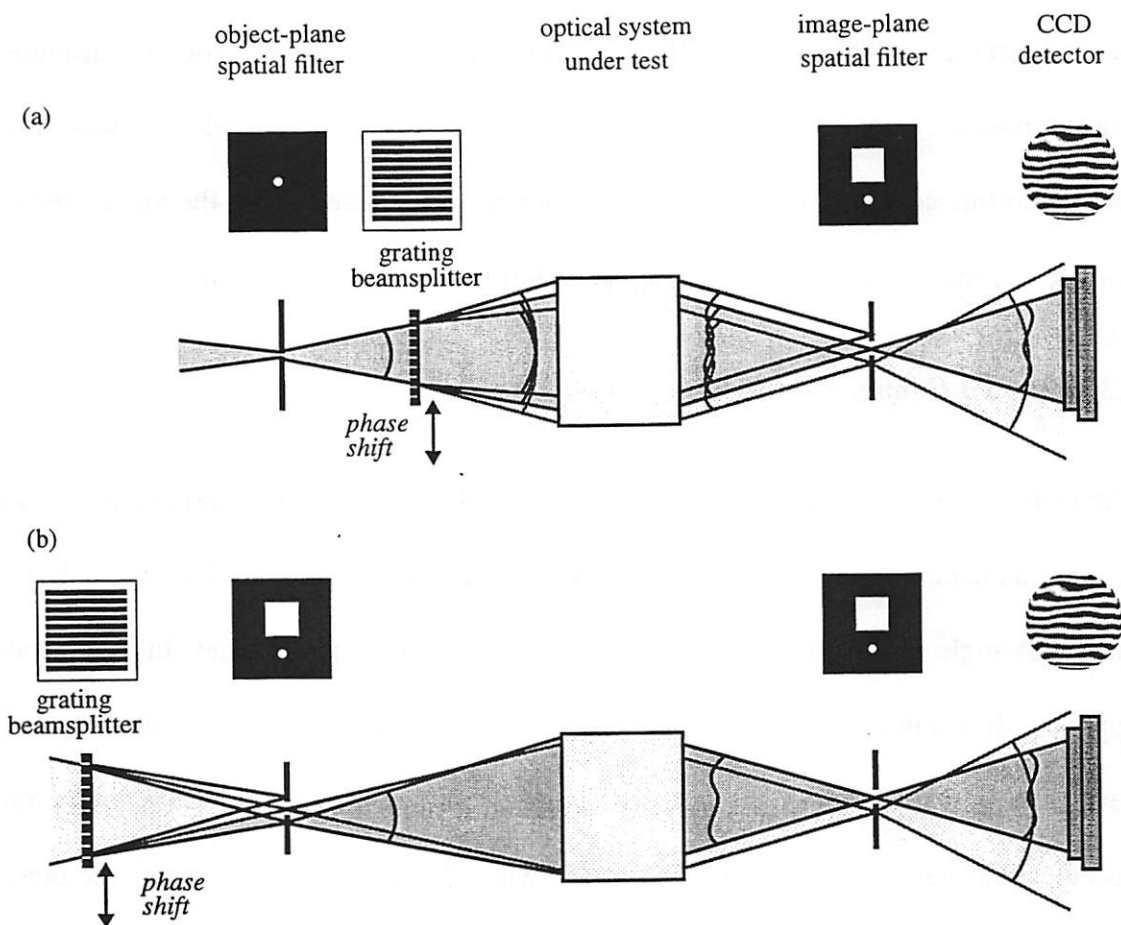


Figure 2-2. Phase-shifting point diffraction interferometer.

Two implementations of the phase-shifting point diffraction interferometer. The interferometer utilizes a small-angle beamsplitter (e. g. grating) and a two-pinhole spatial filter in the image plane. The illuminating beam is divided by a beamsplitter that either (a) follows a single-pinhole entrance spatial filter, or (b) precedes a two-pinhole entrance spatial filter.

image plane, the focal spot separation produced by the beamsplitter must be considerably larger than the lateral extent of each focal pattern.

Beam division introduces the potential to vary the phase of one beam with respect to the other, allowing the use of phase-shifting interferometry. The wavefront can be divided into multiple diffractive orders with a coarse diffraction grating, used either in transmis-

sion or in reflection. Translation of the grating by one grating period introduces a first-diffractive-order phase shift of one full cycle, while the phase of the zero-order transmitted beam remains constant. A grazing-incidence mirror can also be used as a wavefront divider. In this configuration, the mirror surface may be rotated about the virtual source point to introduce a controlled relative phase-shift between the two beams.

2.3.1. PS/PDI Configurations

The numerous possible configurations of the PS/PDI may be divided into two main subgroups, depicted in principle in Figure 2-2. In the first group represented in Figure 2-2(a), the small-angle beamsplitter follows the entrance pinhole spatial filter. In the second approach shown in Figure 2-2(b), beam-splitting precedes the entrance pinhole. When the beamsplitter follows the object-plane spatial filter, it can potentially introduce aberrations into the measured wavefront. This is avoided when the beamsplitter precedes the object plane. To transmit both beams through the interferometer, a two-pinhole filter is then required in both the object and image planes, as illustrated in Figure 2-2(b). The test beam is filtered by a sub-resolution pinhole in the object plane, which removes any beamsplitter aberrations and produces spatially coherent spherical illumination of the test optic, but is not filtered by the large window in the image plane. The reference beam, passed through the large window in the object plane without attenuation, is spatially filtered by the reference pinhole in the image plane.

Using the beamsplitter before the entrance pinhole, rather than after it, also offers higher efficiency and possibly greater fringe contrast. This is illustrated schematically in Figure 2-3, which shows the power flow through the two interferometer configurations,

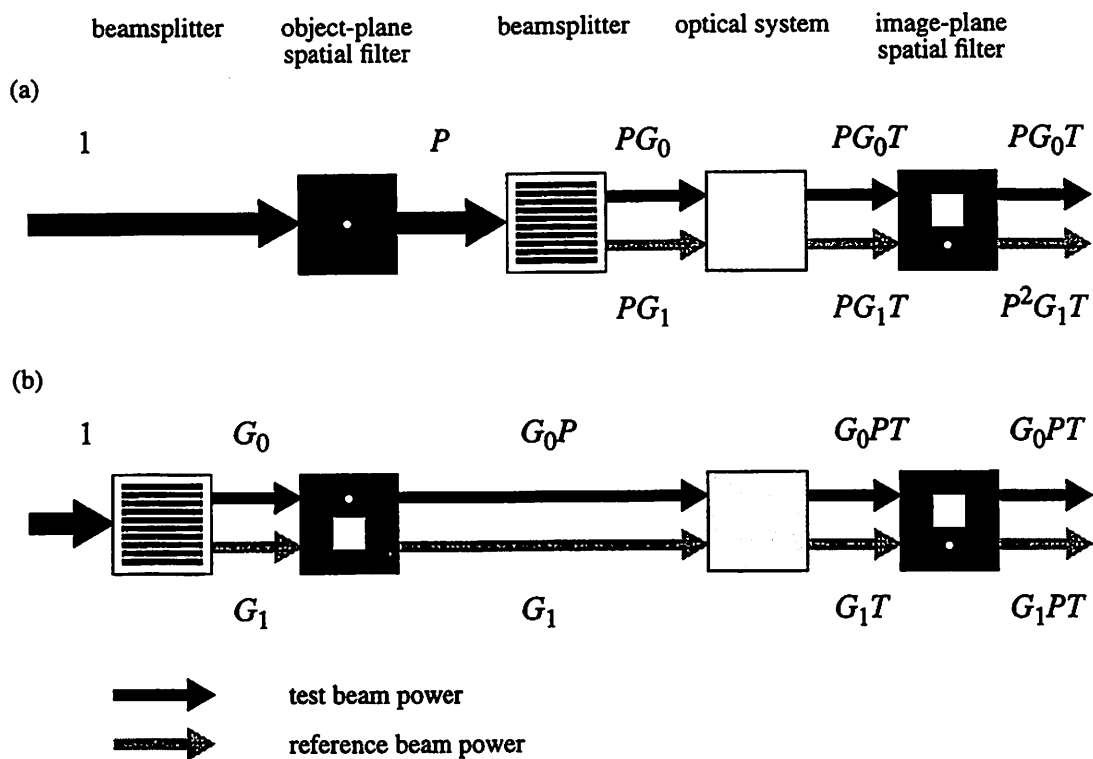


Figure 2-3. Power transmission for two PS/PDI configurations.

A schematic representation the test and reference beam power flow through the phase-shifting point diffraction interferometer. (a) The beamsplitter follows the entrance pinhole. (b) The beamsplitter precedes the entrance spatial filter. The pinhole transmission is P , the window transmission is unity, the beamsplitter efficiencies are G_0 and G_1 , and the optic transmission is T .

given the beamsplitter power efficiencies G_0 and G_1 , the pinhole filter transmission P , the window transmission of unity, and the optical system transmission T . With the beamsplitter after the entrance pinhole, the relative powers in the test and reference beams are PG_0T and P^2G_1T , respectively, while with the beamsplitter before the entrance filter, the relative test and reference powers are G_0PT and G_1PT , respectively. Since the reference wavefront is weaker by a factor of P in the former case, the overall transmission is lower and the fringe contrast may also be smaller than in the latter case.

The PS/PDI scheme with the grating before the entrance filter is most applicable when the illumination beam can be tightly focused to allow the low-angle beamsplitter to spatially separate the foci in the object plane. When the illumination beam is highly aberrated or originates from an extended source, the beam division must follow the entrance pinhole spatial filter.

2.4. Practical Issues in Point Diffraction Interferometry

Point diffraction interferometry techniques employ beamsplitters and pinhole spatial filters in the wavefront phase measurements. These key components influence measurement capability in practice. The spectral bandwidth and the spatial coherence of the illuminating beam also affect the accuracy of the interferometry.

2.4.1. Illumination and Reference Pinholes

In point diffraction interferometry, the measurement accuracy is dependent on the quality of both the illumination and the reference wavefronts that are generated by diffraction from pinhole apertures. Of consequence is the radiation diffracted from a small aperture and observed in the far field, where the illumination wavefront interacts with the optics and the reference wavefront is detected. Diffraction theories predict spherical wavefronts over some finite numerical aperture (NA) in the far field for a given illumination wavelength and pinhole shape and size. Treatments of diffraction from apertures range from scalar field approximations [110-113], appropriate for apertures much larger than the radiation wavelength, to the generally applicable rigorous vector field analysis [114, 115].

Most theoretical treatments of pinhole diffraction are limited to uniformly illuminated, circular or square apertures in thin opaque screens [112, 113, 115, 81]. Scalar diffraction treatments of uniformly illuminated apertures in thin screens predict that the deviation of the far field wavefront from a sphere can be arbitrarily small over a finite numerical aperture as the aperture size is decreased [81]. However, the vector nature of the radiation as well as the three-dimensional geometry of actual fabricated apertures can contribute to deviations from sphericity. Numerical solutions of the rigorous vector field propagation have been determined for several pinhole geometries in a thick absorptive medium under uniform illumination [116]. For pinhole geometries and numerical apertures relevant to EUV point diffraction interferometry at 0.1 numerical aperture, the calculated deviation from wavefront sphericity does not to exceed 0.01 wave peak-to-valley at 13.55-nm wavelength λ for pinholes smaller than 125 nm ($0.92 \lambda/NA$) in diameter [116].

Although most studies have focused on diffraction from uniformly illuminated apertures, the illumination of the pinhole may not be uniform in practice. This is the case for the reference pinhole in both conventional point diffraction interferometry, where the pinhole is placed off the center of the focal pattern, and in phase-shifting point diffraction interferometry, where the pinhole is centered on the focal pattern. In effect, the pinholes “spatially filter” the illumination beam to produce the desired spherical wavefront [110, 117, 118]. To be effective spatial filters, the pinholes must be smaller than the diffraction-limited focus of the test optic, whose central Airy disk [111] diameter is $1.22 \lambda/NA$. In testing EUV optical systems with numerical apertures around 0.1, the diffraction angles are moderate and pinhole diameters are typically several times greater than the wavelength. As a result, simple scalar diffraction theory based on Kirchhoff approximation [110, 111],

which is valid for apertures larger than the wavelength and relatively small diffraction angles [115], is sufficient to provide useful insight into spatial filtering by pinhole apertures.

To determine the proper size of the apertures needed to generate high-quality spherical wavefronts, spatial filtering of aberrated illumination beams was studied. Although the exact nature of the wavefront transmitted through a spatial filter depends on the properties of the illumination beam, much can be learned by considering beam characteristics representative of practical conditions. For PS/PDI intended for testing near diffraction-limited EUV optics, it is relevant to consider the spatial filtering of the reference beam that initially contains a relatively small amount of low-order aberrations. Since the pinhole is centered on the focal pattern, low-order aberrations are transmitted most strongly if the pinhole is too large, while relatively high-order aberrations are filtered quite effectively. For optical systems with circular or annular pupils, low-order aberrations are well described by Zernike polynomials [95-98, 119, 121], which form an orthogonal basis set on a circle or an annulus. The Zernike polynomials represent the aberrations in terms of individual "balanced" aberrations, of which the first few correspond to the classical aberrations [122, 95], including defocus, astigmatism, coma, and spherical aberration. An overview of Zernike polynomials is presented in the Appendix.

The far-field peak-to-valley wavefront error, in cycles or waves, transmitted through a circular pinhole, illuminated with a focused beam containing a single phase aberration, are shown in Figure 2-4 and Figure 2-5 as a function of the pinhole size and the input aberration magnitude for several different input aberrations. The wavefront errors were calcu-

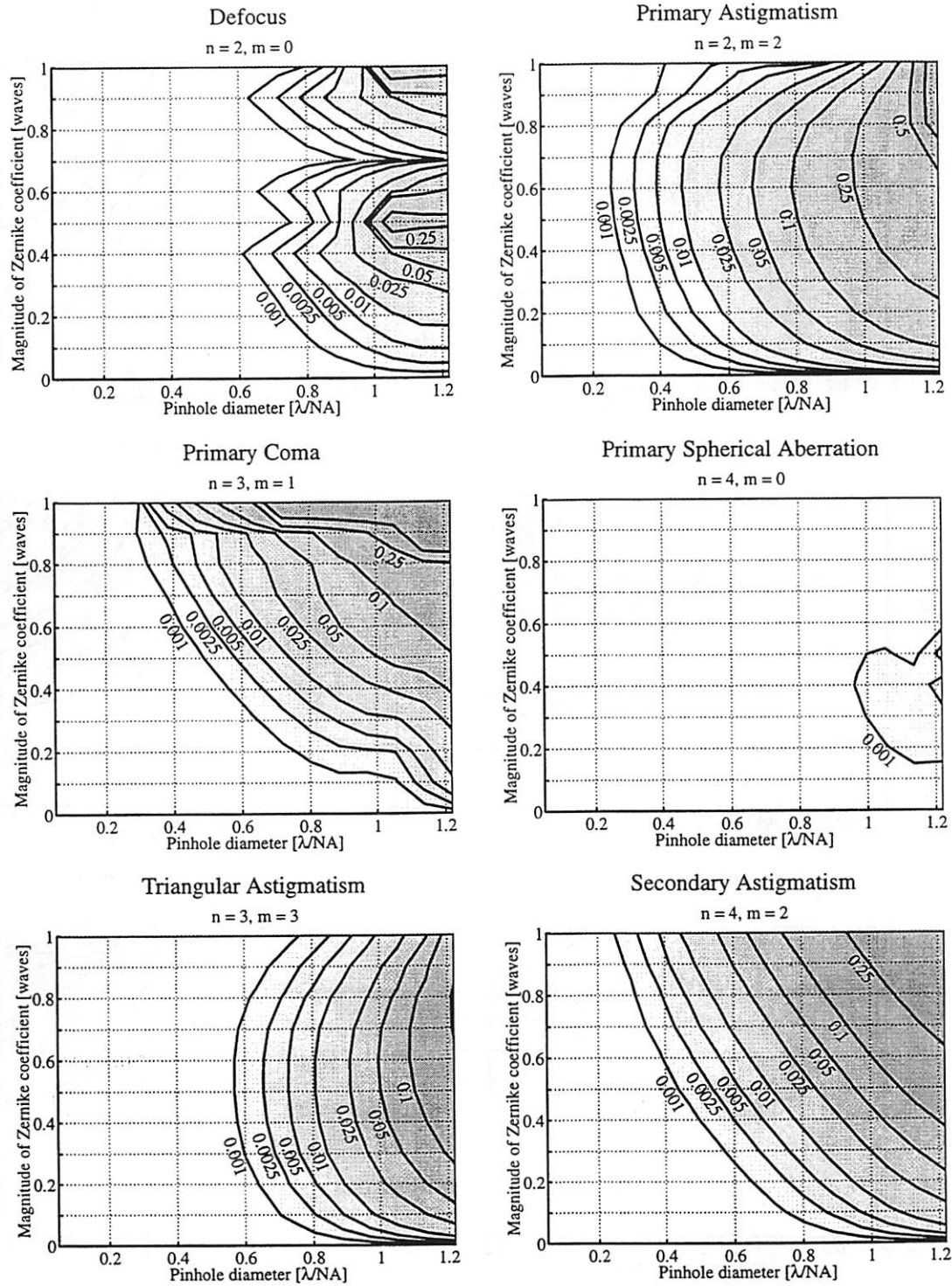


Figure 2-4. Spatial filtering of lowest-order aberrations by circular pinhole apertures.

The peak-to-valley wavefront error, in waves, of an aberrated wavefront transmitted through a circular pinhole at focus. In each graph, the illumination beam contains a single balanced phase aberration (Zernike polynomial term), as indicated. The transmitted errors are shown as functions of input aberration magnitude and spatial filter size.

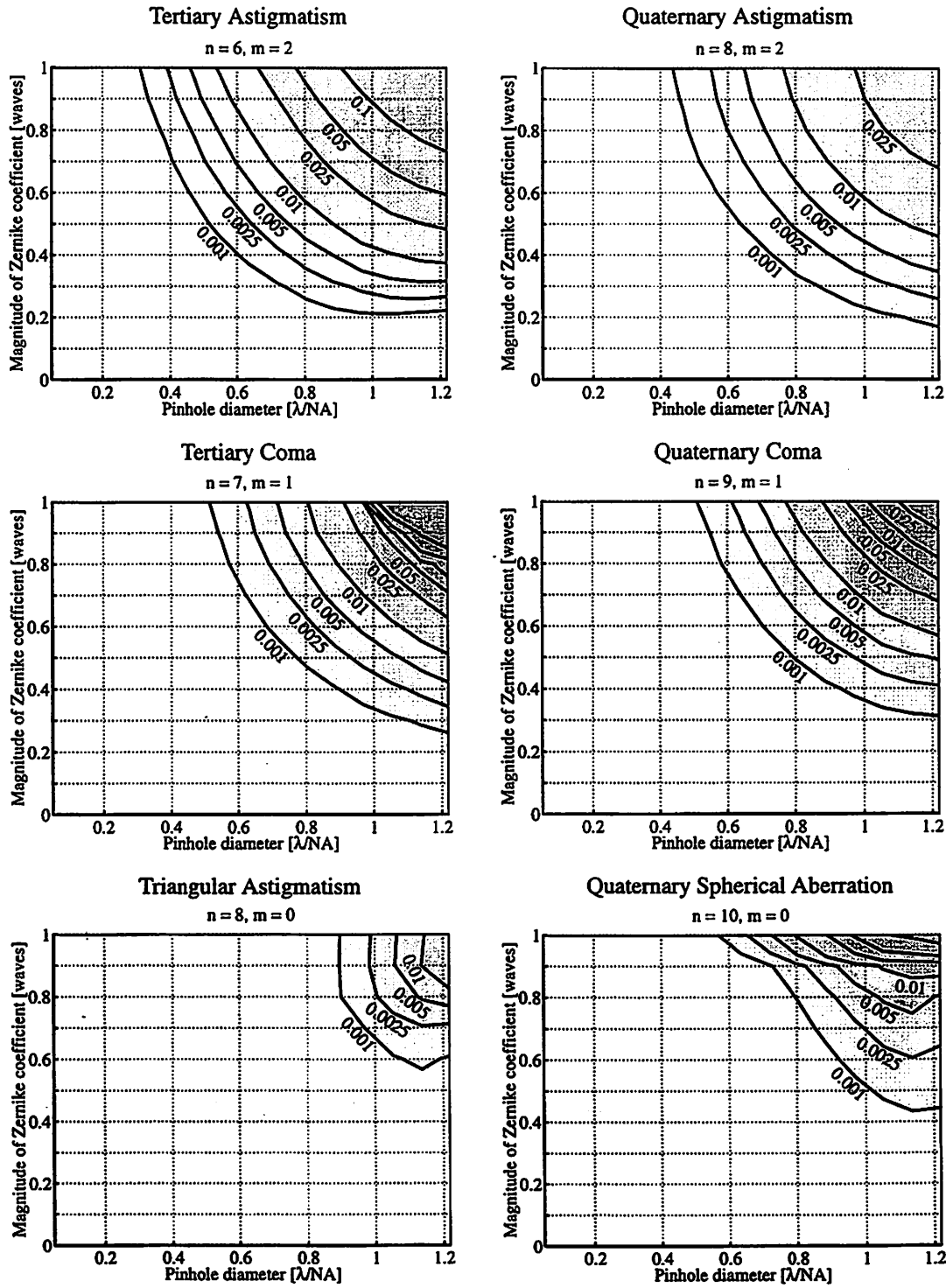


Figure 2-5. Spatial filtering of higher-order aberrations by circular pinhole apertures.

The peak-to-valley wavefront error, in waves, of an aberrated wavefront transmitted through a circular pinhole at focus. In each graph, the illumination beam contains a single balanced phase aberration (Zernike polynomial term), as indicated. The transmitted errors are shown as functions of input aberration magnitude and spatial filter size.

lated for pinholes in a thin opaque screen using scalar diffraction theory. The tilt and the defocus terms have been removed, as they correspond only to rotations and shifts of the coordinate system. The input aberration magnitudes are given in terms of the Zernike polynomial coefficients, which are proportional to the input peak-to-valley wavefront error. The pinhole size is given in the “resolution units” of λ/NA , where λ is the wavelength and NA is the numerical aperture of both the illumination beam and the desired portion of the transmitted reference beam. Figure 2-4 shows the spatial filtering of the lowest-order aberrations, while Figure 2-5 illustrates filtering of several higher-order aberrations. Although defocus is not an aberration produced solely by the test optic, owing to the fact that it also depends on the position of the pinhole filter with respect to the test-wave focus, spatial filtering of a defocused beam gives the tolerance for the displacement of the spatial filter from focus. The figures show that smaller pinholes are more effective spatial filters and that the transmitted deviations from wavefront sphericity generally increase with the magnitude of the input aberrations. In addition, higher-order aberrations are filtered more strongly than the low-order errors. Although in practice the illumination beam contains a mixture of aberrations, Figure 2-4 and Figure 2-5 provide a guideline for selecting the needed pinhole size for highly accurate phase-shifting point diffraction interferometry. For testing optics with wavefront errors on the order of 0.02 wave rms, the reference wavefront quality should be at least an order of magnitude better, or about 0.001 wave rms. Admissible peak-to-valley errors may be somewhat larger, as they are generally several times the size of the rms errors for most wavefront aberrations. Given that and the information in the figures, the pinhole diameter of choice should be roughly one third to one half of the resolution unit of λ/NA . In addition to reducing the

transmitted flux, the use of much smaller pinholes may not improve the wavefront quality due to polarization-induced aberrations [116].

In the conventional PDI, understanding the reference wavefront quality is somewhat more complex because the pinhole filter is not centered on the focused beam. It may be placed almost any place within the focal pattern with non-zero intensity that produces sufficiently high fringe density to enable single-interferogram analysis. In practice, typical fringe densities may be 10 to 40 fringes, which corresponds to lateral pinhole displacement of 5 to 20 λ/NA from the focal center. Since the pinhole samples the fields in one of the “rings” of the focal pattern, which are narrower than the central portion of the focus, the pinholes needed to obtain the desired wavefront quality may be somewhat smaller than in the PS/PDI. Several examples of the wavefront errors transmitted through a circu-

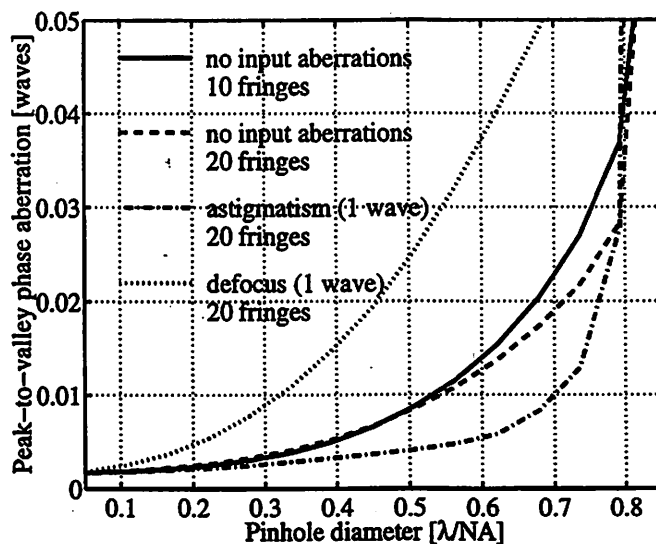


Figure 2-6. Examples of reference wavefront error in PDI.

The calculated peak-to-valley wavefront aberration transmitted through a circular pinhole as a function of the pinhole diameter. The pinhole is laterally displaced from the focus and centered on one of the rings of the focal pattern. Several cases are shown, including two different fringe densities and focal illumination patterns with and without aberrations.

lar pinhole, centered on a ring of the focal pattern, are shown in Figure 2-6. The peak-to-valley wavefront error, excluding the tilt and the defocus terms, is plotted as a function of the pinhole diameter, for pinhole positions corresponding to two different fringe densities and for illumination beams containing either no aberrations, astigmatism, or defocus. The defocus curve is again representative of the interferometer sensitivity to error in the axial positioning of the pinhole filter. The figure shows that even when the pinhole is quite small, the transmitted wavefront contains some aberrations. In all cases considered here, the transmitted wave is dominated by spherical aberration for small pinhole diameters. For larger pinhole diameters, the transmitted aberrations increase in magnitude and change in character. For perfect illumination beams, the transmitted wavefront contains mainly triangular astigmatism and coma. When the input beam is astigmatic, the aberrations are also dominated by astigmatism, while when the input beam is out of focus, the transmitted wavefront includes astigmatism and triangular astigmatism. The magnitude of the aberrations appears to confirm that for comparable spatial filter diameters, the wavefront errors transmitted in the PDI are somewhat larger than those in the PS/PDI.

To accurately evaluate EUV lithographic optics with numerical apertures around 0.1 that operate near 13-nm wavelength using point diffraction interferometry, reference pinholes with diameters around 50-75 nm are required. The pinholes are fabricated in thin, absorber-coated membranes. Since the pinhole structure affects the pinhole flux throughput [116], it is important to select efficient absorber materials, such as nickel or indium antimonide, to minimize the thickness-to-diameter aspect ratios. The patterning techniques of choice include electron beam lithography [123-125] and focused ion beam microfabrication [126, 88].

In testing optical systems with significant demagnification, the required size of the illumination pinhole, relative to the reference pinhole size, scales with the demagnification. As a result, the illumination pinhole fabrication may not be as challenging as the fabrication of the small reference pinholes. While microfabrication remains the suitable patterning scheme for pinhole diameters below 0.5 μm , off-the-shelf laser-drilled pinhole apertures are available for diameters above 0.5 μm .

2.4.2. Beam Overlap and Spatial Filtering of the Test Beam (PS/PDI)

In phase-shifting point diffraction interferometry, the large image-plane window for transmission of the test beam affects the measurement in two ways. First, the size of the transmission window limits the maximum spatial frequency that can be measured in the test wavefront. Second, a portion of the wave illuminating the reference pinhole can be transmitted through the test-wave window, corrupting the quality of the reference wavefront with high-spatial-frequency components. Thus the window size and its separation from the reference pinhole must be selected to transmit the test-wave aberrations of interest and to minimize the unwanted reference-wave transmission. The lateral separation of the test and the reference spots, centered on the window and the reference pinhole, respectively, must be sufficient to prevent significant overlap in the window, but not excessive to avoid fringe densities beyond the spatial resolution of the detector.

A reasonable beam separation in the focal plane is about twenty times the resolution unit of λ/NA , which produces forty far-field fringes. The test window size may also be about twenty λ/NA . The far-field amplitude of unit-intensity unaberrated test and reference beams from an optic with a circular pupil transmitted through a square window of size

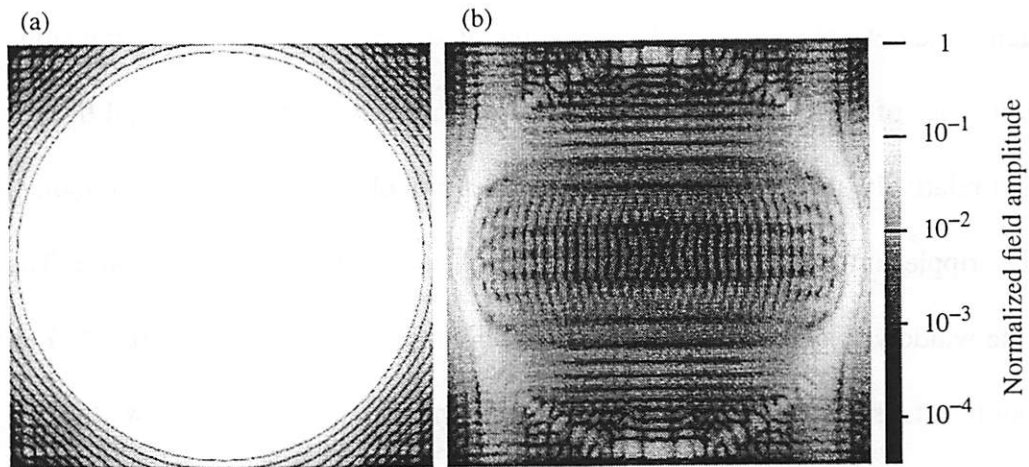


Figure 2-7. Transmission of test and reference beams through the test-beam window.

The calculated field amplitudes of diffraction-limited (a) test and (b) reference beams transmitted through a square window of size $20 \lambda/NA$ by $20 \lambda/NA$. (a) The test beam focus is centered on the window. (b) The reference beam focus is displaced by a distance of $20 \lambda/NA$ in the horizontal direction from the center of the window.

$20 \lambda/NA$ by $20 \lambda/NA$ are shown in Figure 2-7(a) and (b), respectively. The test beam focal spot is centered on the window, while the reference beam focus is horizontally displaced from the window center by a distance of $20 \lambda/NA$. Owing to its sharp boundaries, the window filter introduces small ripples into the test beam, most pronounced at the edges of the illuminated region. The window also transmits the high-pass version of the beam incident on the reference pinhole. Since the high-pass filter is displaced from the pinhole in one direction, it mainly transmits spatial frequencies from that direction, causing the transmitted light to be the strongest along the direction of the beam separation. The effect is most significant at the perimeter of the region that corresponds to the illumination numerical aperture because the beam initially contains a sharp intensity transition at the pupil edge. An apodization of the pupil illumination having smooth intensity transition at the pupil edge would reduce this effect.

The window spatial filter determines the maximum spatial frequency in the test beam that reaches the detector. Specifically, a window of size $N \lambda/NA$ by $N \lambda/NA$ transmits spatial frequencies of up to $2N$ cycles across the optic aperture. Since the spatial filter typically has a relatively sharp cutoff, owed to being a pinhole in an opaque membrane, it introduces ripples into the test beam of spatial frequency corresponding to its size. The effects of the window spatial filter on the test wavefront are quantified in Figure 2-8. For several input beams that contain the single aberration indicated, the figure shows the rms difference, in waves, between the phase of the input test beam and the phase of the beam transmitted by a circular window to the far field. The filter-induced rms phase is shown as a function of the magnitude of the aberrations in the test beam and the diameter of the window filter. As expected, the filter effects increase with decreasing window size and increasing magnitude of the test-beam aberrations. The filtering also affects higher-order aberrations more strongly than lower-order aberrations because they produce foci with larger spatial extent. In general, a spatial filter, which is significantly larger than the focal size, efficiently transmits the desired low-order test-beam aberrations. It also contributes mid-spatial-frequency aberrations, having frequencies determined by its size, that are most pronounced at the edges of the transmitted beam. In summary, when the test beam is relatively unaberrated, and the window size larger than roughly $20 \lambda/NA$ in each linear direction, the filtering does not significantly change the test wavefront.

Along the direction in which the test and the reference foci are separated, the size of the test-beam window is limited by the presence of the reference beam. In the orthogonal direction, the filter size can be as large as practically possible to increase the spatial frequency cutoff for that direction.

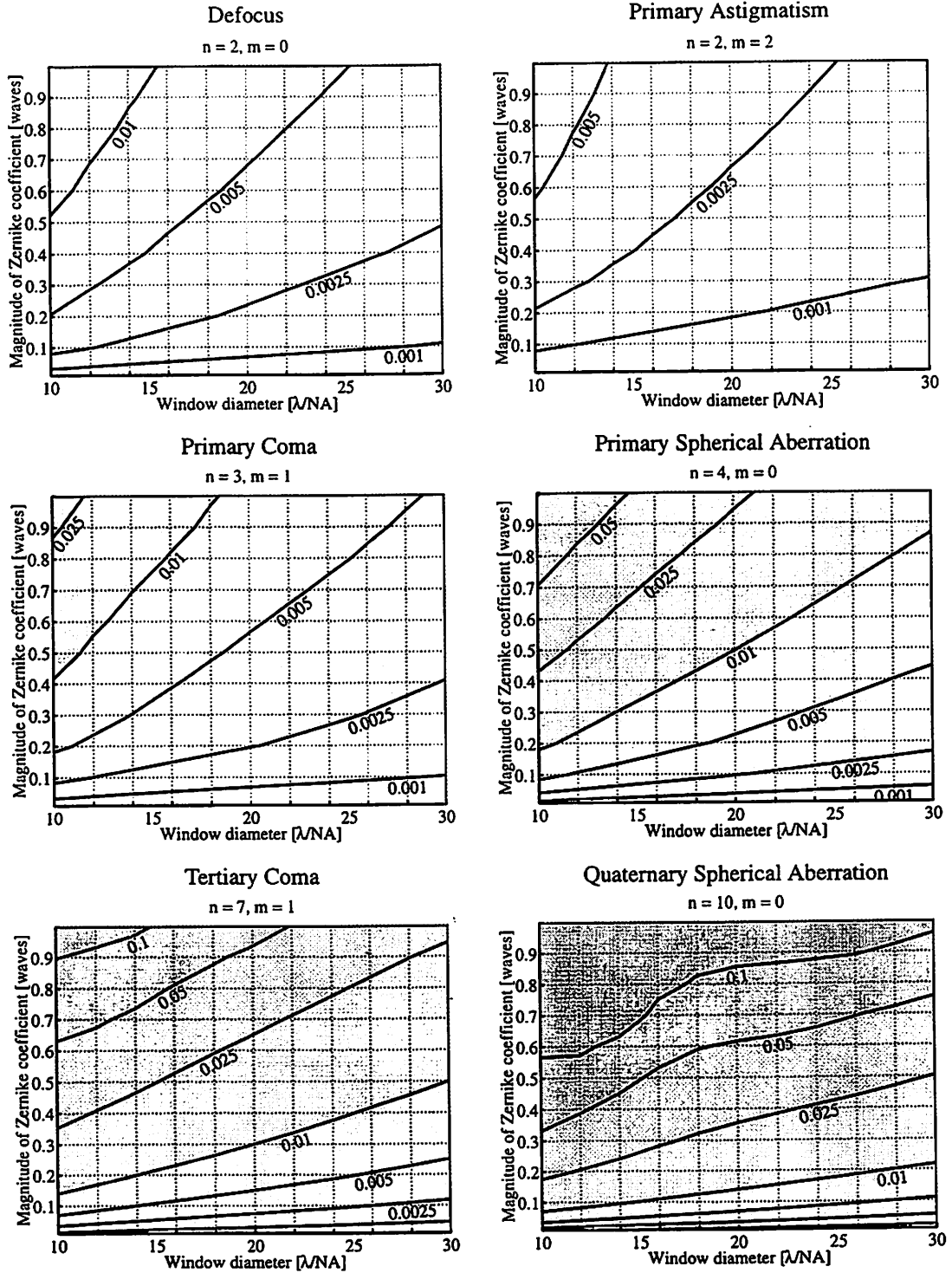


Figure 2-8. Spatial filtering of the test beam.

The calculated rms difference, in waves, between the phase of the illumination test beam and the far-field phase transmitted through a circular window at focus. In each graph, the illumination beam contains a single balanced phase aberration, as indicated. The transmitted errors are shown as functions of input aberration magnitude and spatial filter size.

To understand how the overlap of the test and the reference beams within the window filter affects the detected far-field interference pattern, it is instructive to consider the contrast of the interference between two fully coherent optical fields, with respective intensities I_1 and I_2 . The contrast, or fringe visibility, is defined [127] as

$$(2-1) \quad \text{Contrast} = \frac{I_{max} - I_{min}}{I_{max} + I_{min}} = \frac{2\sqrt{I_1/I_2}}{1 + I_1/I_2},$$

where I_{max} and I_{min} are the maximum and the minimum intensities of the interference pattern. It is plotted in Figure 2-9 as a function of the ratio of intensities in the weaker beam and the stronger beam. The contrast represents a measure of the severity of the test and reference beam overlap, which depends on the relative strengths of the two beams. Ideally, any unwanted interference should be about an order of magnitude smaller than the

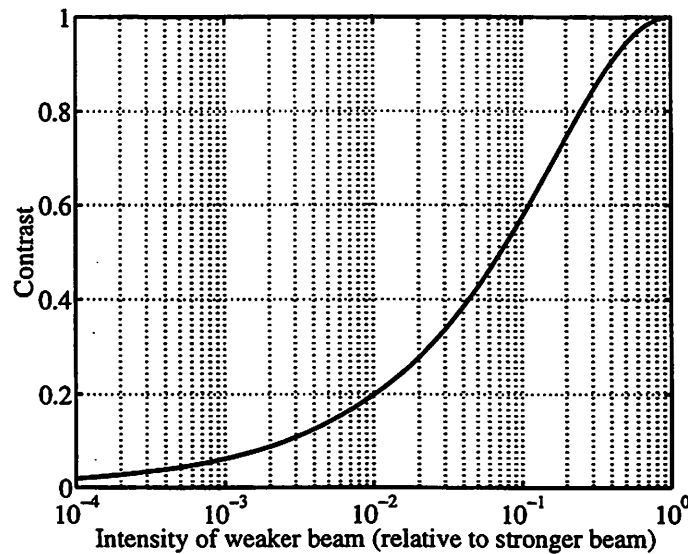


Figure 2-9. Contrast of two-beam interference.

Contrast of the interference of two spatially coherent beams plotted as a function of optical intensity of the weaker beam divided by the optical intensity of the stronger beam.

desired interference fringes. Given that typical fringe contrasts in point diffraction interferometry are greater than about 40%, the unwanted overlap beam should be roughly three orders of magnitude smaller in intensity than the desired signal.

The average intensity of a unit-amplitude, unaberrated reference beam transmitted by the window filter to the far field is shown in Figure 2-10. The intensity is plotted as a function of the window size and the displacement of the window center with respect to the reference-beam focus. For large beam separations and filter sizes that are small relative to the beam separation, the unwanted beam overlap decreases. The profile of the undesired beam is similar to that shown in Figure 2-7(b). This indicates that the beam overlap is severe near the beam edges but relatively small over most of the illuminated region. Thus the average intensity in Figure 2-10 may result in an overly optimistic estimate of the

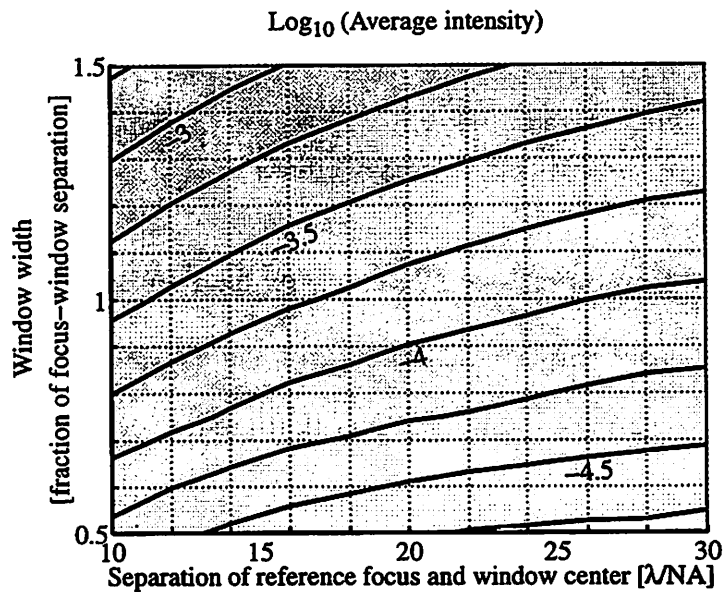


Figure 2-10. Transmission of reference beam through the test-beam window.

The average far-field intensity of the reference beam transmitted by a square the test-beam window. The intensity is plotted as a function of the window size and the distance between the window center and the reference-beam focus.

beam overlap effect near the beam edges. The reference beam contribution to the transmitted wavefront at the pupil edge could be reduced if the illumination of the pupil were apodized to avoid sharp intensity transitions at the pupil edge, rather than uniform as assumed in Figure 2-10. Furthermore, the intensities in Figure 2-10 were calculated with the assumption that the test optic does not contain any mid-spatial-frequency aberrations. Such aberrations may exist in real optics and would add to the unwanted test and reference beam overlap within the test-beam window. However, Figure 2-10 suggests that in practice, the separation of the two image-plane foci should be greater than $20 \lambda/NA$ (40 fringes) and the window size should be comparable to or smaller than that separation.

Both the test-beam spatial filtering and the reference-wave degradation caused by the window filter would be significant for large aberrations in the optical system under test. Consequently, the PS/PDI scheme is best suited for characterizing optics with relatively small aberrations, such as those needed in lithography applications.

2.4.3. Grating Beamsplitter and Fringe Contrast

In phase-shifting point diffraction interferometry, the beamsplitter can either be placed before the object plane, between the object plane and the optic, or between the optic and the image plane. The beam spot separation in the focal plane depends on the angular spread produced by the beamsplitter and on the position of the beamsplitter relative to the object/image plane. To obtain the necessary beam separation at focus and maintain high degree of spatial overlap inside the optical system under test and at the detector, a low-angle beamsplitter placed a large distance from the object/image plane should be used.

Here a transmission grating is considered, as it is the most convenient beamsplitter available for use in the EUV PS/PDI. The spatial separation of the adjacent diffractive orders that is required at focus is typically $20\text{-}30 \lambda/\text{NA}$, where NA is the numerical aperture of the beam that illuminates the grating. At EUV wavelengths near 13 nm and numerical apertures around 0.1, the necessary focal spot separation is typically several micrometers. On the object-side of a demagnifying optical system, this separation is greater by a factor equal to the demagnification. To maintain high degree of spatial overlap of the test and reference beams within the optic and at the detector, the grating should be placed near the pupil plane of the optic because the angular beam separation is then minimized. The grating pitch is determined by the desired fringe density (typically 40-60 fringes) because the number of fringes equals the number of illuminated grating lines. As a consequence, the required grating pitch is quite coarse, typically tens of micrometers to about a millimeter. This is advantageous in phase-shifting interferometry for the control of the grating translation step, which is some fraction of the grating pitch.

When the beamsplitter cannot precede the object plane of the test optic, as shown in Figure 2-2(b), due to an aberrated or extended illumination source, the beamsplitter aberrations may contribute to systematic measurement errors. In a simple planar transmission grating considered here, aberrations can arise from grating substrate non-uniformities, the non-planar illumination of the grating, and from line positioning errors in the grating.

The substrate effects may be completely avoided when a free-standing transmission grating can be used. However, a grating substrate that is nonuniform and optically thick may introduce aberrations into the measurement wavefront. The most commonly used grating

substrates used to support the grating structure are thin membranes made of either silicon nitride or silicon. The membrane thicknesses that minimize attenuation at EUV wavelengths while providing sufficient mechanical strength, vary from about 100 nm for silicon nitride [88] to about 600 nm for silicon [125]. As seen from Table 1-1, in transmission through 600 nm of silicon, 13.4-nm radiation incurs an optical phase shift of 0.0026 wave, relative to propagation in vacuum. For 100-nm of silicon nitride, the relative optical phase shift is 0.19 wave. Unwanted aberrations may be produced by non-uniformities in the membrane thickness, which is typically much less than 10% over the 1 cm² or smaller area of the membrane. Since the membrane substrates are quite optically thin, the aberrations produced by the possible small non-uniformities in the thickness are usually negligible.

In the PS/PDI the planar grating is illuminated by a beam that is either converging to (or diverging from) focus. The variations in the incidence angles over the illuminated area of the grating produce an aberration that is coma-like in nature. The aberration is produced in the non-zero diffractive orders, when the optical path from the grating to the m^{th} diffractive real (or virtual) focus is not compensated by the tilt introduced by the grating. Specifically, for an illumination beam of numerical aperture NA, the optical path difference (OPD) has the form

$$(2-2) \quad \text{OPD} = ms \left(\frac{1}{\sqrt{1/\text{NA}^2 - 1}} - \frac{1}{\sqrt{1/\text{NA}^2 - 1 + \rho^2}} \right) \rho \cos \theta$$

$$= ms \left(\frac{1}{2} \left(\frac{\rho}{\sqrt{1/\text{NA}^2 - 1}} \right)^3 - \frac{3}{8} \left(\frac{\rho}{\sqrt{1/\text{NA}^2 - 1}} \right)^5 + \frac{5}{16} \left(\frac{\rho}{\sqrt{1/\text{NA}^2 - 1}} \right)^7 - \dots \right) \cos \theta,$$

where (ρ, θ) are the normalized beam coordinates in the far field ($|\rho| \leq 1$), m is the grating diffractive order, and s is the spot separation at focus. The OPD was found under the assumption that the beam spot separation is much smaller than the distance between the grating and the beam focus, or equivalently, that the grating pitch is much greater than the wavelength. The aberration has a strong dependence on the numerical aperture, as illustrated in Figure 2-11 that shows the peak-to-valley OPD in the first diffractive order for typical focal spot separations. At low numerical apertures, the aberration is dominated by primary coma ($\rho^3 \cos \theta$), but higher-order coma terms become important above 0.1 NA. Equation 2-2 indicates that the variation in the incidence angles over the grating does not aberrate the undiffracted zero-order beam, but can result in significant aberrations in the non-zero diffractive orders for beam numerical apertures above 0.1. For example, at a

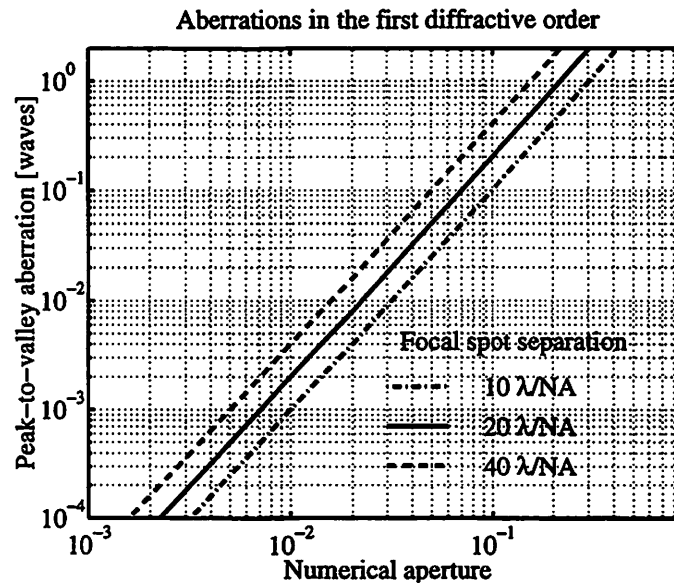


Figure 2-11. Aberrations of a grating illuminated by a converging/diverging beam.

The peak-to-valley coma aberration vs. numerical aperture of the illumination beam. The aberration, produced in the non-zero grating orders when a planar grating is illuminated by a beam converging/diverging to/from focus, depends on the separation of the grating diffractive orders at focus.

numerical aperture of 0.025 and a focal spot separation of $20 \lambda/\text{NA}$, the unbalanced coma in the first diffracted order from Equation 2-2 is 0.0125 wave peak-to-valley. The peak-to-valley and rms magnitudes of the corresponding balanced coma, described by Zernike polynomials, are 0.0042 wave and 0.00074 wave, respectively. At 0.1 numerical aperture, the unbalanced coma becomes 0.20 wave peak-to-valley and the balanced coma scales correspondingly.

Errors in the grating lines can also lead to aberrations in the non-zero diffractive orders of the grating. A grating line position error, a fraction q of the grating period in magnitude, produces a wavefront aberration in the m^{th} diffractive order of mq waves. The aberration profile corresponds to the grating line error profile over the illuminated portion of the grating. It is important to note that the zero-order beam is not affected by either illumination effects or by grating line-placement errors. Consequently, grating aberrations do not affect the test wavefront when the undiffracted zero order is chosen to be the test wavefront in the interferometer.

Placing the beamsplitter before the object plane as in Figure 2-2(b) requires a small-size radiation source and a near diffraction-limited illuminator system, neither of which are currently available at EUV wavelengths. The PS/PDI in Figure 2-2(a) with the beamsplitter after the entrance pinhole may be the only practical configuration in testing EUV optical systems. Although less appealing in principle, with the choice of the zero grating order for the test beam, the grating beamsplitter does not introduce any systematic errors to the wavefront measurement when the grating substrate aberrations are negligible.

The grating transmission function is essentially binary because the material absorption is too high for the possibility of phase gratings near 13-nm wavelength (see Table 1-1). For typical binary gratings with 50% open area, the zero-order beam is about 2.5 times stronger than the first-order beam. In choosing the zero order for the test beam, the weaker beam is further reduced in intensity by the reference pinhole spatial filter. To improve the fringe contrast, the open area of the grating can be reduced. Some of the trade-offs in balancing fringe contrast with the overall efficiency of the interferometer are illustrated in Figure 2-12. Assuming that the grating follows the entrance pinhole, the fringe contrast and the power transmitted through the image-plane pinhole-window spatial filter are shown for grating open areas of 20%, 35%, and 50% for cases when either the zero-order or the first-order beams are filtered by the small pinhole. The illumination beam is

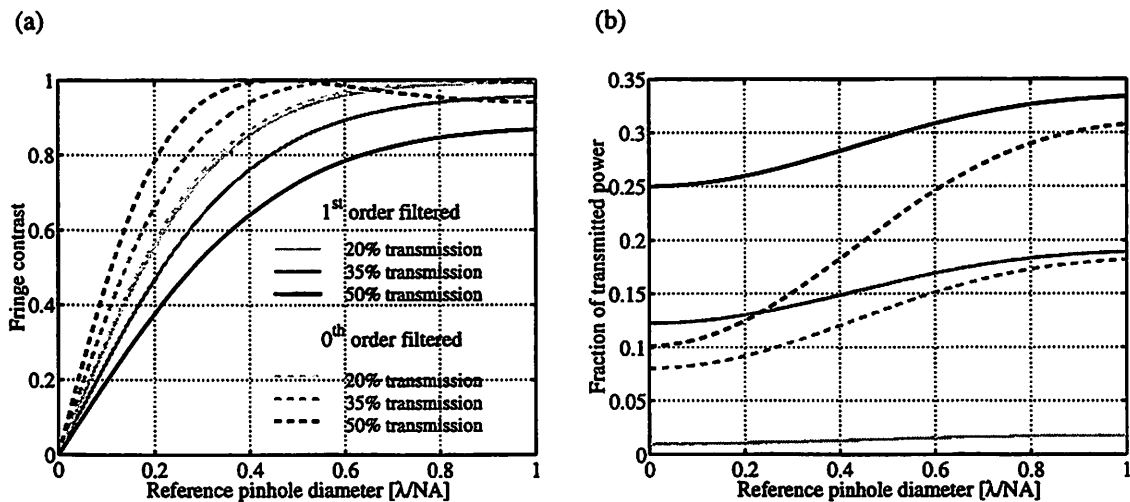


Figure 2-12. Fringe contrast and power transmission vs. pinhole size.

The fringe contrast and the power transmission when a binary grating beamsplitter is used after the entrance pinhole. (a) The far-field fringe contrast produced when an unaberrated beam is spatially filtered by a circular reference pinhole at focus plotted as a function of pinhole diameter. (b) The fraction of the power transmitted by a two-pinhole spatial filter versus diameter of the reference pinhole. The results are shown for grating open areas of 20%, 35%, and 50%, when either the zeroth or the first diffractive order is spatially filtered.

assumed to be unaberrated and the window transmission is taken as unity. The results depend on the size of the reference pinhole filter. The figure confirms that filtering of the weaker beam, rather than the stronger beam, results in lower fringe contrast. However, in the range of useful pinhole diameters, contrasts above 40% are possible even when the weaker beam is filtered. The contrast can be improved at the expense of the interferometer throughput by reducing the grating open area below 50%. The relative merit of this depends on the dynamic range of the detector and on the available flux.

2.4.4. Source Bandwidth

The temporal coherence of the source determines the number of fringes that can be observed in an interferometer. In both the conventional PDI and the phase-shifting PDI, the test and reference waves are spatially displaced in one direction, producing relatively high densities of tilt fringes. The fringe density depends on the lateral displacement s of the reference pinhole from the test-beam focus. At the wavelength λ , the number of tilt fringes in the far field equals $2sNA/\lambda$ over the numerical aperture NA . In the conventional PDI, the fringe density is wavelength dependent. Consequently, relative spectral bandwidths that are much smaller than the inverse of the number of fringes are required. In the phase-shifting PDI with a grating beamsplitter, the focal spot separation s produced by the grating equals $z\lambda/g$, where z is the distance between the grating and the focus and g is the grating pitch. The number of fringes becomes $2sNA/\lambda = 2(z\lambda/g)NA/\lambda = 2zNA/g$. Thus the use of a chromatic beamsplitter leads to wavelength-independent fringe densities. When the reference pinhole can be used to filter the zero grating order and the test window to transmit the wavelength-dependent first order, the temporal-coherence-length requirements are

minimal. On the other hand, when the reference pinhole filters the first grating order, it also serves as a monochromator for the reference beam, while the window spatial filter does not change the temporal bandwidth of the test beam. If a broad-band source were used, spatial filtering of the first diffractive order would reduce fringe contrast. As a result, a relatively spectrally narrow source is needed for the PS/PDI, with the exception of the configuration in which the grating follows the entrance pinhole and the first diffractive order is used for the test beam.

2.4.5. Source Spatial Coherence

Spatially coherent radiation is required to achieve satisfactory fringe contrast in point diffraction interferometry. Although undulator sources can provide sufficient coherent flux for EUV interferometry experiments [36], only a relatively small fraction of the total narrow-band radiation from the undulator, typically 1/10 to 1/100, corresponds to coherent power. The coherent radiation is selected with a pinhole whose size must be somewhat smaller than the coherence area of the radiation [127, 128]. In this section, the effect of spatial coherence of the light source on the quality of the wavefront transmitted through the pinhole is considered. Both the degree of coherence and the far-field phase of the transmitted wavefront are investigated by using a statistical description of the radiation fields, applicable to relatively incoherent sources.

In point diffraction interferometry, the pinhole that select the spatially coherent light is usually placed in the object plane of the optic under test. When a condenser system with a numerical aperture NA_c is utilized to project an image of the mostly incoherent light source onto the entrance pinhole, the coherence area at the pinhole plane is given approx-

imately by $A_c = \lambda^2/4NA_c^2$. Thus the choice of the condenser numerical aperture depends on the pinhole size needed to achieve spherical illumination of the test optic, which is about one third to one half of the resolution unit of λ/NA (on the object side of the test optic). To efficiently transfer spatially coherent radiation to the interferometer, the illuminator numerical aperture NA_c should be somewhat smaller than the entrance numerical aperture NA of the test optic.

Since the entrance pinhole is not illuminated by a spatially coherent beam, the effects of partial coherence on the wavefront produced by the entrance pinhole warrant consideration. Specifically, the reduced spatial coherence may affect the fringe contrast and the phase of the wavefront. For near monochromatic radiation of interest in point diffraction interferometry, the partially coherent radiation is described by the mutual intensity $J_{12}(P_1, P_2)$, given by the cross-correlation of two fields $U(P_1, t)$ and $U(P_2, t)$, or

$$(2-3) \quad J_{12}(P_1, P_2) = \langle U(P_1, t) U^*(P_2, t) \rangle,$$

where the average is taken over time t [127, 128]. The mutual intensity normalized by the geometric mean of the intensities I_1 and I_2 at the two points P_1 and P_2 , known as the complex coherence factor μ_{12} , gives the complex degree of coherence of the light. The complex coherence factor, expressed as

$$(2-4) \quad \mu_{12} = \frac{J_{12}}{\sqrt{J_{11}J_{22}}} = \frac{J_{12}}{\sqrt{I_1 I_2}},$$

ranges from 0 to 1 in magnitude and is directly proportional to the contrast of the interference of the radiation from the two points [127, 128]. To obtain high-contrast interference in the interferometer, the magnitude of the degree of coherence of the radiation transmitted through the entrance pinhole should be close to 1.

The phase of partially coherent radiation is not determined from the first-order properties of the light given by the mutual intensity. For radiation fields produced by an ensemble of sources, the phase can be understood from the statistical properties of the radiation fields. The statistical description of monochromatic, linearly polarized radiation has been used to describe speckle patterns produced by an ensemble of scatterers [129] but can be applied to represent partially coherent radiation from an ensemble of mutually independent sources. In particular, for radiation from undulator beamlines of interest here, which is typically linearly polarized and may be spectrally narrowed with a monochromator, the statistical description applies when the light is relatively spatially incoherent.

Given that the fields from the many individual sources in the undulator beam that contribute to the total field are mutually independent and their phases are uniformly distributed on the interval $(-\pi, \pi)$, the radiation fields can be described by a circular Gaussian probability distribution function [129]. In particular, the probability density function for the real and imaginary parts of the complex field amplitude, A^R and A^I , is given by

$$(2-5) \quad p_{RI}(A^R, A^I) = \frac{1}{2\pi\sigma^2} \exp\left(-\frac{(A^R)^2 + (A^I)^2}{2\sigma^2}\right),$$

where σ^2 is the variance of A^R and A^I . On average, the field components are zero and the intensity is $2\sigma^2$. Given that the field components are related to the intensity I and the phase θ by $A^R = \sqrt{I}\cos\theta$ and $A^I = \sqrt{I}\sin\theta$, the statistics of the intensity and the phase can be determined from the above probability density distribution. The probability densities of the intensity and the phase follow the negative exponential distribution and the uniform distribution on the interval $(-\pi, \pi)$, respectively [129].

To assess the effect of partial coherence on the wavefront phase, higher-order statistics are needed to describe the field at multiple points. The probability distribution of the multiple fields is jointly Gaussian with the cross-correlations between the different points given by the mutual intensity [129]. The joint probability density function of the real and imaginary parts of the fields A_i^R and A_i^I at N different points P_i takes the form [130]

$$(2-6) \quad p_{RI}(A) = \frac{\sqrt{|J_A^{-1}|}}{(2\pi)^N} \exp\left(-\frac{A^T J_A^{-1} A}{2}\right),$$

where the fields are denoted vectorially by $A = [A_1^R \ A_1^I \ A_2^R \ A_2^I \ \dots \ A_N^R \ A_N^I]^T$ and J_A is the matrix of cross-correlations of the field components. The cross correlation matrix, related to the real and imaginary parts μ_{ij}^R and μ_{ij}^I of the mutual coherence factor μ_{ij} for points P_i and P_j and to the variance σ_i^2 of the individual field components, is given by

$$(2-7) \quad J_A = \begin{bmatrix} \sigma_1^2 & 0 & \sigma_1 \sigma_2 \mu_{12}^R & \sigma_1 \sigma_2 \mu_{12}^I & \sigma_1 \sigma_3 \mu_{13}^R & \sigma_1 \sigma_3 \mu_{13}^I & \dots \\ 0 & \sigma_1^2 & -\sigma_1 \sigma_2 \mu_{12}^I & \sigma_1 \sigma_2 \mu_{12}^R & -\sigma_1 \sigma_3 \mu_{13}^I & \sigma_1 \sigma_3 \mu_{13}^R & \dots \\ \sigma_1 \sigma_2 \mu_{12}^R & -\sigma_1 \sigma_2 \mu_{12}^I & \sigma_2^2 & 0 & \sigma_2 \sigma_3 \mu_{23}^R & \sigma_2 \sigma_3 \mu_{23}^I & \dots \\ \sigma_1 \sigma_2 \mu_{12}^I & \sigma_1 \sigma_2 \mu_{12}^R & 0 & \sigma_2^2 & -\sigma_2 \sigma_3 \mu_{23}^I & \sigma_2 \sigma_3 \mu_{23}^R & \dots \\ \sigma_1 \sigma_3 \mu_{13}^R & -\sigma_1 \sigma_3 \mu_{13}^I & \sigma_2 \sigma_3 \mu_{23}^R & -\sigma_2 \sigma_3 \mu_{23}^I & \sigma_3^2 & 0 & \dots \\ \sigma_1 \sigma_3 \mu_{13}^I & \sigma_1 \sigma_3 \mu_{13}^R & \sigma_2 \sigma_3 \mu_{23}^I & \sigma_2 \sigma_3 \mu_{23}^R & 0 & \sigma_3^2 & \dots \\ \vdots & \vdots & \vdots & \vdots & \vdots & \vdots & \dots \end{bmatrix}$$

Substituting the cross-correlation matrix for fields $A_1=A_1^R+iA_1^I$ and $A_2=A_2^R+iA_2^I$ at two points P_1 and P_2 in Equation 2-6, the probability density becomes

$$(2-8) \quad p_{RI}(A_1^R, A_1^I, A_2^R, A_2^I) = \frac{\exp\left(\frac{\frac{\sigma_2}{\sigma_1}|A_1|^2 + \frac{\sigma_1}{\sigma_2}|A_2|^2 - \mu_{12}A_1A_2^* - \mu_{12}^*A_1^*A_2}{2\sigma_1\sigma_2(1-|\mu_{12}|^2)}\right)}{4\pi^2\sigma_1^2\sigma_2^2(1-|\mu_{12}|^2)}$$

Using the relationships between the real and imaginary field components and the intensity and phase, the joint probability density can be expressed in terms of the intensities and the phases at the two points. To obtain the statistical properties of the two phases θ_1 and θ_2 , the joint probability density for the intensities and phases can be integrated over the range of values of the intensities I_1 and I_2 . The resulting joint probability density function for the phases θ_1 and θ_2 is given by [129]

$$(2-9) \quad p_\theta(\theta_1, \theta_2) = \frac{1-|\mu_{12}|^2}{4\pi^2} (1-\beta^2)^{\frac{3}{2}} \left(\beta \sin^{-1} \beta + \frac{\pi\beta}{2} + \sqrt{1-\beta^2} \right),$$

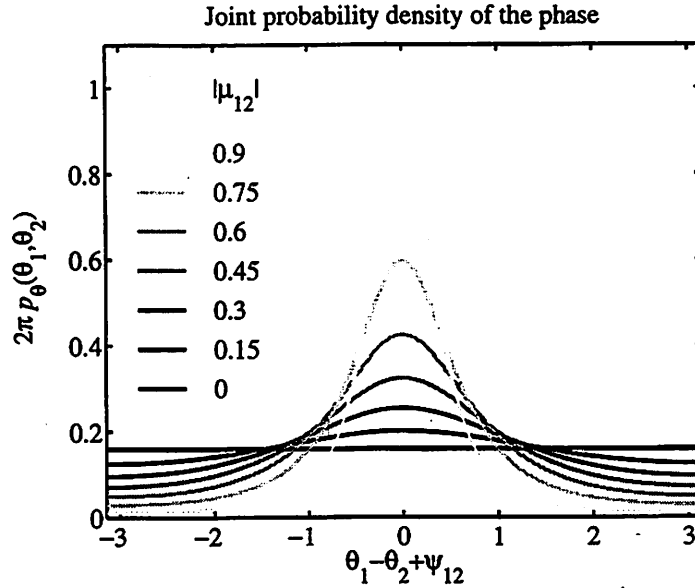


Figure 2-13. Probability density function of the phase at two points.

The joint probability density of the phases θ_1 and θ_2 of monochromatic, polarized radiation field at two points P_1 and P_2 for different values of the mutual coherence factor $\mu_{12} = |\mu_{12}| \exp(i\psi_{12})$.

where $\beta = |\mu_{12}| \cos(\theta_1 - \theta_2 + \psi_{12})$ depends on the mutual coherence factor $\mu_{12} = |\mu_{12}| e^{i\psi_{12}}$.

The probability density function for the phase difference $\theta_2 - \theta_1$, plotted in Figure 2-13, is uniformly distributed on the interval $(-\pi, \pi)$ when the two fields are mutually incoherent and becomes peaked about the mean ψ_{12} as the mutual coherence increases. In the plane of the entrance pinhole, where the field can be thought of as a superposition of fields from an ensemble of independent sources, the mean phase difference ψ_{12} , which corresponds to the phase of the mutual coherence factor μ_{12} , represents the average difference in the phase at the points P_1 and P_2 .

To understand the properties of the phase following the spatial filtering by the entrance pinhole, the radiation field must be propagated to the far field where the wavefront inter-

acts with the optic under test. Since the entrance pinhole size typically exceeds the radiation wavelength, the light propagation can be described by scalar diffraction theory. The far-field amplitude B_n at a point Q_n is the superposition of the amplitudes A_m at points P_m within the pinhole aperture at distances R_{mn} from Q_n . The Fresnel-Kirchhoff diffraction integral [110-111] can be written as a summation over fields at all the points in the aperture, namely

$$(2-10) \quad B_n = \frac{\Delta^2}{i\lambda} \sum_m A_m \frac{\exp\left(\frac{i2\pi R_{mn}}{\lambda}\right)}{R_{mn}},$$

where Δ^2 is the area of each integration element. Since the expansion of the fields B_n is linear in the fields A_m , the propagation corresponds to a linear transformation with the position-dependent weight factors in Equation 2-10. Given the field vectors

$A = [A_1^R \ A_1^I \ A_2^R \ A_2^I \ \dots \ A_N^R \ A_N^I]^T$ and $B = [B_1^R \ B_1^I \ B_2^R \ B_2^I \ \dots \ B_N^R \ B_N^I]^T$, the propagation can be written as

$$(2-11) \quad B = SA,$$

where transformation matrix S consists of 2×2 sub-matrices S_{nm} , describing the coupling between the real and imaginary components of the fields B_n and A_m , given by

$$(2-12) \quad S_{nm} = \frac{\Delta^2}{\lambda R_{mn}} \begin{bmatrix} \sin(2\pi R_{mn}/\lambda) & \cos(2\pi R_{mn}/\lambda) \\ -\cos(2\pi R_{mn}/\lambda) & \sin(2\pi R_{mn}/\lambda) \end{bmatrix}.$$

Given the Gaussian statistics of the radiation in the entrance pinhole plane, the statistical distribution of the far-field amplitudes is also Gaussian and has the form of Equation 2-6. The cross-correlation matrix J_B for the amplitudes B is related to the cross-correlation matrix J_A in Equation 2-7 through the transformation matrix S that describes the geometry of the pinhole aperture and the propagation [130]. Specifically,

$$(2-13) \quad J_B = SJ_A S^T.$$

To consider the effects of the source spatial coherence on the quality of the wavefront diffracted by the entrance pinhole, the cross-correlation matrix of the fields in the entrance pinhole plane must first be determined. The mutual intensity of synchrotron radiation has been reported for the Gaussian approximation [131]. Under this approximation, both the positions and the angular distributions of electrons in the beam are described by two uncorrelated Gaussians, varying along the horizontal and the vertical directions to account for the different beam size in the two directions in many electron storage rings. In addition, the amplitude of the radiation from a single electron is also assumed to be Gaussian at the source. For undulator radiation in the central part of the angular distribution and at the wavelength of the maximum brightness, i. e. for the radiation useful for point diffraction interferometry [36], this assumption represents a good approximation [131].

The electron beam size and angular spread in the horizontal and the vertical directions, corresponding the half-widths at $1/\sqrt{e}$ of the maximum, are denoted by σ_x and σ_y and by σ'_x and σ'_y , respectively. The parameters for the radiation from a single electron are

given by $\sigma_r = \sqrt{\lambda L}/4\pi$ and $\sigma_r' = \sqrt{\lambda/L}$, where λ is the wavelength and L is the length of the undulator [132]. The overall radiation half-widths of the beam intensity and its angular spread in the horizontal and the vertical directions are given by [132]

$$(2-14) \quad \sigma_{Tx} = \sqrt{\sigma_x^2 + \sigma_r^2}, \quad \sigma_{Ty} = \sqrt{\sigma_y^2 + \sigma_r^2}, \text{ and}$$

$$(2-15) \quad \sigma_{Tx}' = \sqrt{\sigma_x'^2 + \sigma_r'^2}, \quad \sigma_{Ty}' = \sqrt{\sigma_y'^2 + \sigma_r'^2}.$$

Using the radiation parameter definitions and denoting the total radiation flux by F , the mutual intensity J_0 between points (x_1, y_1) and (x_2, y_2) at the undulator source is given by [131]

$$(2-16) \quad J_0(x_1, y_1; x_2, y_2) = \frac{F}{4\pi^2 \sigma_{Tx} \sigma_{Ty}} \times$$

$$\exp\left(\frac{\left(x_1^2 + x_2^2\right)\left(1/4\sigma_{Tx}^2 + 4\pi^2\sigma_{Tx}'^2/\lambda^2\right) + 2x_1x_2\left(1/4\sigma_{Tx}^2 - 4\pi^2\sigma_{Tx}'^2/\lambda^2\right)}{2}\right) \times$$

$$\exp\left(\frac{\left(y_1^2 + y_2^2\right)\left(1/4\sigma_{Ty}^2 + 4\pi^2\sigma_{Ty}'^2/\lambda^2\right) + 2y_1y_2\left(1/4\sigma_{Ty}^2 - 4\pi^2\sigma_{Ty}'^2/\lambda^2\right)}{2}\right).$$

As an example, properties of 13-nm radiation from a 8-cm-period undulator with 55 periods at the Advanced Light Source, used in point diffraction interferometry experiments that are described in Chapter 3 and Chapter 5, are considered here. Using the electron beam parameters $\sigma_x = 200 \mu\text{m}$, $\sigma_y = 38 \mu\text{m}$, $\sigma_x' = 18 \mu\text{rad}$, and $\sigma_y' = 9.5 \mu\text{rad}$ and the

single electron radiation parameters $\sigma_r = 19 \mu\text{m}$ and $\sigma_r' = 54 \mu\text{rad}$ [133, 134], the full widths of the mutual coherence factor are 73 and 84 μm in the horizontal and vertical directions, respectively. These are similar to the approximate coherence widths for an incoherent source, given by $\lambda/2NA_x = 80 \mu\text{m}$ and $\lambda/2NA_y = 83 \mu\text{m}$, where $NA = \sqrt{2}\sigma'$ is the numerical aperture of the beam [128]. The fraction of the total power that is coherent equals $\lambda^2 / \left(16\pi^2 \sigma_{Tx} \sigma_{Tx}' \sigma_{Ty} \sigma_{Ty}' \right) = 0.04$.

Since the source is imaged with a condenser system onto the entrance pinhole plane, the mutual intensity in the plane of the pinhole relates to the mutual intensity at the source through a four-dimensional convolution with the condenser amplitude response function $K(P', P)$ between the source point P' and the image point P [127], namely

$$(2-17) \quad J_A(P_1, P_2) = \int \int \int \int_{-\infty}^{\infty} J_0(P_1', P_2') K(P_1', P_1) K^*(P_2', P_2) dP_1' dP_2'.$$

The mutual intensity in the entrance pinhole plane depends on the properties of the illuminator system. A relatively unaberrated condenser may be expected to increase the degree of coherence in forming the image of the source. As an angular low-pass filter, the illuminator system is likely to widen the spatial extent of the mutual intensity function in the source image plane, effectively increasing the degree of coherence. However, if the condenser has significant aberrations that cause substantial scattering of light, it may decrease the degree of spatial coherence.

As illustrated in Figure 2-13, the mean phase difference between any two points in the wavefront is given by the phase of the mutual coherence factor. Equation 2-16 shows that at the undulator source the mutual intensity is purely real. If the source size is significantly smaller than its separation from the illuminator optics, the phase of the mutual coherence factor $J_A(P_1, P_2)$ is approximately zero and the mean phase difference between any two points at the pinhole plane is also zero [127, 135].

Even when the mutual coherence factor in the pinhole plane is real, the propagation to the far field, described by Equation 2-10 and Equation 2-13, introduces a complex phase factor into the mutual intensity. However, in the case of interest here, it can be shown that this phase factor is negligible because the entrance pinhole size is significantly smaller than the distance between the pinhole and the test optic. Given that the assumptions stated here are approximately valid in point diffraction interferometry, the mean phase difference between any two points on a spherical surface centered on the entrance pinhole is zero. Thus the wavefront diffracted from the entrance pinhole is spherical on average and the lack of spatial coherence of the undulator source affects only the contrast in the measurement.

As an example, let us consider an undulator beam with numerical aperture NA_c , uniformly illuminating the entrance pinhole. The mutual coherence factor is assumed to be a circularly symmetric Gaussian with a width that corresponds to the coherence size of $\lambda/2NA_c$. The calculated coherence properties of the wavefront diffracted by the pinhole are illustrated in Figure 2-14. Figure 2-14(a) gives the mutual coherence factor between two points Q_1 and Q_2 that are on the diffracted spherical wavefront at the edge of the

angular cone defined by the numerical aperture NA of interest, as illustrated in Figure 2-14(b). The mutual coherence factor between two points at the edge of the angular cone represents the worst-case degradation in the spatial coherence over the wavefront. The mutual coherence factor is shown as a function of the pinhole diameter, expressed in the resolution units of the illuminator and the optic under test, or λ/NA_c and λ/NA . When the pinhole diameter is smaller than the coherence size $\lambda/2NA_c$ and also sufficiently small to produce a high-quality wavefront over the numerical aperture NA of interest, the magnitude of the degree of coherence is near 1. Thus for pinhole sizes suitable for point diffraction interferometry experiments, the source spatial coherence does not significantly affect the fringe contrast.

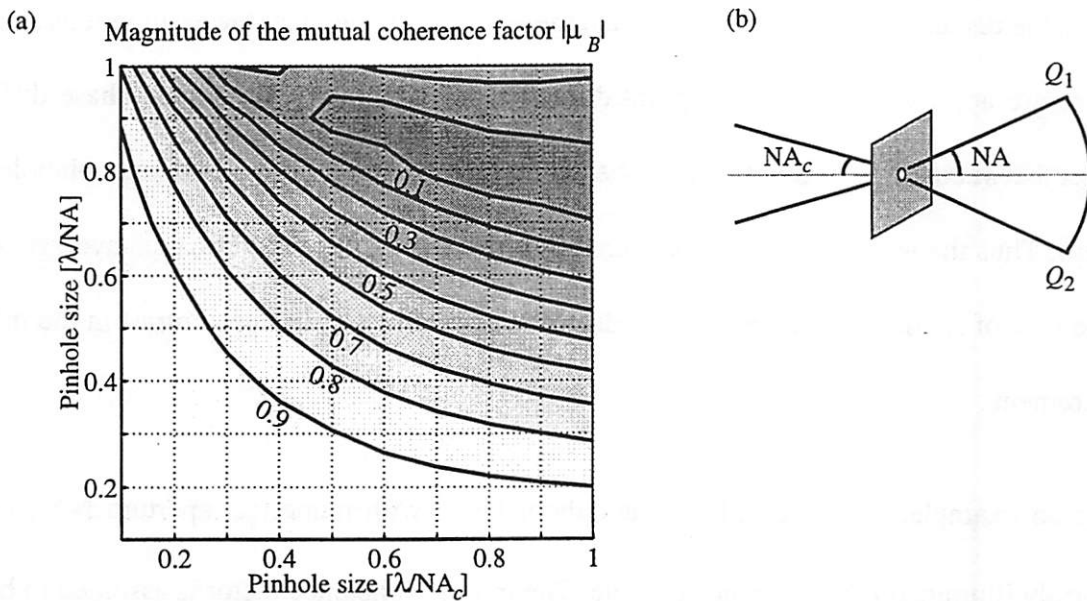


Figure 2-14. The calculated mutual coherence factor in the illumination wavefront.

(a) The magnitude of the mutual coherence factor between two points Q_1 and Q_2 in the wavefront diffracted from a uniformly illuminated entrance pinhole as a function of the pinhole diameter. The pinhole size is given in terms of the resolution unit for the illumination beam (λ/NA_c) and for the diffracted beam (λ/NA). (b) The points Q_1 and Q_2 are at the edge of the angular cone of interest, defined by the numerical aperture NA. The mutual coherence factor at the entrance pinhole plane is assumed to be Gaussian.

In summary, the degree of coherence and the phase of a wavefront diffracted by a pinhole aperture illuminated with an incoherent source can be studied using the method outlined here. In point diffraction interferometry utilizing undulator radiation having a relatively small degree of spatial coherence and an illuminator system to image the source onto the entrance pinhole, the lack of spatial coherence at the source does not significantly affect the quality of the wavefront generated by the entrance pinhole. The surface of constant phase of the wavefront is spherical on average, as required. With a proper choice of the entrance pinhole size, the reduction of the interferogram fringe contrast due to the partial spatial coherence is also not significant.

2.4.6. Systematic Coma Effect and Use of Pupil Reimaging Optics

In point diffraction interferometry, the far-field pattern of the interference between the test and reference beams depends on the properties of the two wavefronts and on their spatial separation. Because the lateral separation of the test and reference beam foci is quite large, the fringe pattern consists mainly of tilt fringes but also contains various orders of the coma aberration. The geometrical effect due to the beam separation is always present even when both beams are perfectly spherical wavefronts. The magnitude of this effect increases with the numerical aperture of the two beams and is found by considering the optical path difference in the far-field between two laterally displaced point sources. For source separation s , the optical path difference up to the fifth order is given by

$$(2-18) \quad \text{OPD} = s \left(\text{NA} \rho \cos \theta - \frac{1}{2} \text{NA}^3 \rho^3 \cos \theta + \frac{3}{8} \text{NA}^5 \rho^5 \cos \theta - \dots \right),$$

where (ρ, θ) are the normalized beam coordinates ($|\rho| \leq 1$) over the numerical aperture NA. The first three terms in the expansion are tilt, primary coma, and secondary coma, respectively. At moderate numerical apertures only the primary coma is significant. For example, at numerical aperture of 0.1 for beam spot separation of $25 \lambda/NA$ at focus, the unbalanced primary coma aberration is 0.25 wave peak-to-valley and the unbalanced secondary coma is 0.0019 wave peak-to-valley. This systematic coma effect must be accounted for in the fringe analysis, as it is inherent to the interferometry technique not to the optical system under test.

The fringe curvature can be corrected in principle with the use of a relay optic, introduced between the image plane and the camera, to image the grating plane onto the detector. Reimaging optics to project an image of the pupil of the system on the detector are commonly used in interferometry in order to minimize propagation and edge diffraction effects in the recorded wavefronts [136, 77]. At EUV wavelengths such optics are currently unavailable. If pupil reimaging were used, a well-corrected relay optic would be needed to avoid introducing distortion into the recorded interference pattern and to minimize the difference in the optical paths of the test and reference waves. Owing to high fringe densities in the PDI, the two beams propagate in slightly different directions through the relay optic and the design of a reimaging optic is quite challenging.

2.5. Data Analysis Techniques

The recorded interference of the test and reference beam must be analyzed to find the unknown phase difference between the two waves. General expression for the intensity

$I(x, y)$ of a fringe pattern detected in a plane (x, y) is given by

$$(2-19) \quad I(x, y) = I'(x, y) + I''(x, y) \cos(\phi_T(x, y) - \phi_R(x, y) + \Delta).$$

The average intensity $I'(x, y)$ is the sum of the individual test and reference wave intensity patterns. The fringe modulation $I''(x, y)$ is proportional to the product of the amplitudes of the two waves and to their degree of coherence. The modulation phase is the difference between the unknown phase $\phi_T(x, y)$ of the test wave and the known phase $\phi_R(x, y)$ of the reference wave. In phase-shifting interferometry a spatially uniform variable phase offset Δ can be also introduced.

The fringe analysis is performed in several stages. The phase difference between the test and reference waves, $\phi_T(x, y) - \phi_R(x, y)$, is found first. If the phase offset Δ between the test and reference waves can be varied, numerous phase-shifting schemes that combine multiple interferograms can be used. For analysis of individual interferograms with large fringe densities, Fourier transform methods are suitable. The modulo- 2π raw phase difference determined by fringe analysis is subsequently “unwrapped” to obtain a phase difference surface. In most interferometers, certain components of the detected phase difference are not properties of the test optic but rather by-products of the measurement. In point diffraction interferometers, they include the tilt, the defocus, and the systematic coma effect. These factors must be removed from the detected phase difference. The final step in the analysis is often the fitting of the phase difference to a set of polynomials, to obtain a compact representation of the measured wavefront in terms of specific well-understood aberrations.

2.5.1. Phase-Shifting Techniques

The ability to vary the relative phase shift between the test and reference beams allows the use of a powerful class of fringe analysis methods that are based on combining multiple interferograms with different relative phase shifts [78, 137]. For example, recording five interferograms in a sequence while varying the phase offset Δ in increments of $\pi/2$ gives

$$\begin{aligned}
 (2-20) \quad I_1(x, y) &= I'(x, y) + I''(x, y) \cos(\phi(x, y)), \\
 I_2(x, y) &= I'(x, y) - I''(x, y) \sin(\phi(x, y)), \\
 I_3(x, y) &= I'(x, y) - I''(x, y) \cos(\phi(x, y)), \\
 I_4(x, y) &= I'(x, y) + I''(x, y) \sin(\phi(x, y)), \\
 I_5(x, y) &= I'(x, y) + I''(x, y) \cos(\phi(x, y)).
 \end{aligned}$$

The unknown phase difference $\phi(x, y)$ can be found simply by combining the multiple interferograms to cancel out the average background intensity $I'(x, y)$ and the fringe modulation $I''(x, y)$. Many different phase-shifting algorithms can be devised and optimized for specific interferometry applications [78, 138]. One of the simplest is the Hariharan algorithm [139, 78], which uses five interferograms with phase step of $\pi/2$ and is very robust with respect to sensitivity in the phase step error. The phase difference in the example fringe patterns of Equation 2-20 given by the Hariharan algorithm is

$$(2-21) \quad \phi(x, y) = \tan^{-1} \left(\frac{2(I_2(x, y) - I_4(x, y))}{2I_3(x, y) - I_5(x, y) - I_1(x, y)} \right).$$

The challenges in phase-shifting interferometry include the complications from inaccurate control of the phase steps Δ . The resulting errors may be reduced by proper choice of phase-shifting algorithms [140, 78] and sometimes by increasing the number of interferograms used in the phase calculation [141]. Analysis of phase-shifting data series can also be performed using an adaptive least-squares algorithm, modified to compensate for irregular phase increments [78, 142].

The primary advantage of phase-shifting interferometry relates to the fact that the phase at each pixel is found independently of other detector pixels, allowing the effects of variations in the background intensity or any fixed-pattern noise to be removed [78]. This ability also improves the spatial resolution of the analysis technique, in comparison to single-interferogram methods such as fringe-location methods and Fourier transform methods [98]. On the other hand, phase-shifting interferometry requires that the multiple interferograms used be recorded under constant experimental conditions, i. e. unchanging interferogram intensity, fringe modulation, and detector properties. This requirement poses demands on the stability of the light source, the interferometer mechanical components, and the test-chamber environment.

2.5.2. Fourier Transform Methods for Single Interferogram Analysis

Single interferogram analysis has traditionally focused on fringe location methods [98, 137], in which the fringe positions are found and the wavefront between the fringes is interpolated. The drawback of the conventional approach is that the interpolation function may not accurately represent the wavefront between the fringes. Fourier transform methods that utilize spatial frequency carriers overcome this limitation [143-147, 78]. The

Fourier transform techniques require relatively large densities of tilt fringes that serve as a spatial frequency carrier modulated by the unknown wavefront. Separating the spatial carrier of frequency \vec{f}_c from the phase difference $\phi(x, y)$ in Equation 2-19, the interferogram intensity can be rewritten as

$$(2-22) \quad I(x, y) = I'(x, y) + I''(x, y) \cos\left(2\pi\vec{f}_c \cdot \vec{x} + \phi(x, y)\right) \\ = I'(x, y) + c(x, y) e^{i2\pi\vec{f}_c \cdot \vec{x}} + c^*(x, y) e^{-i2\pi\vec{f}_c \cdot \vec{x}},$$

where $c(x, y) = \frac{1}{2} I''(x, y) e^{i\phi(x, y)}$. Denoting the frequency-domain quantities by script letters, the Fourier transform of the intensity is

$$(2-23) \quad I(f, g) = I'(f, g) + c(f - f_c, g) + c^*(f + f_c, g).$$

The unknown quantity $c(x, y)$ can be recovered by filtering the Fourier transform of the intensity with a single-side passband filter centered on the carrier frequency \vec{f}_c , shifting the filtered signal to zero frequency, and Fourier transforming back to the space domain. The phase of interest $\phi(x, y)$ is simply the phase of $c(x, y)$. The spatial filtering in the Fourier domain determines the maximum spatial frequency that can be extracted from the interferogram. The use of the passband filter in the Fourier domain requires that the overlap of the background intensity $I'(f, g)$ and the modulated carrier term $c(f - f_c, g)$ be minimal.

2.5.3. Phase Unwrapping and Zernike Polynomial Fitting

The interferogram methods produce the modulo- 2π version of the wavefront of interest. To find the unknown continuous wavefront surface, the 2π phase jumps must be accurately detected and removed. Although simple in principle, phase unwrapping can be challenging in practice in the presence of noise and localized defects in the data. Numerous phase-unwrapping schemes have been devised [148]. The key element in many phase unwrapping methods is the approach for scanning the data to detect discontinuities [148, 142]. Other path-independent techniques utilize some global information about the unwrapped surface [148, 149]. For instance, the unwrapping of the raw phase maps can use a highly filtered, continuous version of the phase maps as a guide to determine the correct phase increments [142].

2.5.4. Zernike Polynomial Fitting

The unwrapped phase maps are often fitted to a set of polynomials to obtain an expansion of the surface in terms of specific low-order aberrations. In optical systems with circular or annular pupils, Zernike polynomials [95-98, 119] are suitable for such an expansion. Some properties of Zernike polynomials are described in the Appendix. The primary and higher-order aberrations correspond to individual Zernike polynomials, orthogonal over a circle or an annulus. However, the analysis domain typically is not a circle or an annulus in practice, owing to the discretization of the data domain. Furthermore, the data may be valid only over an irregular subregion of the measurement domain. Thus to obtain the coefficients of the aberrations described by Zernike polynomials, the fit utilizes an intermediate set of polynomials, orthogonal over the domain of valid data points [150, 119].

First the orthogonal basis set is found by the Gram-Schmidt orthogonalization process, then the data are fitted to minimize the least-squares error in the fit, and finally the intermediate basis set is converted to Zernike polynomials with a linear transformation.

2.5.5. Removing Systematic Coma Effect

In point diffraction interferometry, a systematic coma effect is contained in the fringe pattern when a relay optic to image the plane of the grating on the detector is not used. This coma effect must be excluded from the measured phase because it does not represent an aberration in the test optic. From Equation 2-18, the ratio of the unwanted primary coma and the measured tilt equals $-\frac{1}{2}NA^2$. Thus when the numerical aperture of the system NA is known, the magnitude of geometrical effect is simply the measured tilt scaled by the factor $-\frac{1}{2}NA^2$. If the exact numerical aperture is not known, separate measurements with different tilt orientations can be combined to determine the magnitude of the effect. If needed, higher-order coma terms can be removed analogously.

2.6. Comparison of Phase-Shifting PDI and Conventional PDI

The PS/PDI has three major advantages over the conventional PDI. First, the beam division allows control of the relative phase between the test and reference waves. For instance, a simple translation of a grating beamsplitter perpendicular to the grating lines produces a relative phase shift between any two grating orders. In addition to simplifying the fringe analysis, the phase-shifting capability removes the effects of nonuniform illumination of the optic and any fixed pattern noise, thus yielding improved measurement

accuracy [78]. The second major improvement offered by the PS/PDI is its high efficiency. In the PS/PDI, the reference pinhole samples the center rather than the outer portion of the focused beam, producing an overall reference wavefront attenuation of approximately one order of magnitude rather than three to four orders of magnitude. Thus after accounting for beamsplitter losses, the amount of transmitted light is about two orders of magnitude higher in the PS/PDI design than in the conventional PDI. The third benefit is the reduction of potential reference wavefront aberrations, produced when the reference pinhole is large enough to collect a portion of the beam with significant intensity and/or phase variations. The reference pinhole illumination is more uniform when the pinhole is placed in the wide central portion of the focal pattern in the PS/PDI scheme than when it is positioned in one of the outer “rings” in the PDI.

Disadvantages of the more complex PS/PDI design include the need for greater mechanical stability and the requirement of a more challenging alignment strategy. Also, the phase-shifting PDI is best suited to test relatively unaberrated optical systems, while the conventional PDI can be applied to systems with larger aberrations.

2.7. Conclusion

Point diffraction interferometry is a promising common-path technique for evaluating wavefront aberrations in EUV lithographic optical systems. Both the conventional and the phase-shifting point diffraction interferometers utilize diffraction from sub-resolution pinhole apertures to generate the necessary illumination and reference wavefronts. With the use of diffraction from pinholes of proper size, the interferometric accuracy has the poten-

tial to scale with the wavelength of the radiation used in the measurement. The conventional point diffraction interferometer is simpler and more generally applicable than the phase-shifting design because it is not limited by the magnitude of the aberrations in the test optic. The phase-shifting point diffraction interferometer is best suited to testing optical systems with small aberrations but offers much higher throughput and improved accuracy through phase-shifting.

3 Evaluation of Zone Plate Lenses

3.1. Introduction

Diffractive zone plate lenses play an important role in short-wavelength imaging applications. Owing to their availability at moderate numerical apertures and their good optical imaging performance, these lenses were chosen as the first test optics for at-wavelength wavefront measurements with point-diffraction interferometry at the Advanced Light Source at Lawrence Berkeley National Laboratory [84, 85].

The quality of the extreme ultraviolet (EUV) wavefront produced by several zone plates, fabricated with electron-beam lithography and not optimized for diffraction-limited performance, is considered in this chapter. The properties of the zone plate lenses are evaluated near 13-nm wavelength with measurements of the far-field intensity [151] and with wavefront characterization by conventional point diffraction interferometry [85, 87]. The diffracted far-field intensity from the zone plates contains significant modulation that is consistent with the presence of zone placement errors in the zone plates. The interferometry measurements indicate a small amount of low-order phase aberrations in the diffractive lenses.

3.2. Zonal Placement Errors in Zone Plate Lenses

To achieve good optical performance, the zone plate features must be accurately defined over the sizable area of the zone plate [152]. Here the effects of zone placement fabrication errors on the performance of zone plates are investigated. Experimentally observed zone-plate diffraction patterns are compared to calculated profiles for different zone placement error models to estimate the magnitude of zonal placement errors.

3.2.1. Experimental Observations of Far-Field Intensity Patterns

Measurement of the far-field diffraction pattern of a zone plate optic, performed at beam-line 9 at the Advanced Light Source at Lawrence Berkeley National Laboratory, is schematically represented in Figure 3-1. The experiment is operated with a narrow-band beam at an adjustable wavelength near 13 nm. The zone plate is illuminated with a spatially coherent spherical wavefront from a pinhole source located 2.4 m from the zone plate. The diffracted light is recorded approximately 10 cm from the zone plate with an extreme ultraviolet charge-coupled device (CCD) camera with 1024×1024 pixels and area of one square inch [153, 154].

The zone plate optics tested in this study consist of an electroplated nickel absorber layer on a silicon nitride membrane, patterned with electron-beam lithography. The 200- μm -diameter optics with 611 zones have an 80-nm-wide outer zone. The first diffractive order has a numerical aperture of 0.08 and a focal length of about 1.2 mm at the 13-nm wavelength. Some of the zone plates have an annular aperture with central obscuration ratio of 0.3 to allow separation of the first diffractive order with an order-sorting aperture placed

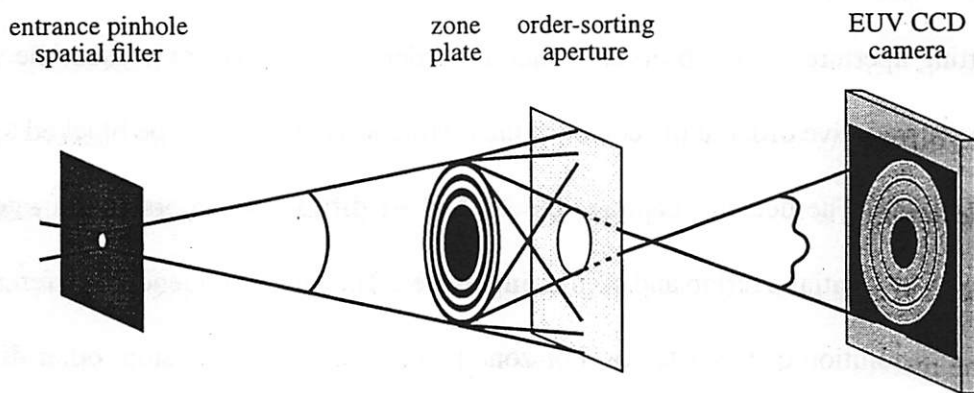


Figure 3-1. Measurement of a far-field diffraction pattern from a zone plate.

Measurement of the far-field intensity in the first diffractive order of a zone plate lens. The entrance pinhole spatial filter provides a spherical illumination beam and the order-sorting aperture filters unwanted diffractive orders.

between the zone plate and its first-order focus. The order-sorting aperture is a 50- μm -diameter pinhole, placed on the optical axis approximately 1 mm from the zone plate optic.

In the fabrication process, the zone plates are defined by exposure of a resist material with an electron beam. Each annular zone is approximated by many rectangular regions, placed at a specified angular orientation and distance from the zone plate center. The exposure begins at the zone plate center and continues radially outward until the entire pattern is written. The stage on which the zone plate samples are mounted during exposure has been characterized [155] and is known to drift slowly due to temperature changes. Because the zone plate exposure typically requires about twenty minutes, the position of the electron beam is corrected with the help of alignment marks several times during the writing process to compensate for the stage drift. Since the zone plate lenses considered here were fabricated, the writing errors have been significantly reduced [156].

Diffraction intensity patterns of a number of zone plate optics both with and without order-sorting apertures were observed. When no order-sorting aperture is used, the undeviated zero diffractive order at the center of the diffraction pattern must be blocked to protect the detector. The detector captures the +1 and -1 diffractive orders which interfere because of their spatial overlap and similar intensities. This high-frequency interference is beyond the resolution of the detector. For zone plates with no central stop, other diffractive orders also contribute to the detected pattern. When an order-sorting aperture is used in combination with a central zone plate obscuration, only the first diffractive order is recorded by the detector.

Figure 3-2(a) illustrates diffraction from a zone plate with no order-sorting aperture. The center of the detector is protected with a beam stop held by four wires visible in the figure. The detected intensity profile is relatively smooth but contains a distinct ring structure that occurs at the radial positions at which the electron beam was realigned during fabrication. The observed intensity structure indicates that stage realignment results in abrupt errors in the zone definition.

Zone placement errors are also evident in the far-field intensity patterns of the first diffractive order of annular zone plates shown in Figure 3-2(b), (c) and (d). The patterns lack the abrupt errors shown in Figure 3-2(a) but contain strong high-frequency modulation that is not explained by residual low-order aberrations. In addition, the modulation is most pronounced along one radial direction and relatively smoother along the direction perpendicular to it. This asymmetry is consistent with the drift of the sample stage along one direction during fabrication. In addition, each of the measured zone plates has a unique

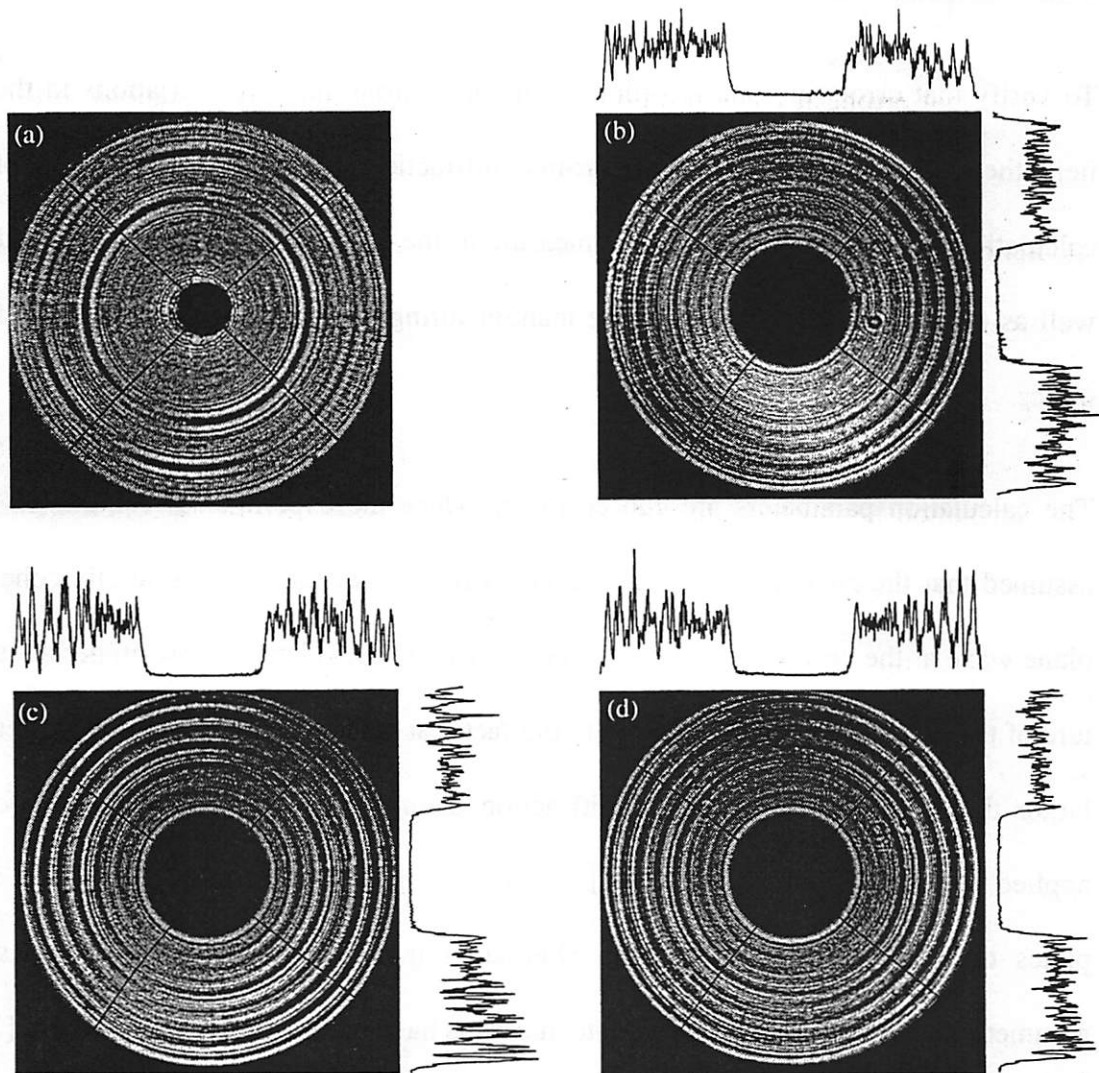


Figure 3-2. Measured far-field intensity patterns from zone plates.

The measured far-field intensity patterns from four different zone plates. (a) Interference of all diffractive orders from a zone plate indicates relatively abrupt errors in the zone placement. (b)-(d) First-diffractive-order light from annular zone plates contains intensity variations consistent with the presence of zone errors. The intensity profiles through the zone plate center are shown for horizontal and vertical directions.

diffraction pattern that can be attributed to zonal errors rather than inherent zone plate diffraction effects. These measurements reveal the presence of zonal errors that can be understood in terms of the known properties of the electron beam writing tool used to define the zone plate pattern.

3.2.2. Calculations of Zonal Error Effects

To verify that errors in zonal positioning produce strong intensity variations in the far field, the effects of such errors on the far-field diffraction were calculated. The goal of the calculations is to obtain a quantitative measure of the observed zonal error magnitude as well as to understand the effect of the manufacturing errors on the performance of the optics.

The calculation parameters are chosen to reproduce the experimental conditions. It is assumed that the zone plates are illuminated with a monochromatic, spatially-coherent, plane wave at the wavelength of $\lambda = 13$ nm. Owing to the relatively low numerical aperture of the zone plates considered and to the fact that zone plate features are significantly larger than the wavelength, scalar diffraction theory in the Fresnel approximation is applied in the calculations [110, 111]. As a good first-order model, ideal binary zone plates that consist of infinitely thin alternating transparent and opaque regions are assumed. The effects of finite zone plate thickness have been considered elsewhere [157].

For the calculation parameters of interest, a large number of data points is needed to accurately represent the zone plate transmission function across the aperture. One computational difficulty is the order-sorting aperture that necessitates calculation of the field in intermediate plane of the order-sorting aperture before the field due to the first diffractive order can be found at the plane of the detector. In these calculations, errors with azimuthal symmetry are considered in order to significantly reduce the computational load. Although errors in the radial direction do not describe two-dimensional errors in real zone

plates, they are representative of the effects along the direction where the two-dimensional errors are most pronounced.

To model the actual fabrication errors, two types of zonal errors are considered here. The properties of the zone plates with errors are compared to the properties of an error-free binary zone plate [152] with n^{th} -zone transition at a radius defined by $r_n^2 = n\lambda f$, where f is the focal length of the first diffractive order.

The first error model represents random fluctuations in zone positioning that can result from sample vibrations or round-off errors in the digital representation of the zone plate position during fabrication. In this model, the positions of zone radii are assumed to have random fluctuations, described by a uniform distribution of width δ . Multiple realizations of the errors are needed to characterize the average behavior of the random errors.

The second type of error attempts to model the stage drift and realignment, which occurs along one cartesian direction, by an error along the radial coordinate. In this “drift-reset” model, the zone plate is divided into p annular regions ($p \geq 2$). Within each region, the zone radii have an additional drift term, linear in the radius, that reaches a maximum radial displacement μ , and is reset to zero at the inner boundary of each region.

To determine the diffracted field, straightforward numerical integration of the Fresnel integral over a nonuniform grid in the plane of the zone plate aperture is employed. To accurately capture the zone edge positions, each zone is represented by a separate grid, uniform in the radial direction. A uniform grid across the entire zone plate aperture may

not adequately describe the zone transitions. In fact, it may represent a zone plate with small amount of random error in the zone widths.

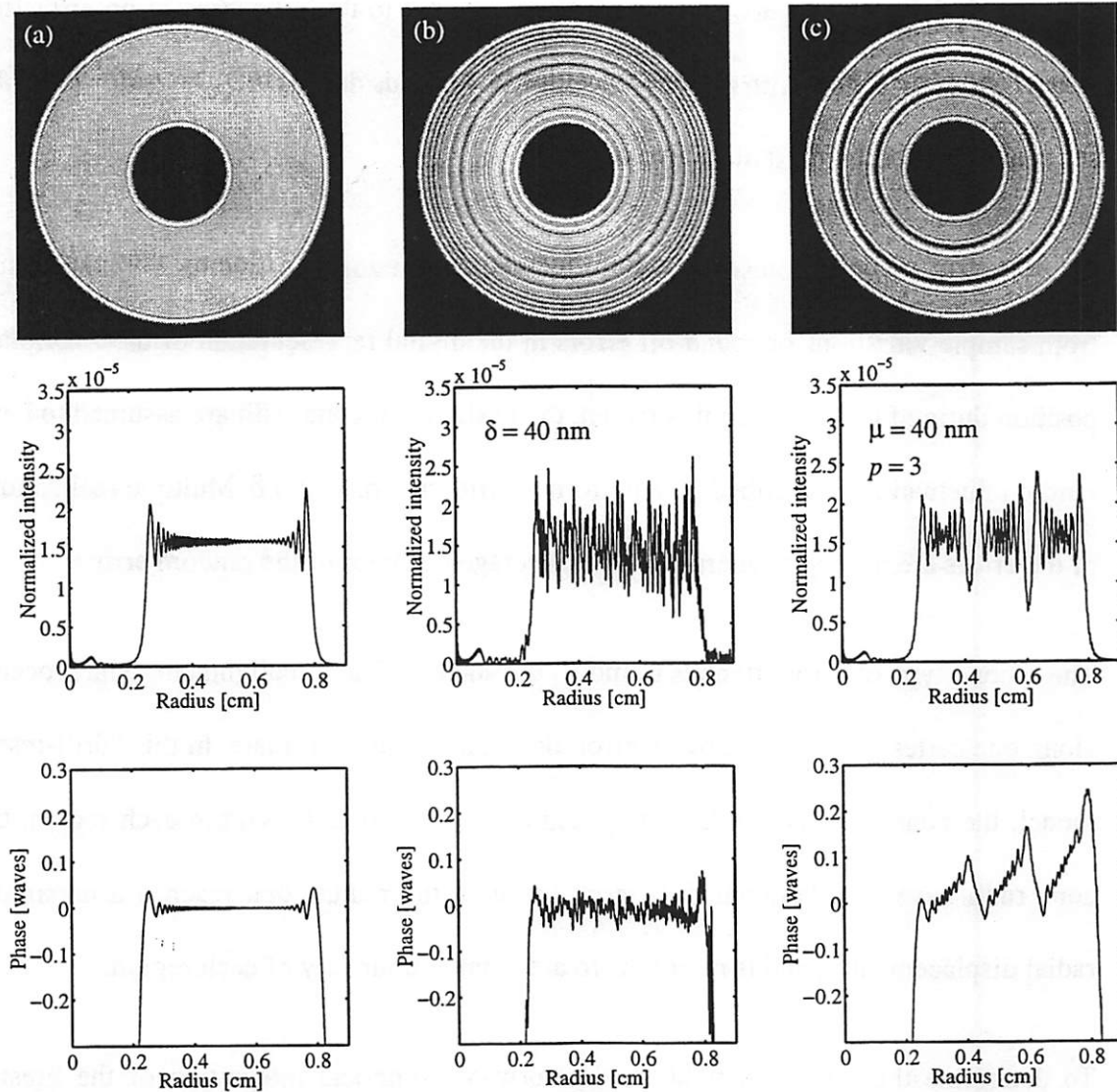


Figure 3-3. Calculated far-field diffraction patterns from zone plates.

(a) Calculated far-field first-diffractive-order intensity and phase of a zone plate with no zone placement errors. Calculated far-field first-diffractive-order intensity and phase of zone plates with (b) random errors in zone edge positions and (c) with three regions of zone edge drift with reset. The error parameters δ and μ in (b) and (c) equal one half of the outer zone width. Two-dimensional intensity patterns as well as the intensity and phase profiles along the radial direction are shown.

3.2.3. Zone Positioning Errors and Far-Field Diffraction

The diffracted fields from 200- μm -diameter zone plate optics with the two types zonal errors were calculated and compared to the diffraction from a zone plate with no zonal errors. Shown in Figure 3-3(a) are the intensity and the phase of the first diffractive order of an ideal annular zone plate at the distance of 10 cm from the zone plate. The intensity pattern exhibits edge diffraction effects but is relatively smooth across the bright region. The on-axis order-sorting aperture causes small amount of spatial filtering of the first-diffractive order but does not produce significant far-field intensity modulation. Figure 3-3(b) and (c) gives the calculated properties of the first diffractive order for annular zone plates with zone placement errors. Figure 3-3(b) shows that random errors in the zone edges produce a random modulation pattern in the far-field intensity and phase. The

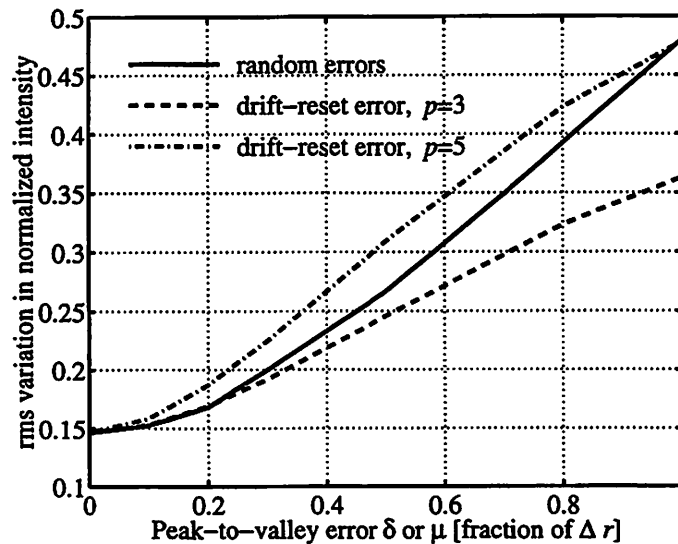


Figure 3-4. Calculated rms variation in the far-field intensity.

The calculated rms variation in the far-field intensity of the first diffractive order vs. the peak magnitude of the zone placement error, given by parameters δ and μ , for several error models.

drift-reset errors cause abrupt transitions in the far-field intensity and phase at the error reset radii, as indicated in Figure 3-3(c). In Figure 3-3(b) and (c) the magnitude of the error parameters δ and μ is 40 nm, or one half of the 80-nm outer zone width Δr . The intensity is normalized to be unity at the zone plate and the curvature is removed from the far-field phase.

The calculations show that the far-field intensity modulation, which can be measured, is quite sensitive to zonal errors. Although the exact zonal error pattern cannot be determined from a far-field intensity measurement, the error magnitude can be estimated from the variation in the measured intensity. Figure 3-4 shows the computed rms variation in the normalized far-field intensity of the first diffractive order for several error models as a function of the peak-to-valley error parameters δ and μ . For the random error model, the curve represents the ensemble average of the rms intensity variation. The intensity, normalized to unity average, was considered in the illuminated region of the zone plate diffraction pattern. Approximately 4000 points along each cartesian direction, needed to

Zone plate	Measured rms variation in normalized intensity	Estimated peak error [fraction of Δr]
A	0.44	0.53 ± 0.10
B	0.30	0.30 ± 0.06
C	0.36	0.41 ± 0.09
D	0.37	0.43 ± 0.09
E	0.31	0.32 ± 0.06

Table 3-1. Estimated zonal errors in several zone plates.

The peak magnitude of the zone positioning error as a fraction of the outer zone width ($\Delta r = 80$ nm) estimated from the variations in the far-field intensity.

adequately sample the intensity pattern, were used to estimate the intensity fluctuations. The intensity variation, which is nonzero even for zone plates without errors due to edge diffraction effects, increases with the zonal error magnitude. Because the different types of errors produce similar rms intensity variations, the peak magnitude of the error in the zone edge position can be estimated from the measured rms far-field intensity variation, as illustrated in Table 3-1 for five different zone plates. The measured and calculated intensity variations were compared at the same "pixel density". These estimates indicate that the peak zone positioning errors in the measured zone plate optics are on the order of four tenths of the outer zone width, or about 30 nm.

3.2.4. Zonal Errors and Optical Performance

To evaluate the effect of zone placement errors on the performance of zone plates, focusing properties and first-order diffraction efficiencies were calculated for zone plates with random zone edge errors and with zone position drift with reset.

In zone plates with several hundred zones, random errors in the zone edge placement represent relatively high spatial frequency errors. These errors reduce the peak intensity of the point spread function but do not widen the central peak. In imaging applications, these errors do not significantly affect the best resolution but do reduce the image contrast. Abrupt errors in the zone placement at several radial positions produce aberrations with mid-spatial-frequency content. Although these aberrations do not widen the central peak of the point spread function, they may scatter a considerable amount of energy near the point spread function center. Consequently, such errors may significantly degrade imaging of objects with dimensions near the resolution limit. The normalized peak intensity of

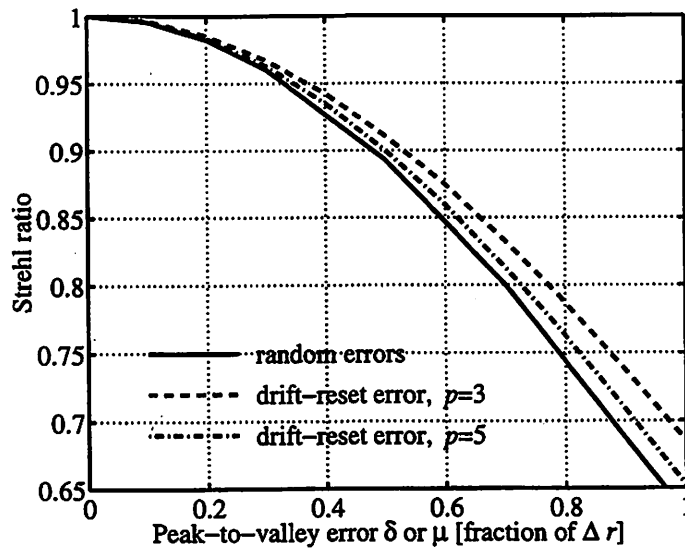


Figure 3-5. Calculated Strehl ratio of zone plates with errors.

The Strehl ratio at focus of the first diffractive zone plate order plotted as a function of the peak magnitude of the zone placement error, given by parameters δ or μ , for several error models.

the point spread function, or Strehl ratio [95], is degraded similarly by both types of zone placement errors, as shown in Figure 3-5 for random errors and for drift-reset errors with three and five drift regions.

In some applications, the diffraction efficiency of zone plate optics with zonal errors may be of interest. The calculations show that the diffraction efficiency into the first diffractive order is strongly affected by random zone placement errors but only slightly changed by drift-reset type errors. For example, the first-order diffraction efficiency of an annular zone plate described in this study is reduced by about 1% for drift-reset type errors with three to five drift regions and an error magnitude of $\mu = 80$ nm. By contrast, random errors of the same magnitude ($\delta = 80$ nm) reduce the first-order diffraction efficiency by about 22%. Here the diffraction efficiency is defined as the fraction of the radiation that

passes through the order-sorting aperture. With this definition, the calculated diffraction efficiency of a zone plate with no zonal errors is within 0.2% of the theoretical value of $1/\pi^2$. The calculated diffraction efficiencies are consistent with the understanding of zonal errors in terms of spatial frequencies. The high-spatial-frequency random errors cause higher-angle scattering and more scattering loss than the drift-reset type errors that contain mostly mid-spatial frequencies and scatter into moderate angles.

3.3. Point Diffraction Interferometry of Zone Plate Lenses

The low-order phase aberrations in the zone plate lenses were evaluated with the conventional point diffraction interferometer near 13-nm wavelength. The measurements indicate near diffraction-limited quality of the wavefront in the first diffractive order. These initial measurements have also confirmed the applicability of point diffraction interferometry to testing near diffraction-limited optics at EUV wavelengths [84, 85, 87].

3.3.1. Interferometry Results

The conventional point diffraction interferometry experiment utilizes a modified version of the zone plate measurement configuration shown in Figure 3-1. The zone plate is illuminated with a spatially-coherent, spherical, narrow-band beam from a 120- μm -diameter pinhole located 2.4 m from the 200- μm -diameter zone plate. The interferometry is performed on the first diffractive order of the annular zone plate, isolated with an order-sorting aperture, operated at a demagnification of 2000 and an image-side numerical aperture of about 0.08. The semi-transparent pinhole membrane, required for the generation of the reference wavefront and the simultaneous transmission of the test beam as shown in

Figure 2-1 on page 19, is placed near the focus at 1.2 mm from the zone plate. The beam interference is recorded at 10 cm from the zone plate with an EUV CCD camera.

An example of the characterization of zone plate lenses with the point diffraction interferometer is presented in Figure 3-6. Additional measurements on zone plates are discussed elsewhere [142, 85]. Figure 3-6(a) shows five interferograms recorded at 12.9-nm wavelength in testing of an annular zone plate lens. The interferograms were analyzed with the Fourier transform method for static fringe pattern analysis [143-146] and the resulting wavefront phase was fit to a set of 37 annular Zernike polynomials [97] with 30% central obscuration, matched to the zone plate aperture central stop. The average wavefront aberration map, without the piston, tilt, defocus, and systematic coma terms, is given in Figure 3-6(b). The Zernike annular polynomial coefficients are plotted in Figure 3-6(c). The indicated uncertainty of each coefficient is the standard deviation of the coefficients determined in the five different measurements. The rms and peak-to-valley aberrations are 0.14 ± 0.02 and 0.72 ± 0.08 wave at 12.9 nm, respectively. These small measured aberrations are indicative of good imaging capabilities of the zone plate lens as well as of the subnanometer resolution and precision of the interferometer.

3.3.2. Understanding of the Measured Astigmatism

The dominant aberration found in the measurements is 0.27 wave of astigmatism, given by annular Zernike coefficients 4 and 5. Neither the measured tilt of the zone plate with respect to the optic axis nor the estimated zone plate ellipticity of 10^{-4} can account for this amount of astigmatism. Some of the astigmatism may be attributed to the zone positioning fabrication errors observed in these zone plates (see Section 3.2.1). Although zone

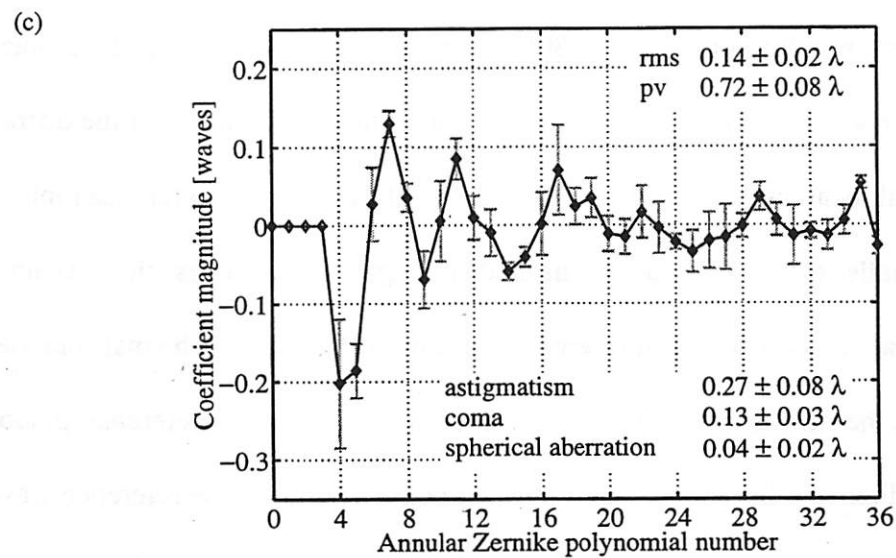
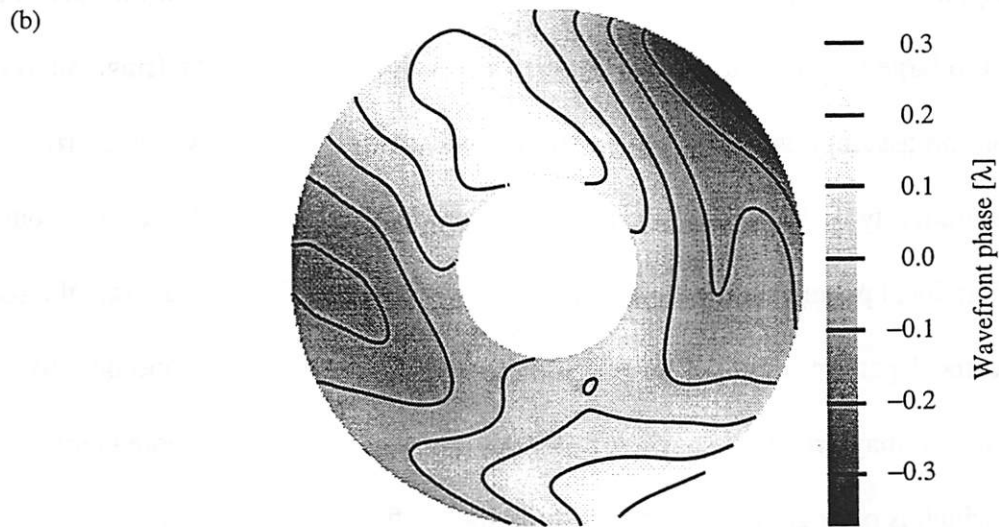
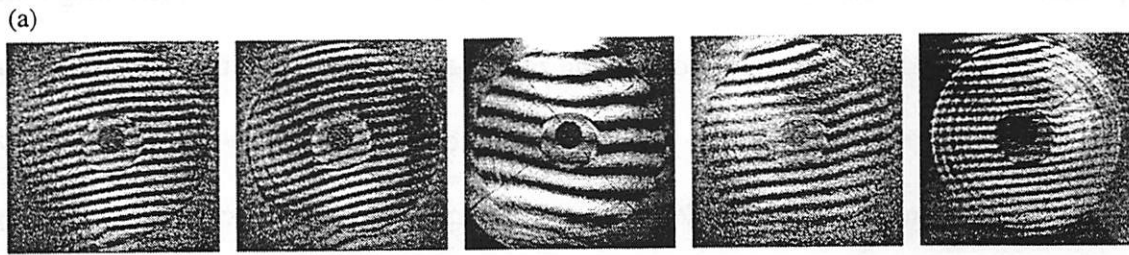


Figure 3-6. Wavefront aberrations of a zone plate lens.

Aberrations of an annular zone plate lens measured at 12.9-nm wavelength. (a) Five measured interferograms were analyzed to determine (b) the average wavefront and (c) the corresponding Zernike annular polynomial coefficients.

placement errors produce mostly high spatial frequency aberrations, their magnitude changes through two azimuthal cycles in the zone plate aperture from the drift of the sample stage during fabrication. This two-cycle variation can potentially contribute to low-order astigmatism. However, in addition to the astigmatism in the optic, some of the astigmatism originates from an imperfect reference wavefront, produced when the reference pinhole is too large to generate a spherical reference wavefront. Since the fringe analysis is based on the assumption of an ideal reference wavefront, reference wave aberrations contribute additively to the measured wavefront error. A large pinhole placed in the outer portion of the focal pattern will sample fields that vary most rapidly along the radial direction of the focal pattern, defined by the pinhole and the focal center. Consequently, an oversize pinhole may produce astigmatism in the reference wavefront oriented along this direction, which is orthogonal to the direction of the far-field interference tilt fringes.

For the optical system in this study, with a 30% obscured annular aperture and a numerical aperture of 0.08 at the operational wavelength near 13 nm, the diameter of the diffraction-limited central focal disk is 175 nm. As discussed in Chapter 2, the reference pinhole, which must be smaller than the diffraction-limited spot size, should be less than 80 nm in diameter to generate a good spherical reference wavefront. Because such small pinholes were unavailable, the measurements were performed with an oversize reference pinhole about 200 nm in diameter. In the five measurements considered here, the reference wavefront contains unwanted aberrations, revealed in the correlation between the measured astigmatic direction and the fringe direction normal shown in Figure 3-7(a). The angular offset between the two directions indicates that both the reference wave and the test optic contribute to the measured astigmatism. Assuming that in each measurement the astigma-

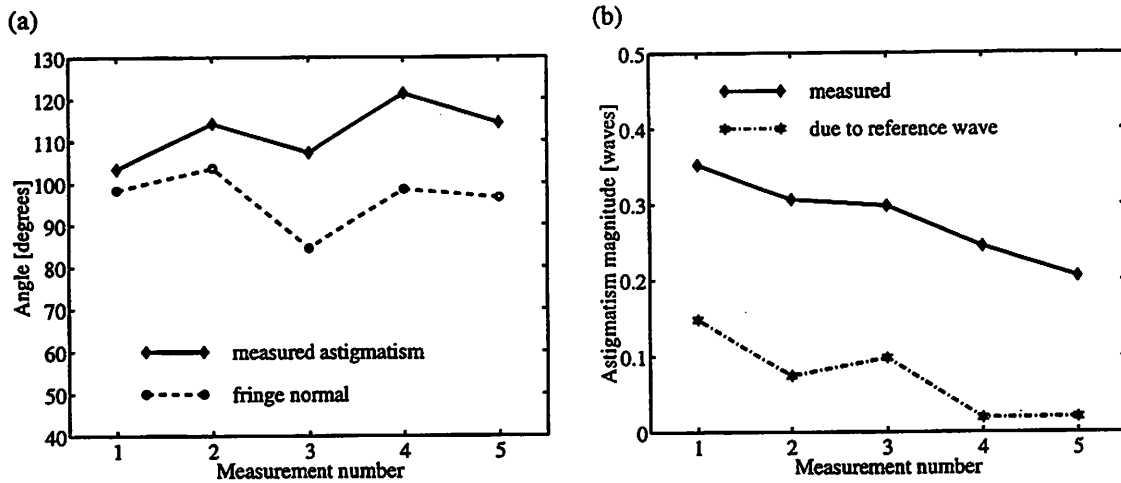


Figure 3-7. Astigmatism in the reference wavefront.

(a) Correlation between the direction of the measured astigmatism and the interferogram fringe direction normal in five measurements of the same lens. (b) The magnitude of the measured astigmatism follows the calculated astigmatism in the reference wavefront.

tism consists of a fixed component due to the test optic and a variable component along the fringe normal due to the reference wavefront, the test and reference wave contributions can be estimated by minimizing the least square deviations from this model. The magnitude of the measured astigmatism, which contains the test and the reference components, as well as the calculated reference-wave astigmatism are compared in Figure 3-7(b). The calculated residual astigmatism in the test optic is 0.23 ± 0.02 wave at 13 nm, with peak at an angle of $115 \pm 5^\circ$. The reference wavefront astigmatism is on the order of 0.1 wave, or about 0.04 wave rms. Although the reference wavefront astigmatism is significant here, this source of systematic error can be made negligible when a proper-size reference pinhole is used.

3.4. Conclusions

The properties of diffractive zone plate lenses with numerical apertures comparable to those of reflective optical systems for EUV lithography have been assessed with wavefront transmission and phase measurements near 13-nm wavelength. The measured far-field diffraction patterns from the zone plate optics indicate the presence of small zone placement errors. Scalar diffraction calculations of zonal errors confirm that the modulation in the far-field intensity is a sensitive indicator of even relatively small zone positioning errors. The comparison of the calculated zone error effects with the measured zone plate intensities shows that the unoptimized zone plate optics, with several hundred zones and an 80-nm outer zone width, have peak zonal placement errors on the order of 30 nm. The random errors in zone positioning correspond to relatively high spatial frequency errors while abrupt errors at few radial positions are primarily mid-spatial frequency aberrations.

The characterization of the low-order aberrations in an annular zone plate lens with the conventional point diffraction interferometer reveals wavefront quality near the diffraction limit at 12.9-nm wavelength. A small amount of astigmatism, about 0.04 wave rms, in the measured wavefront can be attributed to imperfections in the diffractive reference wavefront, produced by oversize reference pinholes. Overall, the wavefront measurements of diffractive zone plate lenses have demonstrated the usefulness of point diffraction interferometry in testing near diffraction-limited optics with numerical apertures around 0.1 at EUV wavelengths.

4 Evaluation of the Phase-Shifting Point Diffraction Interferometer with Visible Light

4.1. Overview

The phase-shifting point diffraction interferometer is suitable for testing near diffraction-limited optical systems over a wide range of wavelengths, from visible to x ray. Before the implementation of this novel interferometer [107, 87] for at-wavelength characterization of the extreme ultraviolet (EUV) lithographic optics, the qualification of its properties was required. A prototype interferometer system using visible light was constructed to verify the capabilities of the new design and to devise a proper alignment strategy for the EUV system.

4.2. Description of the Visible-Light Interferometer

In this proof-of-principle experiment, several versions of the phase-shifting point diffraction interferometer (PS/PDI) that incorporate a transmission grating beamsplitter have been constructed and tested. Two examples of the possible interferometer configurations are given in Figure 2-2 on page 21. The interferometer has been employed to measure aberrations in a number of test optical systems, including microscope objectives and camera lenses. The simplicity of the design allowed relatively quick construction using

readily available components and equipment. In this chapter, few examples of the measurements that have confirmed the usefulness of the interferometer are presented.

4.2.1. Interferometer Components

The light source used in this experiment is a low-power helium-neon laser, producing a single spatial mode at 632.8-nm wavelength. The laser light is collected with a lens and focused onto the object plane of the optical system under test. To match the properties of the test optics, different lenses can be used to control the numerical aperture of the illumination beam. Commercially available laser-drilled pinhole apertures are utilized for the single-pinhole and the two-pinhole spatial filters in the object and image planes. The entrance pinhole size is chosen to coherently overfill the numerical aperture of the test optic and the sub-resolution reference pinhole size is selected to provide a strongly spatially filtered reference wavefront. A coarse Ronchi ruling on a glass substrate serves as the grating beamsplitter and phase-shifting element. The interference fringe patterns are detected with a 512×512 pixel, 6.2×4.6 mm², 8-bit, charge-coupled device (CCD) camera. This PS/PDI experiment is performed on an optical bench for stability but no measures are taken to isolate the system from thermal fluctuations or air turbulence.

4.2.2. Alignment Considerations

The interferometer requires the alignment of the focused beams with the pinhole apertures in the object and image planes of the test optic. In this experiment, alignment strategies both with and without reimaging optics have been employed. The reimaging optics allow the observation of any plane of interest along the beam propagation direction, such as the

plane of the pinhole apertures or the pupil plane of the test optic. The image of the desired plane facilitates the alignment task by allowing the positioning of the pinhole apertures with respect to the beam foci in the image plane, for instance. Since reimaging optics are not readily available at EUV wavelengths, alignment schemes that utilize only the far-field pattern at the CCD detector have also been tested. Both approaches are greatly simplified when the object and image-plane pinhole apertures rest on kinematic mounts that allow repeatable placement of the pinholes in the beam. The techniques investigated in this prototype system have influenced the alignment procedure in the EUV implementation of the interferometer, described in Chapter 5.

4.3. Verification of Interferometer Capabilities

Without the capacity to independently verify the measurements, several consistency checks were devised in order to assess the interferometer performance. The detection of a known aberration and the characterization of an optic at several rotational orientations with respect to the interferometer have allowed the evaluation of the quality of the wavefront measurement.

The measurement consistency can be validated by repeated measurements of the test wavefront containing varying amounts of the defocus aberration. The defocus can be introduced simply by the translation of the image-plane spatial filter along the optic axis. Using the interferometer configuration in Figure 2-2(a) on page 21, this experiment has been performed in the evaluation of a photographic camera lens, operated at an approximate demagnification of 7 and an image-side numerical aperture of about 0.15. The test

optic is illuminated from a 10- μm -diameter single pinhole in the object plane. The beam is divided by a 100- μm -pitch grating beamsplitter, placed between the object plane and the optic, that provides focal spot separation of about 90 μm in the image plane. The test and reference beams are selected with a two-pinhole image-plane spatial filter, consisting of a 100- μm -wide window and 2- μm -diameter pinhole about 50 μm from the edge of the window. Both sub-resolution pinholes are significantly smaller than the diffraction-limited focal diameters of 35 μm and 5 μm in the object and image planes, respectively.

In two separate measurements, illustrated in Figure 4-2, the focus was changed from -0.11 wave to -0.42 wave at 632.8 nm by translation of the image-plane filter by about 35 μm along the optic axis. The larger defocus corresponds to roughly 3.4 times the classical focal tolerance of 0.125 wave [95, 121]. While the recorded fringes are relatively straight near focus, as seen in Figure 4-2(a), the fringe curvature increases with the defocus magnitude, as shown in Figure 4-2(b). However, the added defocus in the wavefront does not significantly affect the residuals low-order aberrations of interest, also presented in Figure 4-2. Without the piston, tilt, and defocus terms, the overall difference in the two wavefronts, reconstructed from the Zernike polynomial fit to the raw phase, is 0.004 wave rms and 0.040 wave peak-to-valley. This consistency in the measured wavefront observed even at a relatively large defocus, indicates adequate spatial filtering by the reference pinhole in the image plane.

The measurement capability of the interferometer can also be assessed by wavefront evaluation for several rotational orientations of the test optic and the interferometer components. In principle, the measured wavefront rotates with the orientation of the test optic

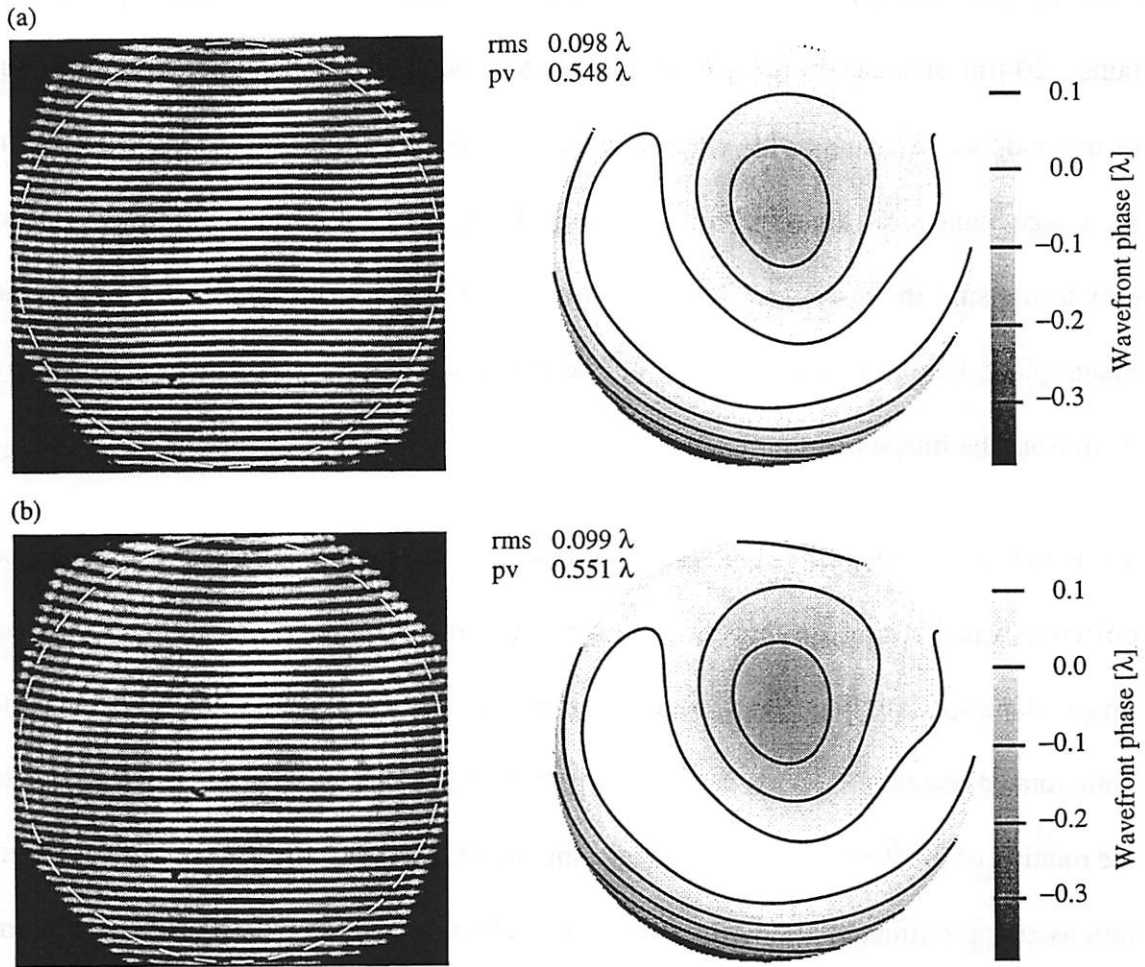


Figure 4-1. Introduction of defocus into the tested wavefront.

The measurement of phase aberrations in a camera lens at two different axial positions of the image-plane spatial filter. The pinhole translation influences the fringe curvature as the defocus is changed from (a) -0.11 wave to (b) -0.42 wave at 632.8-nm wavelength. The measured wavefront phase within a numerical aperture of about 0.15, without the piston, tilt, and defocus terms, is not significantly affected.

but is unaffected by the rotation of the interferometer elements. This experiment involved the measurement of a 4 \times microscope objective lens, operated at a demagnification of 10 and an image-side numerical aperture near 0.11, in order to emulate the 10 \times -demagnification Schwarzschild system later tested at EUV wavelengths. A 100- μm -pitch beamsplitter grating is placed upstream of the object plane, following the configuration shown sche-

matically in Figure 2-2(b) on page 21. The entrance pinhole filter in the object plane contains a 20- μm -diameter sub-resolution pinhole to produce spatially coherent illumination of the optic and a 1-mm-wide window to transmit the second beam. The spatial filter in the image plane consists of a 2- μm -diameter reference pinhole and a 100- μm -wide window to transmit the test wave. The separation of the test and reference wave foci in the image plane is approximately 100 μm . The fringe patterns are detected approximately 2 cm from the image plane.

To assess the repeatability and self-consistency of the measurements, the microscope objective was first measured with three different azimuthal orientations of the object and image plane spatial filters. Subsequently, the aberrations were remeasured twice with the optic rotated counterclockwise by 89° and 181° with respect to the original orientation. In the rotation of the various interferometer components, care was taken to measure the aberrations at approximately the same point in the field of view. The recorded fringe patterns and the image-plane pinhole filter orientations in the five measurements are given in Figure 4-2(a) and (b) respectively. The measured low-order aberrations, without the piston, tilt, defocus, and systematic coma terms, reconstructed from a Zernike polynomial fit to the raw phase data, are illustrated in Figure 4-2(c). The measured wavefront phase is not significantly affected by the rotation of the spatial filters and follows the orientation of the optic, indicated by an arrow in Figure 4-2(c). The wavefront aberrations of this optic obtained in the five measurements are 0.029, 0.027, 0.028, 0.024, and 0.29 wave rms at 632.8 nm, respectively. The rms difference between the any two of the measured phase maps ranges from 0.004 to 0.008 wave, indicating self-consistent agreement to approximately $\lambda/125$.

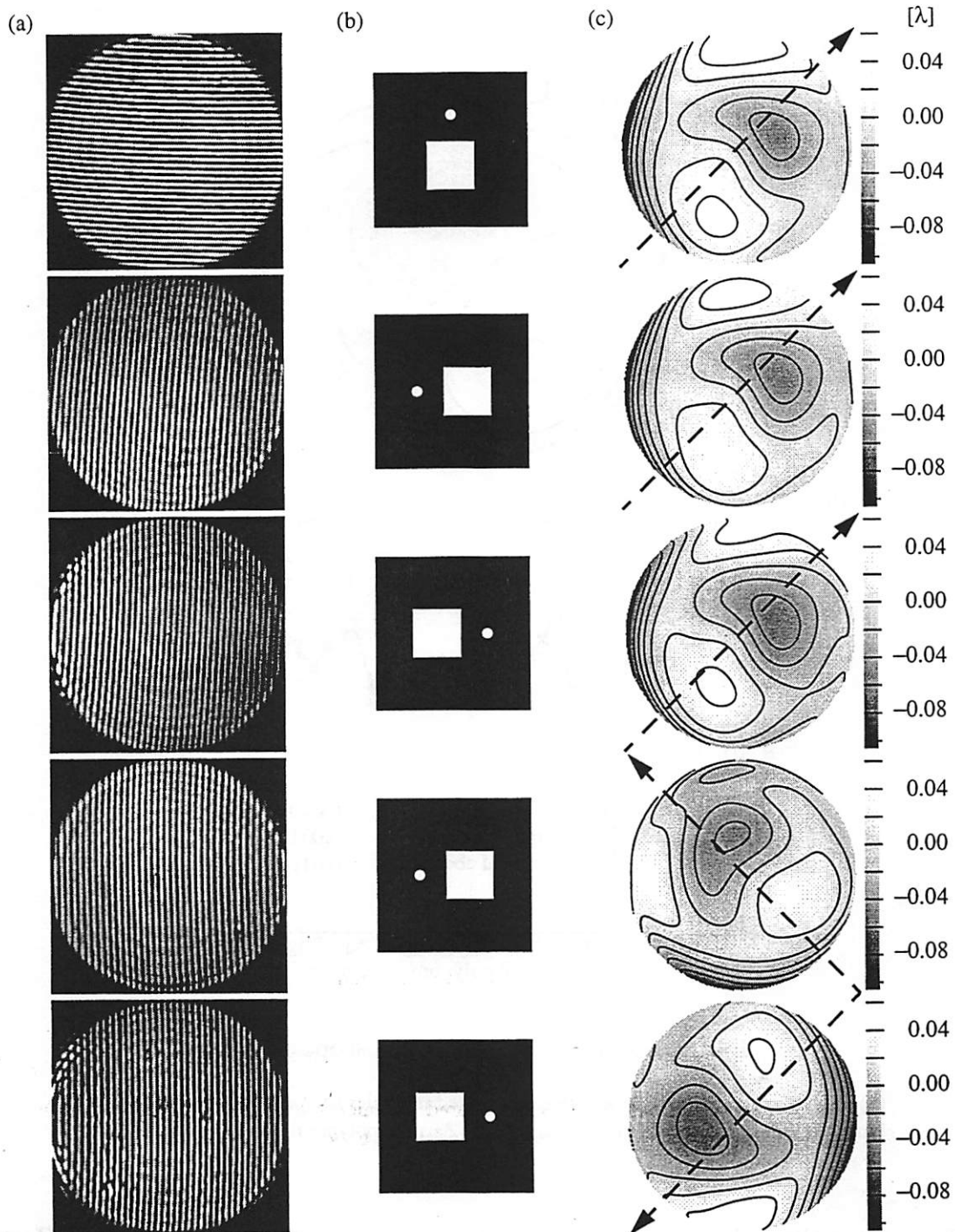


Figure 4-2. Consistency measurements with the rotation of interferometer components.

(a) The interferograms from five measurements of a microscope objective lens recorded at 632.8 nm for several orientations of the pinhole filters and the test optic. (b) The orientation of the image-plane spatial filters in the measurements. (c) The wavefront phase extracted from the interferograms follows the rotational orientation of the test optic, indicated by the arrow. In the fourth and the fifth measurements, the rotations of the optic are 89° and 181° counterclockwise with respect to the first three measurements.

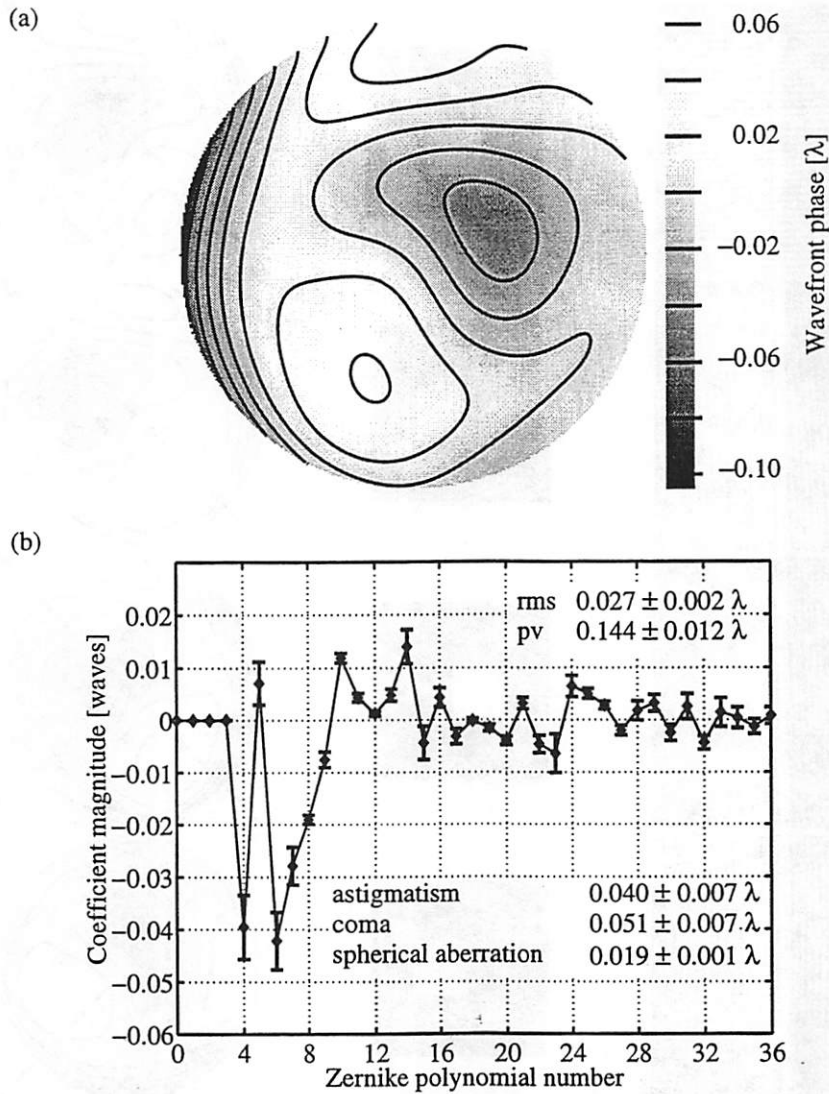


Figure 4-3. Aberrations in a microscope objective.

(a) The average wavefront aberrations measured in a microscope objective lens at a wavelength of 632.8 nm and (b) the corresponding Zernike polynomial expansion.

The average phase aberrations of the microscope objective and the corresponding Zernike polynomial coefficients are given in Figure 4-3(a) and (b). The average wavefront error of 0.027 ± 0.002 wave rms and 0.144 ± 0.012 wave peak-to-valley reveals the ability of the interferometer to characterize nearly diffraction-limited optics. The standard deviation of

the five measured rms wavefront aberrations corresponds to repeatability of ± 0.002 wave rms at 632.8-nm wavelength.

4.4. Conclusions

The phase-shifting point diffraction interferometer has been demonstrated to consistently characterize aberrations in near diffraction-limited optical systems with numerical apertures similar to those of multilayer-coated reflective optics used in EUV projection lithography. The measurement repeatability of a prototype interferometer system is ± 0.002 wave rms at 632.8 nm. The self-consistency of the interferometry, assessed with through-focus measurements and with wavefront evaluation at different azimuthal orientations of the interferometer components and of the test optic, is better than 0.008 wave rms. Although the proof-of-principle experiments have utilized visible light, comparable capabilities are expected at EUV wavelengths because the accuracy of the point diffraction interferometer has the potential to scale with the operational wavelength.

5 At-Wavelength Interferometry of a Schwarzschild Optic for EUV Lithography

5.1. Overview

At-wavelength wavefront characterization plays a key role in the development of near diffraction-limited optical systems for extreme ultraviolet (EUV) lithography. The phase-shifting point diffraction interferometer for wavefront measurements at EUV wavelengths has been implemented and used to evaluate a 10 \times -demagnification, multilayer-coated, Schwarzschild objective, designed for a prototype EUV lithography exposure tool.

In this chapter, the interferometer system implementation is described, including the light source and the illuminator, the Schwarzschild test optic, and the interferometer components. Subsequently, some of the results of the wavefront measurements of the test optic performed at 13.4-nm wavelength are presented. Then, the quality of the measurements is evaluated with numerous experiments designed to reveal the interferometer capabilities. The interferometer stability, the illumination and reference wavefront quality, the alignment sensitivity, and the measurement repeatability and accuracy are considered.

5.2. Light Source and Beamline Optics

The phase-shifting point diffraction interferometer (PS/PDI) for at-wavelength testing of EUV lithographic optics operates at the undulator beamline 12.0 at the Advanced Light

Source (ALS) at Lawrence Berkeley National Laboratory. The properties of the electron storage ring and the undulator magnet structures at the ALS have been described previously [36, 133, 158]. The undulator source and the beamline optics are depicted in Figure 5-1. The 8.0-cm-period undulator magnet structure of $N = 55$ periods provides high-brightness, extreme ultraviolet radiation, tunable from 5 nm to 25 nm in wavelength and linearly polarized with the electric field vector in the horizontal plane. The grazing-incidence beamline optics include a grating monochromator, used to select the desired wavelength, and a Kirkpatrick-Baez (K-B) illuminator [15], designed for optimum transfer of spatially coherent radiation to the interferometer.

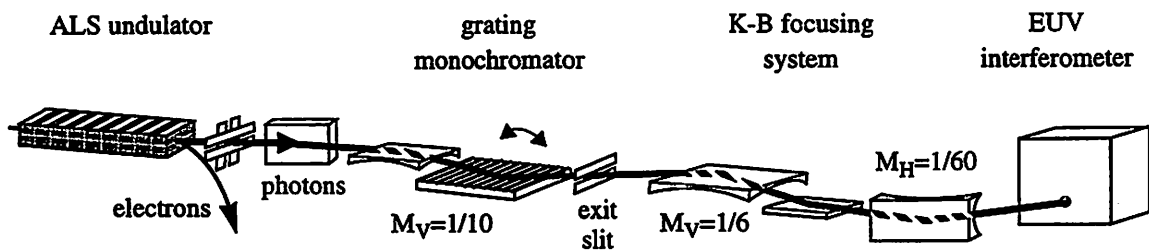


Figure 5-1. Schematic of ALS beamline 12.0.

Components of the undulator beamline 12.0 at the Advanced Light Source. The monochromator is used for wavelength selection. The K-B illuminator, in combination with the monochromator, images the undulator source onto the entrance plane of the interferometer endstation with demagnification by a factor of 60.

The beamline entrance apertures select the central radiation cone [36] from the undulator with relative spectral bandwidth of $1/N$ and divergence half-angle of $77 \mu\text{rad}$. At the undulator, the beam is roughly $400 \mu\text{m}$ by $80 \mu\text{m}$ (horizontal by vertical) in size. The first mirror in the beamline reflects the desired extreme ultraviolet radiation and filters out higher-energy photons in order to reduce the heat load on the subsequent beamline optics. The

monochromator, consisting of a curved mirror and varied line-space grating, then forms a vertically demagnified image (by a factor of ~ 10) of the undulator source at its exit slit. The exit slit is used to select the desired wavelength and bandwidth from the first diffractive grating order. As designed, the full-width half-maximum (FWHM) beam spectral bandwidth $\Delta\lambda$ is proportional to the monochromator exit slit width Δs , namely $\Delta\lambda$ [nm] = 0.762 Δs [mm] [159]. This allows adjustment of the relative spectral bandwidth of the radiation from 1/55, the bandwidth in the central radiation cone, to roughly 1/1000.

The K-B illuminator consists of two adjustable curved mirrors and a fixed, flat, steering mirror between them. The first curved mirror produces a vertical image of the exit slit (with a demagnification of ~ 6), while the second curved mirror forms a horizontal image of the undulator source (demagnified by ~ 60) at the illuminator focus. The image-side numerical aperture (NA) of the K-B system is 0.01 in both directions. However, to minimize the effects of imperfections at the mirror edges, only 0.005 numerical aperture is filled with the central radiation cone. Because the exit slit is reimaged at the interferometer entrance plane, an entrance pinhole, placed at the K-B focus, can provide further monochromatization of the radiation when its size is smaller than the demagnified exit slit width.

Figure 5-2 depicts the beam properties at the K-B focus measured at 13.4-nm wavelength. Figure 5-2(a) shows the beam profile in the vertical direction for several monochromator exit slit widths, measured by scanning a 1.3- μm -diameter pinhole in the beam. As the exit slit is closed to decrease the spectral bandwidth, the vertical beam size decreases. However, due to the aberrations in the K-B illuminator, the vertical beam size is larger than the demagnified exit slit width for the exit slit widths below about 60 μm . The horizontal beam

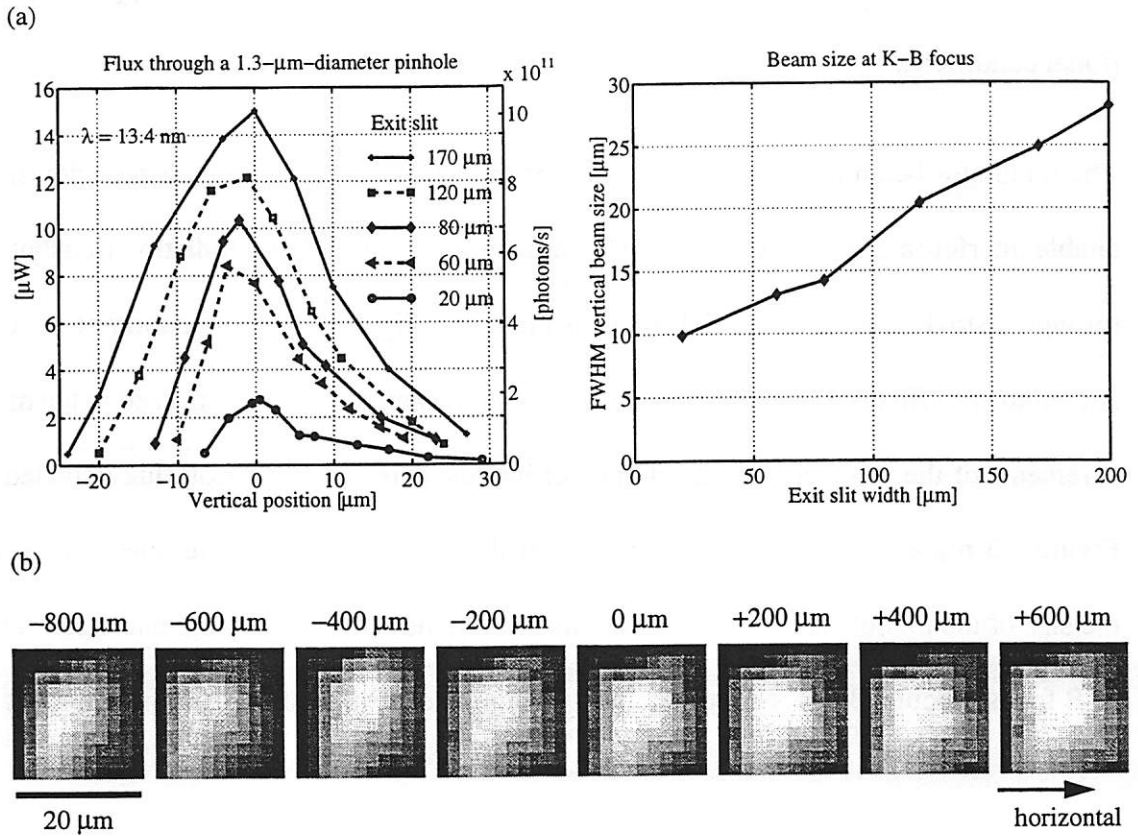


Figure 5-2. Profile of the K-B illuminator focus.

(a) Measured flux transmitted through a 1.3- μm -diameter pinhole, placed at the focus of the K-B illuminator, as a function of the vertical pinhole position and the size of the monochromator exit slit. The corresponding FWHM vertical beam size vs. monochromator exit slit width. (b) Two-dimensional scan of the focal spot with a 0.5- μm -diameter pinhole through focus in 200- μm increments, with the exit slit at 150 μm . Increasing defocus corresponds to moving the pinhole closer to the K-B illuminator. The K-B illuminator was adjusted between the measurements (a) and (b).

size is determined by the source size at the undulator and by the aberrations in the K-B optics. The two-dimensional beam profiles, measured with scans of a 0.5- μm -diameter pinhole, are shown in Figure 5-2(b) for several axial pinhole positions. Although the diffraction-limited depth of focus at numerical aperture of 0.005 and wavelength of 13.4 nm is $\pm 270 \mu\text{m}$, due to the illuminator aberrations, the actual depth of focus is significantly larger and the beam profile is quite insensitive to defocus. Owing to the aberrated illumi-

nator, the FWHM beam size is roughly 10-15 μm in either direction under typical operational conditions.

The undulator beamline is required to deliver the necessary spatially coherent power to enable interferometry measurements. The measured flux of 13.4-nm radiation transmitted through a small pinhole at the K-B focus is plotted in Figure 5-3 as a function of the exit slit width. The flux is normalized for a typical pinhole diameter of 0.5 μm , used in the measurements of the 10 \times Schwarzschild optic of interest here. The radiation flux depicted in Figure 5-3 represents spatially coherent power that is needed for interferometry because the size of the pinhole used in the measurement is on the order of the coherence area at the K-B focus (about 1.3 $\mu\text{m} \times 1.3 \mu\text{m}$ at the wavelength of 13 nm and the illuminator NA of

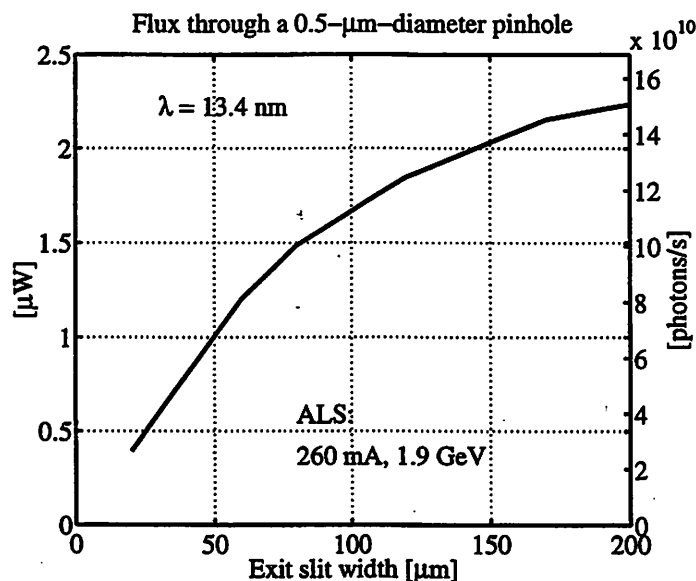


Figure 5-3. Flux at beamline 12.0.

The coherent flux measured at 13.4-nm wavelength at the focus of the K-B illuminator. The flux is normalized to indicate the power transmitted through a 0.5- μm diameter entrance pinhole and plotted vs. the monochromator exit slit width.

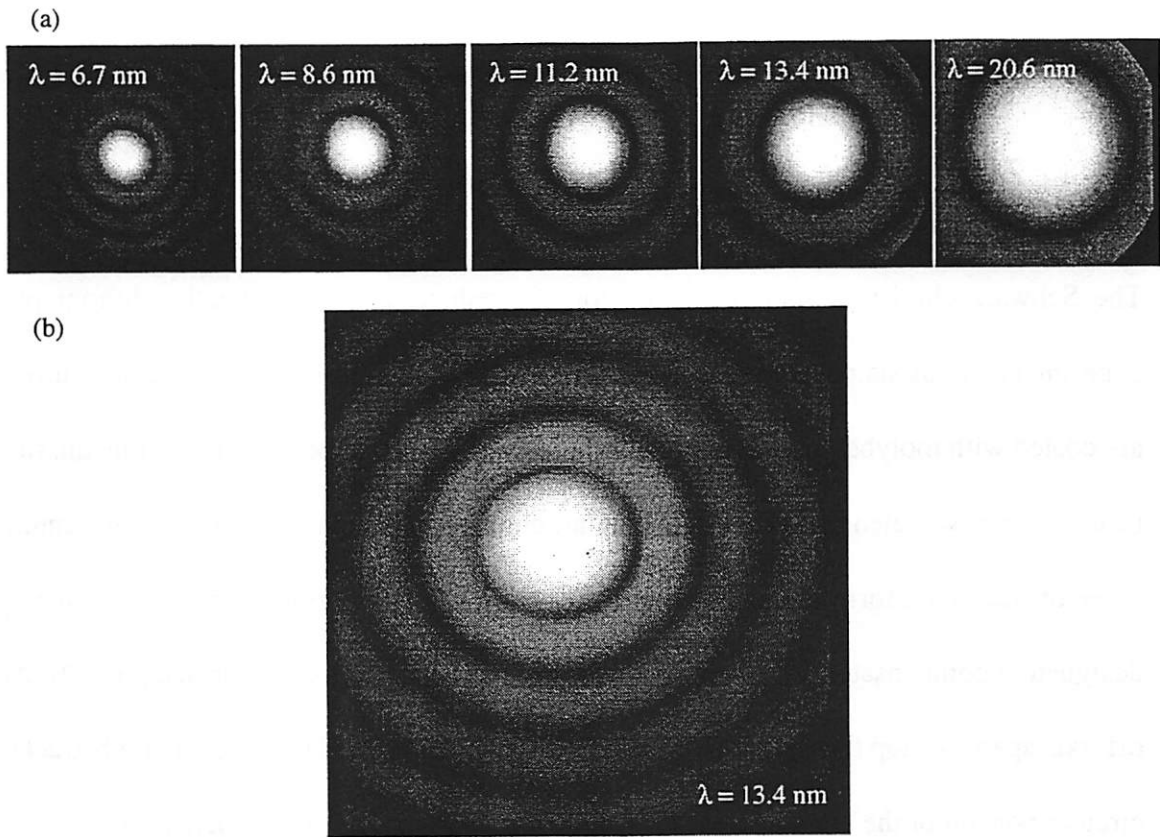


Figure 5-4. Tunable spatially coherent radiation diffracted from pinhole apertures.

(a) Measured far-field diffraction from a 1.0- μm -diameter pinhole at several EUV wavelengths. (b) Far-field diffraction from a 1.4- μm -diameter pinhole measured at 13.4-nm. The camera was closer to the pinhole aperture in (b).

0.005) [128]. The high degree of spatial coherence of the beam over a broad wavelength range is illustrated in Figure 5-4. The figure shows measured intensity patterns of the far-field diffraction from small, nearly circular apertures placed at the focus of the K-B illuminator. The high contrast of the diffraction rings indicates that the transmitted radiation is nearly fully spatially coherent [128]. These measurements indicate that the beamline delivers roughly 7-14 μW of coherent radiation (1-2 μW through a 0.5- μm -diameter pinhole) into a relative spectral bandwidth of 1/350-1/120. After propagation through the interfer-

ometer system, this flux allows acquisition of high-resolution interferograms in exposure times on the order of 5-15 seconds, as determined experimentally.

5.3. The 10× Schwarzschild System

The Schwarzschild test optic, designed for 10×-reduction EUV projection lithography experiments, consists of two nearly concentric spherical mirrors [160, 40]. Both mirrors are coated with molybdenum-silicon multilayer reflective coatings with peak transmission near 13.4-nm wavelength. While the annular, concave secondary is coated with a multilayer of nearly uniform thickness, the convex primary has a graded multilayer coating designed to compensate for the varying angles of incidence across its surface [40, 32]. An off-axis aperture stop that rests on the primary mirror is intended to select an unobstructed circular portion of the annular clear aperture when used for imaging experiments.

A schematic of the Schwarzschild optical system is shown in Figure 5-5 and the optical design parameters are given in Table 5-1. The 10×-demagnifying system has a numerical

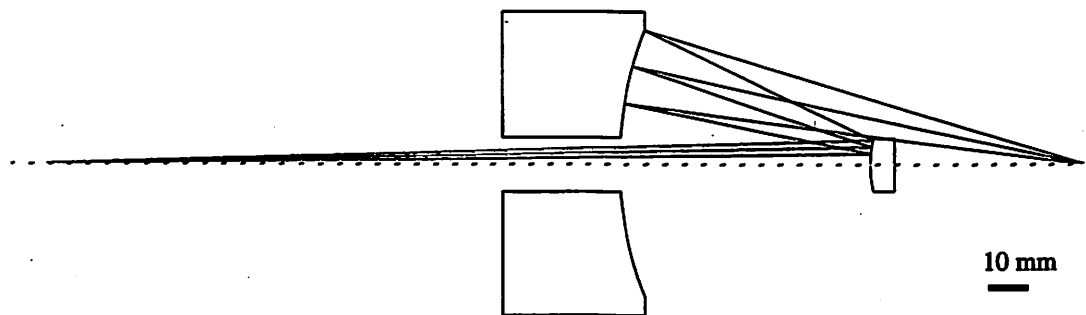


Figure 5-5. The 10× Schwarzschild optical design.

Schematic of the optical design for the 10×-demagnification Schwarzschild optical system. The system consists of a convex primary mirror, a concave secondary mirror, and an off-axis aperture stop at the primary mirror.

aperture of 0.08 and a corrected field of view of 400- μm in diameter in the image plane. The image-side depth of focus of the optical system is about $\pm 1 \mu\text{m}$ at 13-nm wavelength. The numerical aperture of the system is adjustable with a rotatable aperture stop that contains three separate sub-apertures, corresponding to different selectable numerical apertures of 0.06, 0.07, and 0.08. The image plane of the optic, determined during the assembly of the system, is defined by three balls attached to the optical housing. The object plane is not mechanically referenced to the optical housing.

Surface	Radius of curvature [mm]	Distance to the next surface [mm]	Radius [mm]	Decenter [mm]
object	Infinity	251.333	2.0	0
aperture stop	Infinity	0	2.010	5.300
primary mirror	-35.342	-73.955	7.850	0
secondary mirror	109.193	137.697	45.000	0
image	Infinity	0	0.2	0

Table 5-1. Optical design parameters of the 10 \times Schwarzschild system.

The 10 \times -demagnification optical system has a numerical aperture of 0.08 and an image-side field of view 400 μm in diameter.

The optical design has residual wavefront aberrations of about 0.05 wave rms within the 0.08 numerical aperture around 13-nm wavelength. The aberrations are dominated by primary astigmatism, primary coma, and primary triangular astigmatism, all oriented in the direction of the pupil displacement from the optical axis. The design wavefront aberrations, excluding the tilt and defocus terms, are relatively constant over the field of view. The residual rms wavefront error is plotted in Figure 5-6 as a function of the position of

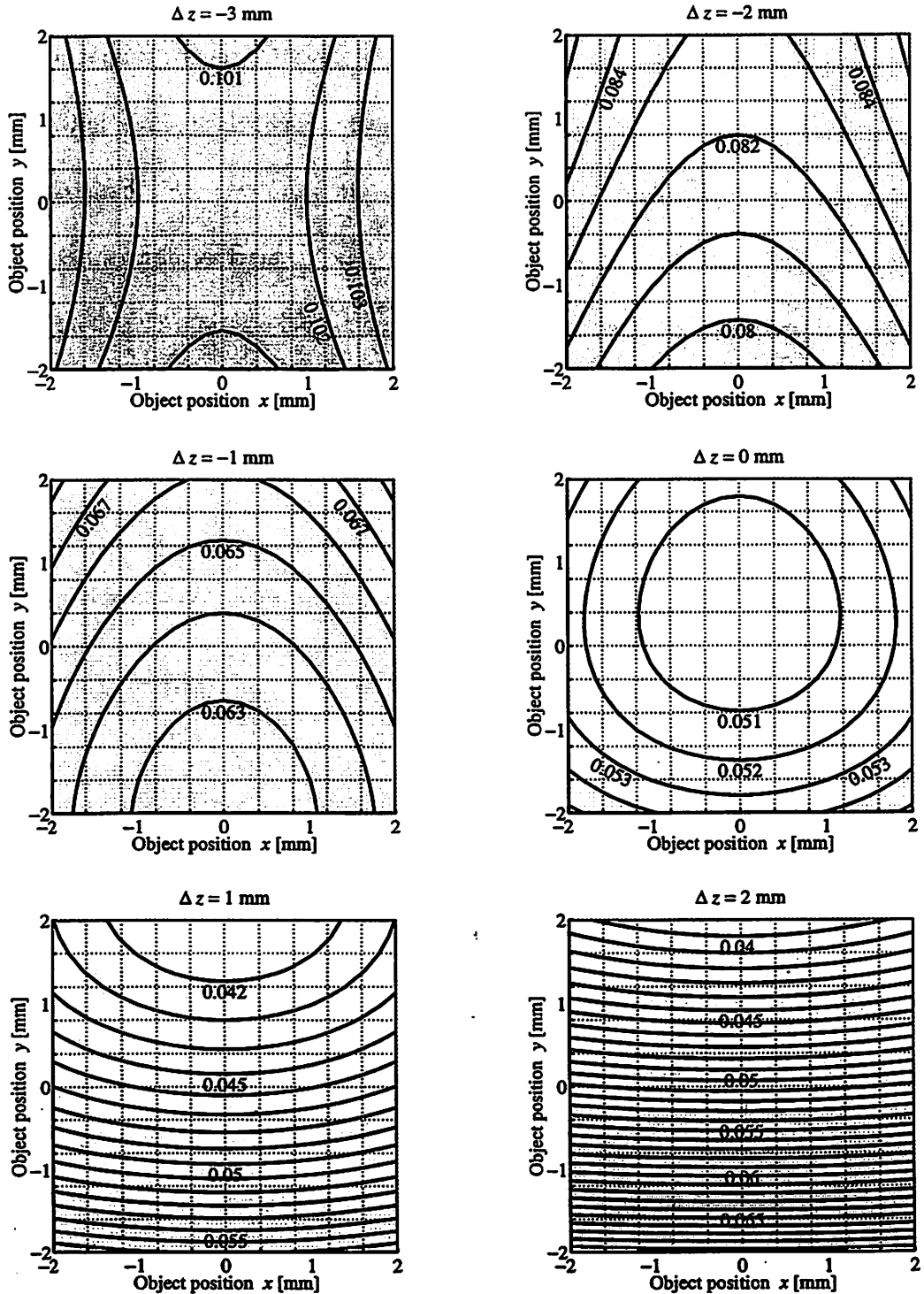


Figure 5-6. Wavefront error variations over the field of view.

The residual rms wavefront error of the 10× Schwarzschild optical design at 13.4-nm wavelength and 0.08 NA vs. the object point position are shown for different displacements Δz of the object point along the optical axis. Positive Δz corresponds to a greater-than-designed distance from the optic.

the object point in the $4 \text{ mm} \times 4 \text{ mm}$ corrected field of view. The wavefront error variations over the field are shown for several positions of the object point along the optical axis. Moving the object point from its intended design position ($\Delta z = 0$) toward the optic ($\Delta z < 0$), the residual wavefront error increases but stays quite uniform over the field. On the other hand, as the object point is moved away from the optic ($\Delta z > 0$), the residual wavefront error decreases somewhat but the field-of-view variations increase. Overall the wavefront error is quite uniform over the field of view even when the object point is misplaced from its intended position along the optical axis. Although only the ideal optical design is considered here, the variations in the wavefront error over the field of view would behave similarly in the presence of mirror and alignment imperfections.

5.4. Interferometer Configuration

The configuration of the phase-shifting point diffraction interferometer for testing the Schwarzschild optical system is illustrated in Figure 5-7. The optic is tested in its intended vertical operational orientation. The EUV beam from the beamline is steered into the optic with an adjustable, multilayer-coated, 45° turning mirror. This mirror enables small angular adjustments in the beam direction needed to optimize the illumination of the optic. The K-B optics focus the beam onto the object plane of the Schwarzschild system, where a sub-resolution entrance pinhole is placed. The pinhole selects spatially coherent radiation from the beam and spatially filters it to illuminate the test optic with a spherical wavefront. A coarse diffraction grating, placed between the object-plane pinhole and the Schwarzschild optic, serves as a small-angle beamsplitter by dividing the wavefront into multiple diffractive orders. On propagation through the test optic, the aberrations of interest are introduced

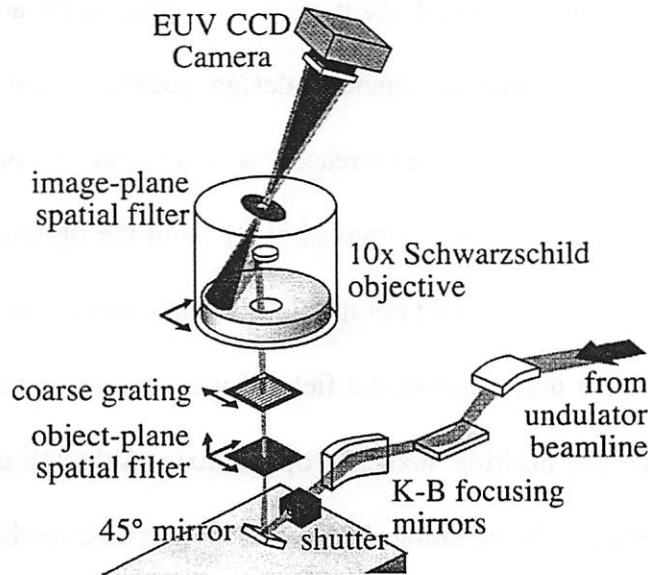


Figure 5-7. Configuration of the PS/PDI for testing the Schwarzschild objective.

Components of the phase-shifting point diffraction interferometer for characterizations of the multilayer-coated 10 \times -demagnification Schwarzschild optical system.

into the spherical illumination beams. Two of the diffractive orders are selected with a spatial filter placed in the image plane of the optic. The zero diffractive order is chosen as the test beam and transmitted through a window, which is significantly larger than the focal spot size. One of the first diffractive orders is spatially filtered by a sub-resolution pinhole to produce a spherical reference wavefront over the numerical aperture of the measurement. The choice of the zero diffractive order for the test beam ensures that the aberrations due to the grating line placement are not introduced into the measured wavefront. Translation of the grating in the direction perpendicular to its lines controls the relative phase shift between the test and reference beams necessary to perform phase-shifting interferometry. The interference of the test and reference beams is recorded with a 1-square-inch silicon

charge-coupled device (CCD) detector optimized for EUV, which is placed 12.7 cm beyond the image plane of the Schwarzschild optic with its surface normal to the central ray of the off-axis beam.

5.4.1. Beamsplitter

The coarse transmission grating used as a beamsplitter and a phase-shifting element in these experiments consists of a 225-nm-thick patterned gold absorber supported by a 100-nm-thick silicon nitride membrane. The 18- μm grating pitch is chosen to provide 4.5- μm separation between the test and reference wave foci in the image plane, which corresponds to about 54 fringes in 0.08 NA. This separation was chosen to minimize the image-plane overlap between the test and reference beams while maintaining sufficient fringe sampling density.

5.4.2. Sub-resolution Pinholes

The object-plane pinholes used in these measurements are commercially available, laser-drilled pinholes with nominal diameters of 0.5 μm . These pinholes are significantly smaller than the diffraction-limited resolution of the test optic on the object-side (Airy disk of 2 μm in diameter at 13.4-nm wavelength and 0.008 NA), ensuring a high-quality illumination wavefront, as discussed in Chapter 2.

The image-plane pinhole spatial filters with diameters of ~50-100 nm for testing the 0.08-NA optic at 13.4 nm can be fabricated by electron beam lithography [123-125] or by focused ion beam microfabrication [126, 88]. Examples of image-plane pinhole apertures used in these experiments are shown in Figure 5-8. Figure 5-8(a) shows a scanning elec-

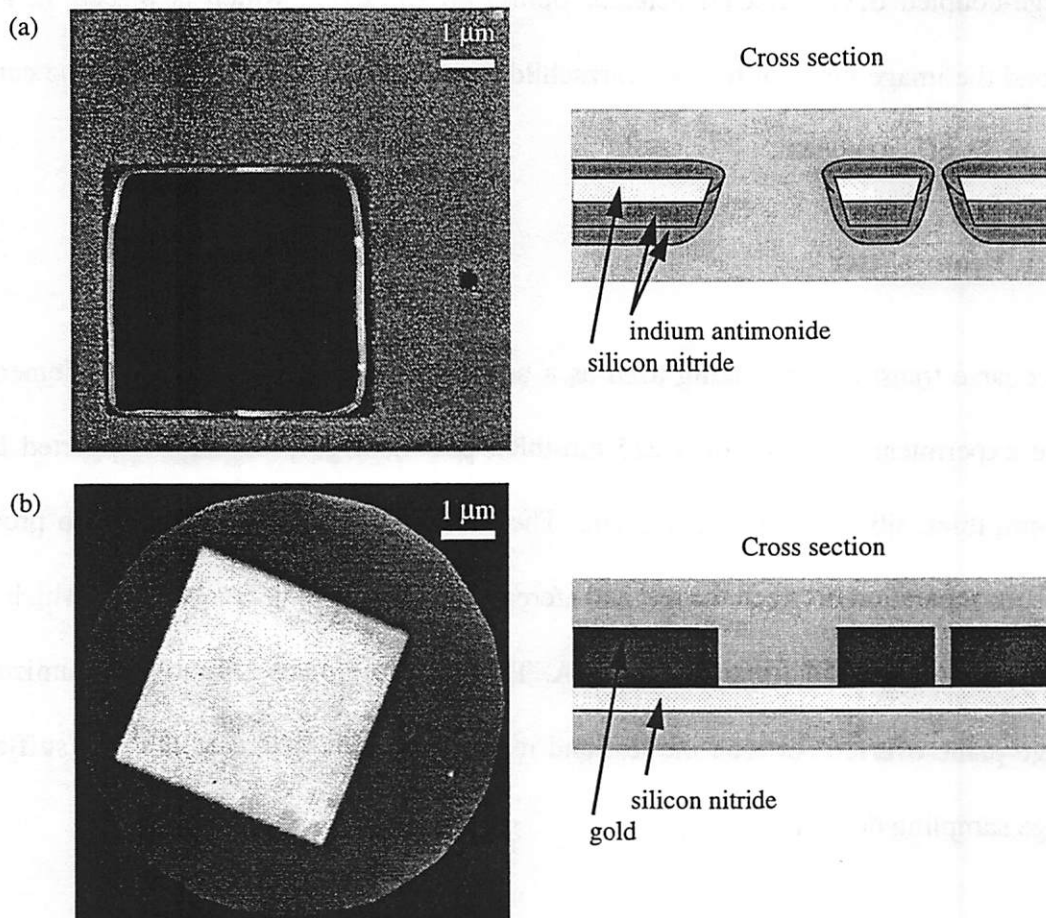


Figure 5-8. Image-plane pinhole spatial filters.

(a) An SEM image and the schematic cross section of the spatial filter fabricated with focused ion beam. Two sub-resolution pinholes of diameters 130 nm (top) and 165 nm (right) next to a $5\ \mu\text{m} \times 5\ \mu\text{m}$ square window. (b) An x-ray image and the schematic cross section of a spatial filter fabricated with electron beam lithography. A 50-nm diameter pinhole filter (bottom right) is next to a $5\ \mu\text{m} \times 5\ \mu\text{m}$ square window. The x-ray microscope image was recorded at a wavelength of 1.6 nm.

tron microscopy (SEM) micrograph and the schematic cross section of the image-plane pinhole apertures drilled by a focused ion beam into a membrane structure consisting of 100 nm of silicon nitride and 100 nm of indium antimonide absorber. After the aperture definition, an additional 70-nm layer of indium antimonide absorber was deposited on each side of the membrane to increase the absorption and also to decrease the size of the sub-

resolution pinholes. Two separate reference pinholes shown in the figure, placed in two orthogonal directions from the center of the test-beam window, allow interferometry measurements with two different grating orientations. The sub-resolution pinholes fabricated with this method and used in the experiments reported here range from 130 nm to 210 nm in diameter. Figure 5-8(b) shows an x-ray microscope image and the schematic cross section of pinhole apertures fabricated by electron beam lithography [123]. The electron beam defines the desired pattern in negative-tone photoresist layer on a silicon nitride membrane. Following the photoresist development, an absorber layer of gold or nickel is electroplated around the photoresist structure. The remaining photoresist is subsequently removed. The pinhole apertures in Figure 5-8(b), consisting of a 250-nm-thick gold absorber layer on a 100-nm-thick silicon nitride membrane, are approximately 50 nm in diameter. The open stencil pinhole apertures, e. g. Figure 5-8(a), are superior to the apertures defined only in the absorber layer, e. g. Figure 5-8(b), because the nitride membrane attenuates the EUV beam (by about 60% at 13.4 nm through 100 nm of silicon nitride) and can alter the properties of the test beam.

5.4.3. Detector

The beam transmitted through the interferometer is recorded with a silicon CCD camera optimized for the detection of EUV radiation [153, 154, 161, 162]. The back-thinned, back-illuminated CCD chip consists of a ~1-inch-square array of 1024×1024 pixels [153, 163]. The dynamic range of the camera used in these measurements is $2^{16} = 65536$ levels. At the maximum scan rate of 430kHz, the detected image can be read out at full resolution in about 2.5 seconds. Lower-resolution images produced by pixel “binning” can be

acquired faster, in about 0.5 seconds with 4×4 binning, for instance. In the interferometry experiments on the Schwarzschild optic, exposure times of 5-15 seconds are needed to obtain a signal of roughly 1000 counts over the background in the fringes at the full resolution of the camera. The exposure time is controlled with a compact, high-speed shutter, placed before the 45° turning mirror, as shown in Figure 5-7.

5.4.4. Alignment Strategy

Successful characterization of the Schwarzschild optical system requires repeatable and stable alignment of the interferometer components. In the first alignment step, the angle of the beam from the beamline must be adjusted with the 45° turning mirror to uniformly illuminate the entrance pupil on the primary mirror of the Schwarzschild optic and to pass through the desired field point in the object and image planes. An alignment target placed in the image plane via a kinematic mount attached to the optical housing can be used to mark the desired image point. Once the beam is steered in the proper direction and the optic is placed at the appropriate position with respect to it, the object-plane pinhole must be positioned within the stationary beam. The pinhole is placed in a kinematic mount attached to a computer-controlled, three-axis stage that allows alignment of the pinhole within the beam. To determine the beam location, a beam position reference is produced by allowing the focused beam to burn a thin mylar membrane held in a kinematic holder identical to the pinhole holder. The beam position reference enables placement of the pinhole near the desired location within the holder. The final alignment of the object pinhole is achieved with the stage that translates the kinematic pinhole holder.

Following the alignment of the entrance spatial filter and the coarse alignment of the beam focus in the image plane, the beam that passes through the system must be transmitted through the image-plane pinhole apertures. In this experiment, the apertures are aligned and fixed to be at the center of the image plane by means of a kinematic mount that rests on the three balls that define the image plane of the Schwarzschild optic. Although the image plane is horizontal, the plane of the pinhole membrane is normal to the off-axis beam propagation direction, which is oriented at about 12.1° from the vertical as shown in Figure 5-7. The fine alignment of the test and reference beams through the system is accomplished by a high-precision translation of the optic and the attached pinhole apertures on a bearing in two lateral directions. The focus is controlled by translation of the object-plane pinhole along the beam propagation direction. Owing to the fact that the image-plane apertures and the optic are moving together, the optic must be adjusted each time the object-plane pinhole is moved, which is needed for adjusting the focus, for instance. On the other hand, the required precision of the translation scales with the demagnification of the optic, in comparison to the precision needed to position the image-plane pinholes independently of the optic. Thus to characterize an optic with $0.1\text{-}\mu\text{m}$ resolution and $10\times$ demagnification, the necessary movement precision is only $0.05\text{-}0.1\ \mu\text{m}$ rather than $0.005\text{-}0.01\ \mu\text{m}$.

To align the reference and test beams through the sub-resolution pinhole and the transmission window in the image plane, the far-field intensity of the beam(s) that is recorded by the CCD detector is used. Since the adjustments of the optic position are performed manually, the recorded images must be acquired quite rapidly to provide real-time feedback. The images are obtained at a reduced resolution, typically binned 4×4 , to minimize the

readout and exposure times. At the reduced resolution, the data are sampled at roughly 4.5 pixels per fringe, compared to about 18 pixels per fringe at full resolution, to provide sufficient detail of the image during alignment. The beams must be placed in their respective positions in the image plane using only the far-field version of the image-plane fields. Since edges of the large square transmission window (see Figure 5-8) are detected quite easily, they can be used as a reference to position the test beam within the window. In order not to confuse the different grating orders, the zero-order beam is typically aligned without the grating beamsplitter in place before the beamsplitter is situated in the beam for the final adjustment.

To obtain an idea of the beam positions in the image plane of the test optic, the Fourier transform of the recorded far-field intensity can be used. It is well known from scalar diffraction theory that the optical fields far away from the focus of an optical system are the Fourier transform of the fields at focus, except for a phase factor not measured by intensity detectors [117, 128]. From the properties of Fourier transforms it then follows that the Fourier transform of the detected far-field intensity is the autocorrelation of the fields at focus [164, 165]. Although its conjugate symmetric nature does not make it as instructive as the beam intensity at focus, the autocorrelation of the fields at focus can provide information about the positions of the focal spots with respect to the pinhole apertures. Several examples of the intensities detected during the interferometer alignment and their corresponding Fourier transform magnitudes are shown in Figure 5-9(a)-(e). Both the intensities and their Fourier transforms are scaled to accentuate the image contrast. In Figure 5-9(a), the interferometer is aligned for data acquisition and the Fourier transform image reveals the test and the reference beams passing through the square window and the reference pinhole,

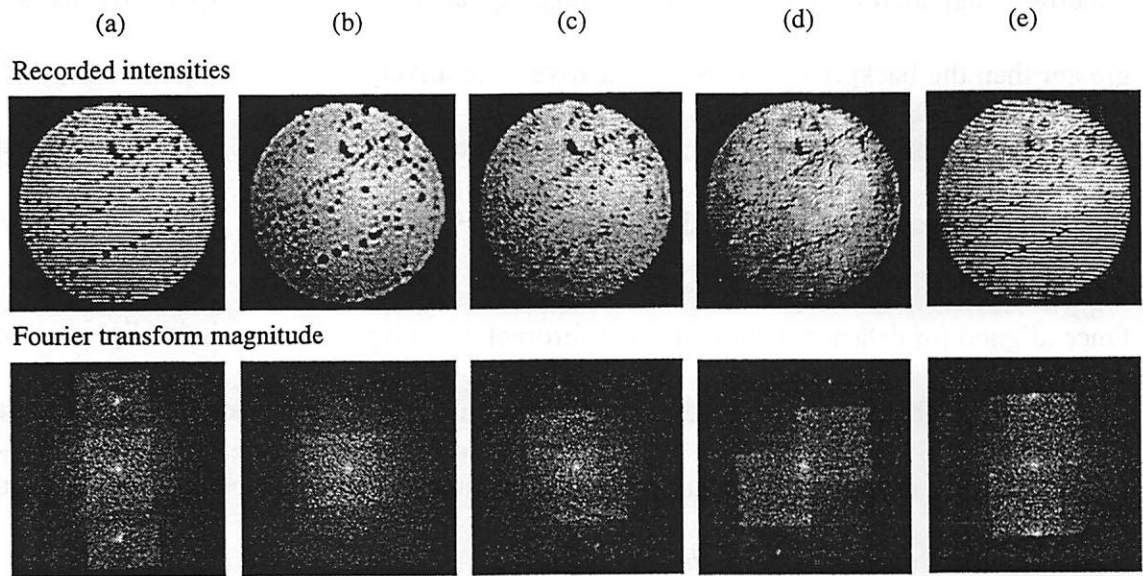


Figure 5-9. Intensities obtained during alignment and their Fourier transforms.

(a)-(e) Several intensity patterns observed during the alignment of the interferometer and the corresponding magnitudes of the Fourier transform of the intensities.

respectively. In Figure 5-9(b), the interferometer is only slightly out of alignment, as apparent from the position of the test beam within the transmission window in the Fourier transform picture. Similarly, the Fourier transform images in Figure 5-9(c) and (d) indicate the beam positions within the window when the interferometer is not aligned. Finally, Figure 5-9(e) shows the shearing fringes produced by the interference of two adjacent grating orders, whose placement at the edges of the transmission window is apparent in the Fourier transform image.

The Fourier transform of the intensity seems to provide information that may be helpful in the alignment of the interferometer. The applicability of the Fourier transform in real-time alignment may be limited by the speed of the data acquisition and the Fourier transform computation. In addition, as seen from Figure 5-9, the position of the beam within the test

window is apparent only because the average signal within the window is significantly greater than the background. This is indicative of relatively strong mid-spatial-frequency scatter in the beam, particular to this Schwarzschild test optic. Without the scatter, the outline of the window may not be easily visible in the Fourier transform.

Once aligned for data acquisition, the interferometer can typically remain in alignment for several hours, demonstrating good mechanical stability despite the fact that the temperature of the system is not controlled. Measured vacuum chamber temperature fluctuations typically do not exceed $\pm 0.5^{\circ}\text{C}$ over 24 hours.

5.5. Results of Interferometric Measurements

Numerous experiments have been done to characterize the aberrations in the Schwarzschild optic and to evaluate the capabilities of the interferometer. Transmission measurements on the Schwarzschild optic reveal contaminants on the mirror surfaces. The initial interferometry measurements were influenced by carbon contamination of the pinhole apertures. Subsequent mitigation of the carbon deposition has allowed extensive characterization of several regions of the annular full aperture of the Schwarzschild optic.

5.5.1. Contamination of Mirror Surfaces and Its Influence on Data Analysis

One of the important measurements in optics evaluation is to characterize the light transmitted through the uniformly illuminated test optic. The intensity of 13.4-nm radiation transmitted through the 0.07-NA sub-aperture of the Schwarzschild optic is shown in Figure 5-10(a). The figure reveals localized contamination of the optical surfaces. Some of

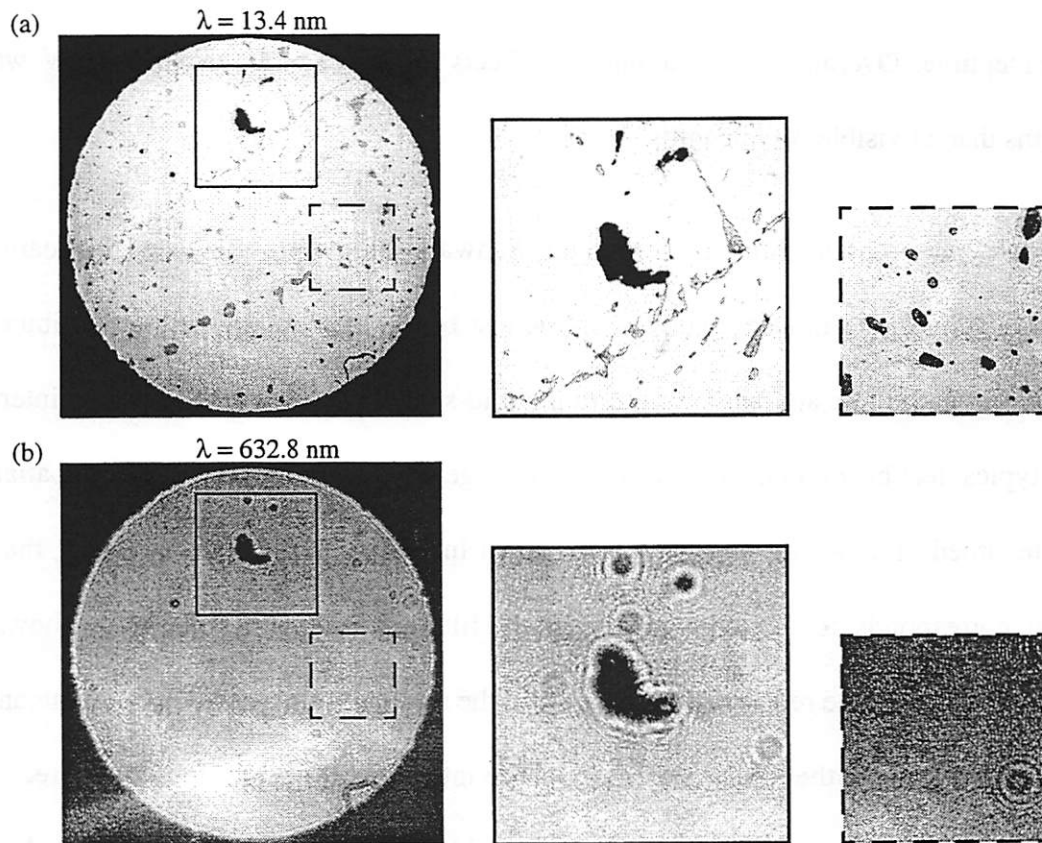


Figure 5-10. Measured transmission through the Schwarzschild optic.

Transmission of light through the Schwarzschild optic at two different wavelengths: (a) 13.4 nm and (b) 632.8 nm. The contamination of the optical surfaces appears quite different at the two wavelengths

the contaminants, most likely particulates on the mirror surfaces, cause complete loss of transmission. Other contaminants, possibly a residue from a wet-cleaning process of the optical substrates or the coated surfaces, lead to 15-30% reduction in the transmitted intensity. Given that the size of the illuminated region is 3.5 mm in diameter on the primary mirror and about 19 mm in diameter on the secondary mirror, the contaminated regions are on the order of 100 μm in size. When the measurement is repeated at the visible wavelength of 632.8 nm, shown in Figure 5-10(b), the transmitted intensity is quite different. The par-

ticulate contamination produces a loss of transmission, but the other residue is nearly imperceptible. Overall, the contamination effects are more pronounced at EUV wavelengths than at visible wavelengths.

Mirror surface contamination present in this Schwarzschild optic attenuates the beam and scatters radiation to moderate angles. In the test beam, the contamination contributes to wavefront amplitude and phase errors in the mid-spatial-frequency regime. The intensity of a typical test beam transmitted through the large window in the image-plane spatial filter, recorded at 13.4 nm wavelength, is shown in Figure 5-11(a). As expected, the test beam corresponds to a moderately spatially filtered version of the beam shown in Figure 5-10(a). In the reference beam, some of the scatter produced by the contaminants is transmitted through the test-beam window. The intensity of the reference beam, recorded at 13.4-nm wavelength, is shown in Figure 5-11(b). The slowly varying background in the reference beam corresponds to the strongly filtered wavefront from the sub-resolution pin-hole needed for the measurement. The nonuniform scatter in the reference beam that is passed through the test window contains spatial frequencies determined by the size of the

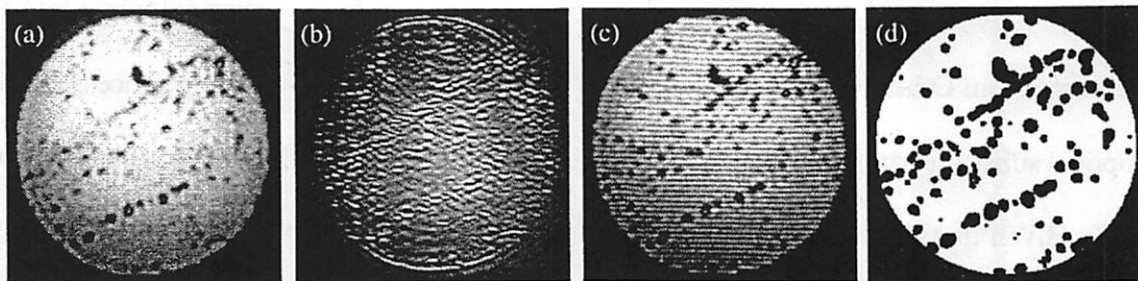


Figure 5-11. Test wave, reference wave, fringes, and analysis domain.

(a) Recorded intensity of a typical test wavefront. (b) Measured intensity pattern of a typical reference wavefront. (c) Typical fringe pattern. (d) Domain of valid data points used in data analysis.

window and its separation from the reference pinhole. Since the unwanted features are produced by scattering from the contaminants, transmitted through a high-frequency bandpass spatial filter, the reference wavefront is corrupted in the vicinity of the blemish regions in the aperture. Figure 5-11(c) shows the interference of the test and the reference beams. Because the reference wavefront quality is compromised near the contaminated areas, the phase difference between the test and reference beams determined by interferogram analysis is meaningful only outside the blemish regions. The data are valid over a domain, shown in Figure 5-11(d), that excludes those regions. The polynomial fit, used to determine the low-spatial-frequency terms in the wavefront, is performed over the domain of the valid data points. As a result, even though the contaminants corrupt the reference wavefront and complicate the data analysis, they do not significantly affect the ability of the interferometer to measure the low-order aberrations of interest in this experiment.

5.5.2. First Measurements - Carbon Contamination Problem

In the first interferometry measurements performed on the 0.07-NA sub-aperture of the Schwarzschild optic, problems with carbon contamination of the pinhole apertures were encountered. Numerous references to surface contamination with carbon, caused by adsorbed and cracked hydrocarbons and catalyzed by exposure to ultraviolet radiation, can be found [166-169]. The initial measurements were performed at pressures on the order of 10^{-5} torr in the test-optic vacuum chamber. Laser-drilled entrance pinholes and image-plane apertures patterned in gold supported by a silicon nitride membrane (see Figure 5-8(b)) were used. The carbon build-up, produced during exposure to the EUV beam, can obstruct the pinhole apertures and degrade the transparency of the silicon

nitride. The contamination-induced nonuniformities in the silicon nitride transmission can affect the test beam and compromise the quality of the measurements. In addition, when the contamination forms on the time scale of typical exposures, successive phase-shifted interferograms are recorded under varying conditions. The phase-shifting data analysis, which relies on combining interferograms recorded under constant conditions, then cannot be applied.

The changes in the measured interferograms caused by carbon contamination build-up are illustrated in Figure 5-12(a). The difference between the first and the sixth interferograms from a phase-shifting series recorded at 13.4-nm wavelength in 30-second exposures is

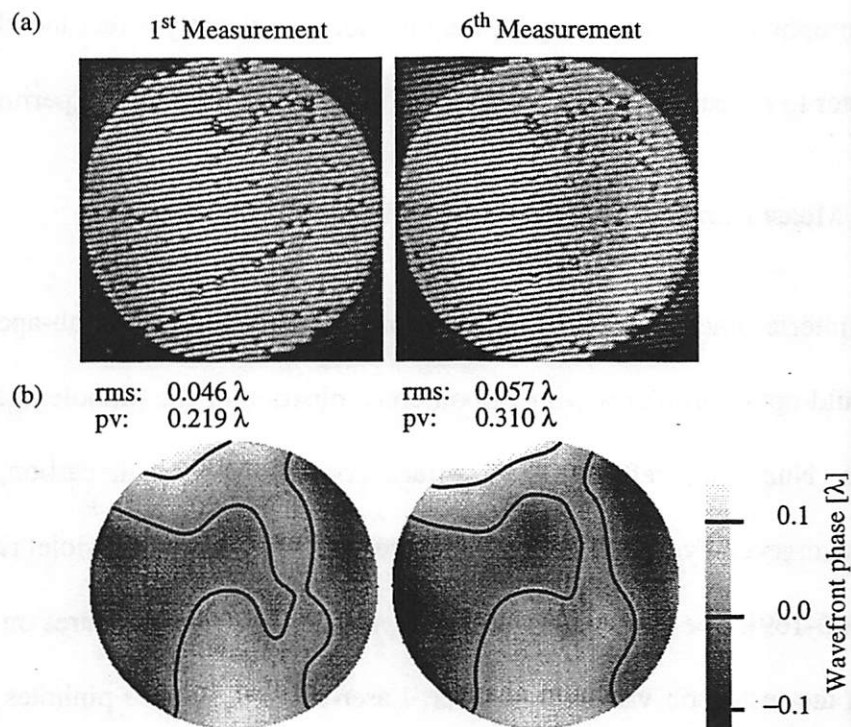


Figure 5-12. Change in measurements due to carbon contamination.

(a) First and sixth interferograms from a sequence of images recorded at 13.4-nm wavelength every 30 seconds. (b) The phase aberrations determined from the interferograms.

apparent. Although phase-shifting analysis is not applicable here, each interferogram in the series can be analyzed separately to determine the effects of carbon contamination on the measured wavefront. The wavefront phase calculated using single interferogram analysis is shown in Figure 5-12(b) for the first and the sixth images in the series.

The most apparent effect of the carbon deposition is the loss in the average recorded image intensity with time, shown in Figure 5-13(a). In this 3-minute measurement, the intensity reduction can be attributed mainly to a loss of transmission through the silicon nitride membrane. The entrance pinhole transmission, which also degrades with contamination build-up, decreased only after 1-2 hours of continuous EUV exposure. Since the contamination rate scales with the intensity of the EUV radiation, the transmission loss from other system components, positioned away from the high-intensity beam focus, is also negligible on the time scale of these measurements. Figure 5-13(a) also shows the peak fringe contrast in two portions of each interferogram. The contrast remains relatively constant as the contaminants are deposited, indicating comparable transmission loss for both the test and the reference beams. However, contamination-induced changes in the phase of the test and reference wavefronts are also present. Figure 5-13(b) shows the measured rms and peak-to-valley phase difference between the test and reference beams versus time. The phase difference appears to increase with the carbon contamination build-up. One explanation is that the contaminants are reducing the size of the reference pinhole spatial filter, which was initially too large. An oversize pinhole would not fully filter the aberrations in the reference beam, which are nearly identical to the aberrations in the test beam before filtering. The detected phase difference would then be smaller than the actual difference between the test

and reference beams. The carbon contamination may reduce the pinhole size and improve the reference wavefront quality, leading to an increase in the measured phase difference.

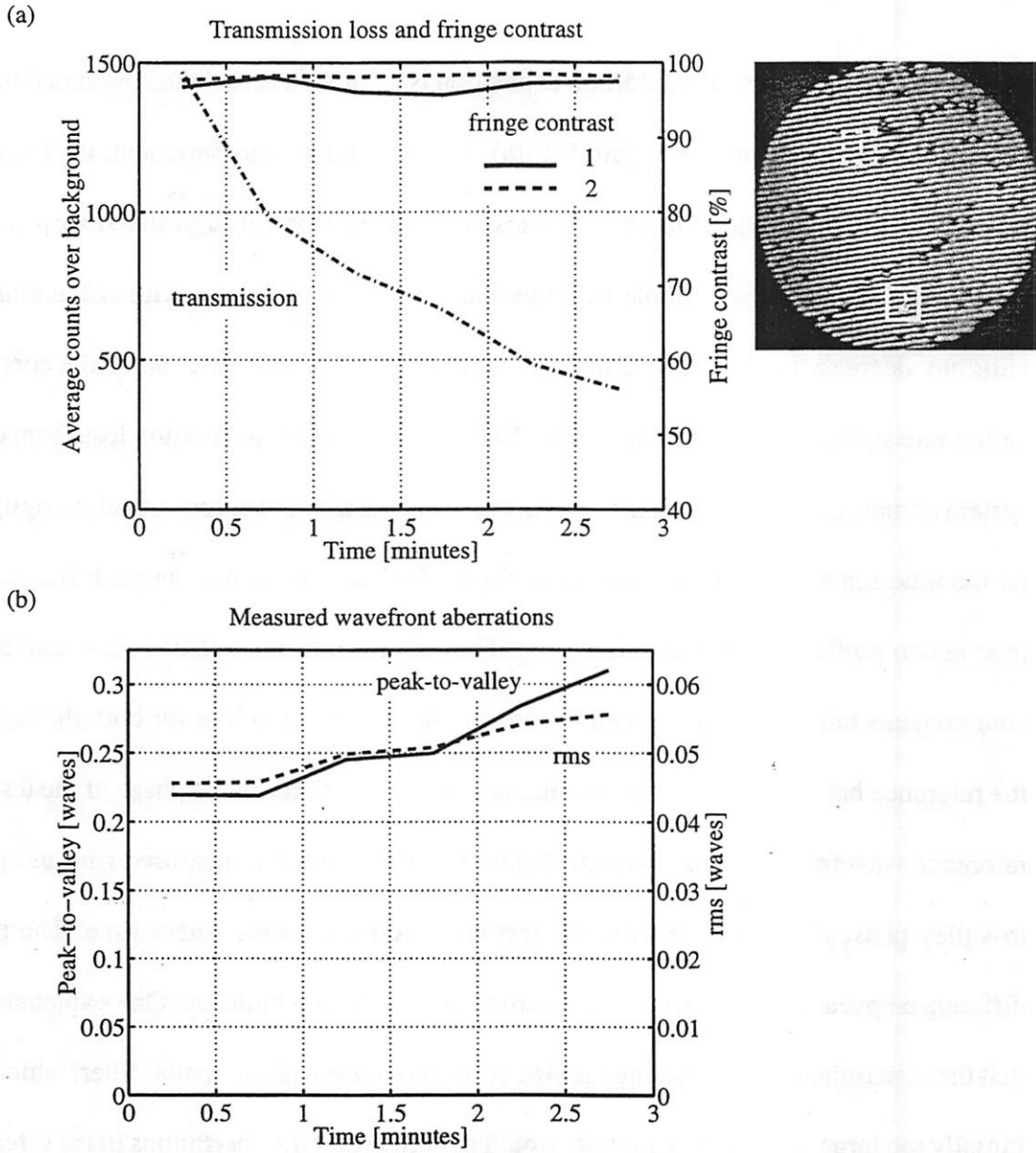


Figure 5-13. The effect of carbon contamination on phase measurements.

(a) Carbon contamination reduces transmission through the interferometer but does not significantly change the fringe contrast. (b) The measured peak-to-valley and rms wavefront aberrations vs. time.

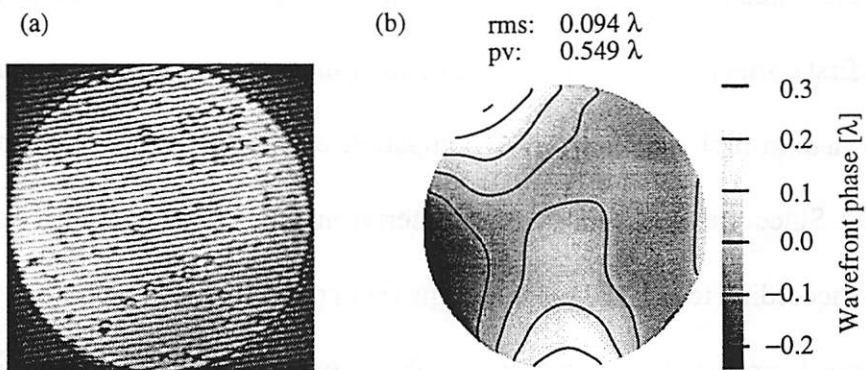


Figure 5-14. First measurements of aberrations of the Schwarzschild optic.

(a) Sample interferogram and (b) wavefront aberrations of the 0.07-NA sub-aperture of the Schwarzschild optic measured at 13.4-nm wavelength.

To minimize the effects of carbon contamination, meaningful measurements were obtained with an undamaged image-plane pinhole aperture by reducing the data acquisition time to a minimum. The aberrations of the 0.07-NA sub-aperture of the Schwarzschild optic determined from five 2-second interferograms are shown in Figure 5-14. The average point-by-point rms variation in the phase from the five separate interferograms was 0.0043 wave, indicating negligible change in carbon contamination during data acquisition. The phase map shown is the Zernike polynomial reconstruction of the average phase from the five interferograms analyzed individually, excluding the tilt and defocus and the systematic coma term. These initial measurements indicate wavefront aberrations of 0.094 wave rms and 0.549 wave peak-to-valley at 13.4-nm wavelength.

The initial measurements revealed unacceptable carbon contamination effects that affected the measurements on the time scale of minutes. To develop reliable interferometry for testing of EUV optics, the contamination had to be significantly reduced. Several improvements were made to the interferometer vacuum system with the goal of drastically reducing

the partial pressures of the residual hydrocarbons, which serve as the source of contaminants. The first corrective measure was the dismantling of the test optic vacuum chamber, followed by a ultra-high-vacuum (UHV) compatible cleaning of most of the interferometer components. Since the re-assembly of the interferometer, all interferometer components are handled according to a UHV practices. The second improvement was an increase in the pumping speed, provided by a new high-volume turbo pump backed by another turbo pump rather than by a mechanical pump. Overall, the base pressure in the interferometer chamber was decreased by about two orders of magnitude. Finally, oxygen gas is bled into the chamber during exposure to EUV light. This is known to mitigate carbon contamination buildup [166-169]. When measurements are performed, the interferometer is first pumped down to a base pressure of 5×10^{-7} torr, then filled with oxygen gas during exposure to EUV light, maintaining a pressure of about 2×10^{-4} torr. These measures have nearly eliminated the contamination problem, allowing the characterization of the Schwarzschild optic to proceed.

5.5.3. The Aberrations of the 10× Schwarzschild Objective

With the improved interferometer in operation, extensive measurements of several regions of the annular full aperture of the Schwarzschild optic have been performed. In these experiments, the image-plane apertures produced by focused ion beam microfabrication (see Figure 5-8(a)) were used. With the open-stencil structures, the problem of contamination of the silicon nitride membrane is avoided and the transmission of the interferometer system is improved.

Three different regions of the annular aperture of the 10× Schwarzschild optic, corresponding to the three sub-apertures in the aperture stop, were characterized at 13.4-nm wavelength. Although the aperture stop is rotatable, it was not moved with respect to the optic in the course of the measurements reported here. The wavefront aberrations of the three

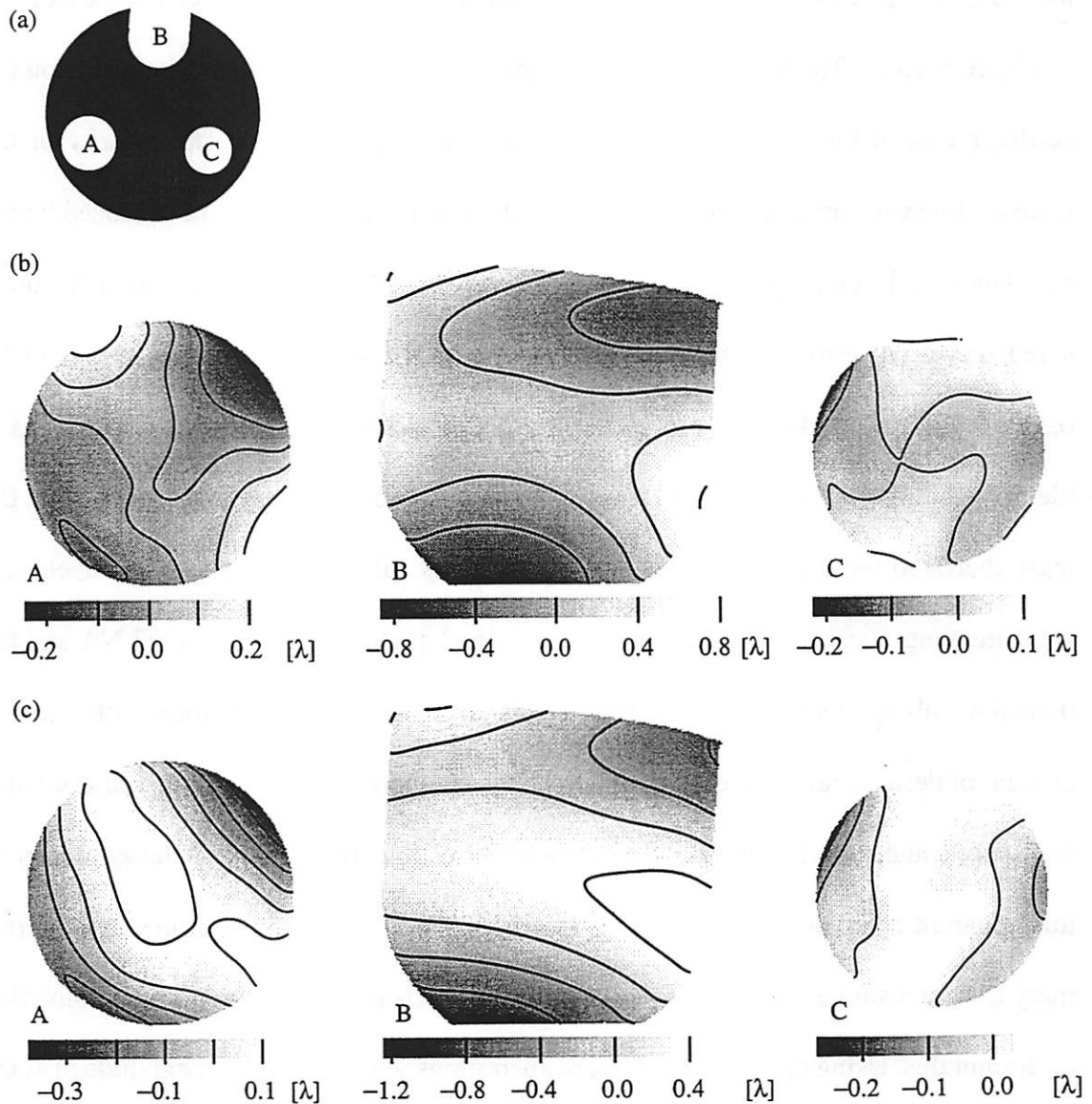


Figure 5-15. Aberrations in three sub-apertures of the Schwarzschild optic.

Optical path difference measured in three different portions of the annular clear aperture at 13.4-nm wavelength. (a) The placement of the sub-apertures in the aperture stop. The measured aberrations (b) at best focus and (c) with some defocus. The defocus for sub-apertures A, B, and C is -0.135λ , -0.22λ , and -0.05λ , respectively.

sub-apertures, reconstructed from the Zernike polynomial fit, are shown in Figure 5-15. The wavefront maps are compiled from multiple measurements of each sub-aperture. Figure 5-15(a) shows the relative position of the different sub-apertures in the aperture stop. The largest sub-aperture is non-circular due to a fabrication error. The aberrations of the 0.08, 0.07, and 0.06-NA sub-apertures, denoted by B, A, and C, respectively, are shown in Figure 5-15(b). The tilt, the defocus, and the systematic coma terms that depend on the configuration of the interferometer are excluded in Figure 5-15(b). The polarity of the measured wavefronts is determined from the changes in the defocus term produced by the translation of the object pinhole with respect to the optic. At 13.4-nm wavelength, the measured wavefront errors of the 0.08, 0.07, and 0.06-NA sub-apertures are, respectively, 0.313, 0.090, and 0.044 wave rms and 1.684, 0.524, and 0.356 wave peak-to-valley. Visible-light interferometry, performed during the assembly of the optic, was used to align the least aberrated region of the optic with the 0.07-NA sub-aperture. These at-wavelength measurements show near diffraction-limited optical quality for both the 0.07-NA and the 0.06-NA sub-apertures. Figure 5-15(c) shows the wavefront aberrations with small amount of defocus reintroduced, to illustrate that the aberrations in fact follow the annulus of the optic and seem to correspond to a zonal fabrication error. Owing to the symmetry of this apparent zonal error, the dominant aberrations in all three sub-apertures are the primary astigmatism and the primary triangular astigmatism, oriented in the radial direction of the annulus. Using the balanced Zernike aberrations scaled to a peak magnitude of 1, the magnitudes of the astigmatism and the triangular astigmatism are 0.548 wave and 0.470 wave for sub-aperture B, 0.195 wave and 0.104 wave for sub-aperture A, and 0.095 wave and 0.031 wave for sub-aperture C, respectively.

5.6. Assessment of Measurement Quality

The measurements of the Schwarzschild system have served to evaluate the optical properties of the optic as well as the capabilities of the EUV phase-shifting point diffraction interferometer. Numerous experiments have been performed to characterize the interferometer stability, the quality of the illumination and the reference wavefronts, the sensitivity to alignment, and the measurement repeatability. The measurements utilizing different grating orders as the test and the reference beams are also compared. Finally, experiments at different focal positions and with different grating orientations are used to estimate the reference wavefront errors.

5.6.1. Measurement Stability

Stability of the interferometer is essential for successful assessment of the aberrated wavefront. In phase-shifting interferometry, the properties and the alignment of the system must remain stable during the time needed to acquire the entire data series of 5, 9, or more interferograms. To assess the interferometer stability, the aberrations can be measured repeatedly without any adjustments of the interferometer. An example of such an experiment performed on the 0.07-NA sub-aperture of the optic is illustrated in Figure 5-16. The figure shows the change in the first 16 Zernike polynomial coefficients extracted from wavefront measurements performed in 6-second exposures at 1-minute intervals over 10 minutes. The experiment indicates that the largest variation occurs in the tilt term, which is directly related to the separation of the reference pinhole and the test-beam focus in the image plane. The overall change in the tilt (coefficients 1 and 2) corresponds to a drift of about 7 nm in the position of the reference pinhole with respect to the test focus. This drift is sig-

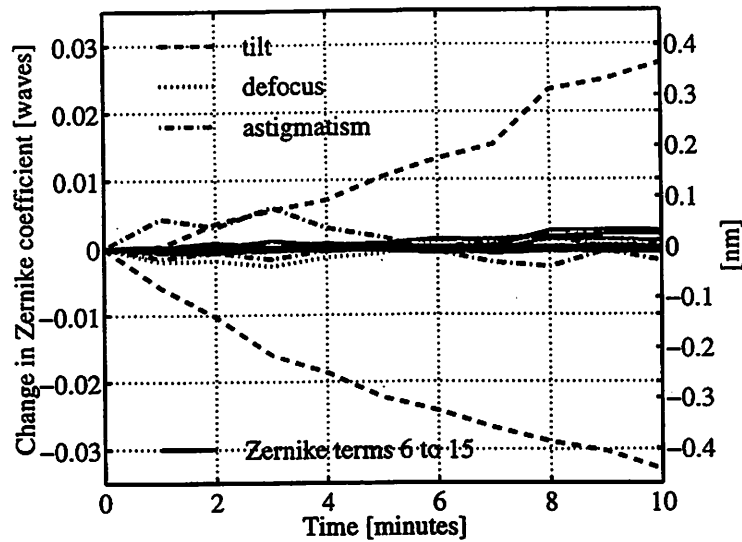


Figure 5-16. Changes in the measured aberrations with time.

The change in the Zernike polynomial coefficients of the measured wavefront phase vs. time, measured at 13.4-nm wavelength. The main change is in the tilt, related to the distance between the reference pinhole and the test focus. Here the change in the tilt is equivalent to about 7-nm drift in the reference pinhole position in 10 minutes. The measured aberrations of interest are not changing significantly on this time scale.

nificantly smaller than the reference beam focal size of about 230 nm in diameter. As a result, the alignment of the interferometer is maintained and the measured wavefront error does not change considerably, as demonstrated by the nearly constant coefficients of the low-order aberrations of interest (Zernike terms 4 to 16). The most significant variation appears in the astigmatism (coefficients 4 and 5), which is the largest aberration measured. Overall, the standard deviations of the 11 measured rms and peak-to-valley wavefront errors are 0.001 wave and 0.008 wave at 13.4-nm wavelength, respectively. Since the phase-shifting interferogram series are typically acquired in times on the order of 1-2 minutes, the measured interferometer stability appears adequate for wavefront characterization with 0.01 wave rms accuracy.

5.6.2. Reference Wavefront Quality

Because interferometry is a comparative technique, the accuracy with which the wavefront under test can be measured is directly related to the properties of the reference wavefront. In the phase-shifting point diffraction interferometer, the reference wavefront is generated by diffraction from a sub-resolution pinhole placed in the image plane of the test optic. The reference pinhole spatially filters the illumination beam to produce a spherical reference wavefront, in principle. The measured reference wavefront quality is discussed in this section and in Section 5.6.6.

With the exception of the experiments discussed in Section 5.5.2, the measurements reported here were performed with reference pinholes patterned using the focused ion beam microfabrication. Only four such pinholes were available for these experiments. The layout of the image-plane spatial filters, consisting of four reference pinholes placed next to two $5\ \mu\text{m} \times 5\ \mu\text{m}$ square test windows separated by $40\ \mu\text{m}$, is indicated in Figure 5-17(a). The reference pinholes are labeled from 1 to 4 for the purposes of this discussion. The SEM images of the four reference pinholes in Figure 5-17(b) reveal the approximate diameters of 130, 165, 210, and 140 nm for Pinholes 1 to 4, respectively. The measured far-field diffraction patterns from the pinholes, shown in Figure 5-17(c) are in good agreement with the pinhole sizes measured by electron microscopy.

The diameters of the available pinholes are somewhat larger than the desired 50-100 nm. As a result, the pinholes may not generate perfectly spherical reference wavefronts. The effectiveness of the spatial filtering by the pinhole apertures can be assessed using scalar diffraction calculations. For example, with the assumption of circular pinhole filters and

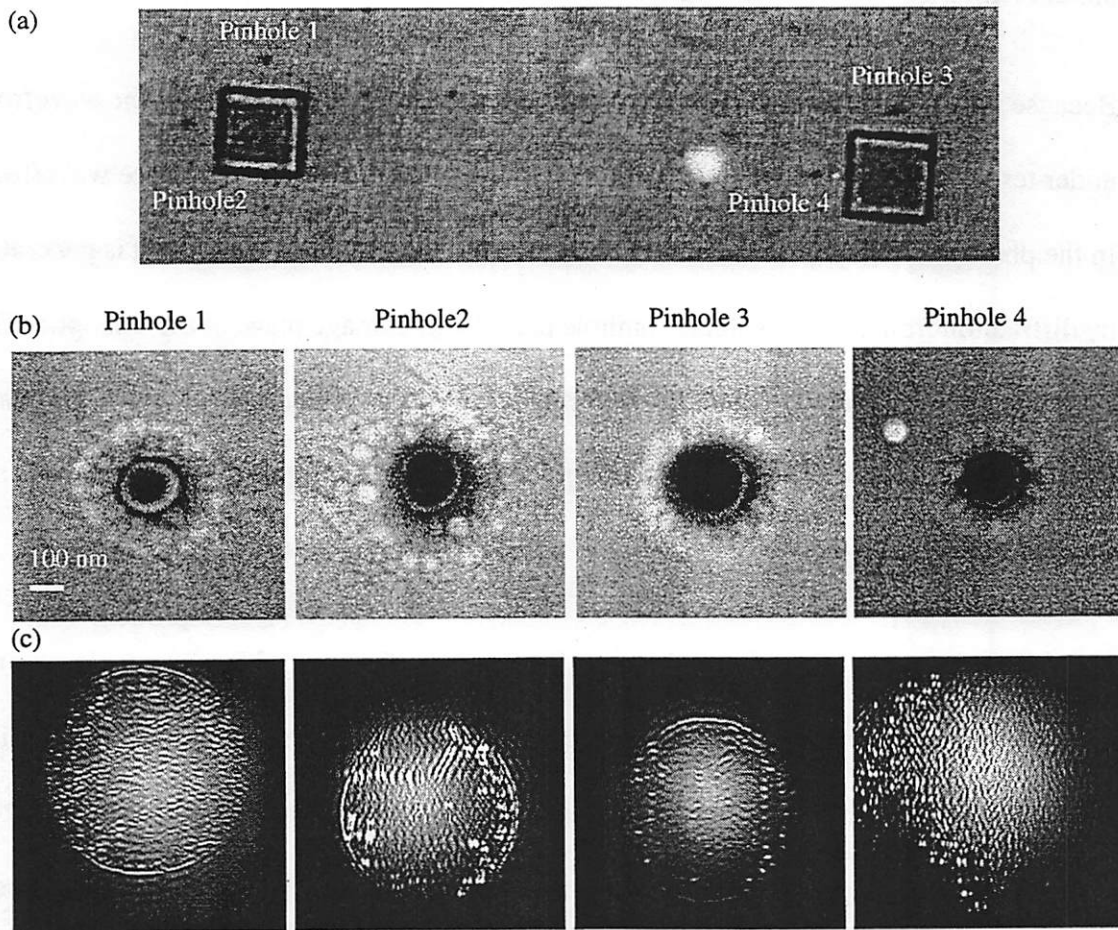


Figure 5-17. Image-plane sub-resolution pinholes.

(a) Visible-light image of the spatial filters used in the image plane. The reference pinholes are next to $5\ \mu\text{m} \times 5\ \mu\text{m}$ square test windows separated by $40\ \mu\text{m}$. (b) SEM images of four reference pinholes fabricated with the focused ion beam. (c) Measured diffraction patterns from the pinholes. From left to right, the mean pinhole diameters are 130, 165, 210, and 140 nm, respectively.

an illumination beam that contains the aberrations measured in the 0.07-NA sub-aperture, the transmitted wavefront errors are 0.004, 0.011, 0.031, and 0.005 wave rms at 13.4-nm wavelength for the pinhole diameters of 130, 165, 210, and 140 nm, respectively. The peak-to-valley errors are 0.020, 0.062, 0.181, and 0.028 wave, respectively. Since primary astigmatism dominates the aberrations, the transmitted wavefront error can also be estimated from Figure 2-4, using the magnitude of the measured astigmatism and the normal-

ized pinhole size. From these estimates as well as from a simple comparison between the pinhole size and the diffraction-limited spot size of about 230 nm, it is clear that Pinhole 3 is too large for accurate measurements. For the 0.06-NA sub-aperture, with smaller aberrations and larger spot size at focus, the spatial filtering is better than for the 0.07-NA sub-aperture. On the other hand, the highly aberrated beam produced by the larger 0.08-NA sub-aperture is not well filtered by three of the four pinholes. As a result, for the 0.06 and 0.07-NA sub-apertures, the wavefront aberrations reported here are compiled from data from Pinholes 1, 2, and 4, unless indicated otherwise. For the 0.08-NA sub-aperture, only data from the smallest Pinhole 1 are presented.

The differences due to the reference pinholes are revealed when the measurements from the different pinholes are compared. The average of all acceptable measurements performed over time period of about two months on the 0.07-NA sub-aperture at 13.4 nm with each of the four reference pinholes is shown in Figure 5-18. The average phase maps, compiled from 9 phase-shifting data series for each of Pinholes 1 and 2, and from 11 phase-shifting series for Pinholes 3 and 4, correspond to the low-order aberrations found from the Zernike polynomial fit and exclude the tilt, the defocus, and the systematic coma. The average rms and peak-to-valley errors and their standard deviations are also indicated in the figure. Since the unfiltered reference beam contains essentially the same aberrations as the test beam, the phase difference between the test wave and the filtered reference wave is reduced when the spatial filtering by the pinhole is inadequate. Thus with relatively large reference pinholes, the measured aberrations are expected to be the smallest for the largest pinhole and vice versa. This is revealed in the measurements shown in Figure 5-18, where the smallest aberrations are found with Pinhole 3, the largest of the four pinholes. The aber-

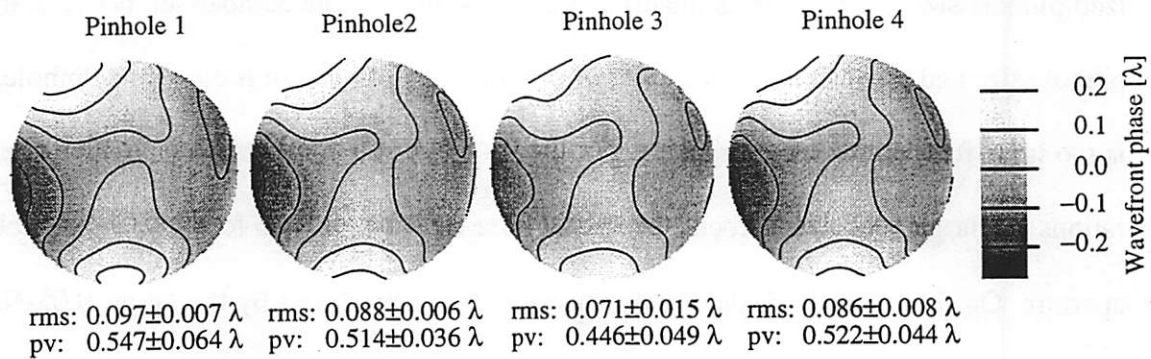


Figure 5-18. The average measured wavefront for different reference pinholes

The average measured wavefront from the 0.07-NA sub-aperture of the Schwarzschild optic for each of the reference pinholes used. The wavefront error measured with reference Pinhole 3 is the smallest as expected when the pinhole is too large to adequately filter the aberrations in the illumination beam.

rations measured at 13.4 nm using the four pinholes with approximate diameters of 130, 165, 210, and 140 nm are, respectively, 0.097 ± 0.007 , 0.088 ± 0.006 , 0.071 ± 0.015 , and 0.086 ± 0.008 wave rms, and 0.547 ± 0.064 , 0.514 ± 0.036 , 0.446 ± 0.049 , and 0.522 ± 0.044 wave peak-to-valley. Excluding the data from Pinhole 3, the average rms phase difference between all combinations of measurements with Pinholes 1, 2, and 4 is 0.012 wave rms at 13.4 nm. The standard deviations of the measured rms and peak-to-valley errors for the three pinholes are 0.005 and 0.014 wave, respectively.

Because the available reference pinholes are not much smaller than the focused beam illuminating them, the pinhole placement within the beam can affect the quality of the reference wavefront. The effect of the alignment in testing the 0.07-NA sub-aperture was evaluated with 7 successive measurements using Pinhole 4, where the position of the optic was adjusted to move the focus over the pinhole aperture. The Fourier transform analysis of the interferograms reveals small differences in the measured wavefront error. The phase

differences for every combination of the 7 measurements are shown in Figure 5-19 in units of 0.01 wave at 13.4 nm. The rms phase difference is indicated above each difference profile. Measurements 3 and 7, performed with the reference pinhole nearly out of alignment

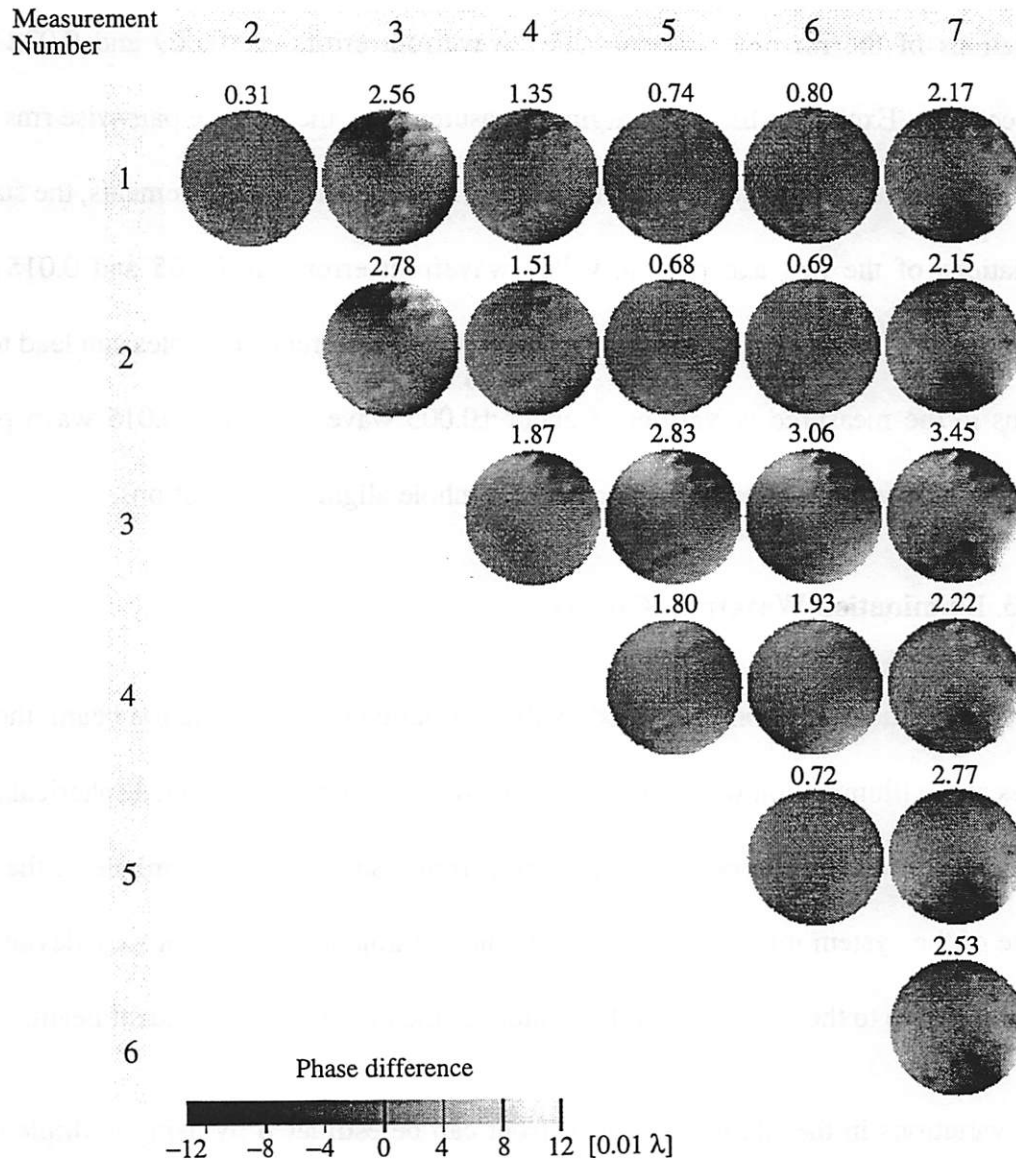


Figure 5-19. The effect of reference pinhole misalignment.

All combinations of the differences in the wavefront phase measured with slightly different alignment of the reference pinhole. The rms phase differences are shown in units of 0.01 wave at 13.4-nm wavelength above each difference map. In measurements 1, 2, 4, 5, and 6, the pinhole alignment was representative of typical alignment conditions. In measurements 3 and 7, the reference pinhole was nearly out of alignment.

with the focal spot, do not represent typical measurement conditions. Closer observation of Figure 5-19 reveals that the measured phase differences are indeed largest for rows and columns in the figure that contain measurements 3 and 7. In the entire measurement set, the average pairwise rms wavefront difference is 0.019 wave rms at 13.4 nm. The standard deviations of the rms and peak-to-valley wavefront errors are 0.009 and 0.032 wave, respectively. Excluding the two marginal measurements, the average pair-wise rms wavefront difference is 0.011 wave rms. Also in the five acceptable measurements, the standard deviations of the rms and peak-to-valley wavefront errors are 0.005 and 0.015 wave, respectively. Consequently, the use of relatively large reference pinholes can lead to variations in the measured wavefront of about ± 0.005 wave rms and ± 0.015 wave peak to valley at 13.4-nm wavelength, under typical pinhole alignment conditions.

5.6.3. Illumination Wavefront Quality

To measure the aberrations produced by the test optic in the illumination beam, the properties of the illumination wavefront need to be well understood. Ideally, a spherical illumination wavefront is generated by diffraction from a sub-resolution pinhole in the object plane of the system under test. Practically, the illumination wavefront may deviate from sphericity due to the properties of the pinhole or the quality of the incident beam.

The variations in the illumination wavefront can be estimated by using multiple object-plane pinholes in the measurements. For instance, in the characterization of the 0.07-NA sub-aperture of the Schwarzschild optic, 29 different measurements were performed, utilizing 9 separate object-plane pinholes, nominally 0.5 μm in diameter. As discussed in Chapter 2, pinholes diameters of 0.5-1.0 μm are adequate to ensure high-quality illumina-

tion, in principle. Owing to the realignment of the reference pinhole, required every time the object pinhole is moved or changed in these measurements, the effect of illumination cannot be isolated. However, the variations in the aberrations measured with the different input pinholes can be compared to the changes due to the different reference pinholes and their alignment. For example, the average rms difference between all combinations of measurements with the nine input pinholes is 0.0126 wave rms at 13.4 nm. For comparison, in the measurements with the three reference pinholes and with the different alignment of the reference pinholes, similar rms phase differences are 0.0122 wave and 0.0106 wave, respectively. Also, the standard deviations of the rms and peak-to-valley errors measured with the nine input pinholes are 0.0055 and 0.036 wave, respectively. Comparable standard deviations of the rms and peak-to-valley aberrations are 0.0047 and 0.014 wave with the three different reference pinholes, and 0.0052 and 0.015 wave for varying alignment conditions. Thus the illumination variations in these measurements do not seem to change the measured wavefront significantly, as expected when sufficiently small object-plane pinholes are used.

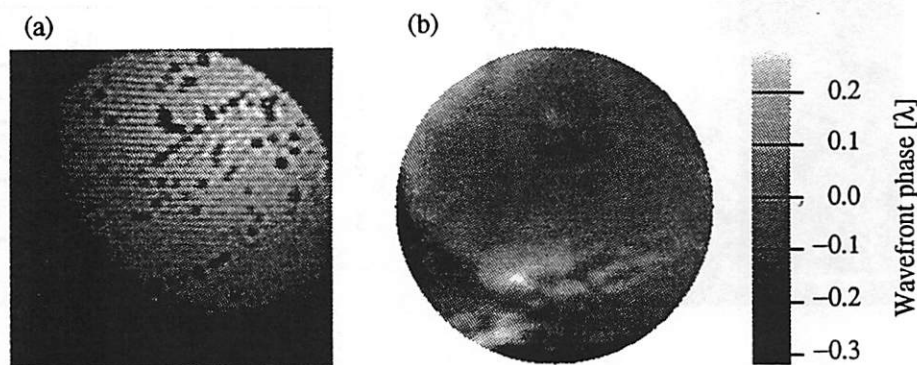


Figure 5-20. The effect of nonuniform illumination wavefront.

(a) Sample interferogram and (b) the measured wavefront when the object-plane spatial filter is too large. (a) The first dark ring in the illumination appears in the interferogram and produces phase error in the wavefront (b).

The use of a large pinhole in the object plane can produce errors in the measured aberrations, especially when regions near a dark diffraction ring are used for the illumination. A wavefront measurement with a misaligned, oversize entrance pinhole, roughly $2\ \mu\text{m}$ in diameter, is shown in Figure 5-20. The recorded interferogram in Figure 5-20(a) reveals the presence of the first diffraction ring from the entrance pinhole in the illumination of the 0.07-NA sub-aperture. Although the phase measurement is noisy in the dark region of the diffraction ring, the wavefront phase is clearly influenced by the illumination pattern, as shown Figure 5-20(b).

Relative to the size of the entrance pinhole, the beam focused on the object plane is significantly larger, as described in Section 5.2, producing quite a uniform illumination of the pinhole. As a result, the pinhole position within the beam should not significantly affect the measured wavefront, as shown in Figure 5-21. In this experiment, five successive

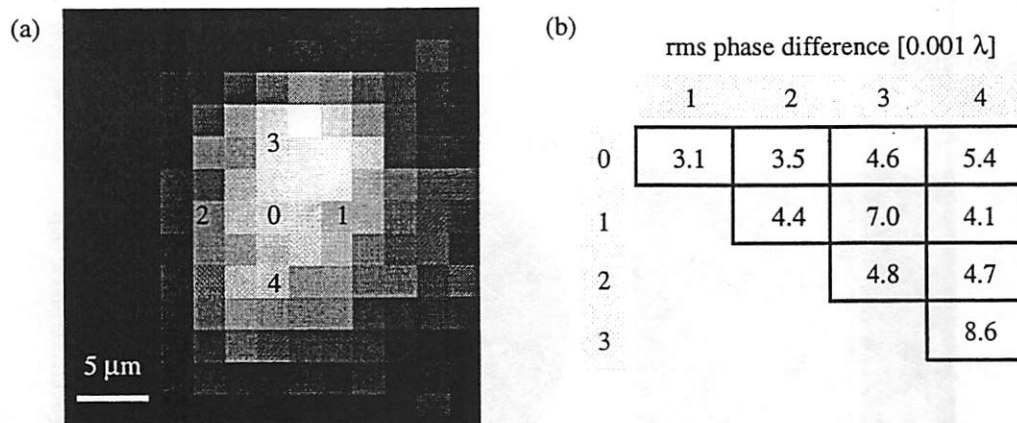


Figure 5-21. The effect of input pinhole misalignment.

(a) The intensity profile of the K-B illuminator focus measured at 13.4-nm wavelength with a 0.5- μm -diameter entrance pinhole. Five positions of the entrance pinhole where interferometry measurements were performed. (b) The measured rms phase difference between all the different pairs of the five pinhole positions, reconstructed from the Zernike polynomial fit.

wavefront measurements were performed, each at a different position of the entrance pinhole in the K-B focus. The beam profile measured with a scan of the 0.5- μm -diameter pinhole and the five pinhole locations are indicated in Figure 5-21(a). Figure 5-21(b) tabulates the rms phase difference for all possible pairs of the five measurements in units of 0.001 wave and 13.4-nm wavelength. The average pairwise difference is 0.0050 wave rms. The standard deviation of the five rms wavefront errors measured is 0.0028 wave. Since this variation is less than that caused by the reference pinhole alignment, by necessity adjusted in each measurement here, this experiment only places an upper bound on the influence of the entrance pinhole illumination on the measured wavefront. However, it also reveals that under typical operational conditions, the effect of the reference pinhole alignment may in fact be smaller than found in Section 5.6.2, where the misalignment was intentional.

Experiment	Standard deviation of the measured rms wavefronts [λ]	Average pairwise difference in the measured rms wavefronts [λ]
3 reference pinholes	0.0047	0.0122
9 input pinholes	0.0055	0.0126
reference pinhole alignment	0.0052	0.0106
input pinhole alignment	0.0029	0.0050

Table 5-2. Measurement variations due to different pinholes and their alignment.

The standard deviation and the average pairwise difference in rms wavefront aberrations measured at 13.4-nm wavelength on the 0.07-NA sub-aperture of the Schwarzschild optic. The variations due to different input and reference pinholes are assessed from 29 separate measurements with 3 reference pinholes and 9 input pinholes. The deviations due to the pinhole alignment are obtained in experiments using a single input pinhole and a single reference pinhole. The input pinhole effects are always influenced by the reference pinhole alignment in this experiment.

The measurement deviations at 13.4-nm wavelength associated with the quality of the illumination and the reference wavefronts are summarized in Table 5-2. The variations are assessed in terms of the standard deviations and the mean pairwise differences in the separate measurements of the rms wavefront error performed on the 0.07-NA sub-aperture of the Schwarzschild optic. Pinhole differences are extracted from 29 measurements with 3 reference pinholes and 9 input pinholes. Alignment effects relate to experiments with individual input and reference pinholes.

5.6.4. Measurement Repeatability

The capabilities of the interferometry have been characterized by repeatability measurements performed on the 0.07-NA sub-aperture of the Schwarzschild optic. The aberrations were first characterized in a series of measurements, performed over several weeks with multiple object-plane input pinholes, three image-plane reference pinholes, and different portions of two orthogonal gratings. Following this series of experiments, the other two sub-apertures of the optic were measured. Subsequently, the 0.07-NA sub-aperture of the Schwarzschild optic was measured again in a second series of experiments. Successive measurements of each sub-aperture require removal of the optic from the vacuum chamber, followed by repositioning of the optic and complete realignment of the interferometer. Because the reference pinholes reside at slightly different field points and the object pinholes are moved for adjustment of the focus, the aberrations are measured at slightly different field points. Using the results from Figure 5-6, the field variations are negligible here for the transverse separations of 0.4 mm in the object plane (40 μm in the image plane) and the typical focal adjustments with the object pinhole of less than 0.5 mm.

The wavefront aberration map and the corresponding Zernike polynomial fit, determined at 13.4-nm wavelength from 29 separate measurements using reference Pinholes 1, 2, and 4 and including both series, are shown in Figure 5-22(a) and (b), respectively. Only a small number of measurements with very poor fringe contrast were excluded from the data. The

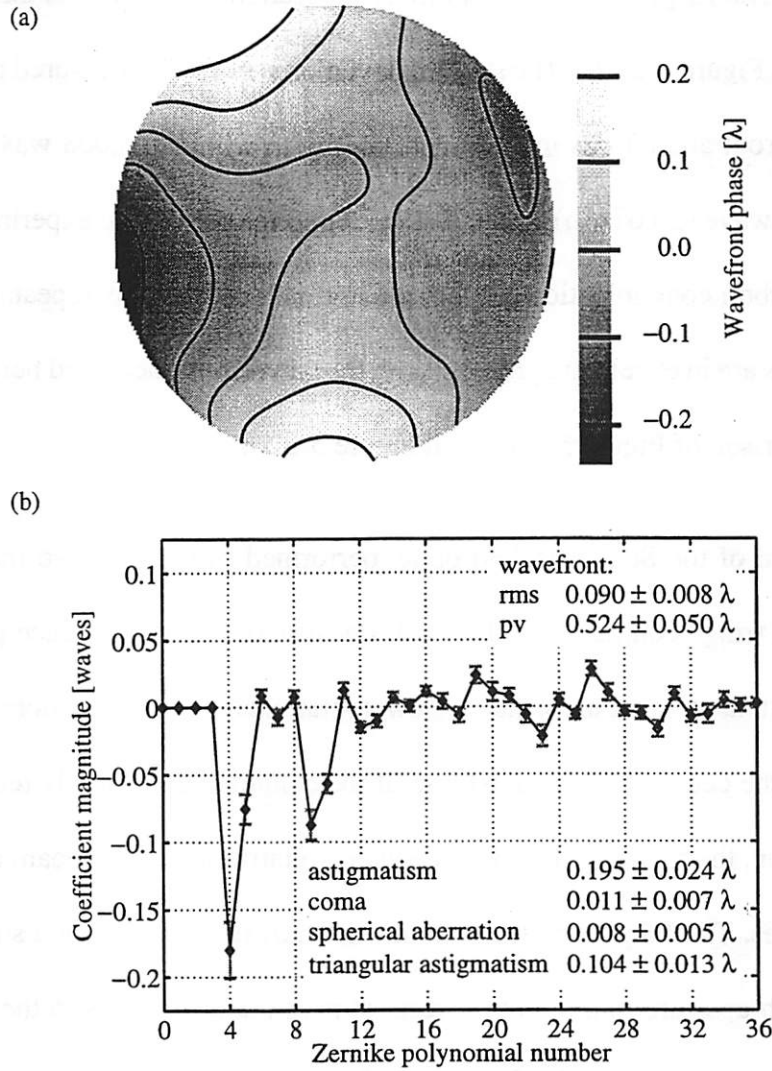


Figure 5-22. Wavefront aberrations on 0.07-NA sub-aperture.

(a) Wavefront aberrations and (b) the Zernike polynomial fit coefficients of the 0.07-NA sub-aperture of the Schwarzschild optic determined from multiple measurements at 13.4-nm wavelength. The Zernike coefficients correspond to polynomials scaled to have a peak magnitude of one. The magnitudes of astigmatism (coefficients 4 and 5), coma (6 and 7), spherical aberration (8) and triangular astigmatism (9 and 10) are indicated. The dominant aberration is astigmatism.

wavefront error of 0.090 ± 0.008 wave (1.20 ± 0.11 nm) rms and 0.524 ± 0.050 wave (7.02 ± 0.67 nm) peak-to-valley, is dominated by astigmatism indicative of a zonal fabrication error described earlier in Section 5.5.3. The error bars of the Zernike polynomial coefficients in Figure 5-22(b) correspond to the rms variation in each term over the 29 measurements. The magnitudes of the primary aberrations and their standard deviations are also given in Figure 5-22(b). The standard deviations of the 29 measured rms and peak-to-valley wavefront aberrations indicate repeatability to within ± 0.008 wave (± 0.11 nm) rms and ± 0.050 wave (± 0.67 nm) peak-to-valley. Although the initial experiments complicated by the carbon contamination problem are not included in this repeatability evaluation, their results are in excellent agreement with the wavefront measured here, as apparent from the comparison of Figure 5-14(b) and Figure 5-22(a).

In the evaluation of the Schwarzschild optic, performed over about two months, a slow reduction in the fringe contrast was observed. Because only four reference pinholes were used in these extensive measurements, a slow contamination of the pinholes with carbon is suspected as the cause of the contrast loss. If the contamination slowly reduces the pinhole transmission, the reference beam is attenuated relative to the test beam and the fringe contrast degrades. The long-term decrease in the contrast, measured in a small region of the 0.07-NA sub-aperture to minimize effects of possible differences in the illumination, is shown in Figure 5-23 for each of the four reference pinholes. Each measurement point represents a phase-shifting interferogram set from experiments at 13.4-nm wavelength. The contrast reduction is especially sharp at the boundary between the data series 1 and 2, where the other two sub-apertures were tested. In view of the carbon contamination problems encountered earlier, the slow reduction in the reference pinhole transmission is not

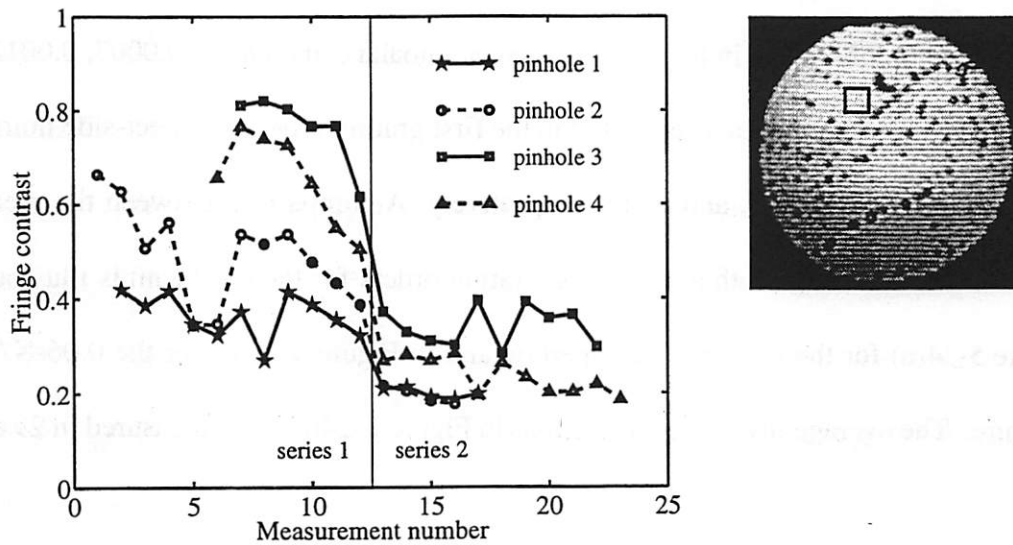


Figure 5-23. Long-term reference pinhole changes.

The fringe contrast in the indicated portion of the 0.07-NA sub-aperture vs. the measurement number for each reference pinhole used. A set of phase-shifting experiments constitutes each measurement. The 0.08-NA and 0.06-NA sub-apertures were characterized between the experiment series 1 and series 2. The slow decrease in the contrast, over roughly two months of operation, indicates gradual loss in reference pinhole transmission.

surprising. The slow progress of the damage found here is a demonstration of the vast improvement in the interferometer vacuum system, considering that all the measurements consisted of 160 phase-shifting data series of 5 to 9 interferograms each, numerous single-interferogram experiments, and prolonged exposures during alignment.

5.6.5. Effect of the Grating Illumination

In Chapter 2, the positioning of the lines in the grating beamsplitter is found to potentially influence the measured wavefront when one of the diffracted grating orders serves as the test beam in the interferometer. However, because the grating is used on the low-NA side of the Schwarzschild optic, the coma aberration due to the curvature of the wavefront incident on the planar grating is not expected to significantly affect the measured wavefront,

even when a diffracted grating order is used as the test beam. Specifically, with the beam-spot separation of $4.5\ \mu\text{m}$ in the image plane, an unbalanced coma of 0.0007, 0.0012, and 0.0017 wave peak-to-valley is expected in the first grating order for object-side numerical apertures of 0.006, 0.007, and 0.008, respectively. A comparison between the measurements that utilize the zeroth and the first grating orders for the test beam is illustrated in Figure 5-24(a) for the 0.07-NA sub-aperture and in Figure 5-24(b) for the 0.06-NA sub-aperture. The average low-order aberrations in Figure 5-24(a) were measured in 29 exper-

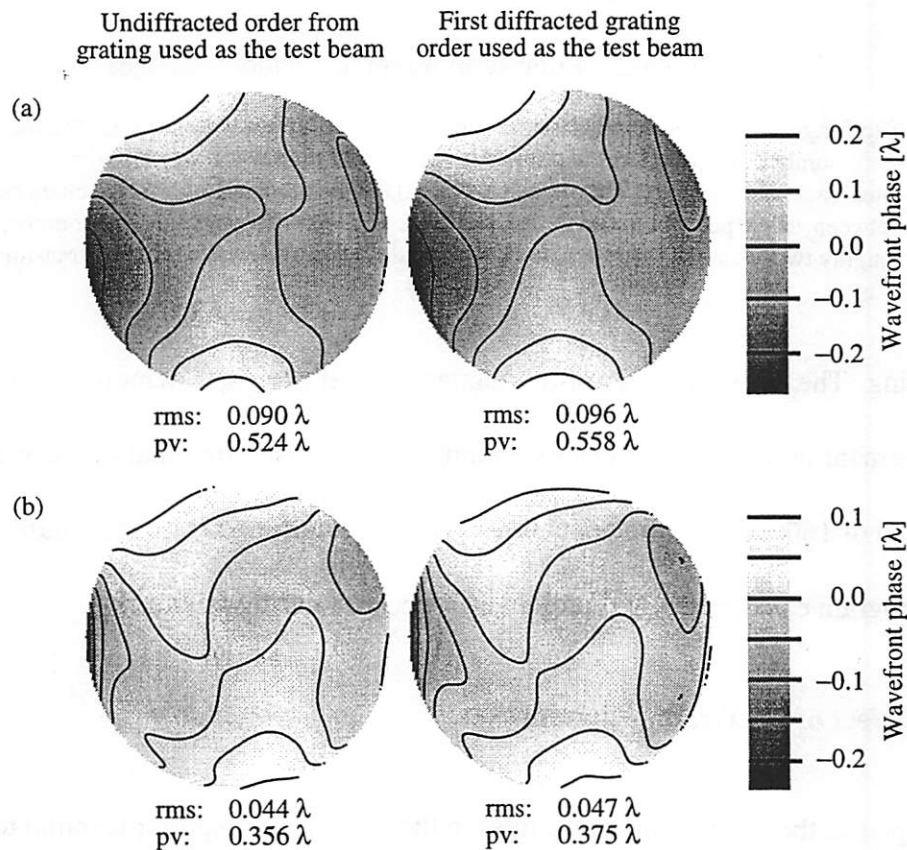


Figure 5-24. The effect the grating line placement.

The average aberrations measured in (a) the 0.07-NA and (b) the 0.06-NA sub-apertures at 13.4-nm wavelength. The measurements having the zero grating order as the test beam are compared to the measurements having the first diffracted order as the test beam. The small differences between the two cases for both sub-apertures indicate negligible aberrations produced by the placement of the grating lines, as expected.

iments with the zero-order test beam and in 2 experiments with the first-order test beam. In Figure 5-24(b), the number of experiments used in the average is 5 and 3 for zero and first-order test beams, respectively. For the 0.07-NA sub-aperture, the phase difference between the zero and first-order measurements is 0.008 wave rms at 13.4 nm and for the 0.06-NA sub-aperture, the difference is 0.007 wave rms. These variations are smaller than the repeatability of the measurements, indicating a negligible effect due to the grating coma aberrations as expected.

5.6.6. Accuracy Considerations

Although good measurement repeatability with the EUV phase-shifting point diffraction interferometer has been demonstrated here, the accuracy of the wavefront measurement is difficult to evaluate. Since the measurement quality must be assessed with certain assumptions about the operation and properties of the interferometer, the accuracy may be affected by unknown systematic errors. On the other hand, the detection of known systematic effects can be useful in the estimation of accuracy.

One possibility in assessing the interferometer accuracy is a measurement of a known aberration. The aberration that can be intentionally introduced with ease is defocus. In testing the Schwarzschild optic, the defocus is added to the wavefront by the translation of the object pinhole along the propagation direction. This translation changes the position of the test-beam focus with respect the reference pinhole plane. The required realignment of the reference pinhole after each focal adjustment is a slight complication here. In principle, a change in the focus does not change the measured aberrations. Two different measurements at three different focal positions each reveal small changes in the measured wave-

front with defocus. The pairwise differences in the low-order aberrations for the 0.07-NA sub-aperture from single interferograms obtained using reference Pinhole 1 are shown in Figure 5-25(a) in units of 0.01 wave at 13.4-nm wavelength. The magnitudes of the balanced defocus are -0.169 , -0.057 , and 0.069 wave for measurements 1, 2, and 3, which represent two approximately equal steps in the defocus. Here, a positive change in the defocus corresponds to translation of the object pinhole toward the optic. The differences between the first two and the second two measurements are about half the difference between the first and the third measurements. Thus, the difference between the measured wavefronts seems to scale with the difference in their relative defocus. The mean differ-

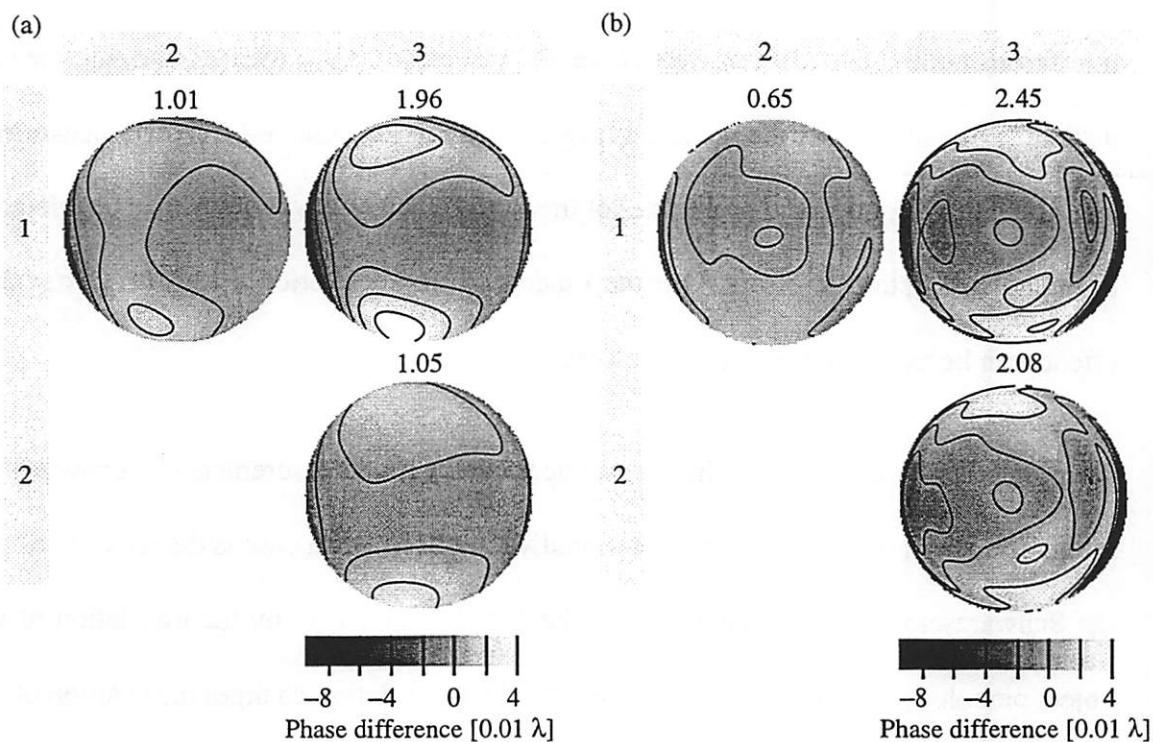


Figure 5-25. The change in the measured aberrations with defocus.

The differences in the wavefront phase measured at 13.4-nm wavelength at three different focal positions. All combinations of wavefront differences are shown for (a) the 0.07-NA sub-aperture and (b) the 0.06-NA sub-aperture. The rms phase differences are shown in units of 0.01 wave at above each difference map.

ence in the measured wavefronts is 0.013 wave rms. Another such measurement, performed with reference Pinhole 4 on the 0.06-NA sub-aperture in three phase-shifting experiments, is presented in Figure 5-25(b). Here the magnitudes of the balanced defocus are -0.151 , -0.041 , and 0.158 wave, respectively. The focal increment between measurements 3 and 2 is about twice the defocus change between measurements 2 and 1. Once again, the differences in the measured aberrations seem to scale with the difference in focus. Here the mean difference in the measured aberrations is 0.017 wave rms.

The magnitude of the defocus used in these measurements is only slightly larger than the classical depth of focus of $\pm\lambda/2NA^2$, which corresponds to 0.125 wave of balanced defocus and a 20% reduction in the peak intensity of a diffraction-limited beam [121, 111]. This degree of defocus is not expected to significantly influence the wavefront measurement, as estimated from Figure 2-4 in Chapter 2 and the normalized size of the reference pinholes. The differences found can be attributed to errors in the reference wavefront, produced mainly by the alignment of the reference pinholes within the focused beam. Overall the reference wavefront error appears to be about 0.015 wave (0.20 nm) rms in a numerical aperture of 0.07.

Detection of the systematic coma effect in the wavefront can also be used to evaluate the measurement quality. As discussed in Chapter 2, the additive systematic coma results from the lateral displacement of the test and reference beam foci. The measured phase difference contains a systematic coma peaked in the direction of the focal displacement, which is perpendicular to lines of the grating beamsplitter. The comparison of two wavefronts obtained with different grating orientations can reveal information about the measurement quality.

To illustrate this, let us consider measurements using two different grating orientations, given by angles θ_1 and θ_2 . Assuming the same focal spot separation s in both cases, the measured phases W_1 and W_2 , in cycles or waves, are given by

$$(5-1) \quad W_1 = W_{T_1} - W_{R_1} + \frac{s}{\lambda} \left(NA\rho - \frac{1}{2}NA^3\rho^3 + \dots \right) \cos(\theta - \theta_1), \text{ and}$$

$$(5-2) \quad W_2 = W_{T_1} - W_{R_2} + \frac{s}{\lambda} \left(NA\rho - \frac{1}{2}NA^3\rho^3 + \dots \right) \cos(\theta - \theta_2),$$

where W_{T_1} and W_{T_2} are the test wavefronts, W_{R_1} and W_{R_2} are the reference wavefronts in the two measurements, and (ρ, θ) are the normalized beam coordinates ($|\rho| \leq 1$) over the radius of the beam with a numerical aperture NA. The phase difference $W_1 - W_2$ between the two measurements, given by

$$(5-3) \quad W_1 - W_2 = W_{T_1} - W_{T_2} + W_{R_2} - W_{R_1} + \frac{s}{\lambda} \left(NA\rho - \frac{1}{2}NA^3\rho^3 + \dots \right) 2 \sin\left(\frac{\theta_1 - \theta_2}{2}\right) \cos\left(\theta - \frac{\pi + \theta_1 + \theta_2}{2}\right),$$

consists of the difference in the two test wavefronts and the two reference wavefronts plus tilt and coma terms whose magnitude and orientation depend on the orientation of the grating beamsplitter in the two measurements. After the tilt term is removed, any deviations in the wavefront difference from the expected coma reveal changes in test wavefront and imperfections in the reference wavefronts. When the test wavefront properties are constant, this comparison can be used to understand the reference wave errors that are unique to each pinhole. Unfortunately, owing to the comparative nature of this test, deviations from sphericity that are common to both diffracted reference wavefronts are not revealed.

In the characterization of the Schwarzschild objective, two nearly orthogonal gratings were employed. Equation 5-3 indicates that when the gratings are orthogonal, or $\theta_1 = \pi/2$ and $\theta_2 = 0$, the difference in the measured wavefronts, in waves, is given by,

$$(5-4) \quad W_1 - W_2 = W_{T_1} - W_{T_2} + W_{R_2} - W_{R_1} + \sqrt{2} \frac{s}{\lambda} NA^3 \rho^3 \cos(\theta - 3\pi/4),$$

where the tilt is excluded and the small terms beyond the primary coma are neglected. For two perfect reference wavefronts and identical test wavefronts, the difference contains only the coma term, peaked at an angle of $3\pi/4$. Given a focal spot separation $s = 4.5 \mu\text{m}$ and a numerical aperture $NA = 0.07$ at a wavelength $\lambda = 13.4 \text{ nm}$, the magnitude of the unbalanced primary coma is 0.163 wave. This corresponds to 0.027 wave of balanced primary coma, described by Zernike polynomials 6 and 7. To assess the reference wavefront errors, a number of measurements performed with two grating orientations are compared in Figure 5-26. The measurement pairs shown were obtained on the 0.07-NA sub-aperture at 13.4-nm wavelength within several minutes of each other using adjacent reference pinholes to minimize the number of variables in the experiment. However, in addition to differences produced by the reference pinholes, each measurement is also influenced by the reference pinhole alignment and by the possible small nonuniformities in the two grating substrates. The differences of the measurement pairs in Figure 5-26(b) or reference Pinholes 1 and 2, and in Figure 5-26(c) for reference Pinholes 3 and 4, are compared to the expected ideal coma aberration in Figure 5-26(a). All wavefront differences are shown on the same scale. In Figure 5-26(b), obtained with Pinholes 1 and 2, the measured difference resembles the expected coma aberration, especially in the first and the third measurements.

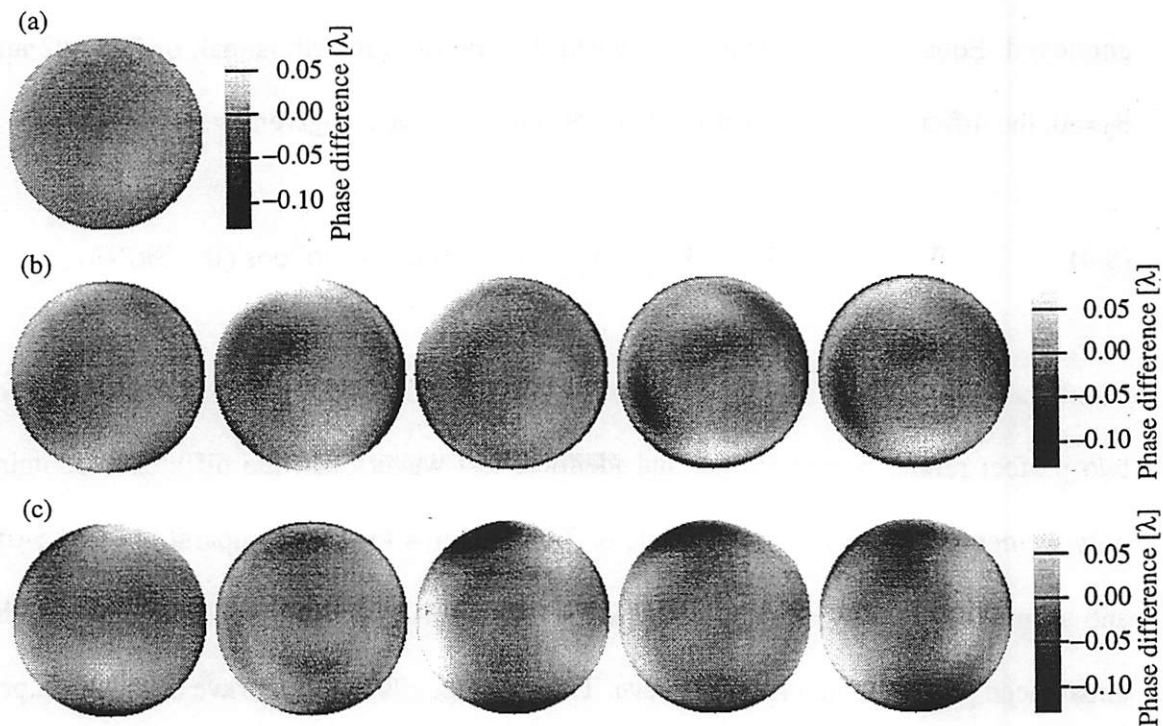


Figure 5-26. The systematic coma effect.

- (a) The expected phase difference between two measurements performed with two mutually orthogonal grating orientations. Examples of the measured phase differences for (b) image-plane Pinholes 1 and 2 and for (c) image-plane Pinholes 3 and 4.

In the five measurements, the deviation $W_{T_1} - W_{T_2} + W_{R_2} - W_{R_1}$ from the expected coma is 0.019 wave rms and 0.131 wave peak-to-valley on average. In Figure 5-26(c), obtained using Pinholes 3 and 4, the difference deviates from the expected coma more significantly. Here the departure $W_{T_1} - W_{T_2} + W_{R_2} - W_{R_1}$ from the expected coma is 0.024 wave rms and 0.157 wave peak-to-valley on average. This is consistent with the anticipated errors in the reference wavefront from Pinhole 3, known to be too large. From the repeatability measurements that include the variations from grating substrate nonuniformities, it may be concluded that the grating substrate effects on the test wavefront are small compared to the reference wave defects. Then, if the two reference wavefronts are independent, the imper-

fections in each of the wavefront is about $1/\sqrt{2}$ times the error in the detected reference wavefront difference. With this assumption and the premise that the error obtained with Pinholes 1 and 2 is representative of the overall measurement, the error in the reference wavefront is about $\pm 0.019/\sqrt{2} = \pm 0.013$ wave (± 0.18 nm) rms. However, this represents only the random component in the reference wavefront imperfections because the difference in two wavefronts does not reveal correlated errors.

Owing to the relatively large size of the reference pinholes, the reference wavefront imperfections probably dominate errors in this extreme ultraviolet phase-shifting point diffraction interferometer. However, the accuracy of the interferometer is also influenced by error contributions from the illumination wavefront, the grating substrate nonuniformities, the pinhole alignment, the detector properties, and data analysis errors. Some of these effects have been investigated here while others are considered elsewhere [142]. The variations in the reference wavefront, evaluated by changing focus, by detecting the systematic coma, and by investigating the alignment sensitivity, appear to be about ± 0.015 wave (± 0.20 nm) rms in a numerical aperture of 0.07.

5.7. Conclusions

The aberrations of a 10 \times -demagnification Schwarzschild optic, designed for EUV lithography experiments, have been characterized with a phase-shifting point diffraction interferometer at a wavelength of 13.4 nm. Measurements of several sub-regions of the annular aperture indicate the presence of zonal fabrication errors. The 0.07-NA sub-aperture has been found to have relatively small aberrations of 0.090 wave (1.21 nm) rms at 13.4-nm

wavelength that are dominated by astigmatism. The measurements of the Schwarzschild optic have also served to evaluate the performance of the PS/PDI design and implementation. The measurement repeatability is ± 0.008 wave (± 0.11 nm) rms. The accuracy of the measurement is probably limited by errors in the reference wavefront, caused by somewhat oversized reference pinholes and estimated to be roughly ± 0.015 wave (± 0.20 nm) rms in a numerical aperture of 0.07.

6 Characterization of Chromatic Effects Due to Multilayer Coatings

6.1. Introduction

One primary advantage of at-wavelength interferometry is its ability to characterize the overall extreme ultraviolet (EUV) wavefront produced by both the mirror surface figure and by the multilayer coatings. Owing to the fact that, upon a change in wavelength, the aberrations due to multilayers change whereas those due to surface errors do not, multilayer effects can be observed directly via wavefront measurements over a range of wavelengths.

In this chapter, a demonstration of chromatic aberrations in the 10× Schwarzschild objective due to the molybdenum/silicon multilayer reflective coatings is presented. The measurements of the wavelength-dependent transmission and phase are compared to transmission and phase calculations based on the multilayer design and on previous measurements of the multilayer period [32]. Some of the possible causes for the discrepancies found are explored.

6.2. Wavelength-Dependent Transmission and Phase

In the characterization of the two-mirror 10× Schwarzschild optic, both the transmitted intensity and the wavefront phase were measured at several EUV wavelengths within the

passband of the multilayer coatings peaked near 13.4-nm wavelength. The transmission through the 0.07-numerical aperture (NA) sub-aperture of the optic at 13.0, 13.2, 13.4 and 13.6 nm is shown in Figure 6-1(a). The transmission through different portions of the aperture reveals a zonal effect that follows the annular full aperture of the optic, described in Chapter 5. Within the coating passband, at 13.2 and 13.4 nm, the transmission is quite uni-

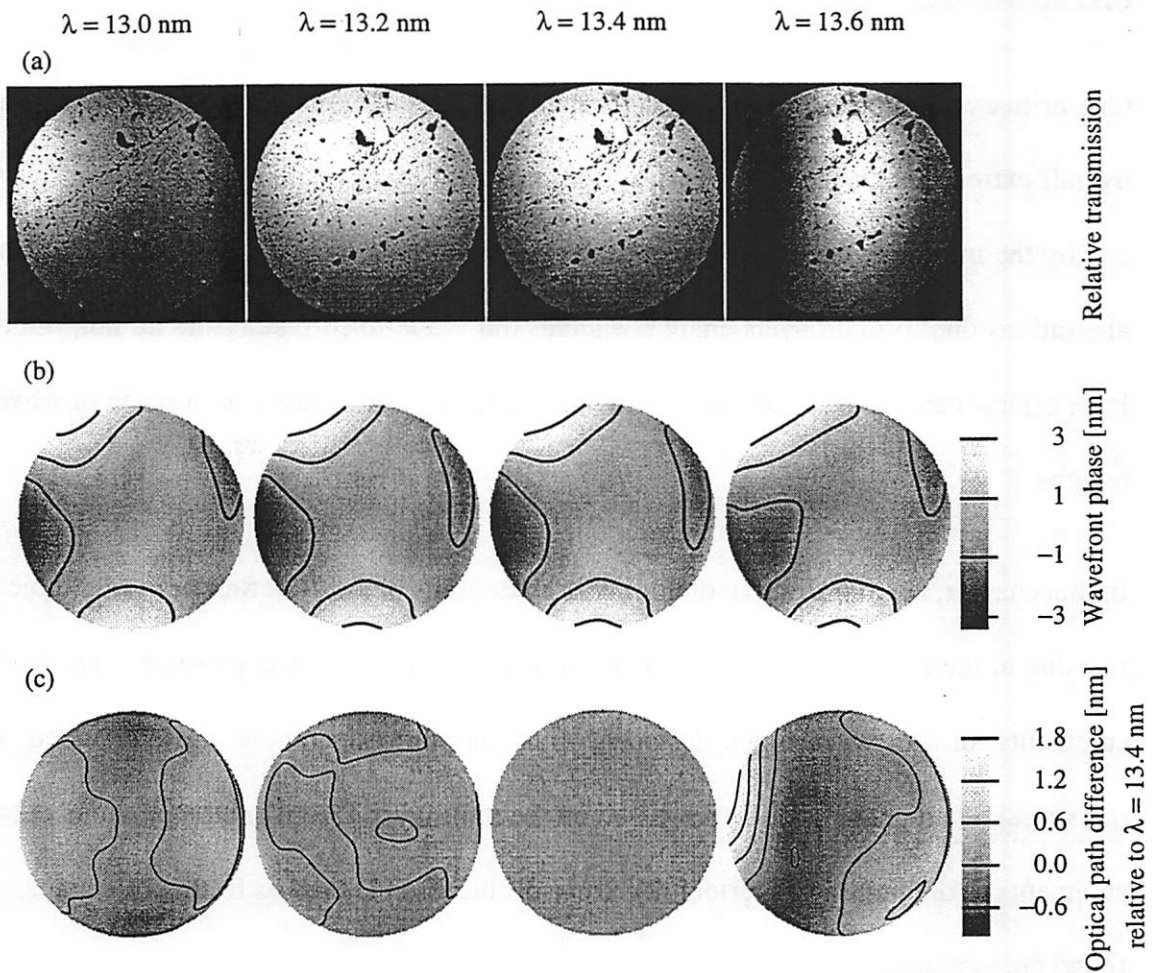


Figure 6-1. Measured transmission and phase vs. wavelength.

Measured chromatic effects produced by multilayer reflective coatings. As the wavelength is changed, (a) the transmission through the optic and (b) the wavefront phase varies. The transmission peak is near 13.4-nm wavelength. (c) The measured differences between the aberrations at the indicated wavelengths and the 13.4-nm wavelength demonstrate the presence of multilayer coating phase aberrations.

form, being lower only near the edges of the annulus. The measured transmission along the center of the annulus is peaked at 13.37-nm wavelength, nearly in agreement with the coating design [32], but the transmission peak is shifted to 13.30 nm on the inner edge of the annulus and to 13.36 nm on outer edge of the sub-aperture. This indicates that the multilayer coating period deviates from its intended value, designed to achieve transmission uniformity better than 99% at 13.4 nm. At the edges of the coating reflectance passband, at 13.0 nm and 13.6 nm, the transmission is very nonuniform. This behavior is not unexpected, even for perfect multilayers, because the coatings are designed to accommodate a range of incidence angles in a limited spectral band. Outside the design passband, the differences in incidence angles across the optic are amplified because the coating properties vary rapidly outside the central transmission lobe.

The phase of the wavefront transmitted through the 0.07-NA sub-aperture of the optic at 13.0, 13.2, 13.4 and 13.6 nm is displayed in Figure 6-1(b). The phase maps, found from phase-shifting analysis of several data series, exclude the piston, tilt, and systematic coma terms but contain the defocus that contributes to the chromatic aberrations. The chromatic phase effects resulting from reflection by the two multilayer mirrors are illustrated in Figure 6-1(c), which shows the difference between the aberrations measured at 13.0, 13.2, 13.4 and 13.6 nm and the aberrations measured at 13.4 nm. Within the coating passband, the differences in the measured wavefronts are small because the wavelength change results primarily in a constant phase offset, not measurable by interferometry. At the passband edges, where nonuniformities in the coating properties are accentuated, the measured phase difference over the aperture is consistent with a radial imperfection in the multilayer coating thickness.

The rms difference between the wavefront measured at different wavelengths and the aberrations at 13.4 nm is given in Figure 6-2(a). This aberration difference, which includes changes in the focus with wavelength, illustrates the magnitude of the chromatic aberrations in the Schwarzschild objective. The wavelength-dependent change in the tilt term produced by the optic, which is not detected by interferometry but can in principle cause chromatic image distortion, is not expected to significantly increase the chromatic aberrations. Based on calculations that utilize the measured period of the multilayer coatings [32], the change in the tilt relative to 13.4-nm wavelength is quite small over the wavelength range measured. The measured chromatic aberrations with the calculated wavelength-dependent tilt term added are also given in Figure 6-2(a). The relative transmission of different radiation wavelengths through the 0.07-NA sub-aperture of the Schwarzschild optic is plotted in Figure 6-2(b). The largest measured wavefront change of about 0.44 nm rms, equivalent to 0.033 wave at 13.4 nm wavelength, appears at a wavelength near 13.6 nm, where the transmission through the optic is reduced by an order of magnitude relative to the peak. The chromatic distortion increases the aberration difference somewhat, but only outside the main transmission lobe. As a result, the chromatic aberrations are not expected to appreciably degrade the image quality for this Schwarzschild optic.

In EUV lithographic optical systems, the fraction of the optical power near the edges of the transmission passband is likely to be quite small, especially when multilayer-coated condenser optics are employed. Although the chromatic aberrations are determined by the optical design and by the properties of the deposited coatings, their effect on the image quality may be negligible, provided that most of the optical power resides within the transmission passband of the imaging system.

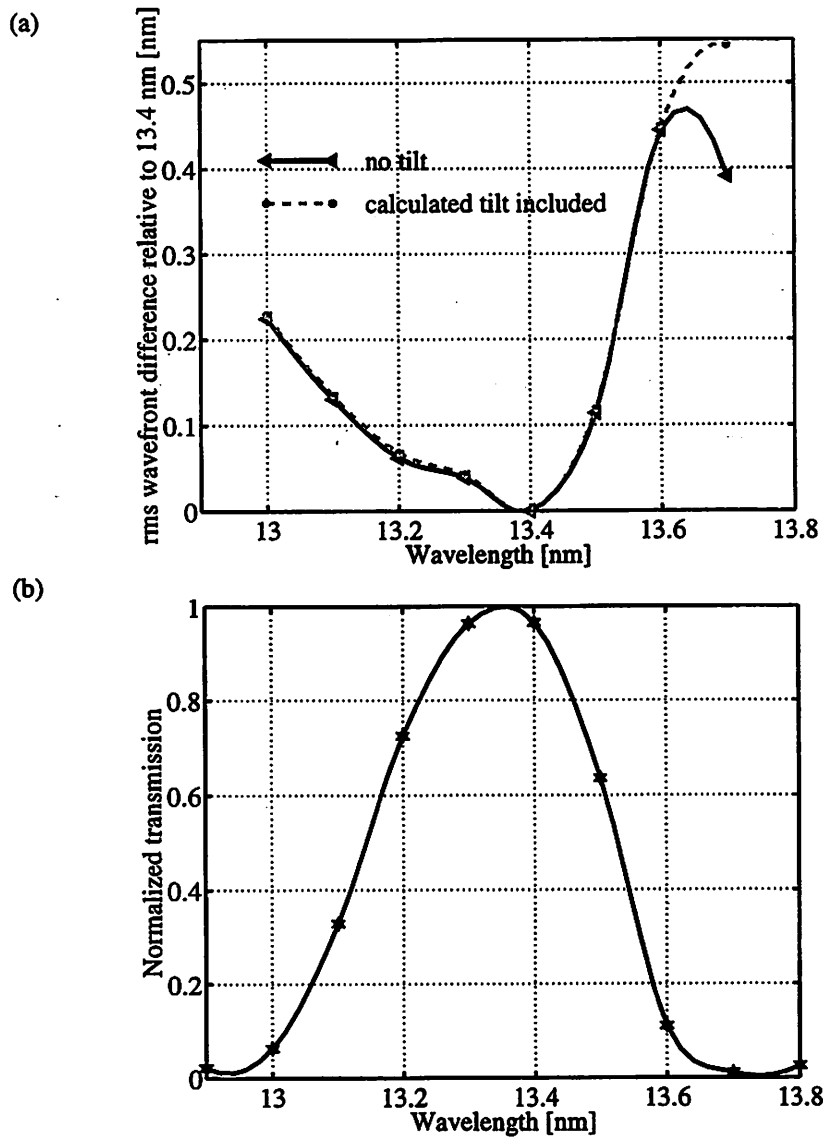


Figure 6-2. Chromatic aberrations and transmission vs. wavelength.

(a) The chromatic aberrations of the 0.07-NA sub-aperture of the Schwarzschild optic are revealed in the measured rms difference between the wavefronts at different wavelengths and the wavefront at 13.4 nm. (b) Overall normalized transmission through the 0.07-NA sub-aperture measured as a function of wavelength.

6.3. Understanding the Measured Coating Properties

The chromatic transmission and phase effects can be used to evaluate the properties of the molybdenum/silicon (Mo/Si) multilayer coatings on the two Schwarzschild mirrors. In this

section, the measured wavelength dependence is compared with the changes in the transmission and the phase calculated from the designed and the previously measured properties of the multilayer coatings. The Mo/Si coatings consist of 40 bilayers with molybdenum-to-silicon thickness ratio of about 0.375. The designed multilayer coating period as well as the multilayer period measured on the two mirror substrates [32, 170] is given in Table 6-1 as a function of the radial position on each mirror substrate. On the primary mirror, the multilayer coatings are graded in thickness and the 0.08-NA aperture stop selects the radial

Radial substrate position [mm]	Multilayer period [nm]	
	Design (maximum, minimum)	Measurement
primary mirror		
3.3	6.875 (6.944, 6.806)	6.8125
3.8		6.8625
4.3		6.9000
4.8		6.9500
5.3	6.925 (6.995, 6.856)	6.9750
5.8		6.9875
6.3		7.0125
6.8	7.035 (7.106, 6.964)	7.0250
7.3		
secondary mirror		
16.0	6.847 (6.916, 6.779)	6.8625
20.0		6.8750
24.0		6.8750
28.0	6.862 (6.930, 6.793)	6.8875
32.0		6.8750
36.0	6.876 (6.945, 6.807)	6.8750
40.0		6.8625

Table 6-1. Multilayer coating design and measurement for the Schwarzschild objective.

The period of multilayer coatings for the primary and secondary mirrors of the 10× Schwarzschild objective vs. the radial position on the mirror substrate from Reference 32. The design tolerances are about ± 0.07 nm, while the reported measurement uncertainty is ± 0.0125 nm. The coatings have 40 bilayers with molybdenum-to-silicon thickness ratio of $\Gamma = 0.375$.

positions of 3.3 to 7.3 mm in the annular aperture. On the secondary mirror with nearly uniform multilayer period, the annular clear aperture ranges from 16.5 to 41 mm in radius. In the reported coating measurement, the multilayer period is determined from measured reflectance versus wavelength data by fitting the measured curves to a model, where the multilayer period is an adjustable parameter [32]. As reported in Reference 32, the period of the deposited multilayer coatings, determined with an experimental uncertainty of ± 0.0125 nm, is within the ± 0.07 nm design tolerance. Refractive indices of coating materials are determined from tabulated optical properties at x-ray wavelengths [13], using specific densities of 10.22 for molybdenum and 2.33 for silicon.

In addition to the coating properties, the calculation of the multilayer effects in the optical system also utilizes the optical design for the Schwarzschild optic, presented in Table 5-1 on page 101. In consideration of multilayer properties, the mirror surface figure errors are neglected because they do not significantly alter the position and orientation of the mirror surface. Unless indicated otherwise, the illumination of the optic from a field point on the optical axis is also assumed. Although the multilayer effects depend on the polarization, only the transverse-electric (TE) polarization need be considered here because the beam in the interferometer experiment is initially TE-polarized and only 0.03% of the total reflected light is coupled into the transverse-magnetic (TM) polarization in propagation through the system [171]. The multilayer calculations utilize two different calculation methods, the transmission line analogy to electro-magnetic wave propagation in materials with multiple boundaries [172] and the successive application of the Fresnel equations [173-175]. The latter method includes the effects of layer interface imperfections.

6.3.1. Transmission Properties of the Schwarzschild Optic

The variations in the transmission properties within the 0.07-NA sub-aperture are examined in Figure 6-3. The transmission measured in the course of the interferometry experiments is plotted as a function of wavelength in Figure 6-3(b) for five small regions of the sub-aperture that are indicated in Figure 6-3(a). The measured transmission is contrasted with the calculated transmission curves in Figure 6-3(c) and Figure 6-3(d), for the multilayer coating design and for the coating period from Reference 32, respectively. Both computations assume perfectly sharp layer boundaries in the multilayer and an ideal optical design with the object point at the center of the field of view.

As designed, the multilayer coatings exhibit excellent transmission uniformity. On the other hand, both measurements of the real coatings reveal transmission nonuniformities along the radial direction of the annular full aperture and near constant transmission only in the azimuthal direction. Relative to the center of the annulus, the transmission peak is shifted toward shorter wavelengths on both its edges. In regard to variations over the sub-aperture, the transmission measured here and that calculated using the reported multilayer period are in good qualitative agreement. In addition to a small offset in the peak wavelengths, the most apparent discrepancy between the two is the transmission bandwidth. The measured full-width half-maximum (FWHM) bandwidth is only about 70% of that found in the calculations. The transmission properties along the radial direction of the annulus are summarized in Figure 6-4 with plots of the transmission curve center (midpoint between the FWHM wavelengths) in Figure 6-4(a) and of the bandwidth in Figure 6-4(b). The radial coordinate corresponds to scaled radial positions within the 0.08-NA pupil with nor-

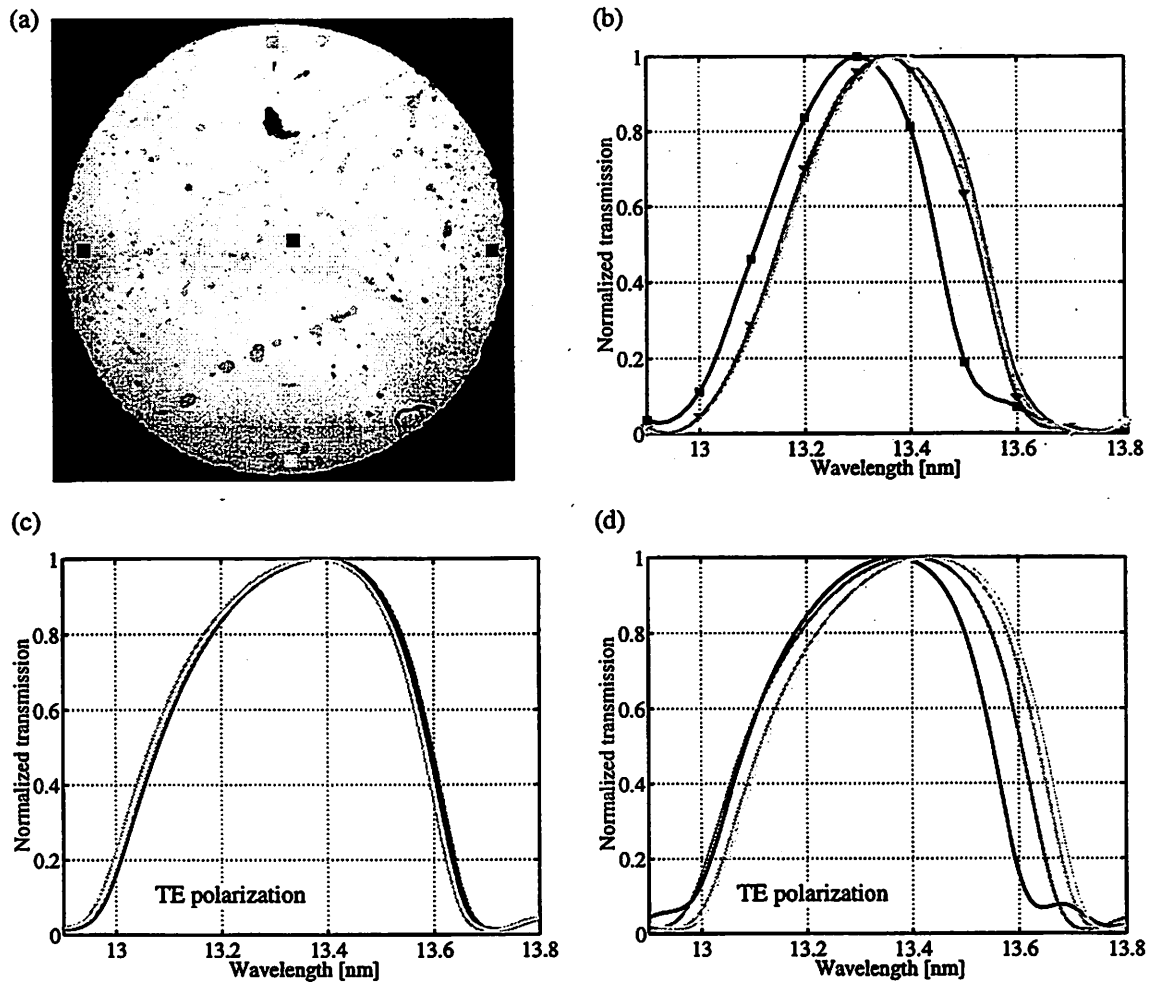


Figure 6-3. Transmission vs. wavelength in different portions of the aperture.

Transmission through the Schwarzschild optic vs. wavelength at (a) the indicated positions within the 0.07-NA sub-aperture. (b) Measured transmission curves are compared to (c) the calculation based on the coating design and (d) the calculation using the multilayer periods measured in Reference 32. Both calculations assume sharp multilayer interfaces.

normalized radius of 1. The results are given for the ideal multilayer design, for the calculation using the previously measured multilayer periods and perfectly sharp layer boundaries, and for two different parts of the annulus measured here. The measurements on regions A and C of the annulus, in proximity to the 0.07-NA and the 0.06-NA sub-apertures, demonstrate comparable properties in the azimuthal direction, as expected.

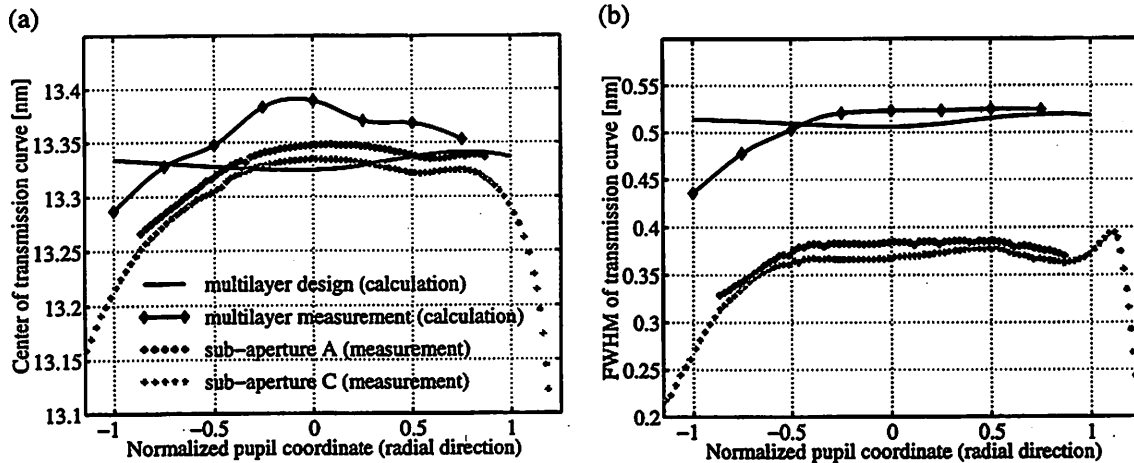


Figure 6-4. The center and the bandwidth of the multilayer transmission curves.

(a) The center and (b) the FWHM bandwidth of the transmission passband for the 10× Schwarzschild optic. Calculations, based on the multilayer design and on previously reported multilayer period measurements with the assumption of perfect multilayer interfaces and TE polarization, are compared to the measurements in two different portions of the annular aperture of the Schwarzschild optic.

6.3.2. Investigation of the Coating Characteristics

The discrepancy between the measurement and the measurement-based calculation of the coating bandwidth has numerous possible explanations in a complex multilayer system with several curved mirrors and graded-period multilayer coatings, possibly illuminated from several directions. The potential causes explored here include the illumination of the optic from different field points, the imperfections of multilayer interfaces, and the mismatch in the passbands of the two Schwarzschild mirrors.

As discussed in Chapter 5, the object plane of the Schwarzschild optic is not mechanically referenced to the optical housing. The positions in the field of view are selected by steering the beam through the center of the image plane defined by three balls on the optical housing. This method places the beam near the center of the intended field of view in the object

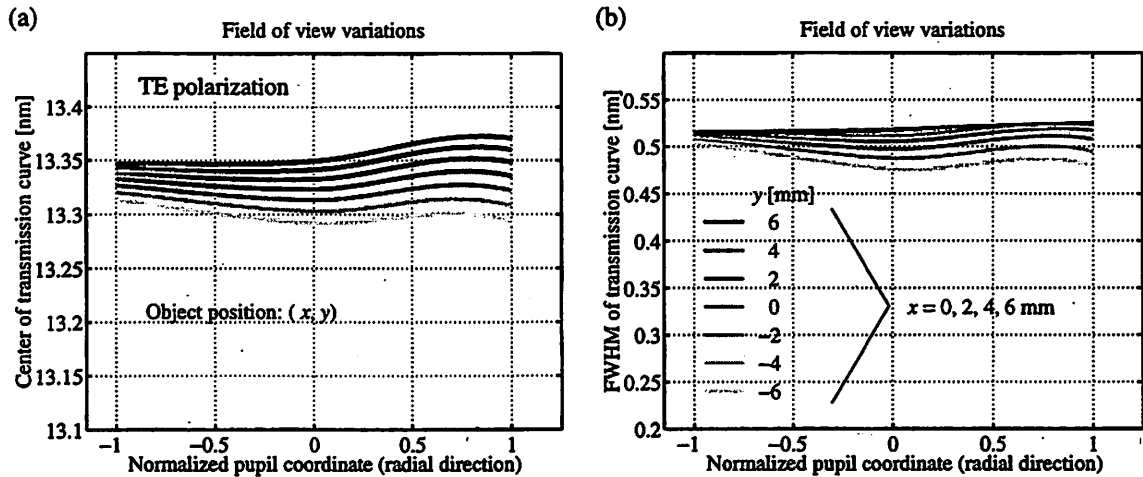


Figure 6-5. Field of view variations in the multilayer transmission curve.

The calculated field-of-view variations in the transmission characteristics along the radial direction of the annular aperture. The computations of (a) the center and (b) the FWHM bandwidth of the transmission passband assume perfect multilayer coatings and utilize the Schwarzschild optical design. The field dependence is given over $12 \times 12 \text{ mm}^2$ object-side field of view, denoted by coordinates (x, y) , where y is the direction of pupil displacement from the optical axis. The corrected object-side field of view is $4 \times 4 \text{ mm}^2$.

plane. However, a displacement of the object pinhole from its desired position with respect to the optic changes the angles of incidence on the multilayers and can potentially affect the coating reflectance. The effect of the object position on the transmission through the optic is presented in Figure 6-5, which shows the transmission curve centers and the bandwidths calculated using the 40-bilayer coating design with perfectly sharp interfaces and a Mo/Si thickness ratio of 0.375. Comparable dependence of the coating properties over the field of view is expected in the presence of aberrations and imperfect multilayer boundaries because the field variations are produced solely by changes in the beam incidence angles. The transmission characteristics along the radial direction of the annular aperture are given over a field of view of $12 \times 12 \text{ mm}^2$, denoted by the object coordinates (x, y) . The transmission changes noticeably only upon translation of the object point in the y direction, along

which the pupil is displaced from the optic axis. Overall, the off-axis displacement of the object pinhole, estimated to be well within a $12 \times 12 \text{ mm}^2$ field in the experiment, do not account for the reduced bandwidth observed experimentally.

The imperfections due to interdiffusion and roughness at the layer boundaries are known to reduce the multilayer transmission bandwidth. The graded interfaces are typically modelled with an error function profile with a specified rms thickness σ that reduces the amplitude reflectivity at each interface by the Debye-Waller factor [21, 174, 176], exponentially decreasing with σ^2 . The impact of graded multilayer interfaces in the Schwarzschild optic on the transmission passband is examined in Figure 6-6 for rms boundary thicknesses up to 1.2 nm. The transmission curve center in Figure 6-6(a) and the FWHM bandwidth in Figure 6-6(b), shown along the radial direction of the annulus, are calculated for 40 Mo/Si layer pairs with thicknesses reported in Reference 32. In addition to a small shift of the

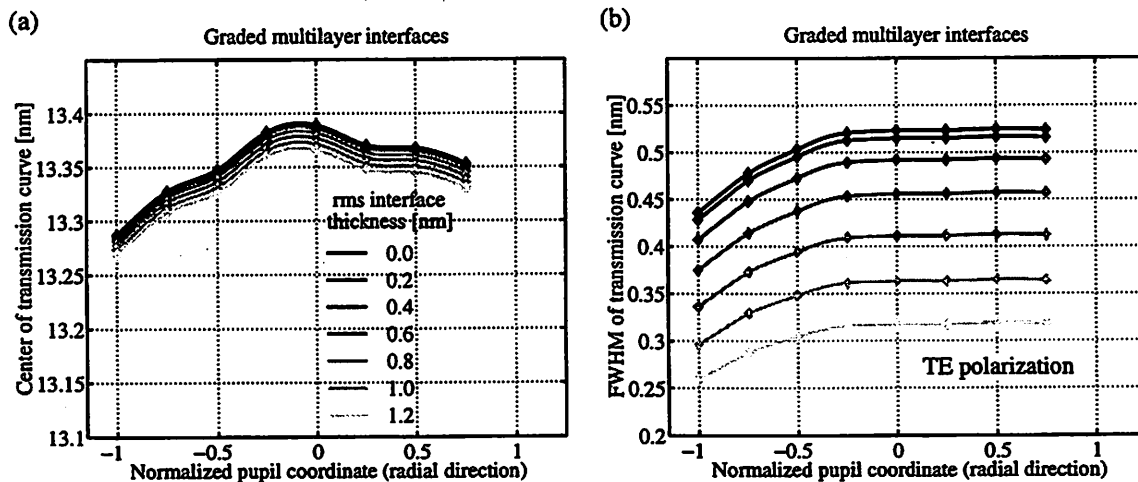


Figure 6-6. Effect of graded multilayer interfaces on transmission.

The calculated transmission properties vs. radial position in the annular aperture of the $10\times$ Schwarzschild system for varying rms thickness of the multilayer interfaces. The substrates are assumed to be coated with 40 Mo/Si bilayers with the period measured in Reference 32 and Mo/Si thickness ratio of 0.375.

passband toward shorter wavelengths, an increase in the rms interface thickness reduces the coating bandwidth. A layer interface thickness of about 0.95 nm rms, considerably larger than the thickness values of about 0.7 nm found in coatings similar to those on the Schwarzschild substrates [26, 170], matches the bandwidth reduction observed experimentally.

A mismatch in the transmission passbands of the two separate mirrors in the Schwarzschild objective can also decrease the overall multilayer bandwidth. The simple model of the coating mismatch, given by a constant offset in the multilayer period on each mirror, is investigated in Figure 6-7, under the assumption of sharp layer interfaces. The multilayer periods of the 40-bilayer coating are assumed to be shifted as indicated from the values reported in Reference 32. The transmission curve properties along the radial direction of the annular aperture are illustrated for two cases that exhibit good agreement with the mea-

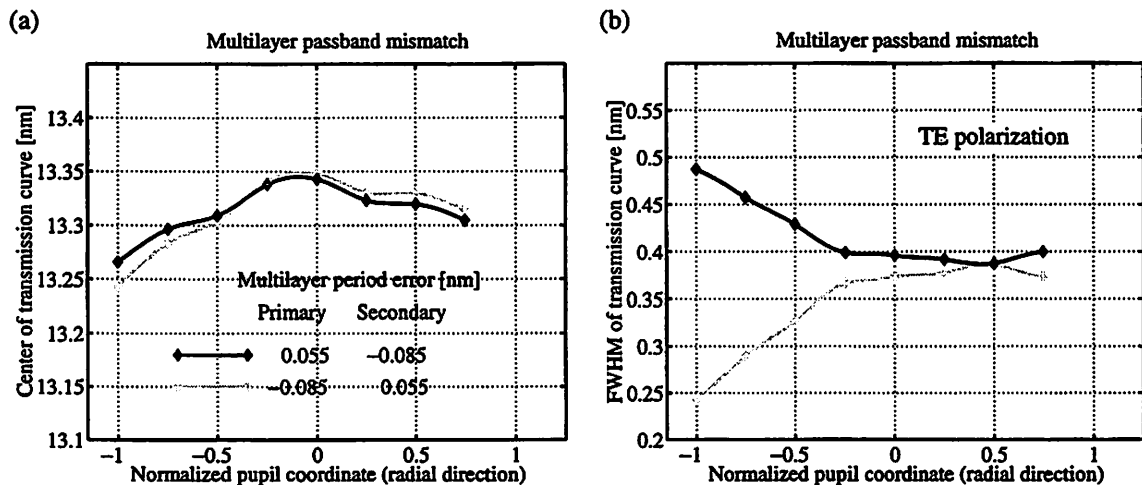


Figure 6-7. Effect multilayer passband mismatch on transmission.

The calculated passband (a) center and (b) width along the radial direction of the annular aperture of the 10× Schwarzschild objective. Multilayer periods are offset from those reported in Reference 32 by the indicated constants.

sured center wavelength of about 13.35 nm (see Figure 6-7(a) and Figure 6-4(a)). In both cases, the multilayer period is offset by 0.055 nm on one mirror and by -0.085 nm on the other mirror. When the multilayer period on the secondary mirror is increased and that on the primary is decreased, rather than vice versa, the calculated bandwidth in Figure 6-7(b) is relatively consistent with the measured bandwidth in Figure 6-4(b). The ability to separate effects on the individual mirrors of the two-mirror combination allows further refinement of the multilayer coating model that fits the present experimental observations.

Both the finite interface thickness and the mismatch of passbands on the two mirrors are likely to contribute to the reduction in the coating bandwidth observed in the Schwarzschild objective. The layer interfacial thickness can be estimated from the reflectance properties of each coating. Although reflectance data are not available for the Schwarzschild mirror coatings, measurements of similar multilayers on flat substrates indicate reflectivities of 63-65% near normal incidence [170, 26]. Assuming that characteristics of the mul-

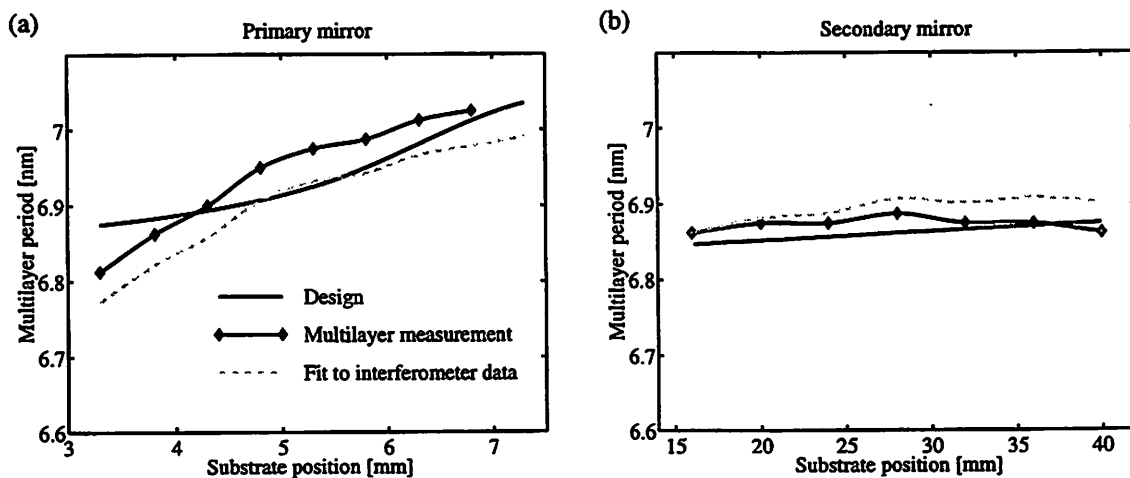


Figure 6-8. Multilayer coating period of Schwarzschild mirrors.

The period of multilayer reflective coatings on (a) the primary and (b) the secondary mirrors vs. the radial position on the substrate. The multilayer design, the measurement from Reference 32, and the model matching the interferometer data are compared.

tilayers deposited under similar conditions are representative of the Schwarzschild mirrors, the near-normal-incidence reflectances of 63-65% correspond to a rms interface thickness of roughly 0.7 nm. Given this interface thickness, the multilayer period offset from the reported values that is needed to match the present measurements consists of both a constant and a linear component, varying along the radius of each substrate. On the primary, the required offset is nearly constant and relatively small (about -0.045 nm). On the secondary, the period change needed increases along the substrate radius, reaching a maximum of about 0.04 nm. For both mirrors, the offset necessary to fit the data exceeds the estimated measurement uncertainty of ± 0.0125 nm [170]. The multilayer periods given by the fit to the interferometer data, by the previously reported measurements, and by the coating design are contrasted in Figure 6-8. The transmission characteristics measured on the Schwarzschild optic and those calculated with the present multilayer model, compared in Figure 6-9, closely coincide in both the center and the bandwidth of the transmission curve.

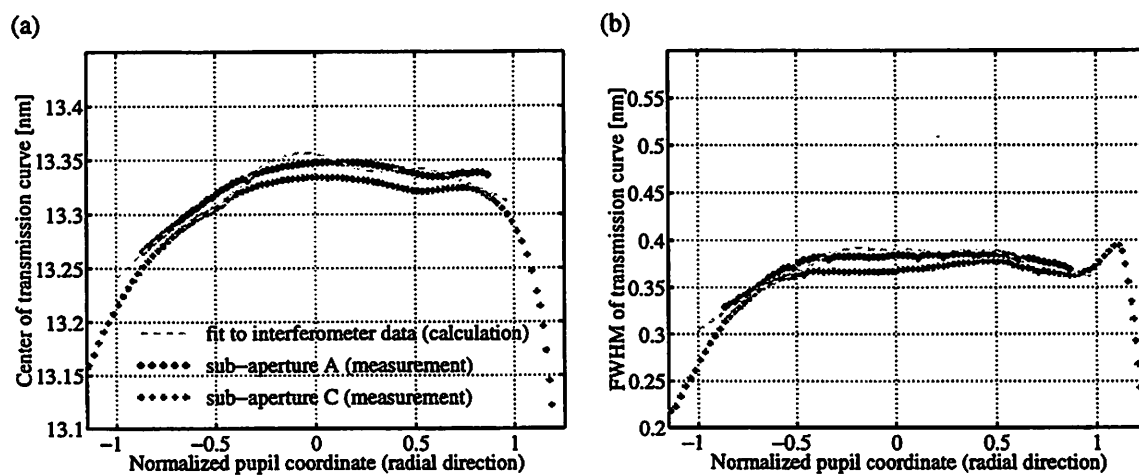


Figure 6-9. Multilayer model to explain transmission data.

The measured transmission properties in two different portions of the annular aperture of the 10 \times Schwarzschild optic are in good agreement with transmission calculations using the multilayer period model in Figure 6-8 and layer interfacial thickness of 0.7 nm.

The measured and calculated transmission characteristics over the aperture of the optic are compared in Figure 6-10 for wavelengths ranging from 12.9 nm to 13.7 nm. The two measurements, shown in Figure 6-10(a) and (b), correspond to the transmission in a 0.08-NA sub-region of the annulus near the sub-aperture C and in the 0.07-NA sub-aperture A, respectively. The calculation over a numerical aperture of 0.08 in Figure 6-10(c), which represents the coating model, assumes multilayer coatings with 40 bilayers, rms interfacial thickness of 0.7 nm, Mo/Si thickness ratio of 0.375, and coating periods given in Figure 6-8. Neglecting the nonuniformities in the illumination of the aperture in the experiment, the coating model shows good consistency with the measurements over the wavelength range considered.

The comparison between the measured and the calculated chromatic phase effects is presented in Figure 6-11 for a 0.07-NA sub-region of the annular aperture. The chromatic aberrations between adjacent wavelengths, separated by 0.1 nm in the range of 12.9 to 13.7 nm, reveal that the model for the coating properties produces good qualitative agreement with measurement not only in the transmission characteristics but also in the measured phase.

Owing to the strong influence of both the interfacial thickness and the multilayer mismatch on the overall coating characteristics, the simplified multilayer model described here represents only one of their possible interactions that fits the measured data. In addition, other potentially significant effects, such as the optical properties of molybdenum and silicon, have not been considered here. However, the small discrepancies found between the measurements on the assembled system and those on the individual mirror substrates demon-

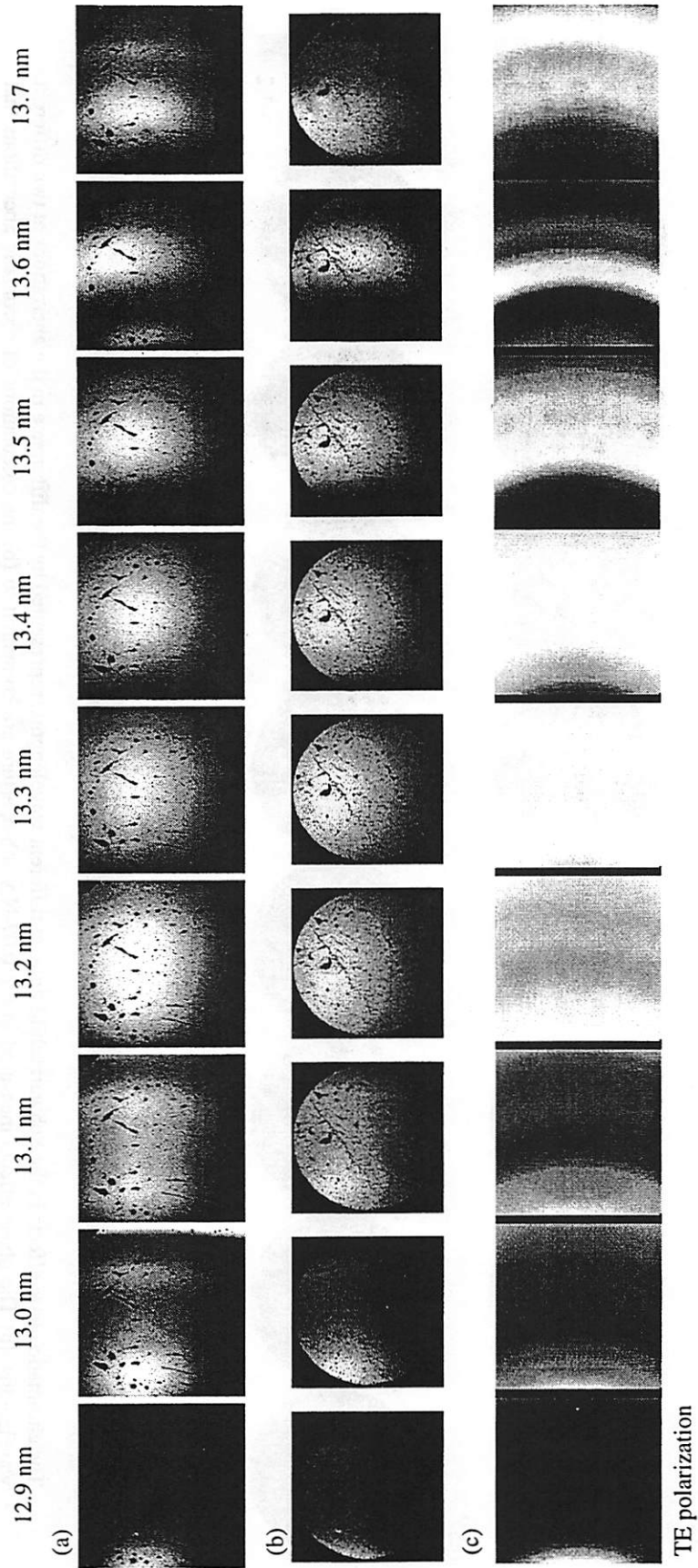


Figure 6-10. Measured and calculated transmission through the Schwarzschild optic.

The transmission through the Schwarzschild optic at different wavelengths. The transmission measured (a) in a 0.08-NA sub-region of the annulus near the sub-aperture C and (b) in the 0.07-NA sub-aperture A are compared to (c) the transmission calculations that assume coatings with 40 bilayers, rms interfacial thickness of 0.7 nm, Mo/Si thickness ratio of 0.375, and coating periods given in Figure 6-8.

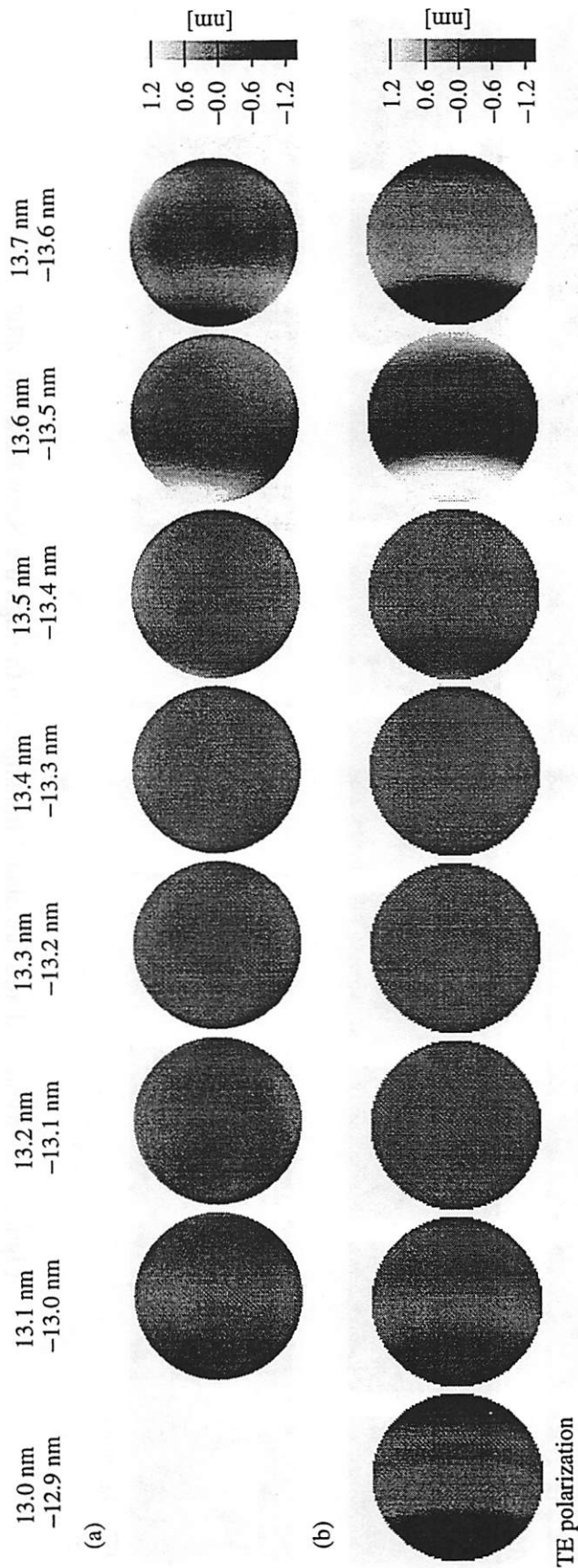


Figure 6-11. Measured and calculated chromatic aberrations in the Schwarzschild optic.

The chromatic phase effects in the Schwarzschild optic at different wavelengths, represented by the difference in the aberrations at two different wavelengths. (a) The phase effects measured in the 0.07-NA sub-aperture are compared to (b) the calculations of chromatic aberrations that assume coatings with 40 bilayers, rms interfacial thickness of 0.7 nm, Mo/Si thickness ratio of 0.375, and coating periods given in Figure 6-8.

strate the need for detailed characterization of the multilayers in EUV optical systems. Measurements of the transmission passband over the aperture of the assembled optical system appear quite valuable in assessing the multilayer coating properties as well as the chromatic effects in the optic.

6.4. Conclusions

The transmission uniformity and the wavefront aberrations in the 10× Schwarzschild objective have been evaluated at several EUV wavelengths near 13.4 nm. Although the presence of phase aberrations due to multilayer coatings has been directly observed, the measurements predict negligible influence of the chromatic aberrations on the image quality. A simple the multilayer model, which accounts for the multilayer period and the layer interface imperfections, produces good qualitative agreement both in the transmission and in the phase aberrations between the multilayer calculations and the experimental observations. The wavelength-dependent transmission and phase effects correspond to multilayer coating characteristics that are somewhat inconsistent with the properties previously measured on the individual coated mirror substrates.

7 Verification of Interferometry with Imaging Experiments

7.1. Overview

Perhaps the most significant value of interferometric wavefront measurements is their ability to predict the imaging performance of optical systems. The interferometry performed on the 10× Schwarzschild optical system indicates a wavefront aberration of 0.090 wave rms at 13.4-nm wavelength over a numerical aperture (NA) of 0.07, due mainly to astigmatism. Image calculations based on the interferometry measurements predict near diffraction-limited imaging performance. The image quality was verified with photoresist exposure experiments performed on the 10×I extreme ultraviolet (EUV) imaging system [40] at Sandia National Laboratories in Livermore, California. The image calculations and the printing experiments, whose similarities provide an independent qualitative verification of the interferometry, are discussed in this chapter.

7.2. Imaging Experiments on an EUV Exposure Tool

The exposure experiment to validate the image quality predicted from the EUV interferometry measurements were performed on the EUV lithography prototype exposure system at Sandia National Laboratories [40, 160]. The Sandia exposure tool utilizes imaging optics identical in optical design, multilayer properties, and housing construction to the

10× Schwarzschild system characterized here. In this tool, shown schematically in Figure 7-1, EUV light from a laser-produced plasma is collected by an ellipsoidal condenser and directed via a 45° turning mirror onto a reflective mask/object at near-normal incidence. The mask illumination is of Köhler type [127], with partial coherence factor of approximately 0.5. The image of the mask pattern, produced with the 10× Schwarzschild optic, is recorded on a photoresist-coated wafer.

The mask images were recorded in the chemically amplified, high-contrast, negative-tone SAL 601 photoresist [65, 177]. The processing of the 100-nm-thick photoresist starts with a 1-minute prebake at 85° C prior to exposure. Following the EUV exposure, the resist is baked at 110° C for 2 minutes and subsequently developed in Microposit MF-322 developer for 8 minutes. A low-resolution scanning electron microscopy (SEM) image of the recorded bright-field mask pattern, presented in Figure 7-2, shows an exposed area of

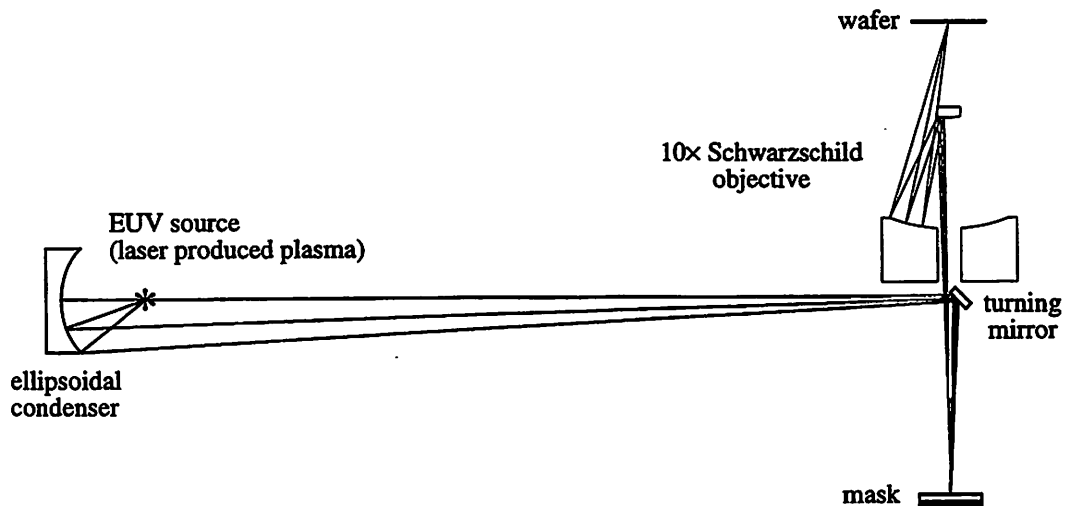


Figure 7-1. Schematic of Sandia 10xI EUV exposure system.

Components of the Sandia 10xI prototype exposure tool for lithography experiments at 13.4-nm wavelength.

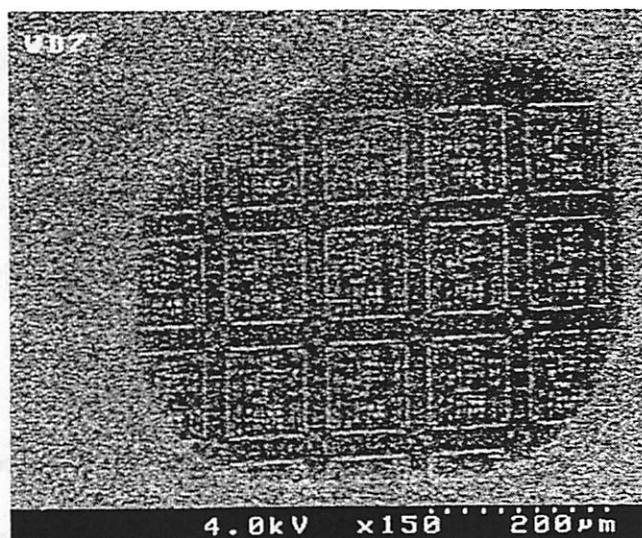


Figure 7-2. Exposure field of the 10× Schwarzschild optic.

An SEM image of the photoresist features printed by the 10× Schwarzschild optic on the Sandia exposure tool. The size of the exposed area is about $500 \times 350 \mu\text{m}^2$.

about $500 \times 350 \mu\text{m}^2$, which approximately corresponds to the 400- μm -diameter corrected field of view.

7.3. Image Calculations Based on Interferometry Measurements

To evaluate the image quality for the Schwarzschild objective, the interferometry data for the 0.07-NA sub-aperture were used to determine the expected image intensities for several test patterns. The images were calculated using the program SPLAT [178], which simulates image formation with partially coherent radiation. The calculations, designed to match the operational conditions of the exposure experiments, were done for a numerical aperture of 0.07, an exposure wavelength of 13.4 nm, an illumination partial coherence factor σ of 0.5, and the measured aberrations of the Schwarzschild optic. The test patterns

considered include a star resolution pattern, suited to reveal the astigmatism detected in the Schwarzschild optic, as well as dense patterns of lines and spaces oriented in two orthogonal directions.

7.4. Comparison of Calculated and Measured Image Quality

Imaging of test patterns that reveal the presence of specific aberrations, recorded at multiple focal positions, can be used to assess the aberrations in an optical system. The small amount of astigmatism measured in the Schwarzschild objective can be detected by printing of a star resolution pattern with varying degrees of defocus. The image intensities of the star test pattern calculated from interferometry wavefront data are compared to the printed photoresist features at several focal positions in Figure 7-3. The defocus ranges from $-4\ \mu\text{m}$ to $4\ \mu\text{m}$, increasing with the separation of the image plane and the optic, and spans several classical focal depths of $\pm 1.37\ \mu\text{m}$ at 13.4-nm wavelength and 0.07 numerical aperture. The image coordinates (x, y) correspond to the positions on the patterned wafer, where y is the direction of the pupil displacement from the optic axis.

The calculated intensity of the bright-field image through focus is given in Figure 7-3(a). Owing to the near diffraction-limited wavefront quality, the imaging is quite good in all directions at best focus. As is expected of an optic having astigmatism as the dominant aberration, somewhat out of focus, the resolution of the optic improves in one direction but degrades in the orthogonal direction. On the other side of focus, the behavior is similar but with the two directions reversed. In the Schwarzschild optic, the peak magnitudes of the astigmatism are found at -11.4° from the x and y axes. Figure 7-3(b) shows the contours

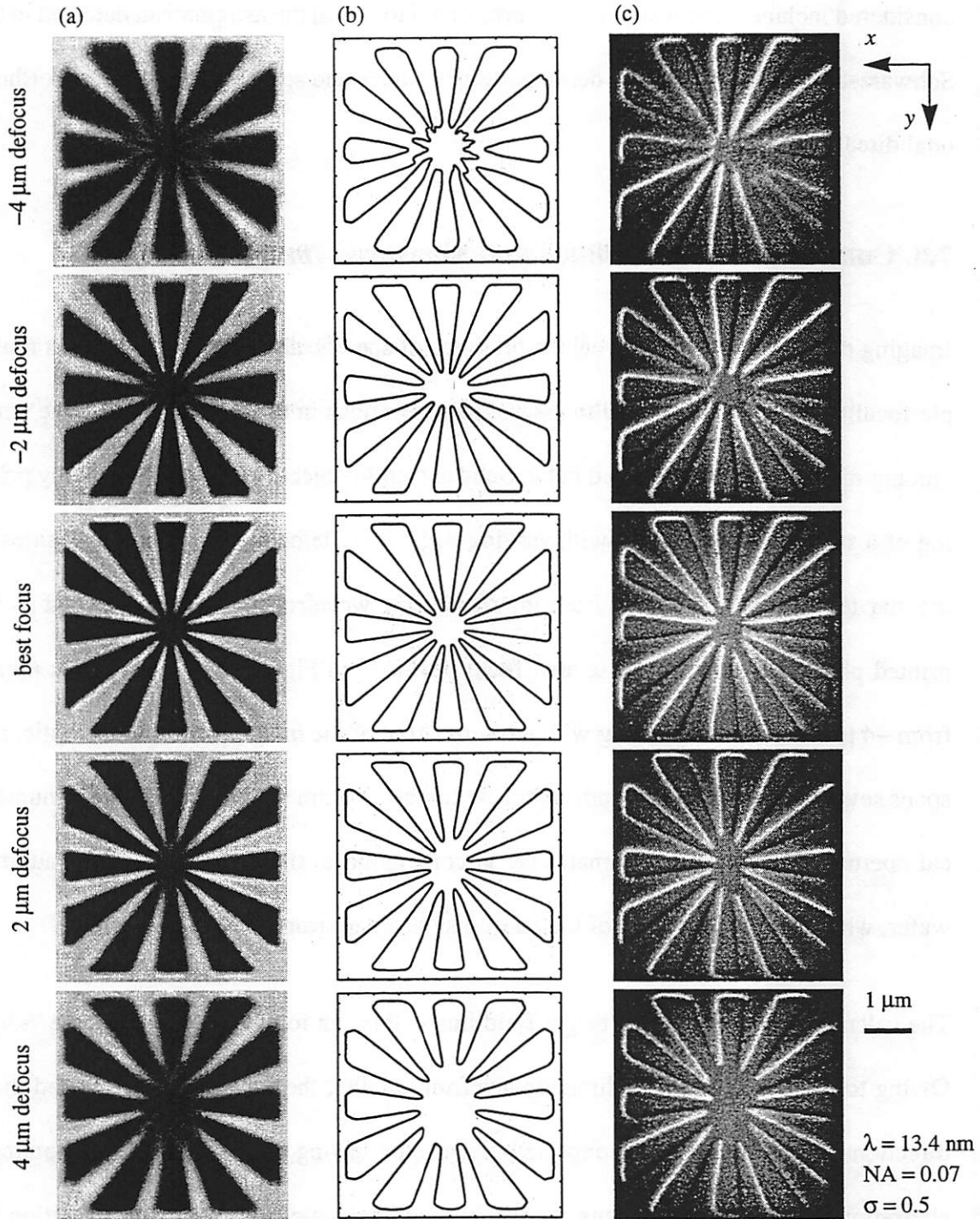


Figure 7-3. Calculated and printed star resolution patterns.

(a) Image intensities at several focal positions of a bright-field star resolution pattern calculated from the measured aberrations of the Schwarzschild optic. (b) Contours of the calculated intensities at different threshold levels for each focal position model the photoresist behavior and variations in the exposure dose. (c) SEM images of the same test pattern recorded experimentally in SAL 601 photoresist show excellent agreement with the calculated predictions.

of the calculated images that can be used to model the photoresist behavior. For a high-contrast photoresist such as SAL 601, the image intensity contours can be taken to represent the position of the photoresist edge in the developed pattern. In Figure 7-3(b) the threshold levels vary as a function of focus to simulate the changes in the exposure dose in the imaging experiment. In a negative-tone photoresist, with solid features in the exposed regions, lower threshold levels correspond to larger doses. Specifically, the normalized intensity contours for defocus of -4 , -2 , 0 , 2 , and $4 \mu\text{m}$ are 0.39 , 0.43 , 0.47 , 0.51 , and 0.55 , respectively. The SEM photographs of the developed photoresist features of the star resolution pattern printed with the Schwarzschild objective are presented in Figure 7-3(c). In SEM imaging of the thin resist layer, the contrast is enhanced by coating the surface with 5 nm of gold and by slightly tilting the sample relative to the electron beam. In terms of the direction and the magnitude of the astigmatic behavior through focus, the printed photoresist images exhibit excellent agreement with the predictions of imaging performance in Figure 7-3(a) and (c).

Printing of line and space features with dimensions near the resolution limit can also be used to assess the image quality. The results of SPLAT calculations for equal line/space patterns using the measured aberrations of the $10\times$ Schwarzschild optic are shown in Figure 7-4. Only the degradation from the measured low-order aberrations is included. For line/space dimensions of 0.075 , 0.1 , 0.15 , and $0.2 \mu\text{m}$, the figure compares the diffraction-limited performance at 13.4 nm and 0.07 NA to the capabilities of the Schwarzschild optic for both x and y feature orientations in terms of image contrast (see Equation 2-1 on page 36). The peak contrast is quite high for features greater than or near the resolution limit, which is $0.12 \mu\text{m}$ as given by the $0.61 \lambda/\text{NA}$ Rayleigh criterion [111], but degrades below

the resolution limit. Each oscillation in the contrast with defocus corresponds to image contrast reversal [121]. Neglecting the scattering from mirror roughness, the peak image contrast produced by the relatively unaberrated Schwarzschild optic is only slightly reduced from the diffraction-limited value. However, the best contrast of the line/space patterns along the x and the y directions occurs at different focal positions, separated by

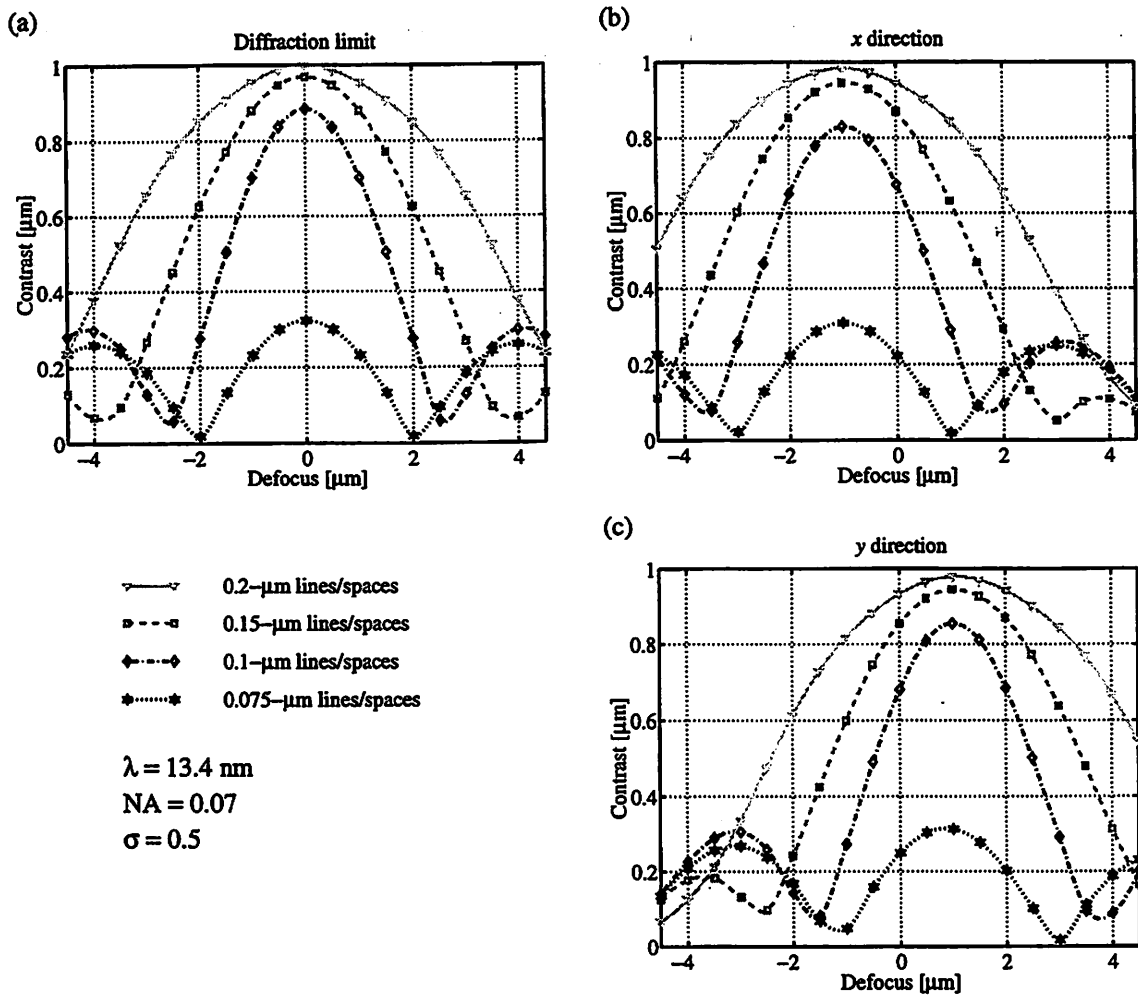


Figure 7-4. Calculated contrast of line/space patterns.

Calculated contrast of equal line/space patterns as a function of defocus, for features 0.075, 0.1, 0.15, and 0.2 μm in size. (a) The diffraction limit is compared to (b)-(c) the performance of the 10 \times Schwarzschild optic predicted from interferometry measurements. Due to the astigmatism in the optic, the best image contrast for line/space features along (b) the x direction and (c) the y direction is produced at different focal positions.

about 2 μm along the optic axis. This is representative of the astigmatism measured in the Schwarzschild optic, whose orientation of -11.4° is approximately aligned with the x and y directions of the imaging system.

At the overall best focus, the contrast of the line/space images formed by the Schwarzschild optic is expected to be approximately independent of the line orientation. The pat-

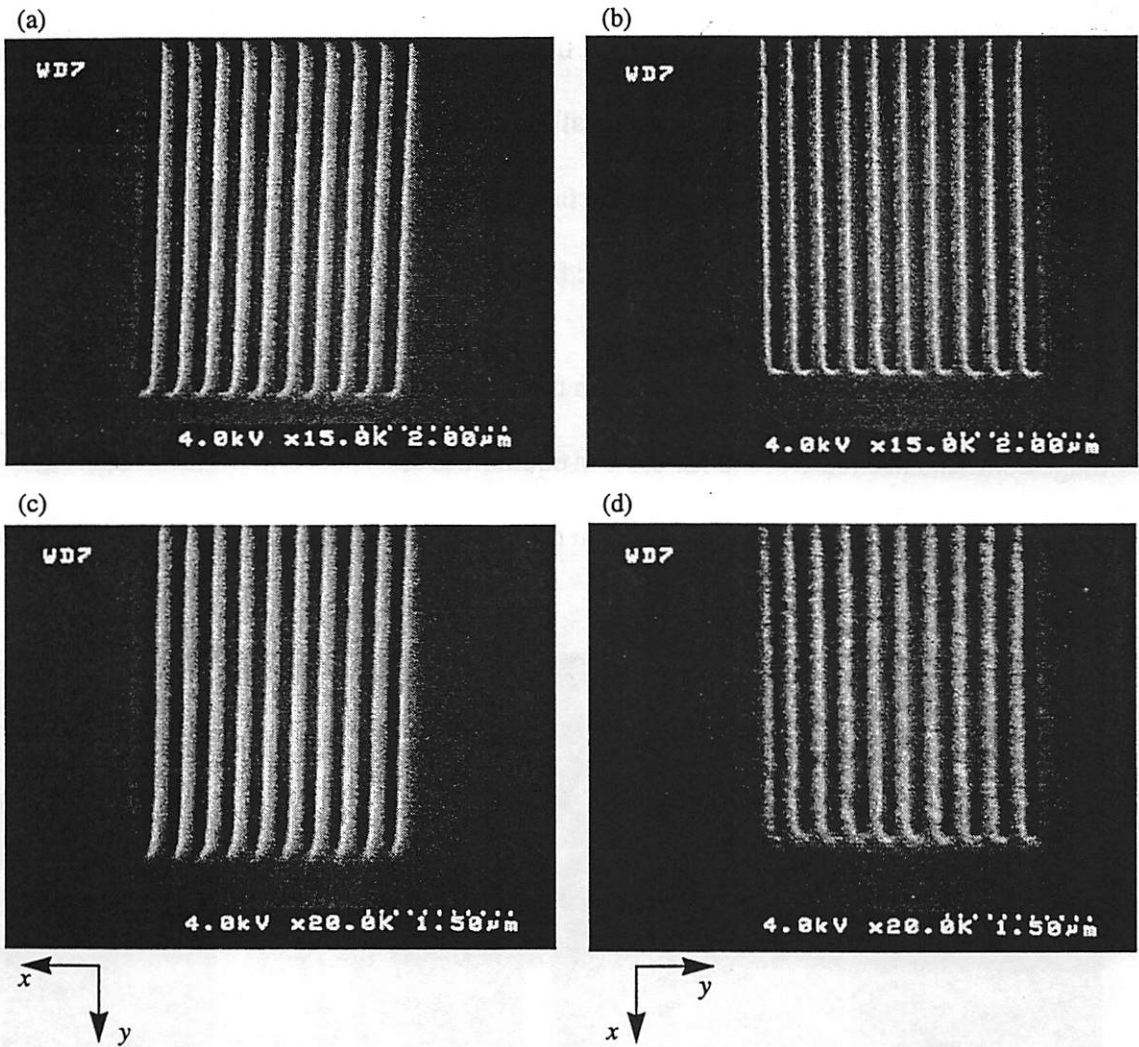


Figure 7-5. Line/space patterns printed by the 10 \times Schwarzschild optic.

SEM images of equal lines and spaces, (a)-(b) 0.2- μm and (c)-(d) 0.15- μm in dimension, recorded in SAL 601 photoresist. The line/space patterns in (a) and (c) are oriented along the x direction and in (b) and (d) along the y direction. The features, recorded near the overall best focus, indicate similar performance in both directions, as expected.

terns of equal lines and spaces recorded in SAL 601 photoresist near the overall best focus with the Schwarzschild objective are shown in Figure 7-5. The 0.2- μm and 0.15- μm features are oriented along the x direction in Figure 7-5(a) and (c), respectively, and along the y direction in Figure 7-5(b) and (d). The recorded patterns exhibit good image fidelity in both directions, as expected, although the lines along the x direction indicate somewhat better quality than those along the y direction. Owing to the experimental uncertainty in the best focal position of $\pm 0.5 \mu\text{m}$, this small discrepancy may be a result of performing the experiment somewhat away from the overall best focus. The slight differences in the focus would be amplified by the contrast reduction resulting from known scattering by rough mirror surfaces in the Schwarzschild optic [75].

The calculations of image quality based on the interferometry measurements indicate peak image contrasts in excess of 0.8 for 0.1- μm equal lines and spaces when the scattering from rough mirror surfaces is neglected. Even in the presence of some scattered flare, this image

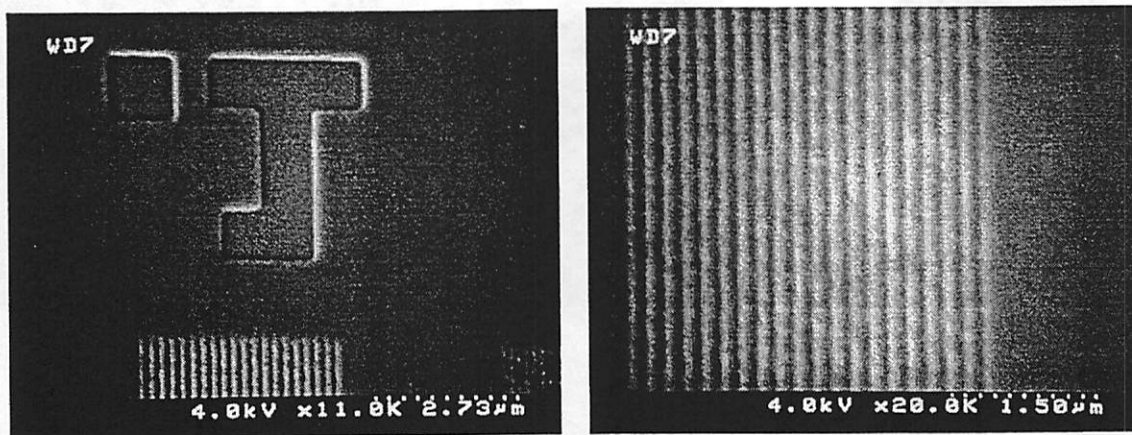


Figure 7-6. Printed 0.1- μm line/space patterns.

SEM images of 0.1- μm lines and spaces printed by the 10 \times Schwarzschild objective in SAL 601 photoresist.

contrast, found for each of the two orthogonal line orientations individually about $1\ \mu\text{m}$ on each side of the overall best focus, should be sufficient to record the $0.1\text{-}\mu\text{m}$ line/space pattern in SAL 601 photoresist [65, 68, 177]. This is demonstrated in Figure 7-6, which shows an array of dense $0.1\text{-}\mu\text{m}$ line/space features, oriented along the x direction, printed with the $10\times$ Schwarzschild optic near the optimum focus.

7.5. Conclusion

The measured aberration magnitude of 0.090 wave rms corresponds to a near diffraction-limited image quality for the 0.07-NA sub-aperture of the $10\times$ Schwarzschild optic. The expected optical performance has been evaluated with image calculations that include the effects of the measured aberrations and verified by imaging experiments that utilize the EUV lithography exposure tool for which the optic was designed. In printing of several test patterns, including the star resolution pattern and the dense line/space features, the image quality observed experimentally is consistent with the astigmatism predicted from interferometry. The strong correlation between the calculated and the observed images is a qualitative confirmation of the accuracy of the interferometry experiments.

8 Effects of Higher-Order Aberrations on Image Quality in Lithographic Optics

8.1. Introduction

The wavefront aberrations in lithographic imaging systems directly impact the latitude of the pattern transfer process. The image fidelity is influenced by the overall wavefront error, composed of aberrations of different spatial frequencies that range from low-order to high-frequency errors, illustrated schematically in Figure 8-1. The low-order aberrations, produced by imperfect figuring of the optical surfaces, affect the size of the smallest printable features. These “figure” errors, containing only a few cycles of variation over the optic aperture, correspond to the classical aberrations [95, 121, 122]. The high-frequency aberrations, caused by micro-roughness of the optical surfaces, produce a flare of scattered radiation that degrades the image contrast. A statistical description of the optical surfaces [99, 179, 73, 101] can be used to evaluate the effect of scatter on the image [100, 180, 181]. In imaging with multilayer mirrors, the effects of multilayer coatings on scattering can also be included [182, 73]. The intermediate range of spatial frequencies, corresponding to roughly ten to about a hundred cycles over the optical aperture diameter, produces low-angle scattering that degrades imaging of features with dimensions near the diffraction-limited resolution. The analysis of the optical performance degradation caused by these mid-spatial-frequency aberrations, sometimes referred to as “ripple”, has been limited

[102, 183]. The relatively low-spatial-frequency content of the ripple aberrations warrants a deterministic description of their effect on the image, rather than a statistical representation that provides the image properties averaged over an ensemble of optical systems with similar characteristics [180].

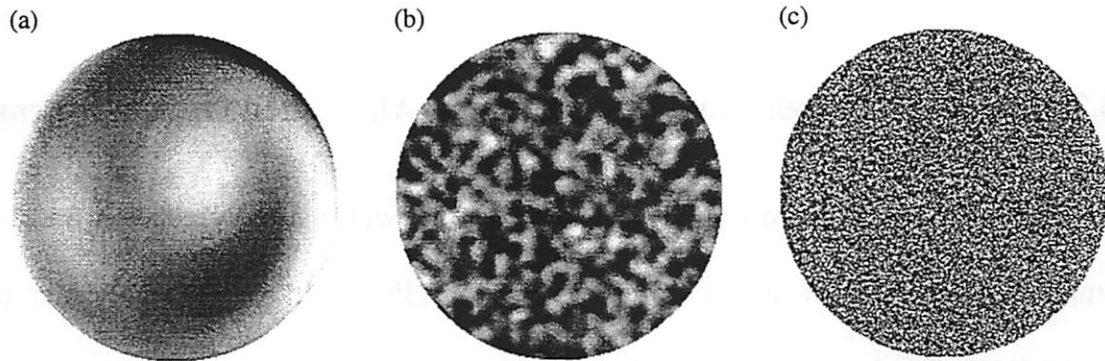


Figure 8-1. Aberrations with different spatial frequencies.

A schematic representation of the wavefront errors at the pupil of an optical system that contain (a) low, (b) medium, and (c) high spatial frequencies.

With the desire for diffraction-limited imaging, the effects of mid-frequency aberrations on image fidelity have become important in the fabrication specification of the optical surfaces. Furthermore, although significant advances have been made in achieving the specified figure [82, 184, 57] and surface finish [75, 185], the mid-frequency errors are still a concern [184, 75]. In the high-performance imaging applications that require precision aspheres, usually produced by diamond-turning optical surfacing tools, the mid-frequency aberrations are especially important.

In this chapter, the image degradation caused by higher-order aberrations is analyzed using the theory of image formation including the effects of partial spatial coherence [186, 127,

135] that is relevant to the lithographic optical systems of interest here. The optical performance is considered in terms of the spatial frequency of the aberrations, the feature dimensions, and the degree of partial coherence. The effects of higher-order aberrations are illustrated with aerial image calculations and an evaluation of the exposure-defocus imaging latitude pertinent in photolithography.

8.2. Partially Coherent Image Formation in Aberrated Optical Systems

The treatment of image formation in optical systems with partially coherent radiation employs the scalar-wave diffraction theory [186, 127, 135]. In lithography applications utilizing spectrally narrow, or temporally coherent, radiation, the light propagation through an optical system is represented by the mutual intensity, describing the spatial coherence in terms of the cross-correlation of the radiation fields at two spatially separated points. A schematic depiction of the lithography system, relevant to optics with both refractive and reflective components, is given in Figure 8-2. The radiation properties of interest at the object plane x_o and the image plane x_i are described by the mutual intensities $J_o(x_o; x_o)$ and $J_i(x_i; x_i)$, respectively. To simplify notation, the coordinates x_o, x_i , etc. represent the two dimensions of the plane of interest. The characteristics of the source and the condenser system are expressed by the mutual intensity $J_o^-(x_o; x_o)$, incident on the object plane. The thin object has an amplitude transmission $F(x_o)$. The projection optics are characterized by the amplitude response function $K(x_o; x_i)$ between the field at a point x_o in the object plane and the field at a point x_i in the image plane. The amplitude response function $K(x_o; x_i)$ is related to the pupil function $\mathcal{K}(f; f')$ by a Fourier transform. In general, the plane of the

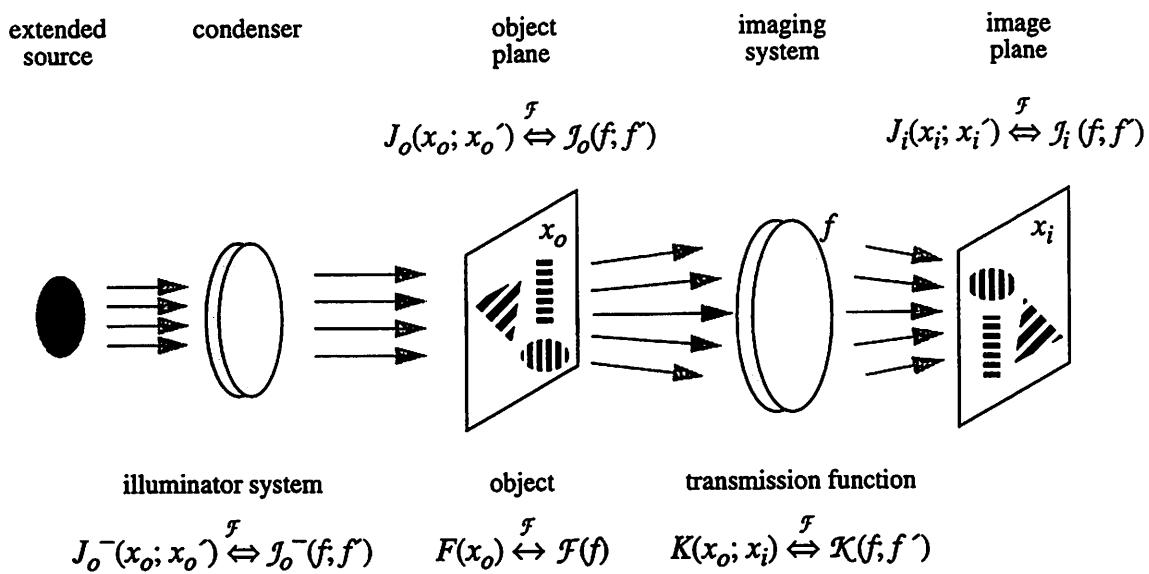


Figure 8-2. Description of an optical lithography system.

The notation used to describe image formation in a lithography system. The radiation properties are described by the mutual intensities $J(x; x')$. The mutual intensity $J_o^-(x_o; x_o)$ incident on the object with transmission $F(x_o)$ represents the characteristics of the illuminator system. The amplitude response function $K(x_o; x_i)$ between a point in the object plane x_o and a point in the image plane x_i describes the properties of the imaging system. The quantities in the spatial-frequency domain, which corresponds to the plane of the imaging system pupil, are denoted by script letters.

imaging system pupil corresponds to the spatial-frequency domain f . The mutual intensities as well as the properties of the object and the projection optics are denoted by script letters in the spatial-frequency domain. In this discussion, the scale normalized coordinates [127] are employed, accounting for the coordinate scaling in the pupil plane and for the lateral magnification from the object to the image plane. The dimensionless spatial coordinates x_o and x_i represent object and image plane distances in resolution units of λ/NA , where NA is the numerical aperture of the optic on the object or the image side. The normalized pupil coordinates f range from -1 to 1 in each linear dimension. With these conventions, the quantities of interest in the space and spatial-frequency domains are related

through two- or four-dimensional Fourier transforms. For instance, the object transmission $F(x_o)$ and the mutual intensity in the object plane $J_o(x_o; x_o')$ are related to their spatial frequency versions $\mathcal{F}(f)$ and $\mathcal{J}_o(f; f')$ by

$$(8-1) \quad F(x_o) = \int \int_{-\infty}^{\infty} \mathcal{F}(f) e^{-2\pi i f x_o} df, \text{ and}$$

$$(8-2) \quad J_o(x_o; x_o') = \iiint \int_{-\infty}^{\infty} \mathcal{J}_o(f; f') e^{-2\pi i (f x_o + f' x_o')} df df'.$$

In addition, the object and image points, x_o and x_i , are assumed to be in the isoplanatic region of the optical system [127], in which the pupil function is spatially invariant and the point amplitude transfer function $K(x_o; x_i)$ depends only on the coordinate differences $x_o - x_i$.

In imaging with partially coherent illumination, the mutual intensities in the object and image planes are related by a four-dimensional frequency response related to the system pupil function [127, 135]. Specifically, in the spatial-frequency domain, the image mutual intensity $\mathcal{J}_i(f; f')$ is the product of the object mutual intensity $\mathcal{J}_o(f; f')$ and the transfer function $\mathcal{K}(f)\mathcal{K}^*(-f')$, or

$$(8-3) \quad \mathcal{J}_i(f; f') = \mathcal{J}_o(f; f') \mathcal{K}(f) \mathcal{K}^*(-f').$$

In the space domain, the image intensity is given by the four-dimensional convolution of the mutual intensity leaving the object $J_o(x_o; x_o')$ with the point amplitude response func-

tion $K(x_o)$ and its complex conjugate. Since the mutual intensity leaving the object corresponds to the product of the incident mutual intensity $J_o^-(x_o; x_o')$ and the product of object transmissions $F(x_o)F^*(x_o')$, the image intensity, obtained from the mutual intensity by setting $x = x'$, has the form

$$(8-4) \quad I_i(x) = \iiint_{-\infty}^{\infty} J_o^-(x_o; x_o') F(x_o) F^*(x_o') K(x-x_o) K^*(x-x_o') dx_o dx_o'.$$

The effect of aberrations on the image formation is contained in the pupil function $\mathcal{K}(f)$. Here the pupil function is factored into a component $\mathcal{K}^0(f)$ that describes the diffraction-limited optical system and a factor $\mathcal{P}(f)$ that includes the effect of aberrations, namely

$$(8-5) \quad \mathcal{K}(f) = \mathcal{K}^0(f) \mathcal{P}(f).$$

The aberration function $\mathcal{P}(f)$ is usually expressed as

$$(8-6) \quad \mathcal{P}(f) = \mathcal{A}(f) e^{i\Phi(f)},$$

where the amplitude component $\mathcal{A}(f)$ and the phase function $\Phi(f)$ correspond to the transmission nonuniformities and the phase aberrations in the optic, respectively. Separating the effects of aberrations from the diffraction-limited performance in Equation 8-3 gives the relationship between the mutual intensity $\mathcal{J}_i(f, f')$ with aberrations and the unaberrated mutual intensity $\mathcal{J}_i^0(f, f')$, or

$$(8-7) \quad \mathcal{J}_i(f, f') = \mathcal{J}_i^0(f, f') \mathcal{P}(f) \mathcal{P}^*(-f').$$

Transforming Equation 8-7 to the space domain, followed by setting $x = x'$, produces the image-plane intensity $I_i(x)$ of the form

$$(8-8) \quad I_i(x) = \int_{-\infty}^{\infty} \int \int \int J_i^0(x_i; x_i') P(x - x_i) P^*(x - x_i') dx_i dx_i'.$$

Thus the aberrated image intensity corresponds to a four-dimensional convolution of the Fourier transform $P(x)$ of aberration function $\mathcal{P}(f)$ and the mutual intensity $J_i^0(x; x')$, describing the image properties in a diffraction-limited system.

8.3. Aberration Frequency, Object Properties, and Coherence

The expression in Equation 8-8 for the aberrated image intensity states that the aberrations produce image degradation through the interactions within the diffraction-limited image pattern, described by the mutual intensity at separate image points x and x' . This aberration-induced pattern correlation occurs over distances determined by the frequency content of the aberration transmission function $\mathcal{P}(f)$. The aberrated image clearly depends on the object characteristics that are contained in the unaberrated mutual intensity $J_i^0(x; x')$. In addition, since the image relates to the mutual intensity, rather than simply the intensity or the field amplitude, the aberration effects depend on the degree of spatial coherence in the system. The relationships among the aberration frequencies, the object characteristics, and partial coherence are explored in this section.

8.3.1. Effect of a Single-Frequency Phase Aberration

To investigate the effect of different aberration frequencies, an aberration function containing a single-frequency phase variation may be considered. For a phase aberration of the form $\Phi(f) = M\cos(2\pi Nf)$ with N cycles over the pupil radius and a peak-to-valley magnitude of M/π waves, the aberration function becomes

$$(8-9) \quad \mathcal{P}(f) = e^{iM\cos(2\pi Nf)},$$

where uniform pupil transmission $\mathcal{A}(f)$ is assumed. This function can be expressed as an infinite sum of complex exponentials with frequencies that are integer multiples of N [187]. Since complex exponentials Fourier transform to delta functions, the space-domain version of the aberration function corresponds to

$$(8-10) \quad P(x) = \sum_{k=-\infty}^{\infty} C_k(M) \delta(x - kN),$$

where the coefficients $C_k(M) = i^{|k|} J_{|k|}(M)$ are expressed in terms of the $|k|^{\text{th}}$ -order Bessel functions. Using the single-frequency phase aberration spectrum in Equation 8-8 gives the aberrated intensity of the form

$$(8-11) \quad I_i(x) = \sum_k \sum_l C_k(M) C_l^*(M) J_i^0(x - kN; x - lN).$$

Thus for sinusoidal phase aberrations with N cycles over the aperture radius, the intensity of the aberrated image consists of a weighted sum of the diffraction-limited mutual inten-

sities at points separated by distances that are integer multiples of $N \lambda/NA$. Consequently, the correlation distances of the aberration-induced image interactions scale with the aberration frequency. The interaction strengths, given by the coefficients C_k , depend on the aberration magnitude M . For small aberrations of interest here, the amplitude of the coefficients C_k that contribute to image degradation ($k \neq 0$) increases with the aberration magnitude M and decreases with the interaction order k [187].

8.3.2. Aberrations Described by Zernike Polynomials

Since the aberrations in optical systems with circular pupils are often expressed in terms of Zernike polynomials [95, 96, 98], described in the Appendix, it is instructive to consider the impact of phase aberrations corresponding to the individual Zernike functions. While Zernike polynomials best describe the low-order figure errors, the high-order Zernike terms may be used to understand the effects of ripple aberrations with roughly five to twenty cycles over the pupil diameter. Although in principle any aberration can be expressed in terms of the polynomials that form an orthogonal basis set on the circular pupil region, the polynomial description of spatial frequencies exceeding about twenty cycles over the aperture diameter becomes impractical. As outlined in the Appendix, each Zernike polynomial $Z_{nm}(r, \theta)$ consists of a n^{th} -order radial polynomial $\mathcal{R}_{nm}(r)$ and a sinusoid in the polar angle θ with m cycles per revolution. The radial and azimuthal orders n and m , related to the spatial frequencies along the radial and the azimuthal directions, are plotted for the first 225 Zernike polynomials in Figure 8-3(a), using the polynomial ordering conventions described in the Appendix.

For a pure phase aberration, consisting of a single Zernike term of a small magnitude M , where $M \ll 1$, the aberrations function $\mathcal{P}(f)$ can be expressed as

$$(8-12) \quad \mathcal{P}(f) = 1 + iM Z_{nm}(f) .$$

Transforming to the space domain, the effect of the aberration expressed by Equation 8-8 becomes

$$(8-13) \quad I_i(x) = I_i^0(x) - 2M \operatorname{Im} \left\{ \int_{-\infty}^{\infty} \int J_i^0(x_i; x) Z_{nm}(x - x_i) dx_i \right\} +$$

$$M^2 \iiint_{-\infty}^{\infty} \int J_i^0(x_i; x_i') Z_{nm}(x - x_i) Z_{nm}^*(x - x_i') dx_i dx_i' .$$

where I_i^0 denotes the diffraction-limited image intensity and Z_{nm} represents the Fourier transform of the Zernike polynomials. The aberrated image intensity consists of the diffraction-limited intensity and the aberration-induced perturbations, determined by the characteristics of the Zernike polynomial transform Z_{nm} given in the Appendix. Generally, the spatial extent of Z_{nm} depends on the radial order n , as illustrated in Figure 8-3(b). In addition to the radius of the first Fourier transform peak, the figure gives the radii enclosing 50% and 90% of the total integrated square modulus, or energy, of the Zernike Fourier transform Z_{nm} . Both the mean spatial frequency and the spatial bandwidth, given approximately by the radius enclosing 50% of the energy and by the radial range between the first peak and the 90% enclosed energy, respectively, appear to increase linearly with the radial order n . Using the radius enclosing 50% of the energy, the approximate correlation dis-

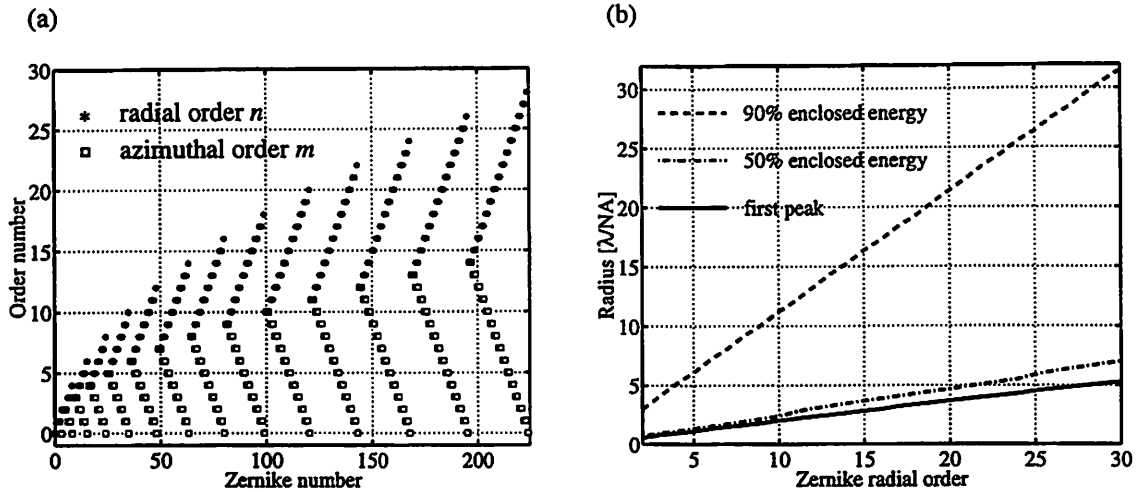


Figure 8-3. High-order Zernike polynomials.

(a) The radial order n and azimuthal order m of Zernike polynomials plotted vs. the polynomial number. (b) The spatial frequencies of Zernike polynomials are related to their Fourier transform. The radius of the 50% enclosed energy, the 90% enclosed energy, and the first peak of the Fourier transform of Zernike polynomials plotted as a function of the radial order n . The focal spot diameter is on the order of $1 \lambda/NA$.

tance of the interactions within the image, induced by a phase aberration corresponding to a Zernike term of radial order n , corresponds to roughly $0.24 n \lambda/NA$.

8.3.3. Aberrations and Pattern Properties

Expressing the aberration effects in terms of the properties of the diffraction-limited image reveals the strong interaction between the image features and the aberrations. This complex dependence allows only rudimentary deductions about the image quality in the presence of aberrations. Since the distances over which the pattern properties become correlated pertain to the spatial frequencies of the aberrations, the impact of aberrations depends on the size and the relative separation of the features. In printing of relatively dense features with dimensions near the resolution limit, the ripple aberrations may in principle degrade the

image quality as much as low-order aberrations. Practically, the comparative effects of the low-order and mid-frequency errors depend on their respective magnitudes. For isolated dark features (in a bright field) of dimensions near the resolution limit, the scattering from all aberration spatial frequencies contributes to the image degradation. Although all aberrations reduce the peak intensity of barely resolvable isolated bright features (in a dark field), mainly the low-order aberrations degrade the image fidelity. Finally, wavefront errors with several distinct spatial frequencies may either degrade or enhance quasi-periodic patterns.

In general, a complete evaluation of imaging performance requires calculations of aerial images for the feature patterns of interest, using the known aberrations of the optical system [188, 9]. However, the impact of wavefront imperfections on different image features may be understood to a certain extent by considering the Fourier transform $P(x)$ of the aberration function $\mathcal{P}(f)$. The magnitude of the spatial distribution $P(x)$ describes the strength of the image interactions caused by the aberrations. The phase of the space-domain aberration function $P(x)$ determines whether the aberration-induced image interactions correspond to constructive or destructive interference, i. e. image enhancement or degradation. The aberration effects are most pronounced for spatial periods of the object pattern that correspond to any possible peaks in the spatial distribution $P(x)$. Thus the examination of the aberration Fourier transform $P(x)$ may reveal the spatial periods of the patterns that are most affected by the aberrations. On the other hand, a uniform spatial spectrum of the aberrations corresponds to an imaging performance that is not strongly dependent on the spatial period of the object pattern. Consequently, in applications requiring good image quality for a variety of feature sizes, a relatively uniform distribution of

aberration spatial frequencies is preferred over distributions which may catastrophically degrade the imaging performance for certain image features.

8.3.4. Dependence of Aberration Effects on Spatial Coherence

The image degradation produced by aberrations depends on the degree of spatial coherence in the optical system through the interactions of the diffraction-limited mutual intensity related to the aberration spatial frequencies. To explore the relationship between coherence parameters and aberration frequencies, the effect of coherence in the presence a single-frequency phase aberration may be considered. Assuming a single-frequency aberration with N cycles over the aperture radius and a small magnitude $M \ll 1$, the dominant aberration contribution to the image given by Equation 8-11 corresponds to the unaberrated mutual intensity between points separated by the fundamental interaction distance of $N \lambda NA$, or

$$(8-14) \quad J_i^0(x; x-N) = \int_{-\infty}^{\infty} \int_{-\infty}^{\infty} \int_{-\infty}^{\infty} J_o^-(x_o; x_o') F(x_o) F^*(x_o') K^0(x-x_o) K^{0*}(x-N-x_o') dx_o dx_o',$$

where the expansion given by Equation 8-4 is included. The effects of coherence on the feature pattern, described by the object transmission $F(x_o)$, appear in the mutual intensity $J_o^-(x_o; x_o')$ incident on the object. The single-frequency aberration shifts the unaberrated amplitude response function $K^0(x_o)$ by N . Since the spatial extent of the illumination mutual intensity and the unaberrated amplitude response functions is limited [127, 135], the effect of the aberration is most prominent in the region of their overlap in

Equation 8-14. The spatial extent of the diffraction-limited amplitude response equals approximately to the resolution unit of λ/NA . In systems employing incoherent sources and condensers producing either critical or Köhler illumination of the object, the input mutual intensity depends only on the coordinate difference $x_o - x_o'$ and spans about $\lambda/\sigma NA$, where σ represents the partial coherence factor. The partial coherence factor σ , inversely proportional to the degree of coherence, is given by the ratio NA_c/NA_o of the numerical apertures of the condenser and the projector (object-side) [127]. Considering the illumination spatial extent of $\lambda/\sigma NA$ and the aberration-induced shift of $N\lambda/NA$ in the response function $K^0(x_o)$, Equation 8-14 suggests that the coherent aberration effects are most significant when the aberration correlation distance is less than the coherence width of $1/\sigma$, or

$$(8-15) \quad N \leq \frac{1}{\sigma}.$$

Thus, roughly speaking, the image perturbations due to aberrations of frequencies that correspond to interaction distances within the coherence width add coherently, while the image effects from higher-frequency aberrations add incoherently.

8.4. Investigation of Aberration Effects with Image Calculations

The influence of aberrations in an optical system may be evaluated with image calculations. For feature patterns of interest, the performance assessment also involves the image quality merit functions, dependent on the imaging application. Multiple descriptors of performance are typically required to qualify lithographic lenses [189]. Owing to the strict lin-

ewidth tolerances and the need for processing latitude in patterning of integrated circuit features, the printed feature dimensions as well as the exposure-defocus process window [190] represent suitable figures of merit in lithographic imaging [188, 189]. In this section, the changes in the exposure-defocus process latitude produced by aberrations are used to evaluate the relative importance of the different aberration frequencies on the image quality in lithography.

8.4.1. Calculation Parameters

To investigate the relationships among aberration frequencies, object features, and partial spatial coherence, the image quality was evaluated in terms of the exposure-defocus process window over a range of parameters. The aerial images used to determine the process window are calculated using the program SPLAT [178] that simulates image formation

Parameters	Values
wavelength λ	13 nm
numerical aperture NA	0.1
partial coherence factor σ	0.1-0.9
features orientation pitch polarity	0.1-mm lines x and y directions 0.2-2.0 mm bright and dark field
aberrations magnitude average frequency	mixture of astigmatism, coma, and spherical aberration 0.05 wave rms 0.7-10 cycles over pupil radius

Table 8-1. Image calculation parameters.

The parameters used to evaluate the effects of the object size, the aberration frequency, and the partial spatial coherence on the image quality.

with partially coherent light. The calculation parameters, chosen to include typical operational conditions in extreme ultraviolet (EUV) projection lithography, are summarized in Table 8-1. The calculations are performed for an exposure wavelength of 13 nm and projection optics with a numerical aperture of 0.1. The 0.1-0.9 range of the partial coherence factor σ , which corresponds to the relative fill of the circular pupil with a circular illumination beam, includes values of 0.5-0.7 typically used in lithography. Since one of the challenges in printing of circuit patterns is the imaging of line features with dimensions near the resolution limit [9, 191, 192], the test patterns chosen here are 0.1- μm -wide periodic lines of pitch varying from 0.2 μm to 2.0 μm . The line features considered include both bright lines in a dark field and dark lines in a bright field, oriented along two orthogonal directions. Aberrations used in the calculation have a magnitude of 0.05 wave rms, which is typical of lithographic stepper lenses [9]. The wavefront errors are composed of equal rms contributions from balanced astigmatism, coma, and spherical aberration terms of the same order. To vary the aberration frequency, over a range of 0.7-10 cycles over the pupil radius, aberration orders from the 3rd to the 43rd are utilized. Since each one of the aberration wavefronts is described by Zernike polynomials of three consecutive radial orders $n-1$, n , $n+1$, the average aberration frequency is taken as 0.24 n cycles over the pupil radius, as described in Section 8.3.2. This choice of aberration profiles with narrow-band spatial-frequency content reveals the relative effects of different spatial frequencies on the image. Two examples of the wavefronts used are given in Figure 8-4(a) and (b). The 3rd-order aberration in Figure 8-4(a) contains Zernike polynomial terms 5, 6, and 8, corresponding to mean radial order of $n = 3$ and average aberration frequency of 0.7 cycles over the pupil radius. Similarly, the 11th-order aberration in Figure 8-4(b), composed of Zernike

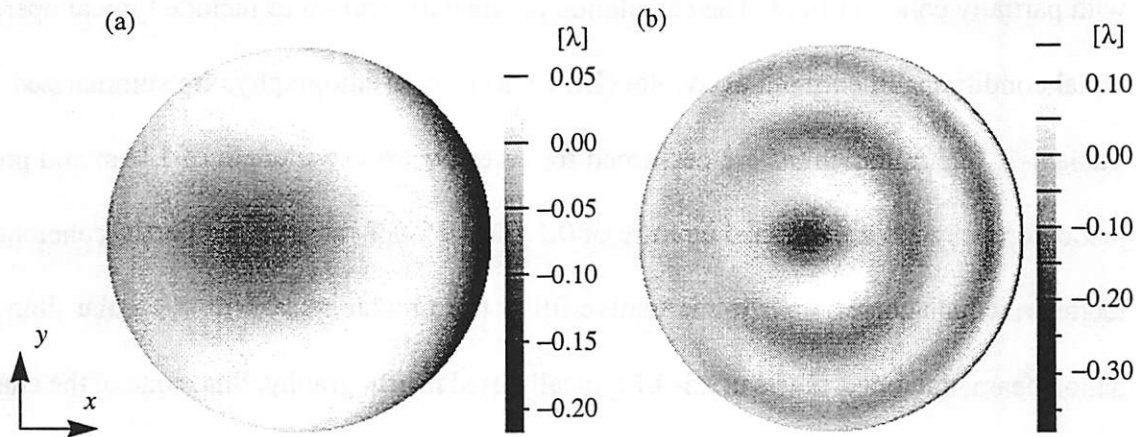


Figure 8-4. Examples of test aberrations.

Two examples of the wavefront phase used to investigate the effects of aberration frequency on the image quality. Each aberration with total wavefront error of 0.05 wave rms consists of equal rms contributions from astigmatism, coma, and spherical aberration of the same order. Wavefronts composed of (a) 3rd order (primary) and (b) 11th order aberrations that correspond to Zernike polynomials 5, 6, 8 and 45, 46, 48, respectively.

terms 45, 46, and 48, has a mean radial order of $n = 11$ and an average aberration frequency of 2.6 cycles over the pupil radius.

The merit function used here to assess the image quality is the reduction in the exposure dose process latitude caused by the aberrations. For a particular image pattern, the exposure latitude corresponds to the exposure dose range that produces critical feature dimensions within specified limits for a given defocus variation. As an example, the process window definitions used in these calculations are illustrated in Figure 8-5 for both diffraction-limited and aberrated projection optics. In this case, the feature of interest is a bright line of 0.1- μm width and 0.35- μm pitch. The plots show the linewidth contours corresponding to a $\pm 10\%$ shift in the critical dimension. The exposure variation, simulated by scaling of the calculated image, bounded by these contours represents the exposure latitude. The $\pm 0.5 \mu\text{m}$ defocus range needed in EUV projection lithography defines the focal latitude. The relative

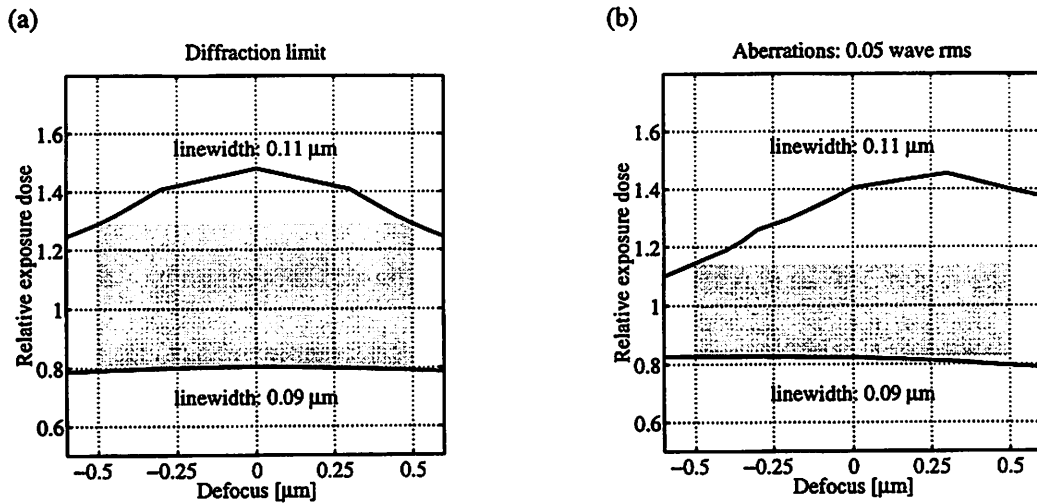


Figure 8-5. Exposure-defocus latitude definition.

The defocus and exposure dose range that produces printed linewidths within specified limits defines the process latitude. Here the process window (shaded) for 0.1- μm line features is given by the exposure dose range that produces linewidths of the aerial image between 0.09 μm and 0.11 μm within a defocus range of ± 0.5 μm . The process window for bright, y-oriented 0.1- μm lines of 0.35- μm pitch imaged at 13 nm, 0.1 NA, and partial coherence factor of 0.5 using an imaging system with (a) no aberrations and (b) the aberrations in Figure 8-4(a).

impact of aberrations is given by the fractional overlap of the exposure-defocus window in the presence of aberrations with the process window of a diffraction-limited imaging system. For a fixed defocus range, the reduction in the process window overlap equals the reduction in the exposure latitude.

8.4.2. Calculation Results

The calculated effects of low and high-order aberrations on bright features in a dark background and dark features in a bright background are summarized in Figure 8-6 and Figure 8-7, respectively. For feature variations along the x and the y directions and for partial coherence factors σ of 0.3, 0.5, and 0.7, the figures show the exposure latitude reduc-

tion caused by the different aberrations as a function of the average aberration frequency and the pitch of the line features. The aberration frequency is given in cycles over the pupil radius and the line pitch in the resolution units of λ/NA . As expected, the image degradation increases with the degree of spatial coherence, proportional to the inverse partial coherence factor $1/\sigma$. In agreement with the general rule that the imaging of dark features is more difficult than the imaging bright features [9], the aberration effects are more severe for dark lines in a bright field than for bright lines in a dark field. The differences in the image fidelity between line features along the x and the y directions result from the non-uniformities of the aberrations over the pupil, illustrated in Figure 8-4. The aberrations vary more strongly along the y direction than along the x direction, affecting line features that are oriented long the y direction more severely than those along the x direction.

Observation of the plots in Figure 8-6 and Figure 8-7 reveals that dense features with dimensions near the resolution limit appear to be affected similarly by aberrations of both low and high spatial frequencies. In this case, the aberrations having different spatial frequencies mainly degrade the contrast of the dense features. In printing isolated features separated by distances exceeding several times the feature size, the low-order aberrations that degrade the line fidelity have a similar effect on the lines of varying spatial periods. In comparison to the low-order aberrations, the image quality of dark isolated features is significantly degraded by high-frequency aberrations. On the other hand, isolated bright features having dimensions on the order of the resolution limit are less influenced by the high-frequency ripple aberrations than by the low-order errors. These observations are consistent with the fact that higher-order aberrations scatter light over distances greater than the resolution.

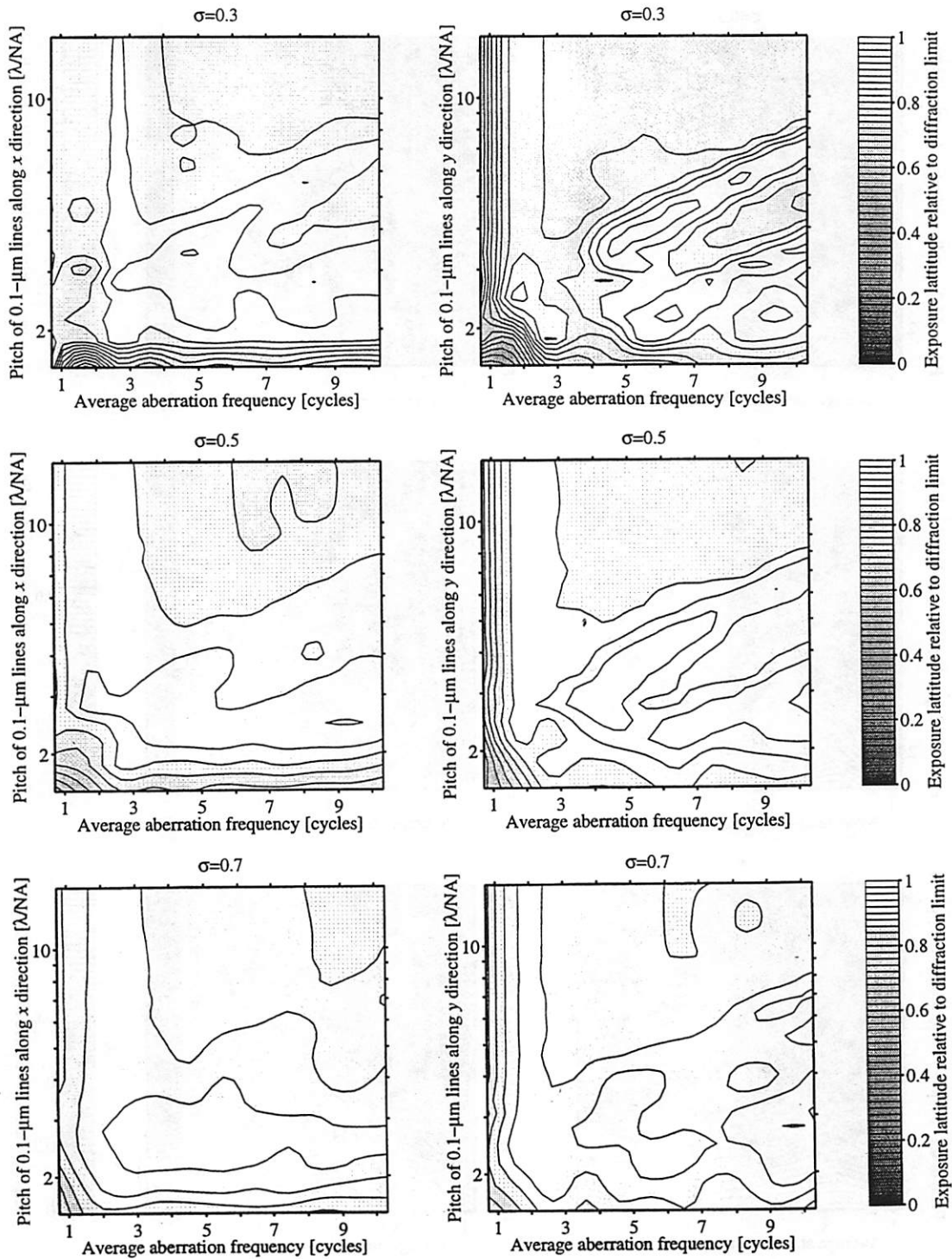


Figure 8-6. Dark-field exposure latitude vs. aberration frequency and line pitch.

The reduction in the exposure latitude, defined as the fractional overlap of the process window of an aberrated system with the window of a diffraction-limited system, for bright 0.1- μm lines in a dark background as a function of the average aberration frequency and the line pitch. For lines oriented along the x and the y directions, the exposure latitude is given for partial coherence factor of 0.3, 0.5, and 0.7.

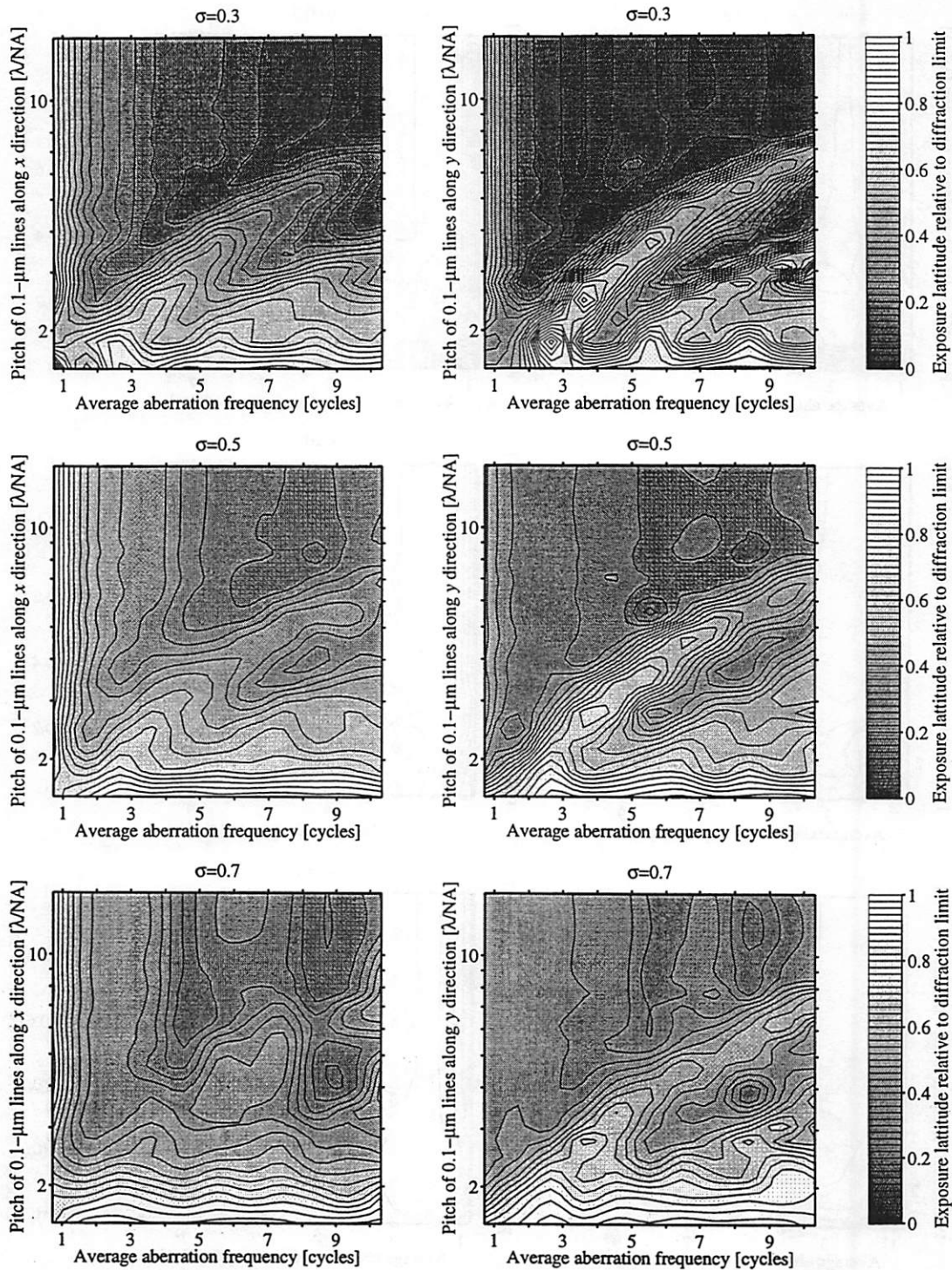


Figure 8-7. Bright-field exposure latitude vs. aberration frequency and line pitch.

The reduction in the exposure latitude, defined as the fractional overlap of the process window of an aberrated system with the window of a diffraction-limited system, for dark 0.1- μm lines in a bright background as a function of the average aberration frequency and the line pitch. For lines oriented along the x and the y directions, the exposure latitude is given for partial coherence factor of 0.3, 0.5, and 0.7.

Figure 8-6 and Figure 8-7 also indicate enhancement of features with certain spatial periods by certain aberration frequencies. This effect occurs when the spatial period of the line features matches an integer multiple of the aberration scattering distance that corresponds to the narrow-band frequency content of the aberrations considered. Since the frequency bandwidth of the Zernike aberration terms used increases with the mean aberration frequency, as shown in Figure 8-3(b), the enhancement appears to decrease somewhat with the aberration frequency. When the aberration distances do not match the spatial periods of the features, for spatial frequencies above roughly three cycles over the pupil radius the effect of higher-order aberrations corresponds to an image contrast degradation that is quite uniform with the spatial frequency.

The impact of the aberration frequency and the partial spatial coherence on the image is illustrated in Figure 8-8. The exposure latitude reduction caused by the different aberrations is given as a function of the average aberration frequency and the partial coherence factor σ for dense lines of 0.2- μm pitch in Figure 8-8(a) and for bright and dark isolated lines of 1.2- μm pitch in Figure 8-8(b). Each plot also indicates the boundary, given by the simple rule of Equation 8-15, that separates the regions where the aberration effects are approximately coherent from the region where they are approximately incoherent. For dense features, the boundary indeed seems to divide the regime where the effects of the aberration are significant from the regime where they are not. For isolated features whose degradation is not a strong function of the aberration frequency for spatial frequencies above several cycles over the aperture, the aberration-induced image degradation appears to be significant even when the aberration correlation distance exceeds the coherence width.

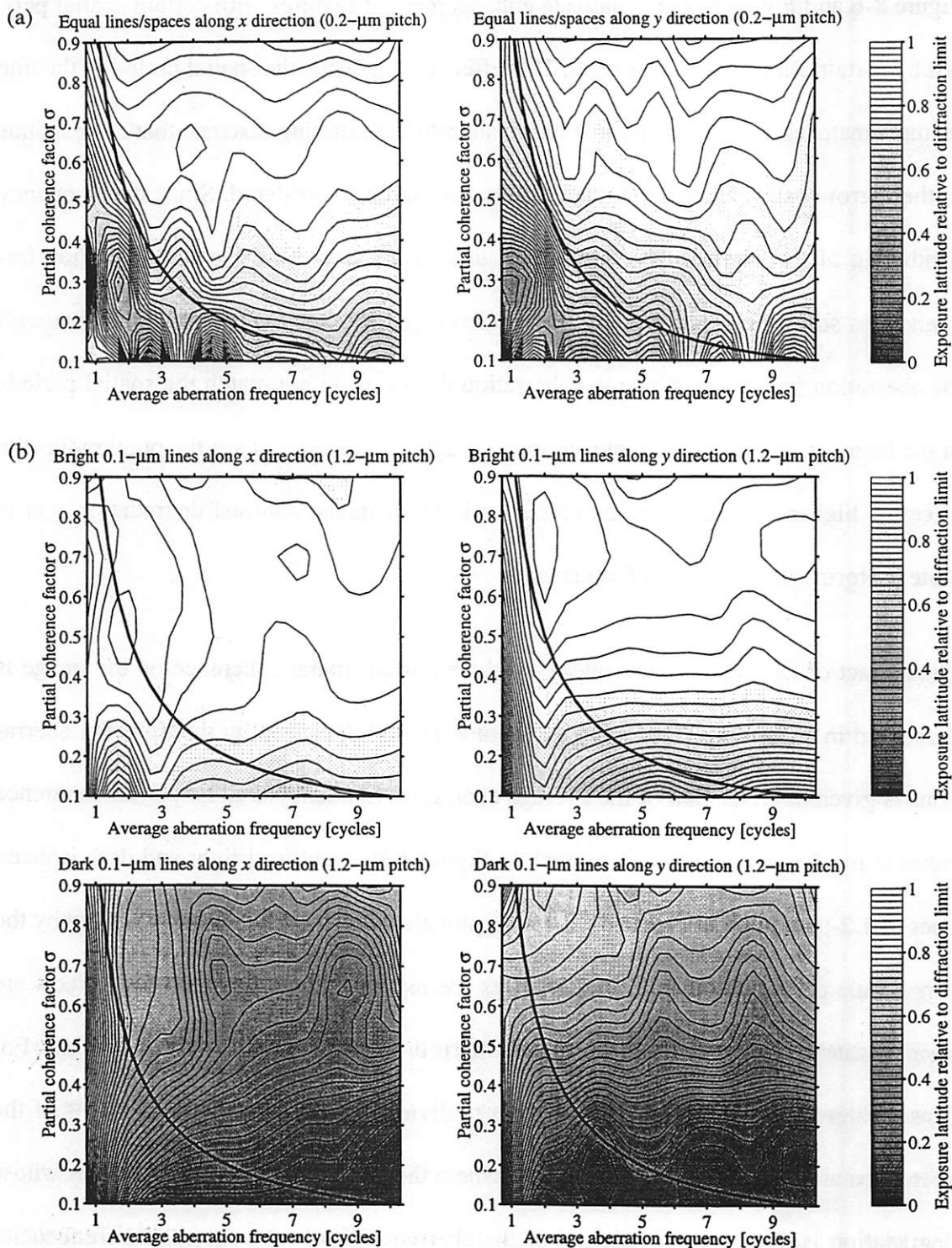


Figure 8-8. Exposure latitude vs. aberration frequency and coherence factor.

The exposure latitude of an aberrated system relative to a diffraction-limited system as a function of the average aberration frequency and the partial coherence factor for (a) dense 0.1- μm lines and (b) isolated bright and dark 0.1- μm lines. The solid curve represents the boundary where the average aberration frequency equals the inverse coherence factor.

8.5. Figures of Merit Including Object Properties

The strong dependence of aberration effects on the object properties necessitates optics performance evaluation for a variety of object features. Although aerial image calculations provide a complete description of imaging quality, simpler merit functions that include the object dependence may be useful for aberration tolerancing and image characterization. Traditionally, the measure of lens quality has been based on the Strehl ratio [95, 121], relevant in microscopy and astronomy applications, which corresponds to the ratio of intensities at the center of the image of an isolated point object in optical systems with and without aberrations. More recently, the bright and dark line ratios have been proposed as merit functions for lithographic projectors [191-193]. For a narrow slit aperture on a dark background, the value of the aberrated intensity at the line center divided by the intensity in the absence of aberrations constitutes the bright line ratio. The dark line ratio describes the intensity dip from a thin dark line in a clear background in optics with and without aberrations. In this discussion, the concept of the line ratio is extended to include the spatial period of the object features. The periodic bright line ratio (PBLR) may be defined as the ratio of intensities in optics with and without aberrations at the center of narrow periodic bright lines in a dark field. Similarly, the periodic dark line ratio (PDLR) corresponds to the intensity decrease in the presence of aberrations relative to the diffraction limit at the center of narrow periodic dark lines in a bright background. The periodic bright and dark line ratios can be found from the expression for image intensity given by Equation 8-4. Under the assumption that the mutual intensity incident on the object plane depends only on the coordinate difference $x_o - x_o'$, valid for the either critical or Köhler illumination

[127], the periodic bright line ratio for lines with a period of $s\lambda/NA$ oriented normal to the unit vector u is given by

$$(8-16) \quad \text{PBLR} = \frac{\int \int_{-\infty}^{\infty} \bar{j}_o(f) \sum_q \sum_{q'} \mathcal{K}\left(f + \frac{qu}{s}\right) \mathcal{K}^*\left(f + \frac{q'u}{s}\right) df}{\int \int_{-\infty}^{\infty} \bar{j}_o(f) \sum_q \sum_{q'} \mathcal{K}^0\left(f + \frac{qu}{s}\right) \mathcal{K}^{0*}\left(f + \frac{q'u}{s}\right) df},$$

and the periodic dark line ratio becomes

$$(8-17) \quad \text{PDLR} = \frac{\int \int_{-\infty}^{\infty} \bar{j}_o(f) \sum_q \text{Re}\left(\mathcal{K}\left(f + \frac{qu}{s}\right) \mathcal{K}^*(f)\right) df}{\int \int_{-\infty}^{\infty} \bar{j}_o(f) \sum_q \text{Re}\left(\mathcal{K}^0\left(f + \frac{qu}{s}\right) \mathcal{K}^{0*}(f)\right) df}.$$

Here $\mathcal{K}(f)$ and $\mathcal{K}^0(f)$ denote the aberrated and the diffraction-limited pupil transmission functions, respectively, and the integers q and q' range from $-\infty$ to $+\infty$.

As an example, the periodic bright line and dark line ratios for the wavefront aberrations described in Section 8.4.1 are given in Figure 8-9(a) and (b), respectively. For a partial coherence factor of 0.5 and feature variations along both x and y directions, the periodic line ratios are plotted as functions of the average aberration frequency and the pitch of the line features. The aberration frequency is given in cycles over the pupil radius and the line pitch in the resolution units of λ/NA . As expected, the trends exhibited by the periodic bright and dark line ratios match the exposure-defocus process latitude calculations for periodic lines illustrated in Figure 8-6 and Figure 8-7.

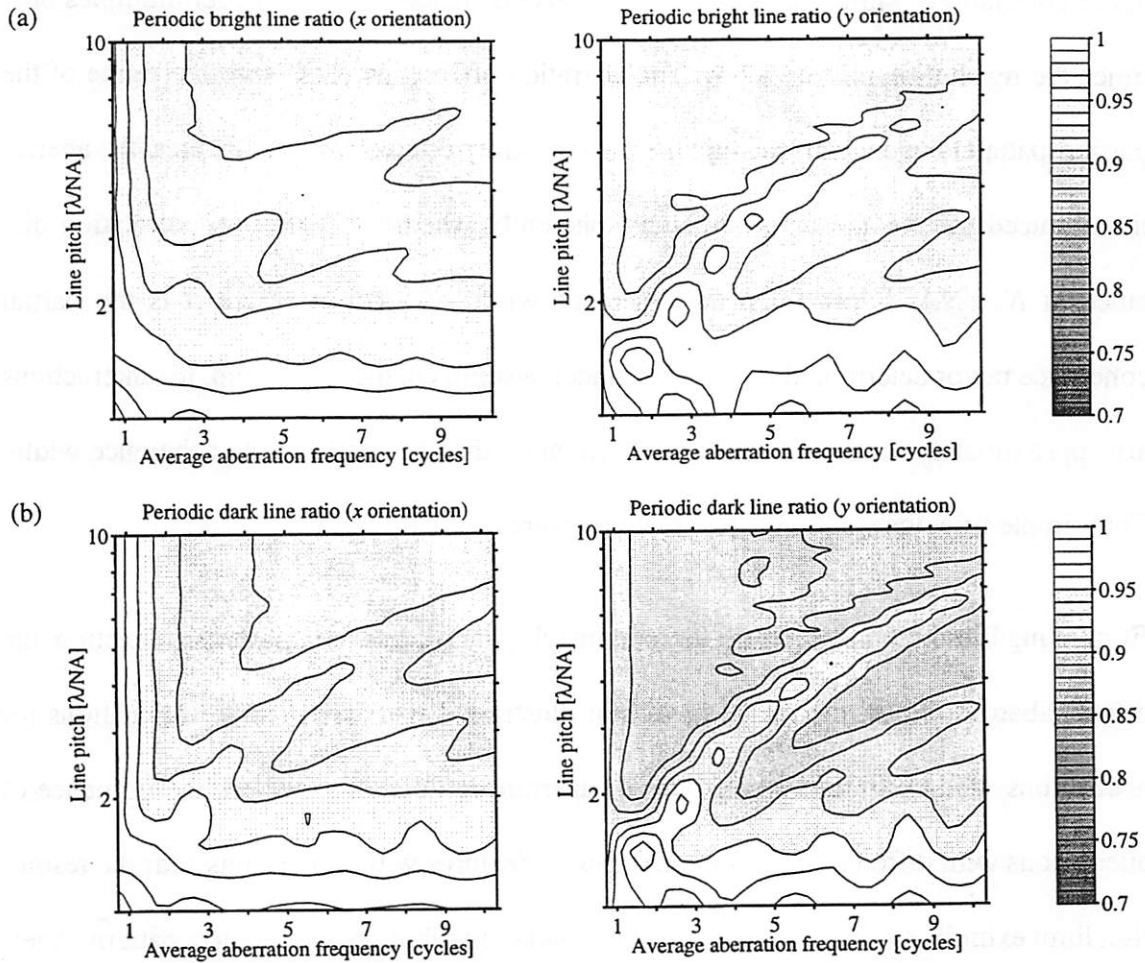


Figure 8-9. Periodic bright and dark line ratios vs. aberration frequency and line pitch.

The periodic (a) bright line and (b) dark line ratios as functions of the average aberration frequency and the line pitch for the aberrations described in Section 8.4.1 and the partial coherence factor of 0.5.

8.6. Conclusion

The degradation of the image quality by wavefront aberrations has been analyzed in general using the theory of image formation with partially coherent radiation. Considering the aberration effects as perturbations of a diffraction-limited image, the aberrations induce correlations within the image that are described by the mutual intensity of the diffraction-limited image. An aberration containing N cycles of variation over the pupil radius pro-

duces correlations within the imaged pattern over distances that are integer multiples of N times the resolution unit of λ/NA . The aberration effects increase with the degree of the partial spatial coherence of the light used. In imaging relatively dense features, the aberration-induced effects add approximately coherently when the aberration correlation distance of $N \lambda/NA$ is less than the coherence width of $\lambda/\sigma NA$, where σ is the partial coherence factor determined by the illuminator system. On the other hand, the interactions are approximately incoherent when the correlation distance exceeds the coherence width. This simple rule does not apply to isolated features.

Employing lithographic exposure-defocus imaging latitude as an image merit function, the effects aberrations on the image have been illustrated with aerial image calculations for aberrations with up to ten cycles over the aperture radius. As expected, the influence of aberrations with different spatial frequencies on features with dimensions near the resolution limit exhibits strong dependence on the spatial distribution of the object pattern. Aberrations of all spatial frequencies degrade dense features similarly. However, only aberrations with frequencies above roughly three cycles over the pupil radius affect imaging of isolated features with dimensions near the resolution limit similarly. To include the dependence of aberration effects on the object properties and on the degree of partial coherence, the periodic line ratios have been proposed as simple merit functions for aberration tolerancing and image characterization in lithographic optics. For line features, the periodic bright and dark line ratios indicate the same image-quality trends as the exposure-defocus process latitude based on aerial image calculations.

9 Summary and Future Work

9.1. Summary of the Research

The imaging performance of extreme ultraviolet optical systems was investigated in this thesis. Motivated by the desire for near diffraction-limited imaging in extreme ultraviolet (EUV) projection lithography, point diffraction interferometry was implemented at wavelengths near 13 nm to evaluate wavefront aberrations in multilayer-coated reflective optical systems with moderate numerical apertures. The goal of the measurements was to develop wavefront-measuring metrology at EUV wavelengths with accuracy beyond the suggested wavefront aberration tolerance of 0.02 wave rms. Following several proof-of-principle experiments, the phase-shifting point diffraction interferometer was used to examine the overall extreme ultraviolet wavefront, produced by mirror surface irregularities and multilayer coating imperfections, in a two-mirror multilayer-coated Schwarzschild optic. To assess the wavefront measurement quality, the measurement repeatability was determined and the reference wavefront accuracy estimated by detecting known systematic aberrations. By employing the Schwarzschild objective in an imaging experiment using a prototype lithography exposure tool, the accuracy of the interferometry measurements was confirmed qualitatively from the consistency between the patterns printed in photoresist and those predicted by calculations based on the interferometry measurements.

Using the wavefront measurements at multiple wavelengths, chromatic aberrations and wavelength-dependent transmission nonuniformities due to the molybdenum/silicon (Mo/Si) multilayer coatings were observed. The effects of chromatic vignetting due to limited multilayer transmission passbands on the imaging performance of the Schwarzschild optic were analyzed. The coating characteristics extracted from the interferometry data on the two-mirror system were also compared to previously reported coating properties measured on individual mirror substrates.

In this work, the effects of residual aberrations on the imaging performance in lithography systems were examined by treating aberrations as perturbations of a diffraction-limited image. The complex relationship between the aberration spatial frequency, the object properties, and the degree of spatial coherence of the radiation was explored with aerial image calculations for aberration spatial frequencies up to ten cycles over the optic aperture radius. To include the object dependence in aberration tolerancing and image characterization, the periodic line ratios were proposed as simple image-quality merit functions.

9.1.1. Point Diffraction Interferometry

The issues concerning accurate wavefront metrology of assembled imaging systems based on point diffraction interferometers were considered in Chapter 2. Both the conventional and the phase-shifting versions of the point diffraction interferometer allow direct measurement of the optical system wavefront from the interference between the unknown test wave and a known reference wave. While the simpler conventional point diffraction interferometer can in principle record aberrations of relatively large magnitudes, the phase-shifting design, suited to the measurement of small wavefront errors, offers significantly

higher throughput and improved accuracy through phase-shifting. In either design, the quality of the reference wavefront and of the wavefront used for the illumination of the test optic, both of which are produced by diffraction of light from sub-resolution pinhole apertures, determines the measurement accuracy. To estimate the size of the pinholes needed for the generation of the desired spherical wavefronts, while accounting for nonuniform illumination of the apertures in the interferometer, scalar-field calculations applicable to diffraction over moderate numerical apertures were employed. To characterize optical systems with moderate numerical apertures ($NA \leq 0.1$) at a wavelength λ with wavefront measurement accuracy on the order of 0.01 wave rms, the diameter of the pinhole needed to diffract a high-quality spherical wavefront corresponds to roughly one third to one half of the resolution unit of λ/NA for the optic under test. With wavefront-generating pinholes of proper size, the interferometric accuracy can potentially scale with the wavelength of the radiation used in the measurement.

The test and the reference beams in point diffraction interferometers follow nearly common paths, allowing measurements with light sources of relatively short temporal coherence lengths. However, the requirement of adequate contrast of the interference fringes demands radiation sources that possess significant spatial coherence. In the extreme ultraviolet spectral region, high-brightness radiation from undulators best meets the spatial coherence requirements of point diffraction interferometers. Although in comparison to other EUV sources, undulators produce relatively spatially coherent radiation, usually only 1/10 to 1/100 of the overall undulator power in the desired spectral band is spatially coherent. Using a statistical description of the radiation fields, the effect of the relative lack of coherence on the spatially filtered wavefront diffracted from the interferometer entrance

pinhole was analyzed. A general method for the characterization of the degree of coherence and the radiation phase, including diffraction of the light by a pinhole aperture, is outlined in Chapter 2 for relatively incoherent sources described by an ensemble of independent radiators. Under the assumptions of the statistical description, the low spatial coherence of the undulator source does not significantly influence the quality of the point diffraction interferometry measurements. With proper choice of the illuminator system for imaging of the source onto the entrance pinhole, the illumination wavefront generated by the entrance pinhole can be nearly spherical and spatially coherent, as required.

9.1.2. Proof-of-Principle Experiments

Conventional point diffraction interferometry measurements of singlet lenses at EUV wavelengths represent one of the key experiments that have enabled later characterization of a two-mirror multilayer-coated system with the phase-shifting point diffraction interferometer. The measurements of the intensity and the phase of the wavefronts from diffractive zone plate lenses, performed near 13-nm wavelength, were discussed in Chapter 3. The presence of small zone placement errors was established from the comparison between the measured far-field intensity patterns from the zone plates and the diffraction calculations for lenses with zonal errors. Relating the calculation results to the measured intensity patterns revealed that the unoptimized zone plate optics, with 600 zones and an 80-nm outer zone width, had peak zonal placement errors on the order of 30 nm. While the intensity measurements provided evaluation of relatively high-frequency wavefront errors caused by imperfect zone positioning, the interferometry measurements allowed the characterization of the low-order aberrations. The interferometric phase measurement

of one annular zone plate showed a wavefront error of 0.14 wave rms at 12.9-nm wavelength. The errors in the reference wavefront due to oversized reference pinholes, estimated to be about 0.04 wave rms in magnitude, were found to influence the measurement of the test wavefront.

The second important step toward the implementation of the phase-shifting point diffraction interferometer at EUV wavelengths was the construction of the phase-shifting interferometer prototype utilizing visible light. Described in Chapter 4, the visible-light measurements were used to evaluate the interferometer capabilities and to explore alignment strategies. The prototype interferometer system, applied in testing of near diffraction-limited lenses, demonstrated measurement repeatability of ± 0.002 wave rms at 632.8-nm wavelength. The measurement self-consistency, found by evaluations of the test wavefront at multiple azimuthal orientations of the interferometer components and of the test optic and by varying the defocus in the wavefront, was better than 0.008 wave rms.

9.1.3. Properties of a Multilayer-Coated Schwarzschild Optic

The phase-shifting point diffraction interferometer implemented at EUV wavelengths was used to characterize the aberrations in a multilayer-coated Schwarzschild objective designed for a prototype EUV lithography system. The Schwarzschild objective, consisting of two spherical mirrors with annular clear apertures, forms 10 \times -demagnified images over a field of view 400- μm in diameter by employing an off-axis circular aperture stop. As reported in Chapter 5, three different portions of the annular aperture, corresponding to three separate aperture stops with numerical apertures of 0.06, 0.07, and 0.08, contained wavefront aberrations of 0.044, 0.090, and 0.313 wave rms at 13.4-nm wavelength. The

wavefront errors consisted mainly of astigmatism, oriented along the azimuth of the annular the clear aperture of the objective. The small wavefront errors in the 0.07-NA and the 0.06-NA sub-apertures correspond to near diffraction-limited imaging performance at extreme ultraviolet wavelengths.

The chromatic vignetting effects, caused by the limited passbands of the Mo/Si multilayer coatings in the Schwarzschild optic, were studied with interferometry and with transmission measurements in Chapter 6. The chromatic phase aberrations and the wavelength-dependent coating transmission nonuniformities were directly observed via measurements at several wavelengths within the coating transmission passband centered near 13.4 nm. The measurements predicted negligible influence of the chromatic aberrations on the formation of the image in an EUV exposure system. Accounting for the layer interface imperfections and for the variations in the multilayer period over each mirror, good qualitative agreement in both the transmission and the phase was obtained between multilayer calculations and the experimental observations. Furthermore, the coating characteristics extracted from the measurements of the two-mirror system were compared to the previously reported coating properties measured on the individual mirrors.

9.1.4. Evaluation and Verification of Interferometer Performance

The capabilities of the interferometer were assessed in terms of the stability and the repeatability of the measurements at an operational wavelength of 13.4 nm. As described in Chapter 5, the observed interferometer stability was found to be adequate for wavefront characterization with 0.01 wave rms accuracy at EUV wavelengths. The measurement repeatability, evaluated with extensive experiments on the 0.07-NA sub-aperture of the

Schwarzschild objective, was established to be ± 0.008 wave (± 0.11 nm) rms. Owing to reference pinholes whose diameters of 130-165 nm were somewhat larger than the 60-100 nm needed to test a 0.07-NA optic at 13.4 nm, the quality of the reference wavefront represented the most significant factor limiting the interferometer accuracy in these measurements. The reference wavefront errors, evaluated by changing the focal component in the measured wavefront and by detecting a systematic coma effect in the fringes, was estimated to be roughly ± 0.015 wave (± 0.20 nm) rms in a numerical aperture of 0.07.

Imaging experiments with the Schwarzschild objective, performed on the EUV lithography exposure tool for which the optic was designed, were used to verify the accuracy of the interferometric wavefront measurements qualitatively. As discussed in Chapter 7, the photoresist patterns printed with the 0.07-NA sub-aperture of the Schwarzschild optic were compared to the image intensities obtained from calculations that accounted for the astigmatic aberrations of 0.090 wave rms measured interferometrically. For several test patterns, including the star resolution pattern and the dense line/space features, the image quality observed experimentally revealed the astigmatism predicted from interferometry. The excellent agreement between the printed features and the interferometry-based image calculations validated the measurement accuracy estimates found in Chapter 5.

9.1.5. Influence of Residual Aberrations on Lithographic Imaging

Employing the theory of image formation with partially coherent radiation, the impact of aberrations on the image quality in lithographic projectors was considered in Chapter 8. Viewing the aberration effects as perturbations of a diffraction-limited image, the aberrations induce correlations within the image that depend on the spatial-frequency content of

the wavefront errors and on the spatial coherence of the radiation used. An aberration with a spatial frequency of N cycles over the pupil radius induces interactions within the image over distances that are integer multiples of N times the optical system resolution unit of λ/NA . The aberration effects scale with the degree of the partial spatial coherence. Since the radiation is essentially coherent over distances given by the coherence width, it was suggested that the aberration effects add coherently when the aberration correlation distance of $N\lambda/NA$ is less than the coherence width of $\lambda/\sigma NA$, where σ is the coherence factor determined by the illuminator system. Similarly, the addition would be incoherent when the correlation distance exceeds the coherence width. This simple relationship, dividing the aberration effects into coherent and incoherent regimes according to aberration frequency, seems to hold in imaging of relatively dense features but does not apply to barely resolvable isolated features.

The effects of aberrations on features with dimensions near the resolution limit were also illustrated with aerial image calculations. Using the exposure-defocus imaging latitude relevant in lithography as a figure of merit, the dependence of the image on the object properties, the aberration frequencies, and the degree of partial coherence was evaluated for aberration spatial frequencies up to ten cycles over the radius of the imaging system pupil. Although a complete assessment of imaging performance generally requires aerial image calculations for a variety of object features, simpler figures of image quality may be useful in aberration tolerancing and image characterization. The periodic bright and dark line ratios, proposed as figures of merit that include the object and the coherence dependencies, were found to indicate similar trends in the image quality as the exposure-defocus imaging latitude based on aerial image calculations.

9.2. Suggestions for Future Work

Additional studies on the extreme ultraviolet point diffraction interferometer are required to achieve accuracy in wavefront-measuring metrology of multilayer-coated mirror systems beyond the sub-nanometer levels demonstrated in this work. Other research topics related to the present study are also of interest for the development of diffraction-limited imaging at extreme ultraviolet wavelengths. The suggestions for future experiments and calculations include:

- 1) Characterization of self-consistency of the phase-shifting point diffraction interferometry measurements, analogous to the experiments in Chapter 5, with sufficiently small reference pinhole apertures.
- 2) Evaluation of the reference wavefront quality from the interference of two wavefronts diffracted by sub-resolution pinhole apertures. The wavefront quality may be explored for different illumination properties, alignment conditions, and spatial separations of the pinholes.
- 3) Theoretical investigation of the sphericity of the wavefront diffracted by small three-dimensional pinhole apertures, including vector-field diffraction over large numerical apertures under nonuniform illumination.
- 4) Point-diffraction interferometry measurement of a complex optical system with a large field of view.
- 5) Experiment to fully correlate multilayer coating properties on individual mirrors with the coating performance in an assembled optical system.

- 6) Development of an interferometric test suitable for the characterization of individual multilayer-coated mirrors at their operational wavelengths. A specific suggestion in need of further consideration is the following type of a shearing interferometer: The surface shape and the coating properties are tested by illuminating the mirror with two “spherical” wavefronts, diffracted from two spatially displaced sub-resolution pin-holes, and observing the reflected wavefronts.
- 7) Determination of the spatial aberration frequency that separates the frequency range, in which deterministic aberration description must be used to examine the image quality, from the region where a stochastic model based on the statistics of mirror surface profiles is sufficient. This spatial-frequency boundary can be found by considering the frequency-dependent variance of the image intensity in the statistical aberration model, either analytically or with Monte Carlo simulations, because the variance represents the deviation of the actual system properties from their ensemble average.

Appendix

A. The Zernike Circle Polynomials

For optical systems with circular pupils, the Zernike circle polynomials provide a convenient representation of a wavefront in terms of distinct aberration terms. Each Zernike polynomial corresponds to a specific balanced aberration. The first few Zernike terms represent the primary aberrations, including piston, tilt, defocus, astigmatism, coma, and spherical aberration. As a set, Zernike polynomials form an orthogonal basis on the unit circle, described by polar coordinates (r, θ) .

The Zernike circle polynomials separate into radial functions $R_{nm}(r)$ and azimuthal sinusoidal components. The polynomials are described by the order n of the radial polynomial $R_{nm}(r)$ and by the number of cycles m of the azimuthal component. In particular, given that $m, n \geq 0$, the Zernike polynomials $Z_{nm}(r, \theta)$ used here are given by

Equation A-1.
$$Z_{nm}(r, \theta) = R_{nm}(r) \begin{cases} \cos(m\theta) \\ \sin(m\theta) \end{cases}, \text{ where}$$

Equation A-2.
$$R_{nm}(r) = \sum_{s=0}^{\frac{n-m}{2}} (-1)^s \frac{(n-s)! r^{n-2s}}{s! \left(\frac{n+m}{2} - s\right)! \left(\frac{n-m}{2} - s\right)!}.$$

analysis label	natural label	radial order n	azimuthal order m	Zernike polynomials	Aberration names
0	0	0	0	1	piston
1	1	1	1	$r \cos \theta$	x tilt
2	2	1	1	$r \sin \theta$	y tilt
3	3	2	0	$2r^2 - 1$	defocus
4	4	2	2	$r^2 \cos 2\theta$	astigmatism at 0°
5	5	2	2	$r^2 \sin 2\theta$	astigmatism at 45°
6	6	3	1	$(3r^3 - 2r) \cos \theta$	x coma
7	7	3	1	$(3r^3 - 2r) \sin \theta$	y coma
8	8	4	0	$6r^4 - 6r^2 + 1$	spherical aberration
9	9	3	3	$3r^3 \cos 3\theta$	triangular astigmatism at 0°
10	10	3	3	$3r^3 \sin 3\theta$	triangular astigmatism at 30°
11	11	4	2	$(4r^4 - 3r^2) \cos 2\theta$	
12	12	4	2	$(4r^4 - 3r^2) \sin 2\theta$	
13	13	5	1	$(10r^5 - 12r^3 + 3r) \cos \theta$	
14	14	5	1	$(10r^5 - 12r^3 + 3r) \sin \theta$	
15	15	6	0	$20r^6 - 30r^4 + 12r^2 - 1$	
16	16	4	4	$r^4 \cos 4\theta$	
17	17	4	4	$r^4 \sin 4\theta$	
18	18	5	3	$(5r^5 - 4r^3) \cos 3\theta$	
19	19	5	3	$(5r^5 - 4r^3) \sin 3\theta$	
20	20	6	2	$(15r^6 - 20r^4 + 6r^2) \cos 2\theta$	
21	21	6	2	$(15r^6 - 20r^4 + 6r^2) \sin 2\theta$	
22	22	7	1	$(35r^7 - 60r^5 + 30r^3 - 4r) \cos \theta$	
23	23	7	1	$(35r^7 - 60r^5 + 30r^3 - 4r) \sin \theta$	
24	24	8	0	$70r^8 - 140r^6 + 90r^4 - 20r^2 + 1$	
25	25	5	5	$r^5 \cos 5\theta$	
26	26	5	5	$r^5 \sin 5\theta$	
27	27	6	4	$(6r^6 - 5r^5) \cos 4\theta$	
28	28	6	4	$(6r^6 - 5r^5) \sin 4\theta$	
29	29	7	3	$(21r^7 - 30r^5 + 10r^3) \cos 3\theta$	
30	30	7	3	$(21r^7 - 30r^5 + 10r^3) \sin 3\theta$	
31	31	8	2	$(56r^8 - 105r^6 + 60r^4 - 10r^2) \cos 2\theta$	
32	32	8	2	$(56r^8 - 105r^6 + 60r^4 - 10r^2) \sin 2\theta$	
33	33	9	1	$(126r^9 - 280r^7 + 210r^5 - 60r^3 + 5r) \cos \theta$	
34	34	9	1	$(126r^9 - 280r^7 + 210r^5 - 60r^3 + 5r) \sin \theta$	
35	35	10	0	$252r^{10} - 630r^8 + 560r^6 - 210r^4 + 30r^2 - 1$	
36	48	12	0	$924r^{12} - 2772r^{10} + 3150r^8 - 1680r^6 + 420r^4 - 42r^2 + 1$	

Table A-1. Zernike circle polynomials used in the data analysis.

The primary (3rd order) aberrations correspond to polynomials 4-8, the secondary (5th order) aberrations to terms 9-15, the tertiary (7th order) aberrations to terms 16-24, etc.

Of the different scalings and orderings of Zernike polynomials that have been reported [95, 96, 98, 119-121], Zernike functions that are scaled to a peak magnitude of unity and ordered as shown in Table A-1 are employed here. The table lists the first 36 Zernike polynomials used to describe the low-order aberrations of interest. The last Zernike term listed appears out order that is given by the ordering of the other polynomials. In the data analysis reported here, it is labeled as number 36 instead of its natural number 48.

In some applications, the Fourier transforms of the Zernike polynomials are of interest. In terms of the polar coordinates (ρ, ϕ) in the frequency domain, the two-dimensional Fourier transform Z_{nm} of the Zernike polynomial Z_{nm} takes the form

$$\text{Equation A-3.} \quad Z_{nm}(\rho, \phi) = (-i)^m (-1)^{\frac{n-m}{2}} \frac{J_{n+1}(2\pi\rho)}{\rho} \begin{Bmatrix} \cos(m\phi) \\ \sin(m\phi) \end{Bmatrix},$$

where J_{n+1} denotes a Bessel function of order $n+1$.

Bibliography

- [1] D. L. White, J. E. Bjorkholm, J. Bokor, L. Eichner, R. R. Freeman, T. E. Jewell, W. M. Mansfield, A. A. MacDowell, L. H. Szeto, D. W. Taylor, D. M. Tennant, W. K. Waskiewicz, D. L. Windt, and O. R. Wood, II, "Soft x-ray projection lithography", *Solid State Technology*, **34** (7), pp. 37-42, 1991.
- [2] N. M. Ceglio and A. M. Hawryluk, "Soft-x-ray projection lithography system design", *OSA Proceedings on Soft X-Ray Projection Lithography*, **12**, edited by J. Bokor, (Optical Society of America, Washington DC, 1991), pp. 5-10.
- [3] K. H. Brown, "Lithography: today's performance, tomorrow's challenges", *OSA Proceedings on Extreme Ultraviolet Lithography*, **23**, edited by F. Zernike and D. T. Attwood, (Optical Society of America, Washington DC 1995), pp. 2-9.
- [4] D. A. Tichenor, G. D. Kubiak, and R. H. Stulen, "Extreme ultraviolet lithography for circuit fabrication at 0.1 μm feature size", *Proceedings of the SPIE*, **2523**, pp. 23-8, 1995.
- [5] K. B. Nguyen, G. F. Cardinale, D. A. Tichenor, G. D. Kubiak, K. Berger, A. K. Ray-Chaudhuri, Y. Perras, S. J. Haney, R. Nissen, K. Krenz, R. H. Stulen, H. Fujioka, C. Hu, J. Bokor, D. M. Tennant, and L. A. Fetter, "Fabrication of metal-oxide-semiconductor devices with extreme ultraviolet lithography", *Journal of Vacuum Science and Technology B*, **14** (6), pp. 4188-92, 1996.
- [6] J. E. Bjorkholm, "Extreme ultraviolet lithography: a technical update", *Journal of Vacuum Science and Technology B*, **15** (6), in press, 1997.
- [7] E. L. Raab, D. M. Tennant, W. K. Waskiewicz, A. A. MacDowell, and R. R. Freeman, "X-ray imaging at the diffraction limit", *Journal of the Optical Society of America A*, **8** (10), pp. 1614-21, 1991.
- [8] D. W. Berreman, "Multilayer reflecting x-ray optical systems: chromatic vignetting by narrow reflection bands", *Applied Optics*, **30** (13), pp. 1741-5, 1991.
- [9] D. M. Williamson, "The elusive diffraction limit", *OSA Proceedings on Extreme Ultraviolet Lithography*, **23**, edited by F. Zernike and D. T. Attwood, (Optical Society of America, Washington DC, 1995), pp. 68-76.

- [10] A. G. Michette, *Optical Systems for Soft X-Rays*, (Plenum Press, New York, 1986), Ch. 1.
- [11] E. Spiller, *Soft X-Ray Optics*, (SPIE Optical Engineering Press, Bellingham, Washington, 1994), Ch 2.
- [12] J. D. Jackson, *Classical Electrodynamics*, Second Edition, (John Wiley and Sons, New York, 1975), Ch. 7.
- [13] B.L. Henke, E.M. Gullikson, and J.C. Davis, "X-ray interactions: photoabsorption, scattering, transmission, and reflection at E=50-30000 eV, Z=1-92", *Atomic Data and Nuclear Data Tables*, **54**, (2), pp. 181-342, 1993.
- [14] P. Beckmann and A. Spizzichino, *The Scattering of Electromagnetic Waves from Rough Surfaces*, (The Macmillan Company, New York, 1963), Ch. 3.
- [15] in Reference 10, Ch. 2.
- [16] J. H. Underwood, "High-energy x-ray microscopy with multilayer reflectors", *Review of Scientific Instruments*, **57** (8), pp. 2119-23, 1986.
- [17] in Reference 11, Ch. 6.
- [18] E. Spiller, "Reflective multilayer coatings for the far UV region", *Applied Optics*, **15** (10), pp. 2333-8, 1976.
- [19] E. Spiller, A. Segmuller, J. Rife, and R. P. Haelbich, "Controlled fabrication of multilayer soft-X-ray mirrors", *Applied Physics Letters*, **37** (11), pp. 1048-50, 1980.
- [20] T. W. Barbee, "Sputtered layered synthetic microstructure (LSM) dispersion elements", *Low Energy X-Ray Diagnostics*, edited by D. T. Attwood and B. L. Henke, (American Institute of Physics, New York, 1981), pp. 131-45.
- [21] in Reference 10, Ch. 4.
- [22] in Reference 11, Ch. 8.
- [23] in Reference 11, Ch. 9.
- [24] H. Kinoshita, K. Kurihara, and H. Takenaka, "Soft x-ray reduction lithography using multilayer mirrors", *Japanese Journal of Applied Physics*, **30**, pt. 1 (11B), pp. 3048-52, 1991.
- [25] N. J. Duddles, "Reflectance coatings for the vacuum/extreme ultraviolet region", *OSA Trends in Optics and Photonics Volume on Extreme Ultraviolet Lithography*, **4**, edited by G. D. Kubiak and D. R. Kania, (Optical Society of America, Washington DC, 1996), pp. 173-6.

- [26] D. L. Windt, R. Hull, and W. K. Waskiewicz, "Interface imperfections in metal/Si multilayers", *Journal of Applied Physics*, **71** (6), pp. 2675-78, 1992.
- [27] S. P. Vernon, D. G. Stearns, and R. S. Rosen, "Ion-assisted sputter deposition of molybdenum-silicon multilayers (for soft x-ray optics)", *Applied Optics*, **32** (34), pp. 6969-74, 1993.
- [28] J. H. Underwood, E. M. Gullikson, and K. B. Nguyen, "Tarnishing of Mo/Si multilayer x-ray mirrors", *Applied Optics*, **32** (34), pp. 6985-90, 1993.
- [29] D. G. Stearns, R. S. Rosen, and S. P. Vernon, "Multilayer mirror technology for soft-x-ray projection lithography", *Applied Optics*, **32** (34), pp. 6952-60, 1993.
- [30] H. Takenaka, T. Kawamura, Y. Ishii, T. Haga, and H. Kinoshita, "Evaluation of Mo-based multilayer EUV mirrors", *OSA Proceedings on Extreme Ultraviolet Lithography*, **23**, edited by F. Zernike and D. T. Attwood, (Optical Society of America, Washington DC, 1995), pp. 26-32.
- [31] T. D. Nguyen, C. Khan-Malek, and J. H. Underwood, "Achievement of low stress in Mo/Si multilayer mirrors", *OSA Proceedings on Extreme Ultraviolet Lithography*, **23**, edited by F. Zernike and D. T. Attwood, (Optical Society of America, Washington DC, 1995), pp. 56-60.
- [32] D. L. Windt and W. K. Waskiewicz, "Multilayer facilities required for extreme-ultraviolet lithography", *Journal of Vacuum Science and Technology B*, **12** (6), pp. 3826-32, 1994.
- [33] D. L. Windt, W. L. Brown, C. A. Wolkert, and W. K. Waskiewicz, "Variation in stress with background pressure in sputtered Mo/Si multilayer films", *Journal of Applied Physics*, **78** (4), pp. 2423-30, 1995.
- [34] H. Takenaka, T. Kawamura, and T. Haga, "Heat resistance of Mo/Si multilayer EUV mirrors with interleaved carbon barrier layers", *OSA Trends in Optics and Photonics Volume on Extreme Ultraviolet Lithography*, **4**, edited by G. D. Kubiak and D. R. Kania, (Optical Society of America, Washington DC, 1996), pp. 169-72.
- [35] K. M. Skulina, C. S. Alford, R. M. Bionta, D. M. Makowiecki, E. M. Gullikson, R. Soufli, J. B. Kortright, and J. H. Underwood, "Molybdenum/beryllium multilayer mirrors for normal incidence in the extreme ultraviolet", *Applied Optics*, **34** (19), pp. 3727-30, 1995.
- [36] D. T. Attwood, G. Sommargren, R. Beguiristain, K. Nguyen, J. Bokor, N. Ceglio, K. Jackson, M. Koike, and J. Underwood, "Undulator radiation for at-wavelength interferometry of optics for extreme ultraviolet lithography", *Applied Optics*, **32** (34), pp. 7022-31, 1993.

- [37] G. E. Sommargren, "Point diffraction interferometry at soft x-ray wavelengths", *OSA Proceedings on Soft X-Ray Projection Lithography*, **18**, edited by A. M. Hawryluk and R. H. Stulen, (Optical Society of America, Washington DC, 1993), pp. 100-4.
- [38] W. T. Silfvast, M. C. Richardson, H. Bender, A. Hanzo, V. Yanovsky, F. Jin, and J. Thorpe, "Laser-produced plasmas for soft x-ray projection lithography", *Journal of Vacuum Science and Technology B*, **10** (6), pp. 3126-33, 1992.
- [39] D. A. Tichenor, G. D. Kubiak, M. E. Malinowski, R. H. Stulen, S. J. Haney, K. W. Berger, L. A. Brown, R. R. Freeman, W. M. Mansfield, O. R. Wood II, D. M. Tennant, J. E. Bjorkholm, T. E. Jewell, D. L. White, D. L. Windt, and W. K. Waskiewicz, "Soft-x-ray projection imaging using a laser plasma source", *OSA Proceedings on Soft X-Ray Projection Lithography*, **12**, edited by J. Bokor, (Optical Society of America, Washington DC, 1991), pp. 54-7.
- [40] D. A. Tichenor, A. K. Ray-Chaudhuri, G. D. Kubiak, S. J. Haney, K. W. Berger, R. P. Nissen, G. A. Wilkerson, R. H. Stulen, P. H. Paul, R. W. Arling, T. E. Jewell, E. Tejnil, W. C. Sweatt, W. W. Chow, J. E. Bjorkholm, R. R. Freeman, M. D. Himel, A. A. MacDowell, D. M. Tennant, L. A. Fetter, O. R. Wood II, W. K. Waskiewicz, D. L. White, D. L. Windt, "10x reduction imaging at 13.4 nm", *OSA Proceedings on Extreme Ultraviolet Lithography*, **23**, edited by F. Zernike and D. T. Attwood, (Optical Society of America, Washington DC, 1995), pp. 89-97.
- [41] G. D. Kubiak, L. J. Bernardez, K. D. Krenz, D. J. O'Connell, R. Gutowski, and A. M. M. Todd, "Debris-free EUVL sources based on gas jets", *OSA Trends in Optics and Photonics Volume on Extreme Ultraviolet Lithography*, **4**, edited by G. D. Kubiak and D. R. Kania, (Optical Society of America, Washington DC, 1996), pp. 66-71.
- [42] M. Ito, S. Katagiri, H. Yamanashi, E. Seya, T. Ogawa, H. Oizumi, and T. Terasawa, "Optical technology for EUV lithography", *OSA Trends in Optics and Photonics Volume on Extreme Ultraviolet Lithography*, **4**, edited by G. D. Kubiak and D. R. Kania, (Optical Society of America, Washington DC, 1996), pp. 9-12.
- [43] M. A. Klosner and W. T. Silfvast, "Feasibility of various discharge configurations for high intensity lithium vapor discharge source at 13.5 nm for EUVL", *OSA Trends in Optics and Photonics Volume on Extreme Ultraviolet Lithography*, **4**, edited by G. D. Kubiak and D. R. Kania, (Optical Society of America, Washington DC, 1996), pp. 80-3.
- [44] M. A. Klosner, H. A. Bender, W. T. Silfvast, and J. J. Rocca, "Intense plasma discharge source at 13.5 nm for extreme-ultraviolet lithography", *Optics Letters*, **22** (1), pp. 34-6, 1997.

- [45] S. J. Haney, K. W. Berger, G. D. Kubiak, P. D. Rockett, and J. Hunter, "Prototype high-speed tape target transport for a laser plasma soft-x-ray projection lithography source", *Applied Optics*, **32** (34), pp. 6934-7, 1993.
- [46] G. D. Kubiak, K. D. Krenz, K. W. Berger, T. G. Trucano, P. W. Fisher, and M. J. Gouge, "Cryogenic pellet laser plasma source targets", *OSA Proceedings on Extreme Ultraviolet Lithography*, **23**, edited by F. Zernike and D. T. Attwood, (Optical Society of America, Washington DC, 1995), pp. 248-54.
- [47] D. Torres, F. Jin, M. Richardson, and C. DePriest, "Characterization of mass-limited ice droplet laser plasmas", *OSA Trends in Optics and Photonics Volume on Extreme Ultraviolet Lithography*, **4**, edited by G. D. Kubiak and D. R. Kania, (Optical Society of America, Washington DC, 1996), pp. 75-9.
- [48] R. D. Watson and R. H. Stulen, "Analysis of thermally induced distortion of optics for soft-x-ray projection lithography", *OSA Proceedings on Soft X-Ray Projection Lithography*, **12**, edited by J. Bokor, (Optical Society of America, Washington DC, 1991), pp. 37-41.
- [49] A. M. Hawryluk and N. M. Ceglio, "Power loading limitations in soft x-ray projection lithography", *Journal of X-Ray Science and Technology*, **4** (3), pp. 167-81, 1994.
- [50] W. C. Sweatt, "High-efficiency condenser design for illuminating a ring field", *OSA Proceedings on Soft X-Ray Projection Lithography*, **18**, edited by A. M. Hawryluk and R. H. Stulen, (Optical Society of America, Washington DC, 1993), pp. 70-2.
- [51] G. E. Sommargren and L. G. Seppala, "Condenser optics, partial coherence, and imaging for soft-x-ray projection lithography", *Applied Optics*, **32** (34), pp. 6938-44, 1993.
- [52] D. M. Tennant, J. E. Bjorkholm, R. M. D'Souza, L. Eichner, R. R. Freeman, J. Z. Pastalan, L. H. Szeto, O. R. Wood II, T. E. Jewell, W. M. Mansfield, W. K. Waskiewicz, D. L. White, D. L. Windt, and A. A. MacDowell, "Reflective mask technologies and imaging results in soft x-ray projection lithography", *Journal of Vacuum Science and Technology B*, **9**(6), pp. 3176-83, 1991.
- [53] A. M. Hawryluk, N. M. Ceglio, and D. P. Gaines, "Reflection mask technology for x-ray projection lithography", *Journal of Vacuum Science and Technology B*, **7** (6), pp. 1702-4, 1989.
- [54] K. B. Nguyen, D. T. Attwood, T. Mizota, T. Haga, and H. Kinoshita, "Imaging of EUV lithographic masks with programmed substrate defects", *OSA Proceedings on Extreme Ultraviolet Lithography*, **23**, edited by F. Zernike and D. T. Attwood, (Optical Society of America, Washington DC, 1995), pp. 193-203.

- [55] S. P. Vernon, D. R. Kania, P. A. Kearney, R. A. Levesque, A. V. Hayes, B. Druz, E. Osten, R. Rajan, and H. Hedge, "Reticle blanks for extreme ultraviolet lithography: ion beam sputter deposition of low defect density Mo/Si multilayers", *OSA Trends in Optics and Photonics Volume on Extreme Ultraviolet Lithography*, 4, edited by G. D. Kubiak and D. R. Kania, (Optical Society of America, Washington DC, 1996), pp. 44-8.
- [56] K. B. Nguyen, A. A. MacDowell, K. Fujii, D. M. Tennant, and L. A. Fetter, "At-wavelength inspection of EUVL mask defects with a 1x Offner ring-field system", *OSA Trends in Optics and Photonics Volume on Extreme Ultraviolet Lithography*, 4, edited by G. D. Kubiak and D. R. Kania, (Optical Society of America, Washington DC, 1996), pp. 49-53.
- [57] D. R. Kania, D. P. Gaines, D. S. Sweeney, G. E. Sommargren, B. La Fontaine, S. P. Vernon, D. A. Tichenor, J. E. Bjorkholm, F. Zernike, and R. N. Kestner, "Precision optical aspheres for extreme ultraviolet lithography", *Journal of Vacuum Science and Technology B*, 14 (6), pp. 3706-8, 1996.
- [58] T. E. Jewell, "Reflective systems design study for soft x-ray projection lithography", *Journal of Vacuum Science and Technology B*, 8 (6), pp. 1519-23, 1990.
- [59] D. L. Shealy, C. Wang, and V. K. Viswanathan, "Design and analysis of multimirror soft-x-ray projection lithography systems", *OSA Proceedings on Soft X-Ray Projection Lithography*, 12, edited by J. Bokor, (Optical Society of America, Washington DC, 1991), pp. 22-6.
- [60] V. K. Viswanathan and B. E. Newman, "Development of reflective optical systems for XUV projection lithography", *OSA Proceedings on Soft X-Ray Projection Lithography*, 12, edited by J. Bokor, (Optical Society of America, Washington DC, 1991), pp. 30-3.
- [61] T. E. Jewell, "Four-mirror ring-field system for EUV projection lithography", *OSA Proceedings on Extreme Ultraviolet Lithography*, 23, edited by F. Zernike and D. T. Attwood, (Optical Society of America, Washington DC 1995), pp. 98-102.
- [62] W. C. Sweatt, "Ring-field EUVL camera with large etendu", *OSA Trends in Optics and Photonics Volume on Extreme Ultraviolet Lithography*, 4, edited by G. D. Kubiak and D. R. Kania, (Optical Society of America, Washington DC, 1996), pp. 178-80.
- [63] T. E. Jewell, K. P. Thompson, and J. M. Rodgers, "Reflective optical designs for soft x-ray projection lithography", *Proceedings of the SPIE*, 1527, pp. 163-73, 1991.
- [64] T. E. Jewell, "Optical system design issues in development of projection camera for EUV lithography", *Proceedings of the SPIE*, 2437, pp. 340-6, 1995.

- [65] G. D. Kubiak, D. A. Tichenor, W. W. Chow, W. C. Sweatt, and M. D. Himel, "Resist performance in soft x-ray projection lithography", *Proceeding of the SPIE*, **1924**, pp. 18-29, 1993.
- [66] W. M. Mansfield, J. E. Bjorkholm, A. A. MacDowell, R. R. Freeman, L. H. Szeto, G. N. Taylor, D. M. Tennant, W. K. Waskiewicz, D. L. Windt, D. L. White, O. R. Wood II, R. M. D'Souza, and A. R. Neureuther, "Effects of absorption on resist performance in soft-x-ray projection lithography", *OSA Proceedings on Soft X-Ray Projection Lithography*, **12**, edited by J. Bokor, (Optical Society of America, Washington DC, 1991), pp. 129-31.
- [67] G. D. Kubiak, E. M. Kneeder, K. W. Berger, and R. H. Stulen, "Resist characterization at soft-x-ray wavelengths", *OSA Proceedings on Soft X-Ray Projection Lithography*, **12**, edited by J. Bokor, (Optical Society of America, Washington DC, 1991), pp. 124-8.
- [68] S. Wolf and R. N. Tauber, *Silicon Processing for the VLSI Era: Volume 1 - Process Technology*, (Lattice Press, Sunset Beach, California, 1986), Ch. 12.
- [69] K. Early, D. M. Tennant, D. Y. Jeon, P. P. Mulgrew, A. A. MacDowell, O. R. Wood II, G. D. Kubiak, and D. A. Tichenor, "Characterization of AZ PN114 resist for soft-x-ray projection lithography", *Applied Optics*, **32** (34), pp. 7044-49, 1993.
- [70] D. R. Wheeler, G. D. Kubiak, A. K. Ray-Chaudhuri, and C. Henderson, "Basic issues associated with four potential EUV resist schemes", *OSA Trends in Optics and Photonics Volume on Extreme Ultraviolet Lithography*, **4**, edited by G. D. Kubiak and D. R. Kania, (Optical Society of America, Washington DC, 1996), pp. 33-8.
- [71] G. N. Taylor, R. S. Hutton, S. M. Stein, C. H. Boyce, B. LaFontaine, A. A. MacDowell, D. R. Wheeler, G. D. Kubiak, A. K. Ray-Chaudhuri, K. W. Berger, and D. A. Tichenor, "Extreme UV resist technology: the limits of silylated resist resolution", *Proceedings of the SPIE*, **2437**, pp. 308-30, 1995.
- [72] M. Hanratty, "Surface imaging resists: promises, practices and prospects", *OSA Trends in Optics and Photonics Volume on Extreme Ultraviolet Lithography*, **4**, edited by G. D. Kubiak and D. R. Kania, (Optical Society of America, Washington DC, 1996), pp. 28-32.
- [73] D. L. Windt, W. K. Waskiewicz, and J. E. Griffith, "Surface finish requirements for soft x-ray mirrors", *Applied Optics*, **33** (10), pp. 2025-31, 1994.
- [74] M. D. Himel, "Optic fabrication and metrology for soft x-ray projection lithography", *OSA Proceedings on Soft X-Ray Projection Lithography*, **18**, edited by A. M. Hawryluk and R. H. Stulen, (Optical Society of America, Washington DC, 1993), pp. 108-9.

- [75] D. P. Gaines, D. W. Sweeney, K. W. DeLong, S. P. Vernon, S. L. Baker, D. A. Tichenor, and R. Kestner, "Surface characterization of optics for EUV lithography", *OSA Trends in Optics and Photonics Volume on Extreme Ultraviolet Lithography*, 4, edited by G. D. Kubiak and D. R. Kania, (Optical Society of America, Washington DC, 1996), pp. 103-6.
- [76] J. D. Briers, "Interferometric testing of optical systems and components: a review", *Optics and Laser Technology*, 4 (1), pp. 28-41, 1972.
- [77] E. R. Cochran, "Limitations of phase-measuring interferometry for surface characterization and testing: a review", *Proceedings of the SPIE*, 1776, pp. 151-7, 1992.
- [78] D. Malacara, ed., *Optical Shop Testing*, Second Edition, (John Wiley & Sons, Inc., New York, 1992), Ch. 14.
- [79] J. C. Wyant and V. P. Bennett, "Using computer generated holograms to test aspheric wavefronts", *Applied Optics*, 11 (12), pp. 2833-9, 1972.
- [80] J. C. Wyant, "Interferometric testing of aspheric surfaces", *Proceeding of the SPIE*, 816, pp. 19-39, 1987.
- [81] G. E. Sommargren, "Phase shifting diffraction interferometry for measuring extreme ultraviolet optics", *OSA Trends in Optics and Photonics Volume on Extreme Ultraviolet Lithography*, 4, edited by G. D. Kubiak and D. R. Kania, (Optical Society of America, Washington DC, 1996), pp. 108-12.
- [82] R. Kestner, "Precision asphere fabrication and metrology to tolerances <1 nm rms", *Optical Society of America Topical Meeting on Extreme Ultraviolet Lithography, Boston, Massachusetts, May 1-3, 1996*, not published.
- [83] K. A. Goldberg, R. Beguiristain, J. Bokor, H. Medeck, K. Jackson, D. T. Attwood, G. E. Sommargren, J. P. Spallas, and R. Hostetler, "Point diffraction interferometer at EUV wavelengths", *OSA Proceedings on Extreme Ultraviolet Lithography*, 23, edited by F. Zernike and D. T. Attwood, (Optical Society of America, Washington DC 1995), pp. 134-41.
- [84] K. A. Goldberg, R. Beguiristain, J. Bokor, H. Medeck, K. Jackson, D. T. Attwood, G. E. Sommargren, J. P. Spallas, and R. Hostetler, "At-wavelength testing of optics for EUV", *Proceedings of the SPIE*, 2437, pp. 347-54, 1995.
- [85] K. A. Goldberg, R. Beguiristain, J. Bokor, H. Medeck, D. T. Attwood, K. Jackson, E. Tejnil, and G. E. Sommargren, "Progress toward $\lambda/20$ EUV interferometry", *Journal of Vacuum Science and Technology B*, 13 (6), pp. 2923-7, 1995.

- [86] K. A. Goldberg, E. Tejnil, S. H. Lee, H. Medeck, D. T. Attwood, K. H. Jackson, and J. Bokor, "Characterization of an EUV Schwarzschild objective using phase-shifting point diffraction interferometry", *Proceedings of the SPIE*, **3048**, pp. 264-70, 1997.
- [87] E. Tejnil, K. A. Goldberg, H. Medeck, R. Beguiristain, J. Bokor, and D. T. Attwood, "Phase-shifting point diffraction interferometry for at-wavelength testing of lithographic optics", *OSA Trends in Optics and Photonics Volume on Extreme Ultraviolet Lithography*, **4**, edited by G. D. Kubiak and D. R. Kania, (Optical Society of America, Washington DC, 1996), pp. 118-23.
- [88] E. Tejnil, K. A. Goldberg, S. H. Lee, H. Medeck, P. J. Batson, P. E. Denham, A. A. MacDowell, J. Bokor, D. T. Attwood, "At-wavelength interferometry for extreme ultraviolet lithography", *Journal of Vacuum Science and Technology B*, **15** (6), in press, 1997.
- [89] Z. Tan, A. A. MacDowell B. LaFontaine, J. Russo, J. E. Bjorkholm, D. Tennant, D. Taylor, M. Himel, O. R. Wood, II, W. K. Waskiewicz, D. L. Windt, D. White, S. Spector, A. K. Ray-Chaudhuri, and R. H. Stulen, "At-wavelength metrology of EUV cameras using lateral-shearing interferometry", *OSA Proceedings on Extreme Ultraviolet Lithography*, **23**, edited by F. Zernike and D. T. Attwood, (Optical Society of America, Washington DC 1995), pp. 151-60.
- [90] A. K. Ray-Chaudhuri, R. H. Stulen, W. Ng, F. Cerrina, S. Spector, Z. Tan, J. Bjorkholm, and D. Tennant, "EUV Metrology of Multilayer Optics", *OSA Proceedings on Extreme Ultraviolet Lithography*, **23**, edited by F. Zernike and D. T. Attwood, (Optical Society of America, Washington DC, 1995), pp. 161-6.
- [91] J. E. Bjorkholm, A. A. MacDowell, O. R. Wood II, Z. Tan J., B. LaFontaine, and D. M. Tennant, "Phase-measuring interferometry using extreme ultraviolet radiation", *Journal of Vacuum Science and Technology B*, **13** (6), pp. 2919-22, 1995.
- [92] A. K. Ray-Chaudhuri, K. D. Krenz, R. P. Nissen, S. J. Haney, C. H. Fields, W. C. Sweatt, and A. A. MacDowell, "Development of extreme ultraviolet interferometry for laser plasma source operation", *OSA Trends in Optics and Photonics Volume on Extreme Ultraviolet Lithography*, **4**, edited by G. D. Kubiak and D. R. Kania, (Optical Society of America, Washington DC, 1996), pp. 128-32.
- [93] A. K. Ray-Chaudhuri, K. D. Krenz, R. P. Nissen, S. J. Haney, C. H. Fields, W. C. Sweatt, and A. A. MacDowell, "Initial results from an extreme ultraviolet interferometer operating with a compact laser plasma source", *Journal of Vacuum Science and Technology B*, **14** (6), pp. 3964-8, 1996.

- [94] B. LaFontaine, D. L. White, A. A. MacDowell, Z. Tan, D. M. Tennant, O. R. Wood II, "Extreme ultraviolet moiré interferometry", *OSA Proceedings on Extreme Ultraviolet Lithography*, **23**, edited by F. Zernike and D. T. Attwood, (Optical Society of America, Washington DC, 1995), pp. 167-70.
- [95] M. Born and E. Wolf, *Principles of Optics*, Sixth Edition, (Pergamon Press, Oxford, 1980), Ch 9.
- [96] V. N. Mahajan, "Zernike circle polynomials and optical aberrations of systems with circular pupils", *Applied Optics*, **33** (34), pp. 8121-4, 1994.
- [97] V. N. Mahajan, "Zernike annular polynomials and optical aberrations of systems with annular pupils", *Applied Optics*, **33** (34), pp. 8125-7, 1994.
- [98] in Reference 78, Ch. 13.
- [99] K. L. Lewotsky, A. Kotha, and J. E. Harvey, "Performance limitations of imaging microscopes for soft x-ray applications", *Proceedings of the SPIE*, **1741**, pp. 32-9, 1992.
- [100] E. L. Church and P. Z. Takacs, "Specification of surface figure and finish in terms of system performance", *Applied Optics*, **32** (19), pp. 3344-53, 1993.
- [101] D. G. Stearns, D. P. Gaines, B. LaFontaine, G. E. Sommargren, D. W. Sweeney, D. R. Kania, and N. M. Ceglio, "Nonspecular scattering in EUV lithography: determining specifications for surface finish", *OSA Trends in Optics and Photonics Volume on Extreme Ultraviolet Lithography*, **4**, edited by G. D. Kubiak and D. R. Kania, (Optical Society of America, Washington DC, 1996), pp. 167-8.
- [102] W. B. Wetherell, "Effects of mirror surface ripple on image quality", *Proceedings of the SPIE*, **332**, pp. 335-351, 1982.
- [103] W. P. Linnik, "A simple interferometer for the investigation of optical systems", *Proceedings of the Academy of Sciences of the U.S.S.R.*, **5**, pp. 208-210, 1933.
- [104] R. N. Smartt and J. Strong, "Point-diffraction interferometer", *Journal of the Optical Society of America*, **62**, p. 737A, 1972.
- [105] R. N. Smartt and W. H. Steel, "Theory and application of point-diffraction interferometers", *Japanese Journal of Applied Physics*, **14** (suppl. 14-1), pp. 351-6, 1975.
- [106] in Reference 78, Ch. 3.
- [107] H. Meddecki, E. Tejnil, K. A. Goldberg, and J. Bokor, "A phase-shifting point diffraction interferometer", *Optics Letters*, **21** (19), pp. 1526-8, 1996.

- [108] O. Y. Kwon, "Multichannel phase-shifted interferometer", *Optics Letters*, **9** (2), pp. 59-61, 1984.
- [109] R. J. Speer, M. Chrisp, D. Turner, S. Mrowka, and K. Tregidgo, "Grazing incidence interferometry: the use of the Linnik interferometer for testing image-forming reflection systems", *Applied Optics*, **18** (12), pp. 2003-12, 1979.
- [110] G. R. Fowles, *Introduction to Modern Optics*, Second Edition, (Dover Publications, Inc., New York, 1989), Ch. 5.
- [111] in Reference 95, Ch. 8.
- [112] E. W. Marchand and E. Wolf, "Diffraction at small apertures in black screens", *Journal of the Optical Society of America*, **59** (1), pp. 79-90, 1969.
- [113] C. Cerjan, "Scalar wave diffraction from a circular aperture", *OSA Proceedings on Extreme Ultraviolet Lithography*, **23**, edited by F. Zernike and D. T. Attwood, (Optical Society of America, Washington DC 1995), pp. 142-150.
- [114] in Reference 95, Ch 11.
- [115] in Reference 12, Ch. 9.
- [116] K. A. Goldberg, E. Tejnil, and J. Bokor, "A 3-D numerical study of pinhole diffraction to predict the accuracy of EUV point diffraction interferometry", *OSA Trends in Optics and Photonics Volume on Extreme Ultraviolet Lithography*, **4**, edited by G. D. Kubiak and D. R. Kania, (Optical Society of America, Washington DC, 1996), pp. 133-7.
- [117] J. W. Goodman, *Introduction to Fourier Optics*, Second Edition, (McGraw-Hill Book Company, Inc., New York, 1996), Ch 5.
- [118] S. Ramo, J. R. Whinnery, and T. Van Duzer, *Fields and Waves in Communication Electronics*, Second Edition, (John Wiley and Sons, New York, 1984), Ch. 14.
- [119] J. Y. Wang and D. E. Silva, "Wave-front interpretation with Zernike polynomials", *Applied Optics*, **19** (9), pp. 1510-18, 1980.
- [120] *Code V Reference Manual*, ver. 8.10, p. 2A-595-6, (Optical Research Associates, Pasadena CA, 1996).
- [121] V. N. Mahajan, *Aberration Theory Made Simple*, (SPIE Optical Engineering Press, Bellingham, Washington, 1991).
- [122] B. R. A. Nijboer, "The diffraction theory of optical aberrations. Part I: General discussion of the geometrical aberrations", *Physica*, **10** (8), pp. 679-92, 1943.
- [123] E. H. Anderson, private communication.

- [124] J. P. Spallas, R. E. Hostetler, G. E. Sommargren, and D. R. Kania, "Fabrication of extreme-ultraviolet point-diffraction interferometer aperture arrays", *Applied Optics*, **34** (28), pp. 6393-8, 1995.
- [125] D. M. Tennant, E. L. Raab, M. M. Becker, M. L. O'Malley, J. E. Bjorkholm, and R. W. Epworth, "High resolution germanium zone plates and apertures for soft x-ray focalometry", *Journal of Vacuum Science and Technology B*, **8** (6), pp. 1970-4, 1990.
- [126] C. H. Fields, W. G. Oldham, A. K. Ray-Chaudhuri, K. D. Krenz, and R. H. Stulen, "Initial experiments on direct aerial image measurements in the extreme ultraviolet", *OSA Trends in Optics and Photonics Volume on Extreme Ultraviolet Lithography*, **4**, edited by G. D. Kubiak and D. R. Kania, (Optical Society of America, Washington DC, 1996), pp. 124-7.
- [127] in Reference 95, Ch 10.
- [128] J. W. Goodman, *Statistical Optics*, Second Edition, (John Wiley and Sons, New York, 1985), Ch 5.
- [129] J. W. Goodman, "Statistical properties of laser speckle patterns", *Laser Speckle and Related Phenomena*, edited by J. C. Dainty, (Springer-Verlag, Berlin, 1984), pp. 9-75.
- [130] P. Z. Peebles, Jr., *Probability, Random Variables, and Random Signal Principles*, Third Edition, (McGraw-Hill, Inc., New York, 1993), Ch. 5.
- [131] R. Coisson, "Spatial coherence of synchrotron radiation", *Applied Optics*, **34** (5), pp. 904-8, 1995.
- [132] K.-J. Kim, "A new formulation of synchrotron radiation optics using the Wigner distribution", *Proceedings of the SPIE*, **582**, pp. 2-9, 1985.
- [133] *ALS Handbook*, Pub-643, Rev. 2, (Lawrence Berkeley Laboratory, Berkeley, California, 1989).
- [134] D. T. Attwood, private communication.
- [135] in Reference 128, Ch. 7.
- [136] Z. Malacara and D. Malacara, "Design of lenses to project the image of a pupil in optical testing interferometers", *Applied Optics*, **34** (4), pp. 739-42, 1995.
- [137] D. W. Robinson and G. T. Reid, eds., *Interferogram Analysis: Digital Fringe Pattern Measurement Techniques*, (Institute of Physics Publishing, Bristol, 1993), Ch. 3.
- [138] in Reference 137, Ch. 4.

- [139] P. Hariharan, B. F. Oreb, and T. Eiju, "Digital phase-shifting interferometry: a simple error-compensating phase calculation algorithm", *Applied Optics*, **26** (13), pp. 2504-5, 1987.
- [140] K. Creath, "Comparison of phase-measurement algorithms", *Proceedings of the SPIE*, **680**, pp. 19-28, 1986.
- [141] J. Schwider, R. Burow, K.-E. Elssner, J. Grzanna, R. Spolaczyk, and K. Merkel, "Digital wave-front measuring interferometry: some systematic error sources", *Applied Optics*, **22** (21), pp. 3421-32, 1983.
- [142] K. A. Goldberg, *Extreme Ultraviolet Interferometry*, Ph. D. Thesis, (University of California at Berkeley, Berkeley CA, 1997).
- [143] M. Takeda, H. Ina, and S. Kobayashi, "Fourier-transform method of fringe pattern analysis for computer-based topography and interferometry", *Journal of the Optical Society of America*, **72** (1), pp. 156-60, 1982.
- [144] W. W. Macy, Jr., "Two-dimensional fringe-pattern analysis", *Applied Optics*, **22** (23), pp. 3898-901, 1983.
- [145] D. J. Bone, H.-A. Bachor, and R. J. Sandeman, "Fringe-pattern analysis using a 2-D Fourier transform", *Applied Optics*, **25** (10), pp. 1653-60, 1986.
- [146] T. Kreis, "Digital holographic interference-phase measurement using the Fourier transform method", *Journal of the Optical Society of America A*, **3** (6), pp. 847-55, 1986.
- [147] in Reference 137, Ch. 5.
- [148] in Reference 137, Ch. 6.
- [149] R. J. Green and J. G. Walker, "Phase unwrapping using a-priori knowledge about the band limits of a function (optical interferometry)", *Proceedings of the SPIE*, **1010**, pp. 36-43, 1989.
- [150] D. J. Fisher, J. T. O'Bryan, R. Lopez, and H. P. Stahl, "Vector formulation for interferogram surface fitting", *Applied Optics*, **32** (25), pp. 4738-43, 1993.
- [151] E. Tejnil, K. A. Goldberg, E. H. Anderson, J. Bokor, "Zonal placement errors in zone plate lenses", *OSA Trends in Optics and Photonics Volume on Extreme Ultraviolet Lithography*, **4**, edited by G. D. Kubiak and D. R. Kania, (Optical Society of America, Washington DC, 1996), pp. 138-42.
- [152] in Reference 10, Ch. 8 and Ch. 9.

- [153] T. Wilhein, D. Rothweiler, A. Tusche, F. Scholze, and W. Meyer-Ilse, "Thinned, back-illuminated CCDs for x-ray microscopy", *X-Ray Microscopy IV*, edited by V. Aristov and A. I. Erko, Chernogolovka, Russia, 1994, pp. 470-474.
- [154] W. Meyer-Ilse, T. Wilhein, and P. Guttmann, "Thinned, back-illuminated CCD for x-ray microscopy", *Proceedings of the SPIE*, **1900**, pp. 241-5, 1993.
- [155] E. H. Anderson, V. Boegli, M. L. Schattenburg, and D. Kern, "Metrology of electron-beam lithography systems using holographically produced reference samples", *Journal of Vacuum Science and Technology B*, **9** (6), pp. 3606-11, 1991.
- [156] E. H. Anderson, V. Boegli, and L. P. Muray, "Electron beam lithography digital pattern generator and electronics for generalized curvilinear structures", *Journal of Vacuum Science and Technology B*, **13** (6), pp. 2529-34, 1995.
- [157] V. E. Levashov and A. V. Vinogradov, "Analytical theory of zone plate efficiency", *Physical Review E*, **49** (6, pt. B), pp. 5797-803, 1994.
- [158] *Center for X-Ray Optics X-Ray Data Booklet*, Pub-490, Rev., (Lawrence Berkeley Laboratory, Berkeley, California, 1986).
- [159] E. M. Gullikson, private communication.
- [160] D. A. Tichenor, G. D. Kubiak, M. E. Malinowski, R. H. Stulen, S. J. Haney, K. W. Berger, R. P. Nissen, R. L. Schmitt, G. A. Wilkerson, L. A. Brown, P. A. Spence, P. S. Jin, W. C. Sweatt, W. W. Chow, J. E. Bjorkholm, R. R. Freeman, M. D. Himel, A. A. MacDowell, D. M. Tennant, O. R. Wood II, W. K. Waskiewicz, D. L. White, D. L. Windt, and T. E. Jewell, "Development and characterization of a 10x Schwarzschild system for SXPL", *OSA Proceedings on Soft X-Ray Projection Lithography*, **18**, edited by A. M. Hawryluk and R. H. Stulen, (Optical Society of America, Washington DC, 1993), pp. 79-82.
- [161] Princeton Instruments, Inc., Trenton NJ, product information on the internet, <http://www.prinst.com/imagprod.htm#1024sf>, 1997.
- [162] Photometrics, Ltd., Tucson AZ, product information on the internet, <http://www.photomet.com/products/prod.cam.html>, 1997.
- [163] Scientific Imaging Technologies, Inc. (SITE), formerly Tektronix, Beaverton, OR, Model ST-003 CCD, <http://www.site-inc.com/003.html>, product information on the internet, 1997.
- [164] R. E. Ziemer, W. H. Tranter, and D. R. Fannin, *Signals and Systems: Continuous and Discrete*, Second Edition, (Macmillan Publishing Company, New York, 1989), Ch. 4.
- [165] in Reference 117, Ch. 3.

- [166] K. Boller, R. P. Haelbich, H. Hogrefe, W. Jark, "Investigation of carbon contamination of mirror surfaces exposed to synchrotron radiation", *Nuclear Instruments and Methods in Physics Research*, **208** (1-3), pp. 273-9, 1983.
- [167] B. R. Muller, J. Feldhaus, F. Schafers, and F. Eggenstein, "Cleaning of carbon contaminated vacuum ultraviolet optics: influence on surface roughness and reflectivity", *Review of Scientific Instruments*, **63** (1), pp. 1428-31, 1992.
- [168] R. A. Rosenberg, J. A. Smith, and D. J. Wallace, "Plasma cleaning of beamline optical components: contamination and gas composition effects", *Review of Scientific Instruments*, **63** (1), pp. 1486-9, 1992.
- [169] W. K. Warburton and P. Pianetta, "In situ optical element cleaning with photon activated oxygen", *Nuclear Instruments and Methods in Physics Research A*, **A319** (1-3), pp. 240-3, 1992.
- [170] D. L. Windt, private communication.
- [171] T. E. Jewell, "Effect of amplitude and phase dispersion on images in multilayer-coated soft-x-ray projection systems", *OSA Proceedings on Soft X-Ray Projection Lithography*, **12**, edited by J. Bokor, (Optical Society of America, Washington DC, 1991), pp. 113-8.
- [172] in Reference 118, Ch. 8.
- [173] J. H. Underwood and T. W. Barbee, Jr., "Layered synthetic microstructures as Bragg diffractors for x rays and extreme ultraviolet: theory and predicted performance", *Applied Optics*, **20** (17), pp. 3027-34, 1981.
- [174] in Reference 11, Ch. 7.
- [175] V. G. Kohn, "On the theory of reflectivity by an x-ray multilayer mirror", *Physica Status Solidi B*, **187** (1), pp. 61-70, 1995.
- [176] A. Caticha, "Reflection and transmission of x rays by graded interfaces", *Physical Review B*, **52** (13), pp. 9214-23, 1995.
- [177] G. D. Kubiak, R. Q. Hwang, M. T. Schulberg, D. A. Tichenor, and K. Early, "Chemically amplified soft-x-ray resist: sensitivity, resolution, and molecular photodesorption", *Applied Optics*, **32** (34), pp. 7036-7043, 1993.
- [178] K. K. Toh and A. R. Neureuther, "Identifying and monitoring effects of lens aberrations in projection printing", *Proceedings of the SPIE*, **772**, pp. 202-9, 1987.

- [179] E. L. Church and P. Z. Takacs, "Specification of the figure and finish of EUV mirror in terms of performance requirements", *OSA Proceedings on Extreme Ultraviolet Lithography*, **23**, edited by F. Zernike and D. T. Attwood, (Optical Society of America, Washington DC 1995), pp. 77-82.
- [180] D. G. Stearns, "Image degradation due to scatter in a distributed optical system: a theoretical treatment", not published, 1996.
- [181] J. E. Harvey, K. L. Lewotsky, and A. Kotha, "Effects of surface scatter on the optical performance of x-ray synchrotron beam-line mirrors", *Applied Optics*, **34** (16), pp. 3024-32, 1995.
- [182] E. Spiller, D. Stearns, and M. Krumrey, "Multilayer x-ray mirrors: interfacial roughness, scattering, and image quality", *Journal of Applied Physics*, **74** (1), pp. 107-18, 1993.
- [183] R. E. Parks, "Optical specifications and tolerances for large optics", *Proceedings of the SPIE*, **406**, pp. 98-105, 1983.
- [184] D. A. Tichenor, A. K. Ray-Chaudhuri, G. D. Kubiak, K. B. Nguyen, S. J. Haney, K. W. Berger, R. P. Nissen, Y. E. Perras, P. S. Lin, L. I. Weingarten, P. N. Keifer, R. H. Stulen, R. N. Shagam, W. C. Sweatt, T. G. Smith, O. R. Wood, II, A. A. MacDowell, J. E. Bjorkholm, T. E. Jewell, F. Zernike, B. L. Fix, and H. W. Hauschildt, "Progress in the development of EUV imaging systems", *OSA Trends in Optics and Photonics Volume on Extreme Ultraviolet Lithography*, **4**, edited by G. D. Kubiak and D. R. Kania, (Optical Society of America, Washington DC, 1996), pp. 2-8.
- [185] D. Golini, S. Jacobs, Y. Zhou, E. Fess, and M. Atwood, "Aspheric surface generation requirements for magnetorheological finishing", *OSA Trends in Optics and Photonics Volume on Extreme Ultraviolet Lithography*, **4**, edited by G. D. Kubiak and D. R. Kania, (Optical Society of America, Washington DC, 1996), pp. 98-102.
- [186] H. H. Hopkins, "On the diffraction theory of optical images", *Proceedings of the Royal Society A*, **217**, pp. 408-432, 1953.
- [187] M. Abramowitz and I. Stegun, eds., *Handbook of Mathematical Functions with Formulas, Graphs, and Mathematical Tables*, (Dover Publications, Inc., New York, 1965), Ch. 9.
- [188] J. E. Gortych and D. Williamson, "Effects of higher-order aberrations on the process window", *Proceedings of the SPIE*, **1463**, pp. 368-81, 1991.
- [189] C. J. Progler and D. M. Byrne, "Merit functions for lithographic lens design", *Journal of the Vacuum Science and Technology B*, **14** (6), pp. 3714-8, 1996.

- [190] A. E. Rosenbluth, D. Goodman, and B. J. Lin, "A critical examination of submicron optical lithography using simulated projection images", *Journal of Vacuum Science and Technology B*, **1** (4), pp. 1190-5, 1983.
- [191] J. E. Gortych and D. S. Goodman, "Heights and positions of maxima of partially coherent images of clear lines", *Applied Optics*, **33** (10), pp. 2069-74, 1994.
- [192] J. E. Gortych and D. S. Goodman, "Line ratio and image formation in photolithographic projectors", *Applied Optics*, **33** (10), pp. 2075-82, 1994.
- [193] H. H. Hopkins and B. Zalar, "Aberration tolerances based on the line spread function", *Journal of Modern Optics*, **34** (3), pp. 371-406, 1987.